Modification of the physical properties of intermetallics with the CeScSi structure type by light element insertion (H, C)

Tadhg Mahon

To cite this version:

Tadhg Mahon. Modification of the physical properties of intermetallics with the CeScSi structure type by light element insertion (H, C). Material chemistry. Université de Bordeaux, 2017. English. NNT : 2017BORD0779 . tel-01699063

HAL Id: tel-01699063

https://theses.hal.science/tel-01699063

Submitted on 16 Feb 2018

THÈSE PRÉSENTÉE
POUR OBTENIR LE GRADE DE

DOCTEUR DE

L'UNIVERSITÉ DE BORDEAUX

ÉCOLE DOCTORALE DES SCIENCES CHIMIQUES

PHYSICO-CHIMIE DE LA MATIÈRE CONDENSÉE

Par **Tadhg MAHON**

Modification of the physical properties of intermetallics with the CeScSi structure type by light element insertion (H, C)

Soutenue le 31/10/2017

Membres du jury :
M. GAUDIN, Etienne
Maître de Conferences, ICMCB-CNRS, Directeur de thèse
Mme. TENCÉ, Sophie
Chargée de Recherche, ICMCB-CNRS, Co-directrice de thèse
M. MAGLIONE, Mario,
Directeur de Recherche, ICMCB- CNRS, Examinateur
M. YARTYS, Volodymyr,
Professor, Institute for Energy Technology, Kjeller, Norway, Rapporteur
Mme. PAUL-BONCOUR, Valérie,
Directeur de Recherche, ICMPE-CNRS, Rapporteur
M. ISNARD, Olivier,
Professeur, Université Grenoble Alpes, Institut Néel CNRS, President
M. MALAMAN, Bernard,
Professeur Emérite, Université de Lorraine, Institut Jean Lamour CNRS, Examinateur
M. CHEVALIER, Bernard,
Directeur de Recherche Emérite, ICMCB- CNRS, Invité

Titre: Modification des propriétés physiques d'intermétalliques de type structural CeScSi par insertion d'éléments légers (H, C)

Résumé: Dans ce travail on a étudié l’insertion d’éléments légers dans des intermétalliques *TRMX* (*TR* = Terre-Rare, *M* = métal de transition, *X* = Si ou Ge) qui cristallisent dans le type structural CeScSi. Cette structure contient deux types de sites interstitiels dans lesquels il est possible d’insérer des éléments légers : un site tétraédrique TR_4 et un site octaédrique TR_2M_4.

Pour tous les composés étudiés au cours de ce travail (GdScGe, NdScSi, CeTiGe,...) on a observé systématiquement une insertion des atomes d’hydrogène dans les sites tétraédriques TR_4. Dans certains cas les atomes d’hydrogène occupent également les sites octaédriques TR_2M_4. Ceci a conduit à l’obtention de deux type d’hydrures : $TRMX$H et $TRMX\mathrm{H}_{1,5}$ pour lesquels on observe une très forte diminution de l’ordre magnétique et des changements significatifs des propriétés de conduction électrique par rapport aux phases initiales.

L’insertion de carbone par fusion des éléments à l’aide d’une procédure en plusieurs étapes permet d’obtenir des phases $TR\mathrm{ScSiC}_x$ avec un taux de carbone variable ($0 \leq x \leq 0{,}5$) qui correspond à un remplissage plus ou moins partiel du site octaédrique $\mathrm{TR_2M_4}$. Cette insertion de carbone induit également une diminution des températures d’ordre magnétique (de Curie et de Néel respectivement pour NdScSi et CeScSi).

Dans une deuxième étape on a montré qu’il est possible d’insérer partiellement de l’hydrogène dans les sites $\mathrm{TR_4}$ laissés vacants. Des changements de type d’ordre magnétique ont été observés contrairement aux hydrures et carbures précédents. Des études systématiques de diffraction neutronique ont permis de déterminer les structures magnétiques à basse température de la plupart de ces nouvelles phases d’insertion.

Mots clés: Intermétalliques, Cristallographie, Magnétisme, Hydrure, Carbure, Insertion

Title: Modification of the physical properties of intermetallics with the CeScSi structure type by light element insertion (H, C)

Abstract: Rare earth based intermetallics *RTX* (*R* = rare earth, *T* = transition metal, *X* = Si, Ge) crystallising in the layered CeScSi structure type contain vacant interstitial sites that can be filled by light elements to modify the initial physical properties. Hydrogenation studies on CeScSi-type compounds show that hydrogen atoms are inserted in the tetrahedral (R_4) sites and sometimes in the octahedral ($R_2\mathrm{Sc}_4$) sites. This causes an anisotropic expansion of the unit cell with a decreasing and c strongly increasing. It also drastically lowers the magnetic ordering temperatures of the parent materials and changes their resistivity behaviour.

We developed a multi-step process to synthesise intermetallic carbides ($RTX\mathrm{C}_X$) with controllable C content. Neutron diffraction shows that C occupies only the $R_2\mathrm{Sc}_4$ sites of the *R*ScSi compounds (*R* = La-Nd and Gd) causing the increase of the *a* cell parameter and the decrease of the *c* one. We obtain $R\mathrm{ScSiC}_X$ solid solutions with $0.0 \leq x \leq 0.5$ for *R* = Ce and $0.25 \lesssim x \leq 0.5$ for *R* = Nd. Carburation reduces the Curie and Néel temperature of the NdScSi and CeScSi pristine phases, respectively.

As the R_4 tetrahedra are empty in the $R\mathrm{ScSiC}_X$ carbides, we have succeeded in hydrogenating these materials (*R* = Ce and Nd). However, due to the antagonistic structural distortion induced by C and H insertion respectively, only around 15 % of the R_4 sites could be filled for a final composition of $R\mathrm{ScSiC}_{0.5}\mathrm{H}_{\sim 0.15}$. It also changes the type of magnetic behaviour from a ferromagnetic order to an antiferromagnetic order in $\mathrm{NdScSiC}_{0.5}$.

Neutron diffraction experiments have been performed to determine the magnetic structures of these new insertion compounds.

Keywords: Intermetallics, Crystallography, Magnetism, Hydride, Carbide, Insertion

Institut de Chimie de la Matière Condensée de Bordeaux

ICMCB/CNRS – UPR 9048
87 Avenue du Dr Albert Schweitzer, 33600 Pessac

For my Grandmother, whose
belief in the transformative
power of education led me to
this point

Table of Contents

Résumé du Manuscrit de Thèse de Tadhg MAHON

Titre : Modification des propriétés physiques d'intermétalliques de type structural CeScSi par insertion d'éléments légers (H, C)

Thèse effectuée à l'Institut de Chimie de la Matière Condensée de Bordeaux (ICMCB) sous la direction de Sophie TENCÉ et Etienne GAUDIN

Ce travail de thèse concerne l'influence de l'insertion d'atomes d'hydrogène et de carbone sur les propriétés structurales et magnétiques de composés intermétalliques ternaires de type CeFeSi ou CeScSi. Le mémoire de thèse est constitué de cinq chapitres : le premier constitue un rappel de l'état de l'art sur le sujet et expose le contexte scientifique et les objectifs de ce travail, le second présente les différentes méthodes expérimentales de synthèse et de caractérisation qui ont été utilisées pour cette étude et les trois chapitres suivants sont dédiés aux résultats expérimentaux sur les hydrures, carbures et les carbures-hydrures respectivement.

Chapitre 1: Introduction

L'insertion d'éléments légers (H, B, C, N) peut être utilisée pour ajuster les propriétés magnétiques de composés intermétalliques. Dans le cas de composés riches en fer comme $R_2Fe_{14}B$ et $La(Fe_{1-x}Si_x)_{13}$, l'insertion d'hydrogène permet d'augmenter significativement la température de Curie (T_C) des matériaux utilisés comme aimants permanents (Fruchart *et al.*, (1997)). Cette approche peut être aussi utilisée pour modifier de façon réversible les propriétés optiques de couches minces comme dans le cas des miroirs réversibles où la transition métal-semi-conducteur s'accompagne du passage d'un état réfléchissant à un état transparent (Huiberts *et al.*, (1996)). L'insertion de bore est plus rarement étudiée, mais l'a été notamment pour des composées de type R_5Si_3 (Mayer and Felner, (1974)). L'insertion de carbone, utilisée depuis des millénaires pour produire de l'acier, a aussi été particulièrement étudiée pour accroitre la température de Curie T_C dans des composés de type R_2Fe_{17} (Fruchart *et al.*, (1994)), $La(Fe_{1-x}Si_x)_{13}$ (Zhang *et al.*, (2013)) et $RFe_{12-x}Mo_x$ (Skolozdra *et al.*, (1995)). Enfin l'insertion d'azote permet elle aussi d'augmenter la valeur de T_C dans des composés de type Sm_2Fe_{17} afin d'obtenir des aimants permanents intéressants (Katter *et al.*, (1992); Liu *et al.*, (1993)).

Dans le cas des composés *R*MX de type CeFeSi (*R* = Terre-Rare, M = Métal de transition, X = métal p), plusieurs études ont montré qu'il est possible d'insérer un atome d'hydrogène par unité formulaire avec la formation de l'hydrure *R*MXH. Cette insertion d'hydrogène induit deux effets principaux qui entrent en compétition : l'augmentation du volume de la maille qui peut être comparé à l'application d'une pression négative et l'apparition d'une liaison *R*-H qui aura tendance à diminuer les interactions magnétiques entre atomes de terre-rare (Chevalier et al. (2009). Dans le cas des composés à base de cérium (*R* = Ce), on a cherché à utiliser cet effet volumique afin de les amener dans la zone du point critique quantique (située entre un état magnétique et un état non-magnétique) dans laquelle on peut envisager l'apparition d'un état supraconducteur. De plus, la découverte en 2008 d'une nouvelle famille de composés supraconducteurs à base de fer cristallisant dans une structure similaire à celle de ces hydrures (appelée ZrCuSiAs) a relancé l'intérêt pour cette famille de composés. Cette démarche a été récemment couronnée de succès puisqu'un état supraconducteur a été observé pour le composé LaFeSiH (arXiv:1701.05010) en dessous d'une température critique de 9 K. D'autres modulations intéressantes des propriétés magnétiques par insertion d'hydrogène ont été observées pour des composés NdMnSi (Tencé *et al.*, (2009)), NdCoSi (Chevalier *et al.*, (2010)a) et NdCoGe (Chevalier *et al.*, (2010)a).

Dans le cas des composés de type CeScSi, les premières études sur l'insertion d'hydrogène ont montré une diminution importante de la température d'ordre magnétique (par exemple GdTiGe → GdTiGeH (Gaudin *et al.*, (2011)), *R*ScSi et *R*ScGe (*R* = La, Ce) (Chevalier *et al.*, (2010)b). Des travaux préliminaires ont été aussi effectués pour étudier l'insertion de bore et de carbone dans des composés *R*TiGe (*R* = Y, Gd-Tm) (Klosek, (2002); Lemoine, (2011)). Le faible nombre d'études dans la littérature de l'insertion d'éléments légers dans ce type de phases est en partie à l'origine des motivations de ce travail.

Chapitre 2: Méthodes Experimentales

Les échantillons de départ ont été synthétisés par fusion des éléments (nettoyés et polis) à l'aide d'un four à arc ou d'un four à induction. Après fusion, les lingots sont placés dans des ampoules en quartz scellées sous vide et mises dans un four à haute température (800 °C ou 900 °C). Les lingots après fusion et après recuit sont caractérisés par diffractions de rayons X sur poudre et par des mesures magnétiques effectuées avec un magnétomètre S.Q.U.I.D. Des mesures de diffraction neutronique ont été menées pour notamment localiser les éléments légers et déterminer les structures magnétiques. Ces mesures ont été faites sur les lignes G4.1, G4.4 et 3T2 au Laboratoire Léon Brillouin (LLB) à Saclay, sur D1B et D2B à l'Institut Laue-Langevin à Grenoble et sur C2 à Chalk River, Canada. Des mesures de chaleur spécifique et de résistivité ont été faites avec un PPMS de Quantum Design. Finalement, le dosage de carbone été accompli avec un Eltra CS800 carbon/sulphur determinator.

Chapitre 3: L'hydrogénation des composées de type CeScSi

Ce chapitre traite de l'effet de l'hydrogénation des composés CeTiGe, NdScSi et GdScGe sur leurs propriétés physiques.

Transition structurale et hydrogénation de CeTiGe

Des études précédentes sur CeTiGe ont montré qu'il peut cristalliser dans les types structuraux CeFeSi et CeScSi. Toutefois, il y a actuellement un désaccord dans la littérature sur l'identité de la forme haute température (est-ce la forme CeFeSi ou la forme CeScSi) et même sur la présence d'une transition polymorphique. Dans un premier temps nous avons cherché à trancher ce débat.

Les éléments Ce, Ti et Ge ont été préparés dans les proportions 32,5 :34.5 :33,0 avant d'être fondus dans un four à arc. Après fusion, les échantillons, sous forme de blocs, ou de pastilles de poudre compactée, ont été enfermés dans des ampoules de quartz scellées sous vide avant un recuit à 900 °C pendant 2 semaines. Après ce recuit initial la diffraction par rayons X (DRX) montre la présence de d'une phase principale CeTiGe de type structural CeFeSi, avec une phase secondaire Ce_5Ge_3 en faible quantité. Ensuite nous avons fait une étude en température pour rechercher une éventuelle température de transition structurale en effectuant différents recuits de trois jours à 900, 1000 et 1100 °C sur des pastilles de CeTiGe. Les diagrammes de DRX pour ces trois échantillons sont représentés dans la Figure 1. Les pics indiqués avec un * et un ¤ sont caractéristiques des types structuraux CeFeSi et CeScSi respectivement et peuvent être utilisés comme marqueurs de la présence ou de l'absence de la forme structurale. Nous avons observé que la forme structurale

CeScSi est stabilisée après les recuits à 1000 °C et 1100°C et la forme CeFeSi après le recuit à 900°C. On a donc mis en évidence l'existence d'une transition structurale entre 900°C et 1000°C. Cependant la durée de recuit nécessaire pour observer cette transition ne nous a pas permis de déterminer plus précisément cette température de transition.

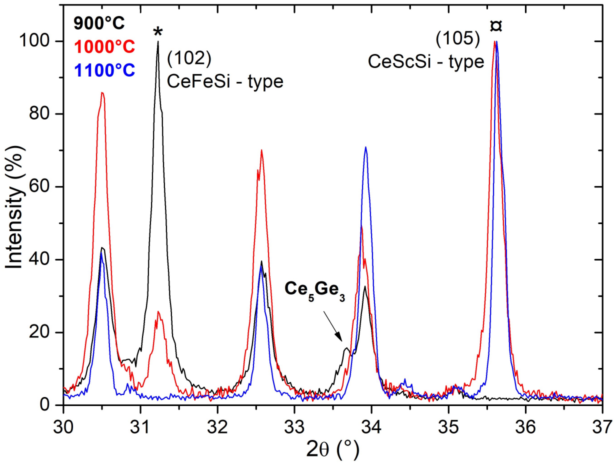

Figure 1. Diffractogramme des rayons X sur poudre du composé CeTiGe après recuit à 900, 1000 et 1100 °C (pastille de poudre compactée).

On a mis également en évidence une cinétique de changement structural beaucoup plus lente dans le cas d'un échantillon sous forme de bloc. Après 3 jours de recuit dans le même four à 1100°C on observe seulement 10% de phase haute température (HT), de type CeScSi, et 90% de phase basse température (LT), de type CeFeSi. Cette différence très importante dans la cinétique de transition structurale explique sans aucun doute les controverses dans la littérature autour de la stabilisation de ces formes structurales.

CeTiGe-HT absorbe 1,5 atomes d'hydrogène par unité formulaire en chauffant sous 5 bar d'H_2 à 350 °C pendant quelques heures. Cela induit une contraction du paramètre *a* de 4,15434(5) Å à 4,0889(2) Å et une augmentation du paramètre *c* de 15,8824(2) à 16,9917(9) Å. Par diffraction neutronique nous avons localisé les atomes d'hydrogène dans les tétraèdres Ce_4 (0 0,5 0,25) et les pyramides à basse carré de Ti_4Ce (0 0 0,521(1)). On obtient le même hydrure qui dérive de la structure CeScSi si on part de la forme LT. L'insertion d'hydrogène permet d'induire la transition structurale entre les formes LT et HT avec des conditions beaucoup plus douce en température et une cinétique beaucoup plus rapide.

CeTiGe est un système non-magnétique de type fermion lourd (Deppe *et al.*, (2009)) avec un comportement paramagnétique de type Curie-Weiss indiquant un état de valence +3 pour Ce sans contribution magnétique des atomes de titane. L'hydrure présente un comportement magnétique différent à basse température (Figure 2). On peut penser qu'il existe un ordre magnétique à basse température mais il n'a pas encore été possible de le caractériser. Des études complémentaires sont donc nécessaires pour aller plus loin dans ce travail.

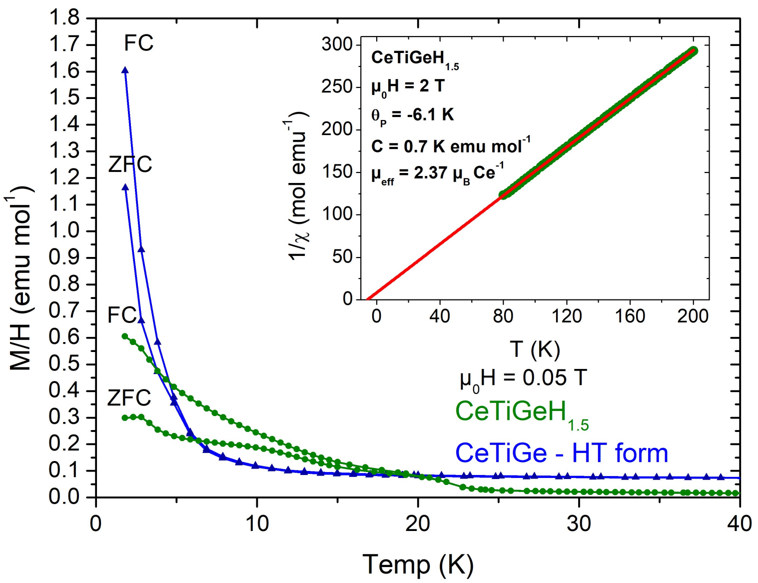

Figure 2. Courbes de magnétisation de type ZFC-FC pour la forme haute température de CeTiGe et son hydrure. L'Encart montre l'évolution de l'inverse de la susceptibilité à haute température modélisée par une loi de type Curie-Weiss.

Hydrogénation de NdScSi

NdScSi cristallise dans le type structural CeScSi. Des mesures d'absorption indiquent que NdScSi, comme CeTiGe, absorbe 1,5 atomes d'hydrogène par unité formulaire. Cela induit une expansion de la maille avec une diminution du paramètre *a* de 4,2894(6) à 4,22(1) Å et une augmentation du paramètre *c* de 15,705(3) à 16,928(2) Å. Pour confirmer ces résultats, un suivi de l'absorption du deutérium par diffraction neutronique *in-situ* a été mené à bien. Cela a été réalisé en effectuant la deutération à 350 °C sous une pression de 5 bars de D_2. L'affinement du diffractogramme obtenu en cours d'absorption est montré dans la **Figure 3** et les paramètres structuraux sont donnés dans le tableau 1.

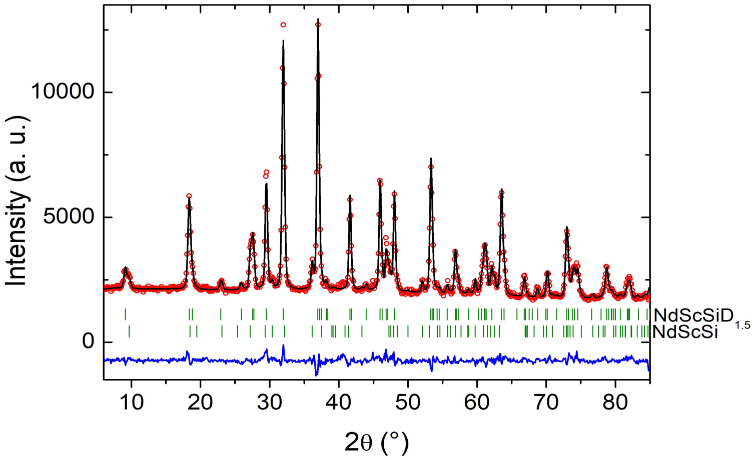

Figure 3. Affinement Rietveld du diffractogramme de diffraction neutronique, mesuré à température ambiante après 15h de deuteration de NdScSi. Les tirets en vert en haut correspondent aux pics de Bragg de la phase NdScSiD$_{1,5}$ et ceux en bas à la phase NdScSi.

Tableau 1. Coordonnées atomiques et paramètres de déplacement isotrope U_{iso} ou équivalent U_{eq} (pm^2) de NdScSi et $NdScSiD_{1.47(3)}$. U_{eq} est égal au tiers de la trace du tenseur U_{ij}.

Phase	Atome	Wyckoff	x	y	Z	U_{eq}/U_{iso}* (pm^2)	Occ.
NdScSi	Nd	4*e*	0	0	0.32347(1)	76(1)	1
	Sc	4*c*	0	½	0	91(1)	1
	Si	4*e*	0	0	0.12285(8)	80(2)	1
$NdScSiD_{1.47(3)}$	Nd	4*e*	0	0	0.316(1)	94(8)*	1
	Sc	4*c*	0	½	0	148(8)*	1
	Si	4*e*	0	0	0.109(1)	86(7)*	1
	D1	4*d*	0	½	¼	195(17)*	1.01(1)
	D2	4*e*	0	0	0,518(1)	234(32)*	0.47(3)

La diffraction neutronique a permis de confirmer la localisation des atomes de deutérium dans les sites 4*e* (pyramide à base carrée) avec les coordonnées (0 0 0,518(1)). Comme les sites 4*e* adjacents sont très proches, un seul des deux sites peut être rempli. Le remplissage simultané des deux sites donnerait des distances D-D beaucoup trop courte (0,60(2) Å). De plus, ce suivi de l'insertion du deutérium dans la phase initiale NdScSi ne montre pas l'existence de phases intermédiaires avec des taux variables d'hydrogène. On n'observe que des mélanges de NdScSi et $NdScSiH_{1,5}$.

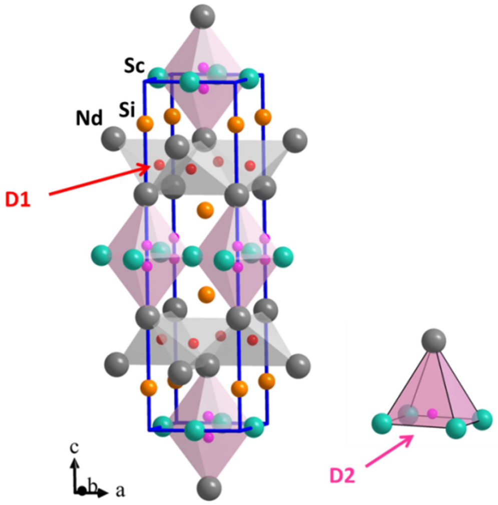

Figure 4. Structure cristalline de $NdScSiD_{1,5}$ avec les sites tétraédrique et pyramide à base carrée occupés par D tracés. Le site D2 dans la pyramide à base carrée est tracé sur le côté droit.

La structure cristalline de $NdScSiD_{1,5}$ est représentée sur la Figure 4. L'hydrogénation induit une contraction des sites tétraédrique, des couches Nd_2 et des couches ScSi. L'augmentation importante du paramètre c induit un éloignement des couches Nd_2 et ScSi, on peut donc en conclure que l'hydrogénation augmente le caractère 2D de la structure initiale.

NdScSi est un composé ferromagnétique avec une température de Curie, T_C, de 171 K (Singh *et al.*, (2004)). L'hydrure $NdScSiH_{1,5}$ possède un ordre magnétique en dessous de 4 K. La Figure 5 montre les mesures de l'aimantation en fonction de la température et l'encart présente l'évolution de l'inverse de la susceptibilité en fonction de la température avec la modélisation avec une loi de type Curie-Weiss. Le moment magnétique effectif correspond à celui attendu pour Nd^{3+}. En conclusion, l'hydrogénation a réduit significativement la température d'ordre de NdScSi mais des mesures supplémentaires sont nécessaires pour comprendre le type d'ordre magnétique observé à basse température pour $NdScSiH_{1,5}$.

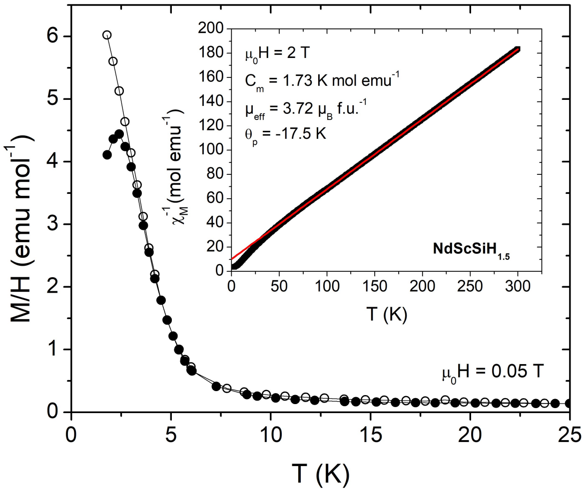

Figure 5. Evolution du rapport M/H (aimantation divisée par le champ magnétique H) en fonction de la température pour $NdScSiH_{1,5}$ (mode ZFC : symbole fermé et FC : symbole ouvert). L'Encart montre l'inverse de la susceptibilité à haute température sous un champ de 2 T modélisée par une loi de type Curie-Weiss.

L'hydrogénation de GdScGe

Pour l'étude de l'hydrogénation nous avons utilisé deux conditions expérimentales différentes. La première a été faite à 350 °C sous 40 bars d'H_2 (sample 1) et la deuxième à 350 °C sous 5 bars d'H_2 (sample 2). Contrairement aux autres systèmes dans cette étude, les mesures d'absorption indiquent que GdScGe, un composé de type CeScSi, absorbe seulement un atome d'hydrogène par unité formulaire. La Figure 6 montre que cela est en d'accord avec la composé GdTiGe (Gaudin *et al.*, (2011)) qui a la même type structural. Les changements structuraux associés à l'absorption de l'hydrogène dans ce système sont les mêmes que dans les autres cas: le paramètre *a* décroit de 4,2527(6) à 4,192(2) Å et le paramètre *c* augmente de 15,563(3) à 16,740(8) Å.

La composé parent GdScGe est ferromagnétique en dessous de la température de Curie T_C = 350 K (Couillaud *et al.*, (2011)). Cette température d'ordre est très élevée par rapport aux autres composés à base de Gd et également plus haute que celle du Gd pur. Ceci peut sembler étonnant car la densité de Gd dans ce composé est plus faible que dans le métal pur. Comme dans les autres systèmes étudiés, l'insertion d'hydrogène a un effet significatif sur les propriétés magnétiques.

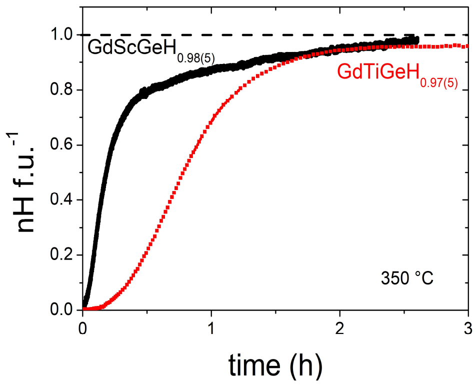

Figure 6. Courbes d'absorption de l'hydrogène en fonction du temps pour GdScGe (sample 2) et GdTiGe.

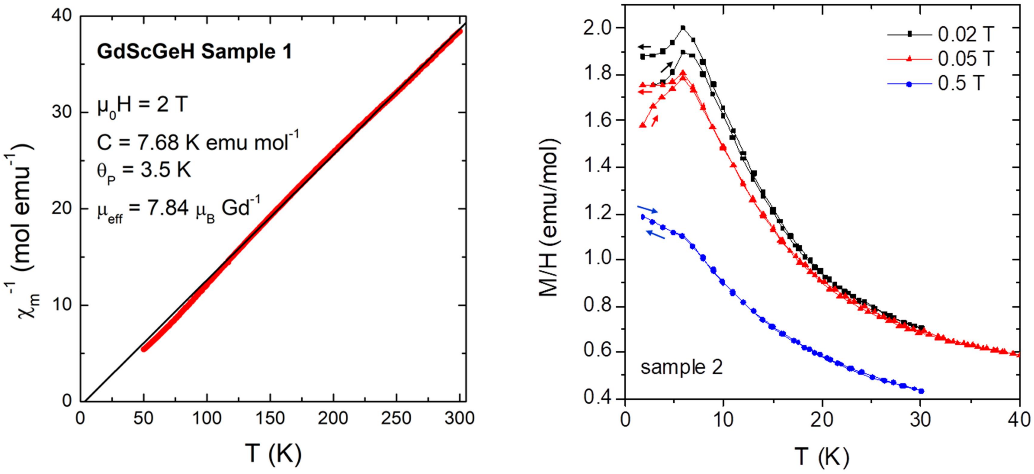

Figure 7. GdScGeH : (à gauche) évolution de l'inverse de la susceptibilité magnétique en fonction de la température pour un champ appliqué de 2 T. La droite tracée en noir correspond à la modélisation en considérant une loi de type Curie-Weiss. (à droite) évolution du rapport M/H en fonction de la température (mesures ZFC et FC respectivement indiquées par des flèches orientées vers la droite et la gauche).

Sur la Figure 7 (à gauche) L'évolution de la susceptibilité magnétique en fonction de la température suit une loi de type Curie-Weiss à haute température. Le moment effectif calculé μ_{eff} = 7,84 μ_B est en accord avec le moment attendu pour un ion Gd^{3+} (7,94 μ_B). La valeur légèrement positive de θ_P indique l'existence d'interactions de type ferromagnétique. A droite dans la même figure nous montrons les courbes d'aimantation ZFC-FC sous plusieurs champs appliqués. Suite à l'hydrogénation la température d'ordre magnétique de 350 K dans le composé initial tombe à 6 K pour l'hydrure (valeur confirmée par des mesures de chaleur spécifique), donc l'effet de l'hydrogène sur les propriétés magnétiques est significatif.

Un effet de l'insertion de l'hydrogène encore plus intéressant est observé pour les propriétés de transport électronique. Les évolutions de la résistivité normalisée à 290 K avant et après hydrogénation sont présentées dans la Figure 8. Cette normalisation a été faite car nous n'avons pu travailler que sur des pastilles de poudre de compacité relativement faible. Il n'a donc pas été possible de remonter à la résistivité intrinsèque. Nous voyons clairement sur ces courbes que GdScGe a un comportement métallique classique avec une résistivité qui décroit avec la température. Après hydrogénation on observe un changement significatif de l'évolution de la résistivité normalisée qui correspond cette fois-ci plutôt à celle d'un système non-métallique avec une remontée de la résistivité en descendant en température.

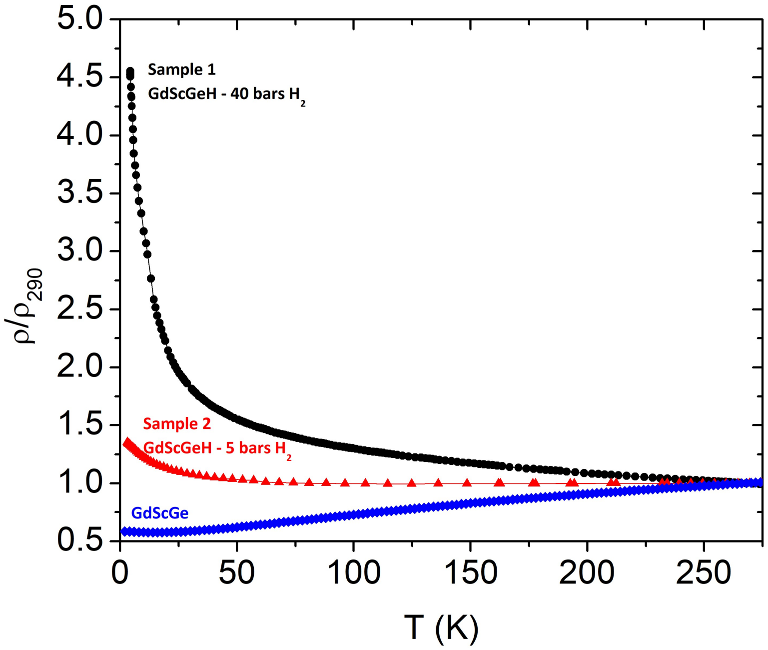

Figure 8. Dépendance de la résistivité normalisée ρ/ρ290K en fonction de la température pour les composées GdScGe et ses hydrures : GdScGeH sample 1 et sample 2.

Conclusions du Chapitre 3

Les matériaux avec le type structural CeScSi sont capables d'accepter entre 1 et 1,5 atomes d'hydrogène par unité formulaire. Ceci induit une expansion anisotrope de la maille avec le paramètre *a* qui diminue et le paramètre *c* qui augmente fortement. Des atomes d'hydrogène peuvent occuper des sites tétraédrique R_4 ce qui correspond à un atome d'hydrogène par unité formulaire et des sites pyramides à basse carré RT_4 avec un taux d'occupation d'un demi ce qui correspond à 0,5 atomes d'hydrogène par unité formulaire. On a également montré que l'insertion d'hydrogène dans la forme CeFeSi de CeTiGe provoque une transition structurale avec formation d'un hydrure dont la structure dérive de celle de CeScSi.

L'hydrogénation du composé de type fermion lourd CeTiGe amène le système vers un état magnétique. Par contre, l'insertion d'hydrogène dans des systèmes déjà magnétiques comme NdScSi ou GdScGe diminue fortement leurs températures d'ordre magnétique. Finalement, l'insertion d'hydrogène dans GdScGe provoque un changement important du type de conductivité électronique avec passage d'un état métallique vers un état non-magnétique.

Chapitre 4: Insertion du carbone dans NdScSi et CeScSi

L'insertion de carbone a été réalisée en partant de graphite en poudre compactée sous forme de pastille. Dans un premier temps les éléments métalliques ont été fondus ensemble au four à arc, puis le lingot obtenu a été placé dans un four à induction avec la pastille de graphite. Cette première étape a permis de faire réagir le carbone avec les éléments métalliques. Finalement, le lingot est refondu au four à arc pour permettre la fusion des carbures binaires réfractaires qui ont tendance à se former au cours de la première étape de synthèse au four à induction.

Comme on peut le voir sur la Figure 9, l'insertion de carbone dans le système NdScSi provoque une expansion anisotrope de la maille avec le paramètre *a* qui augmente de 4,2894(6) à 4,4107(4) Å et le paramètre *c* qui diminue de 15,705(3) à 15,389(1) Å. Ce changement de métrique de la maille est donc inverse de celui observé après insertion d'hydrogène. La diffraction des rayons X sur monocristal confirme la présence de carbone dans les sites octaédrique Sc_4Nd_2 (0, 0, 0,5) et que les autres sites interstitiels sont vides.

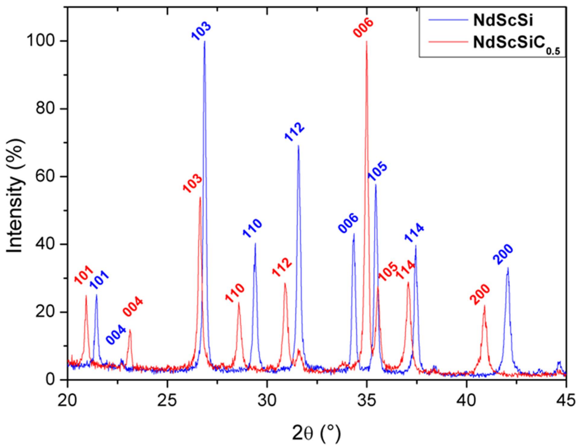

Figure 9. Diffractogrammes des RX pour les échantillons NdScSi et $NdScSiC_{0,5}$ obtenus après recuit

On a mis en évidence l'existence de carbures de compositions intermédiaire ($0,25 \leq x \leq 0,5$ pour $NdScSiC_x$ et $0,00 \leq x \leq 0,5$ pour $CeScSiC_x$). Pour des échantillons $NdScSiC_x$ avec des compositions faibles en carbone ($0 < x \leq 0,25$) on observe un mélange entre la phase initiale NdScSi et la phase $NdScSiC_{0,25}$. Afin d'étudier avec précision l'existence de solutions solides dans ces systèmes il a été nécessaire de mettre en place une méthode de dosage du carbone. Pour cela nous avons dosé le carbone total dans les échantillons par combustion avec la méthode décrite dans le chapitre 2. Cette valeur a été combinée avec les pourcentages massiques de chaque phase présente dans les échantillons en considérant une stœchiométrie idéale en carbone pour les carbures secondaires. Sur la Figure 10 on peut voir l'évolution des paramètres de maille en fonction du taux de carbone dosé. On peut constater que l'évolution de ces paramètres est linéaire en fonction du taux de carbone ce qui est en accord avec l'existence d'une solution solide pour $NdScSiC_x$ ($0,25 \leq x \leq 0,5$) et $CeScSiC_x$ ($0,00 \leq x \leq 0,5$).

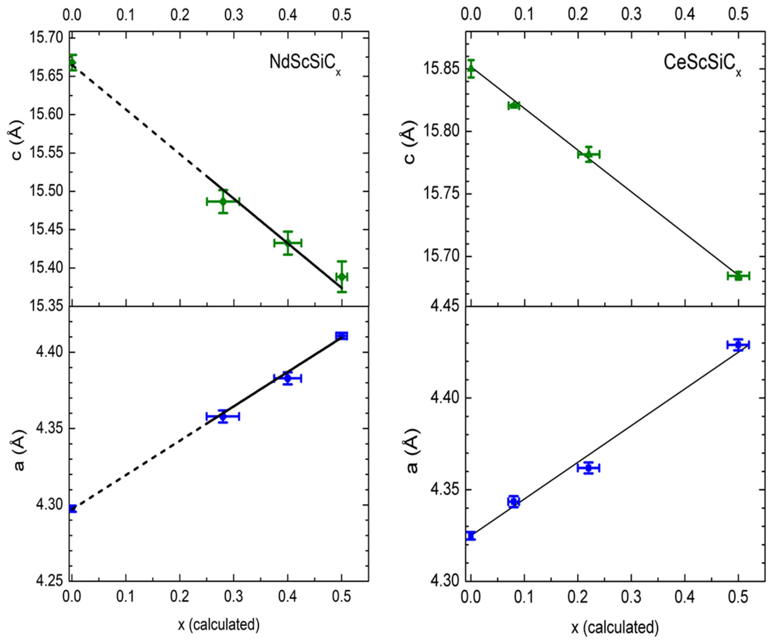

Figure 10. Paramètres de maille en fonction du taux de carbone pour NdScSiC$_x$ (gauche) et CeScSiC$_x$ (droite). Les barres d'erreurs correspondent à 3σ pour l'axe Y et σ pour l'axe x. Les lignes noires correspondent à l'ajustement linéaire des données et la ligne pointillée est une extrapolation vers la valeur x=0.

Au niveau structural, l'insertion du carbone dans le site octaédrique R_2Sc_4 provoque sa contraction le long de l'axe c afin de renforcer les liaisons *R*-C. Cela amène à une augmentation de la distance entre les plans *R* mais également à un rapprochement des couches R_2 et ScSi d'où une augmentation du caractère 3D de la structure initiale (voir Figure 11).

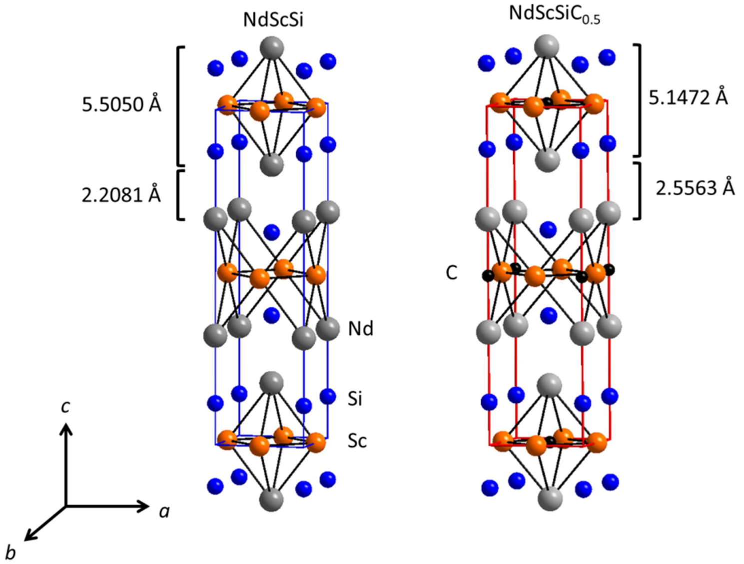

Figure 11. Structures cristallines de NdScSi et NdScSiC$_{0,5}$ avec les distances entre les plans de Nd et entre les 2 atomes de Nd qui forment le site octaédrique dans lequel s'insère C.

Comme pour l'hydrogénation, l'insertion de carbone a un effet prononcé sur les propriétés magnétiques du composé initial. Le composé NdScSi est ferromagnétique en dessous de la température de Curie T_C égale à 171 K. Cette température diminue de façon linéaire en fonction du taux de carbone inséré jusqu'à 51 K pour le carbure limite NdScSiC$_{0,5}$ (figure 12).

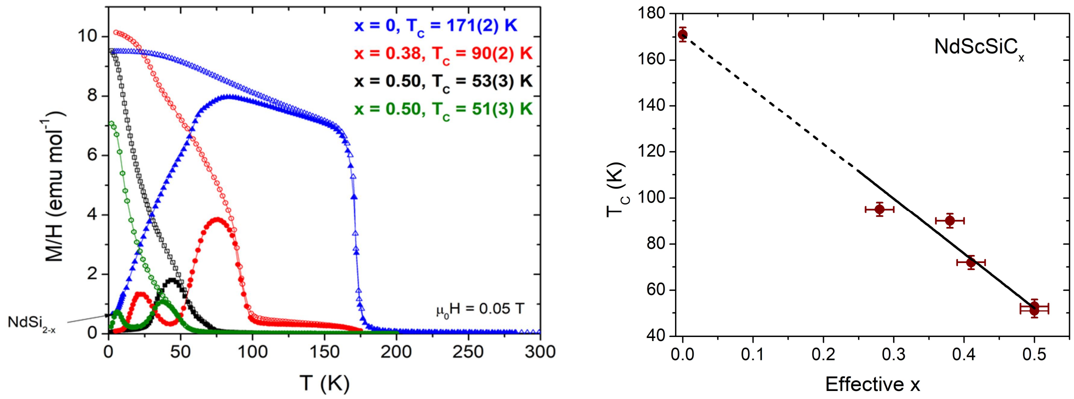

Figure 12. A gauche) les courbes ZFC (symboles pleins) et FC (symboles vides) pour des échantillons du système NdScSiC$_x$. A droite) évolution de la température de Curie des composés NdScSiC$_x$ en fonction de x.

La structure magnétique du composé NdScSiC$_{0,5}$ a été déterminée par diffraction des neutrons à basse température. La structure magnétique (Figure 13) montre un alignement des moments magnétiques de Nd selon l'axe *c*. La structure magnétique du composé initial n'étant pas connue nous l'avons donc comparée à celle de la phase homologue NdScGe (Figure 13). On peut constater une forte similarité entre ces 2 structures avec cependant l'existence d'un léger basculement des moments portés par les atomes de Nd par rapport à l'axe c (angle de 54(2)°) dans le cas de NdScGe.

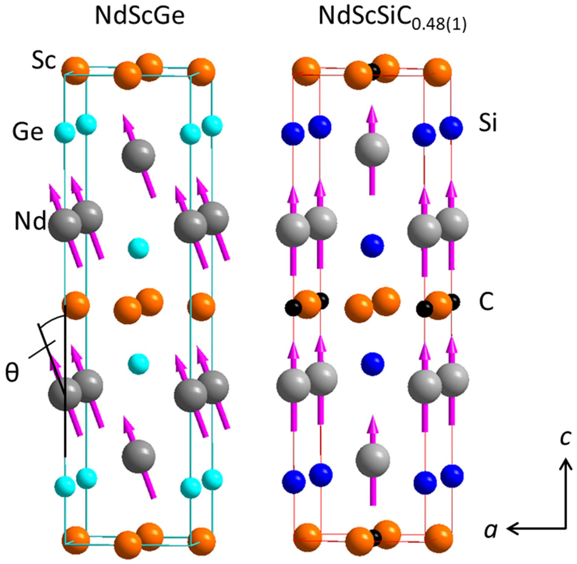

Figure 13. Structures magnétiques de NdScGe (Manfrinetti *et al.*, (2008)) et NdScSiC$_{0,47(1)}$ à 1,5 K. Pour NdScGe θ = 54(2)°.

La Figure 14 montre les courbes M/H en fonction de la température (à gauche) et l'inverse de la susceptibilité en fonction de la température (à droite) pour CeScSiC$_{0,5}$. L'insertion du carbone dans CeScSi réduit la température d'ordre antiferromagnétique de T$_N$ = 27 K à 13,5 K avec l'apparition d'un autre pic autour de 5 K pour le carbure. La modélisation des données par une loi de type Curie-Weiss a permis de confirmer la valence +3 du cérium (figure 14 à droite).

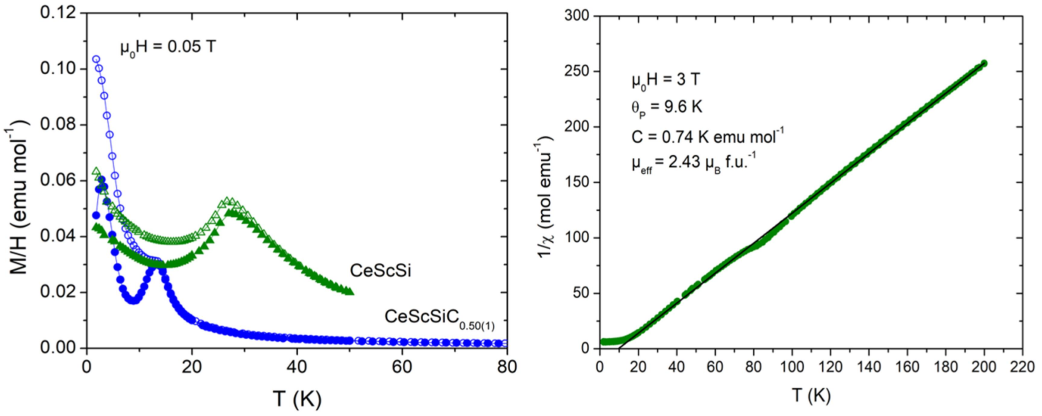

Figure 14. Gauche) courbes de susceptibilité ZFC-FC pour CeScSiC$_x$ (x = 0 and 0,50(1)) à 0,05 T. Droite) l'inverse de la susceptibilité en fonction de la température sous un champ appliqué de 3 T pour l'échantillon CeScSiC$_{0,50(1)}$.

Pour L'étude de la structure magnétique de ce composé une mesure en diffraction neutronique a été menée sur la ligne G4.1 au LLB, Saclay. Avec cette méthode nous confirmons la T$_N$ de 13,5 K avec un vecteur de propagation **k** = (0 0 0). En dessous de cette température, les moments de Ce s'alignent dans le plan *ab,* formant des couches de Ce ferromagnétiques couplées antiferromagnétiquement selon l'axe *c* (figure 15). De plus, nous voyons que le deuxième pic autour de 5 K est intrinsèque à notre phase principale CeScSiC$_{0,5}$ et correspond à une réorientation de spins. En dessous de 5 K, les moments de Ce ne sont plus contenus dans le plan *ab :* ils sont dirigés selon un angle de 24,8 ° avec l'axe *c* (figure 15). Le couplage magnétique reste le même entre les couches ferromagnétiques.

La Figure 15 montre les structures magnétiques a haute et basse température pour CeScSi (publié par Ritter *et al.*, (2016)). Le composé parent montre une réorientation de spins du même type que dans le carbure mais cela n'est pas visible dans les mesures ZFC-FC. La différence principale entre la structure magnétique de CeScSi et celle de CeScSiC$_{0,5}$ est le couplage magnétique entre les plans adjacents. Dans CeScSi il est ferromagnétique alors que dans CeScSiC$_{0,5}$ il devient antiferromagnétique.

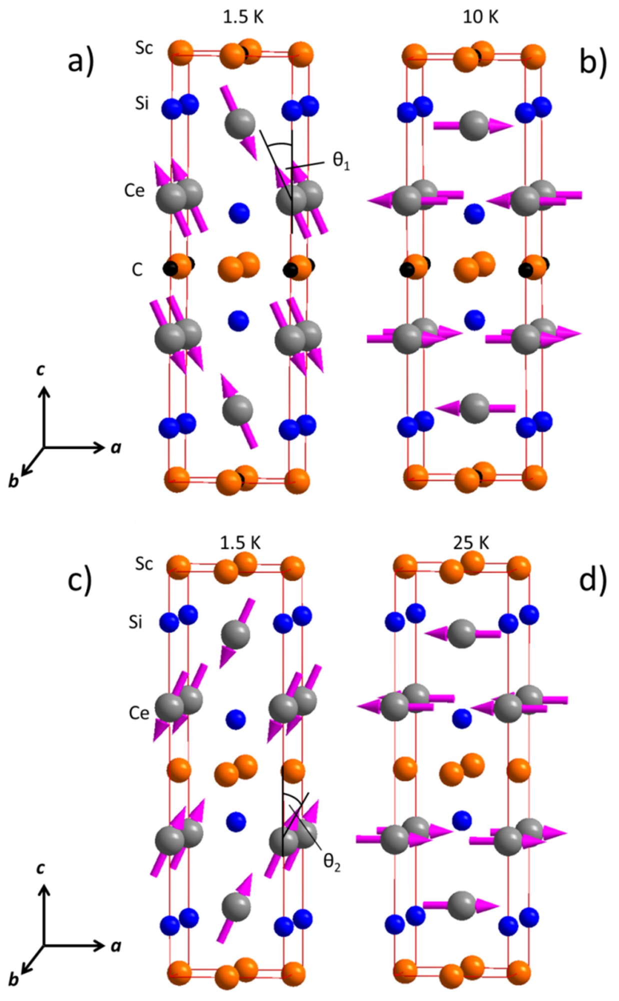

Figure 15. Structures magnétiques de $CeScSiC_{0,50(1)}$ à 1,5 K (a) et 10 K (b). (θ_1 = 24,8 °) et de CeScSi à 1,5 K (c) et 25 K (d) publié par Ritter *et al.*, (2016). (θ_2 = 54 °)

Conclusions du Chapitre 4

Nous avons développé une méthode de synthèse qui nous permet de synthétiser des carbures d'intermétalliques avec une structure de type CeScSi par insertion de carbone pendant la fusion. Les atomes de carbone occupent les sites octaédriques Sc_4Nd_2. Cela induit une expansion anisotrope de la maille avec le paramètre *a* augmentant et le paramètre *c* diminuant. Nous pouvons également faire varier le taux de carbone dans le système, de $0,25 \leq x \leq 0,5$ dans NdScSi et de $0,0 \leq x \leq 0,5$ dans CeScSi. L'insertion de carbone dans NdScSi provoque une réduction de la température d'ordre magnétique T_C jusqu'à 51(3) K, avec une relation linéaire entre le taux de carbone et la T_C. La structure magnétique du carbure consiste en des moments Nd alignés selon l'axe *c*. Dans CeScSi le remplissage total du site induit une réduction de la température de Néel de 27 K à 13,5 K. Sa structure magnétique est constituée de plans ferromagnétiques d'atomes de Ce avec les moments alignés dans le plan *ab* et un couplage antiferromagnétique entre les plans adjacents. On observe une réorientation de spins à 5 K en dessous de laquelle les moments se réorientent vers l'axe *c* formant ainsi un angle de 24,8 ° avec cet axe. Le remplissage partiel du site du carbone a un effet plus complexe que l'on n'a pas pu déterminer pendant cette étude. Des études plus poussées sont donc requises.

Chapitre 5: L'insertion d'hydrogène dans $NdScSiC_{0,5}$ et $CeScSiC_{0,5}$

Rappelons que les atomes de carbone n'occupent que des sites octaédriques dans les composées *R*ScSiC$_x$. Nous avons donc exposé les deux carbures $NdScSiC_{0,5}$ et $CeScSiC_{0,5}$ à une pression d'hydrogène tout en chauffant, pour essayer d'insérer de l'hydrogène dans les sites tétraédriques vides de terre-rare de ces composés. Finalement nous observons un faible changement des paramètres de maille sous 40 bars de H_2 et à 450 °C, en accord avec une probable insertion d'hydrogène (*a* diminue de 4,4107(4) à 4,3996(4) Å et *c* augmente de 15,389(1) à 15,4612(3) Å.)

La structure cristalline de $NdSc_{0,92(1)}SiC_{0,5}H_{0,14(1)}$ a été déterminée par diffraction neutronique à haute résolution réalisée sur D2B à l'ILL, Grenoble. L'affinement de ces données indique la présence d'une sous-stœchiométrie en Sc. De plus, il confirme la présence d'hydrogène dans les sites tétraédriques Nd_4 uniquement. Ces sites ne sont occupés qu'à 14 %, ce qui explique le faible changement de paramètres de la maille observé. La structure affinée est détaillée dans le tableau 2 et représentée dans la Figure 16.

Tableau 2 La structure cristalline affinée de $NdSc_{0.92(1)}SiC_{0,5}H_{0.14(1)}$. *a* = 4,39986(4) Å et *c* = 15,4657(3) Å.

Atome	x	y	Z	B_{iso} (Å^2)	Occ.
Nd	0	0	0,333(1)	0,55(2)	1,00
Sc	0	0,5	0	0,55(2)	0,92(1)
Si	0	0	0,127(2)	0,55(2)	1,00
C	0	0	0,5	0,33(5)	0,50(2)
H1	0	0,5	0,25	1,7(3)	0,14(1)

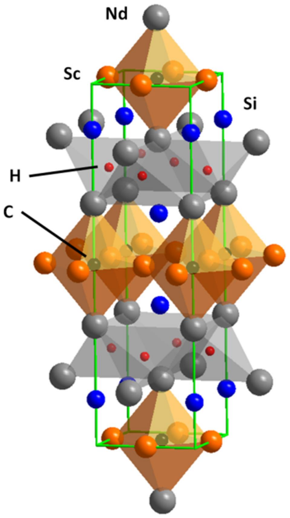

Figure 16. Structure cristalline de $NdSc_{0,92(1)}SiC_{0,5}H_{0,14(1)}$ mettant l'accent sur les sites octaédrique et tétraédrique pour les atomes de carbone et d'hydrogène respectivement.

Le faible taux d'occupation des sites tétraédriques s'explique par des contraintes structurales liées aux effets structuraux antagonistes de l'insertion d'hydrogène et de carbone. Un effet comparable est observé au cours de l'hydrogénation de $CeScSiC_{0,5}$ avec un taux d'hydrogène légèrement plus élevé (25(4) %).

De point vu magnétique, l'hydrogénation de $NdScSiC_{0,5}$ a un effet particulièrement intéressant. Comme nous l'avons vu dans le premier chapitre, l'hydrogénation a tendance à détruire le magnétisme dans les composés de type CeScSi. Néanmoins, après insertion d'hydrogène dans le composé ferromagnétique de départ (T_C = 55 K), le carbure-hydrure présente un ordre antiferromagnétique en dessous de 10 K comme on peut le visualiser sur les courbes d'aimantation ZFC-FC de la Figure 17 (gauche). La Figure 17 (droite) montre l'inverse de la susceptibilité en fonction de la température sous un champ appliqué de 2 T. Cela nous indique que $NdSc_{0,92(1)}SiC_{0,5}H_{0,14(1)}$ est un composé paramagnétique de type Curie-Weiss avec un moment effectif correspondant à celui de Nd^{3+}. La température paramagnétique de Curie indique aussi que les interactions locales sont principalement ferromagnétiques.

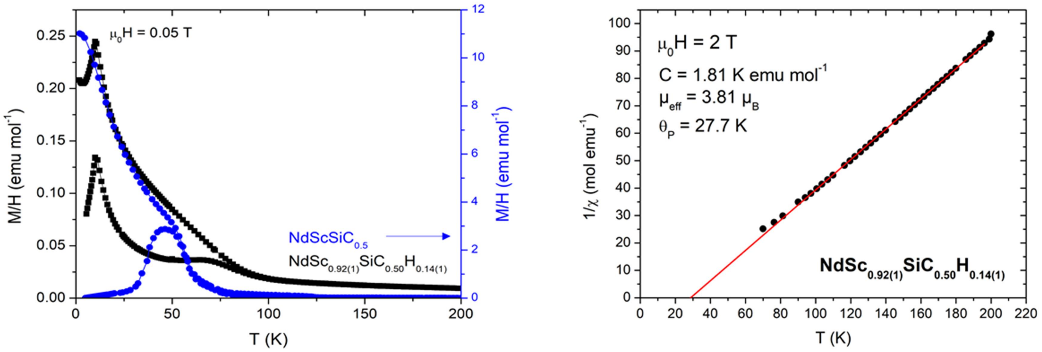

Figure 17. Gauche) courbes de susceptibilité ZFC-FC pour $NdScSiC_{0,5}$ et $NdSc_{0,92(1)}SiC_{0,5}H_{0,14(1)}$ sous un champ appliqué de 0,05 T. Droite) l'inverse de la susceptibilité en fonction de la température sous un champ appliqué de 2 T pour l'échantillon $NdSc_{0,92(1)}SiC_{0,50}H_{0,14(1)}$.

La structure magnétique de ce composé a été déterminée. Elle est formée de moments d'atomes de Nd alignés selon l'axe *c* formant des couches ferromagnétiques couplées + - + - selon l'axe *c*. L'insertion d'hydrogène change donc le signe du couplage entre des double couches de Nd selon l'axe *c* (voir Figure 18).

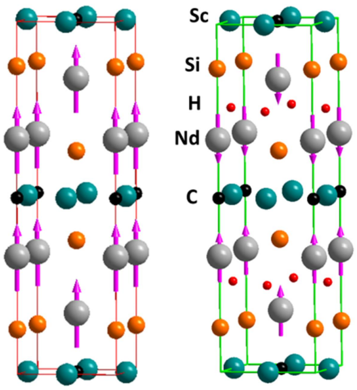

Figure 18. Structure magnétique de $NdScSiC_{0,5}$ (gauche) et $NdSc_{0,92(2)}SiC_{0,5}H_{0,14(1)}$ (droite)

Concernant $CeSc_{0,90(2)}SiC_{0,5}H_{0,25(4)}$, les courbes d'aimantation ZFC-FC (Figure 19) montrent trois anomalies : un faible saut autour de 23 K, un maximum large vers 13 K et une remontée à 3,5 K.

Compte tenu de la difficulté à interpréter ces données, nous avons réalisé des mesures complémentaires de chaleur spécifique car cette technique est moins sensible aux phases secondaires. Les résultats suggèrent que la température d'ordre magnétique de $CeSc_{0,90(2)}SiC_{0,5}H_{0,25(4)}$ est d'environ 13,5 K. Donc il semblerait que l'insertion d'hydrogène ne change pas la température d'ordre magnétique de $CeScSiC_{0,5}$. Des mesures de diffraction neutronique sont en cours pour déterminer sa structure magnétique et confirmer ce résultat.

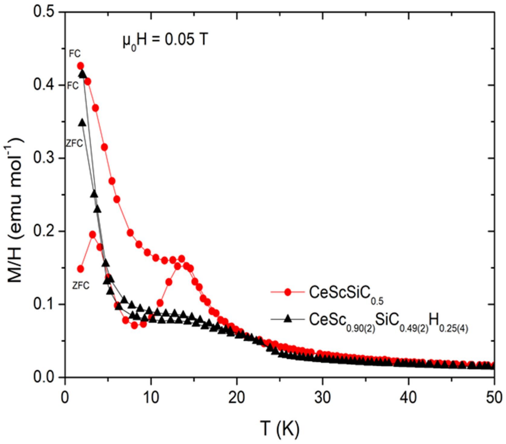

Figure 19. Les courbes de susceptibilité ZFC-FC pour $CeScSiC_{0,5}$ et $CeSc_{0,90(2)}SiC_{0,49(2)}H_{0,25(4)}$ sous un champ magnétique appliqué de 0,05 T.

Conclusions de Chapitre 5

Nous avons montré que l'hydrogène peut s'insérer dans les sites tétraédriques vides des carbures $RScSiC_{0,5}$ (R = Ce, Nd) avec un faible taux d'occupation. Cela induit un changement de paramètres de la maille en accord avec l'insertion d'hydrogène dans les composées *R*ScSi sans carbone (*a* décroisant, *c* croisant), mais avec un changement global qui est beaucoup plus faible. La faiblesse de ce changement est due au faible taux d'occupation des sites tétraédriques. Les liaisons fortes Nd-C ancrent les plans de Nd et empêchent la contraction des sites tétraédriques nécessaire à l'établissement de distances R-H classiques. Donc ces liaisons Nd-C empêchent le remplissage total des sites. L'hydrogène change le type d'ordre magnétique dans $NdScSiC_{0,5}$ d'un ordre ferromagnétique (T_C = 55 K) vers un ordre antiferromagnétique (T_N = 10 K). Les mesures d'aimantation ZFC-FC ne suffisent pas pour déterminer clairement le type d'ordre magnétique dans $CeSc_{0,90(2)}SiC_{0,5}H_{0,25(4)}$ mais des mesures de chaleur spécifique montre que la température d'ordre ne change pas entre le carbure et le carbure-hydrure.

Conclusions générales

Nous avons présenté nos travaux sur l'insertion d'éléments légers dans des systèmes intermétalliques de type structurale CeScSi. Grâce aux études en températures nous avons prouvé que la forme CeScSi de CeTiGe est la forme haute température. Nous avons montré que ces composés possèdent deux sites différents pour l'insertion d'hydrogène: des sites tétraédriques de terres rares (R_4) et des pyramides à basse carrés (T_4R) formés par les plans carrés d'éléments de transition avec un atome de terre rare au sommet. L'occupation de ces sites donne un taux d'hydrogène maximal de 1,5 atomes d'H par unité formulaire, sans formation d'hydrures intermédiaires. Cela est possible dans des composés CeTiGe et NdScSi, mais dans GdScGe, seulement 1 atome d'H par unité formulaire peut être inséré, ce qui laisse supposer que seuls les sites R_4 sont disponibles dans ce composé. L'insertion d'hydrogène induit une expansion anisotrope de la maille, le paramètre *a* diminuant et le paramètre *c* augmentant.

Des atomes de carbone peuvent être insérés dans la maille des composées de départ au cours de la fusion des éléments. Il occupe les sites octaédriques (Sc_4R_2) formés de plans carrés de Sc avec deux atomes des terres rares aux sommets et ces sites peuvent être partiellement remplis ($0,25 \leq x \leq 0,5$ pour NdScSi et $0,0 \leq x \leq 0,5$ pour CeScSi). L'insertion de carbone induit une expansion anisotrope de la maille mais avec une tendance inverse à celle de l'insertion d'hydrogène (*a* augmentant et *c* diminuant). L'hydrogénation augmente le caractère 2D de la maille alors que la carburation augmente son caractère 3D. Finalement, nous pouvons mettre de l'hydrogène dans les sites tétraédriques des carbures $R\text{ScSiC}_{0,5}$ avec un faible taux d'occupation. L'effet structural antagoniste de l'insertion de carbone et d'hydrogène empêche le remplissage complet de ces sites.

L'hydrogénation peut avoir des effets différents sur les propriétés physiques selon les propriétés initiales. Dans le composé fermion lourd CeTiGe l'insertion d'H crée un état magnétique que nous ne pouvons pas identifier à ce jour avec nos mesures. Par contre, l'insertion d'H dans des systèmes déjà magnétiques a un effet destructeur sur l'ordre magnétique. NdScSi passe d'un état ferromagnétique avec une température de Curie T_C = 171 K à un composé qui s'ordonne en dessous de 4 K. De même, GdScGe, qui possède une température de Curie égal à 350 K, s'ordonne magnétiquement en dessous de 6 K après hydrogénation. Insérer du carbone dans NdScSi a pour effet de réduire, de façon linéaire, la T_C jusqu'à 51(1) K dans le carbure rempli ($\text{NdScSiC}_{0,5}$). La structure magnétique de ce carbure a des moments de Nd orienté selon l'axe *c* avec un couplage ferromagnétique entre tous les moments. Le remplissage des sites octaédriques avec le carbone dans CeScSi cause une réduction de la température de Néel de 27 K à 13,5 K. Sa structure magnétique consiste en des monocouches ferromagnétiques de Ce avec les moments orientés dans le plan *ab* et un couplage antiferromagnétique entre les couches selon l'axe *c*. En dessous de 5 K cette structure subit d'une transition structurale en dessous de laquelle les moments magnétiques se dirigent hors du plan *ab* formant un angle de 24,8 ° avec l'axe *c*.

L'un des effets les plus intéressants observés pendant cette étude est la modification des propriétés de transport électronique observé dans GdScGe pendant l'hydrogénation. L'insertion d'hydrogène dans ce composé change la conductivité métallique du composé parent vers un conducteur non-métallique. Cet effet mérite des études plus poussées et des calculs DFT sont en cours pour expliquer ce phénomène.

Références

Chevalier, B., Tencé, S., André, G., Matar, S. F., Gaudin, E., ((2010)a) 'From antiferromagnetic to ferromagnetic ordering induced by hydrogenation of the compounds NdCoSi and NdCoGe', *Journal of Physics: Conference Series*, 200(3), p. 32012. doi: 10.1088/1742-6596/200/3/032012.

Chevalier, B., Hermes, W., Heying, B., Rodewald, U. Ch., Hammerschmidt, A., Matar, S. F., Gaudin, E., Pottgen, R., ((2010)b) 'New Hydrides REScSiH and REScGeH (RE = La, Ce): Structure, magnetism, and chemical bonding', *Chemistry of Materials*, 22(17), pp. 5013–5021. doi: 10.1021/cm101290f.

Couillaud, S., Gaudin, E., Franco, V., Conde, A., Pottgen, R., Heying, B., Rodewald, U. Ch., Chevalier, B.,((2011)) 'The magnetocaloric properties of GdScSi and GdScGe', *Intermetallics*, 19(10), pp. 1573–1578. doi: 10.1016/j.intermet.2011.06.001.

Deppe, M., Caroca-Canales, N., Hartmann, S., Oeschler, N., Geibel, C., ((2009)) 'New non-magnetically ordered heavy-fermion system CeTiGe', *Journal of Physics: Condensed Matter*, 21(20), p. 206001. doi: 10.1088/0953-8984/21/20/206001.

Fruchart, D., Bacmann, M., de Rango, P., Isnard, O., Liesert, S., Miraglia, S., Obbade, S., Soubeyroux, J.-L., Tomey, E., Wolfers, P.,((1994)) 'R2Fe17 and RM12 carbide and carbonitride synthesis from heavy hydrocarbon compounds', *Journal of Alloys and Compounds*, 203(C), pp. 157–163. doi: 10.1016/0925-8388(94)90728-5.

Fruchart, D. et al. ((1997)) 'Hydrogen in hard magnetic materials', *Journal of Alloys and Compounds*, 253–254, pp. 121–127. doi: 10.1016/S0925-8388(96)03063-0.

Gaudin, E., Matar, S. F., Pottgen, R., Eul, M., Chevalier, B.,((2011)) 'Drastic Change of the Ferromagnetic Properties of the Ternary Germanide GdTiGe through Hydrogen Insertion', *Inorganic Chemistry*, 50(21), pp. 11046–11054. doi: 10.1021/ic201579r.

Huiberts, J. N., Griessen, R., Rector, J. H., Wijngaarden, R. J., Dekker, J. P., de Groot, D. G., Koeman, N. J.,((1996)) 'Yttrium and lanthanum hydride films with switchable optical properties', *Nature*, 380(6571), pp. 231–234. doi: 10.1038/380231a0.

Katter, M., Wecker, J., Kuhrt, C., Schultz, L., ((1992)) 'Magnetic properties and thermal stability of Sm2Fe17Nx with intermediate nitrogen concentrations', *Journal of Magnetism and Magnetic Materials*, 117(3), pp. 419–427. doi: 10.1016/0304-8853(92)90099-A.

Klosek, V. ((2002)) Contribution to the study of the structural and electronic properties of equiatomic RTX (T = Ti, V, Cr, Mn, Fe; X = Si, Ge) and the quaternary RTiGECx and RCr2Si2C, where R is an alcaline earth, yttrium, lanthanum or a lanthanide. Université Henri Poincaré, Nancy 1, France.

Lemoine, P. ((2011)) Contribution à l ' étude des propriétés structurales et magnétiques de composés intermétalliques isotypes de CeScSi et Th 6 Mn 23. Université Henri Poincaré, Nancy, France.

Liu, J. P., Brabers, J. H. V. J., Winkelman, A. J. M., Menovsky, A. A., de Boer, F. R., ((1993)) 'Synthesis and magnetic properties of R2Co17Nx type interstitial compounds', *Journal of Alloys and Compounds*, 200(1–2), pp. L3–L6. doi: 10.1016/0925-8388(93)90461-U.

Manfrinetti, P., Morozkin, A. V., Isnard, O., Henry, P., Palenzona, A., ((2008)) 'Magnetic structure of the CeScSi-type RScGe compounds (R = Pr, Nd, Tb)', *Journal of Alloys and Compounds*, 450(1–2), pp. 86–91. doi: 10.1016/j.jallcom.2006.11.057.

Mayer, I. and Felner, I. ((1974)) 'Nowotny phases of M5X3-type rare-earth silicides and germanides with boron', *Journal of the Less Common Metals*, 37(1), pp. 171–173. doi: 10.1016/0022-5088(74)90021-6.

Ritter, C., Provino, A., Manfinetti, P., Pathak, A. K.,((2016)) 'Tetragonal to triclinic structural transition in the prototypical CeScSi induced by a two-step magnetic ordering: a temperature-dependent neutron diffraction study of CeScSi, CeScGe and LaScSi', *Journal of Physics: Condensed Matter*, 29(4), p. 45802. doi: 10.1088/1361-648X/29/4/045802.

Singh, S. K., Dhar, S. K., Manfrinetti, P., Palenzona, A., Mazzone, D., ((2004)) 'High magnetic transition temperatures in RScT (R = Pr, Nd and Sm; T = Si and Ge) compounds: Multiple spin reorientations in PrScGe', *Journal of Magnetism and Magnetic Materials*, 269(1), pp. 113–121. doi: 10.1016/S0304-8853(03)00583-3.

Skolozdra, R. V., Tomey, E., Gignoux, D., Fruchart, D., Soubeyroux, J. L.,((1995)) 'On the new interstitial RFe10,5Mo1,5Cx series (R=rare earth metal): synthesis and magnetic properties', *Journal of Magnetism and Magnetic Materials*, 139(1–2), pp. 65–76. doi: 10.1016/0304-8853(95)90029-2.

Tencé, S., André, G., Gaudin, E., Bonville, P., Al Alam, A. F. Matar, S. F., Hermes, W. Pottgen, R., Chevalier, B., ((2009)) 'Huge influence of hydrogenation on the magnetic properties and structures of the ternary silicide NdMnSi', *Journal of Applied Physics,* 106(3), p. 33910. doi: 10.1063/1.3190488.

Zhang, H., Hu, F.X., Sun, J. Shen, B., ((2013)) 'Effects of interstitial H and/or C atoms on the magnetic and magnetocaloric properties of La(Fe, Si)13-based compounds', *Science China Physics, Mechanics and Astronomy*., 56(12), pp. 2302–2311. doi: 10.1007/s11433-013-5357-1.

THÈSE PRÉSENTÉE
POUR OBTENIR LE GRADE DE

DOCTEUR DE

L'UNIVERSITÉ DE BORDEAUX

ÉCOLE DOCTORALE DES SCIENCES CHIMIQUES

PHYSICO-CHIMIE DE LA MATIÈRE CONDENSÉE

Modification of the physical properties of intermetallics with the CeScSi structure type by light element insertion (H, C)

Par Tadhg MAHON

General Introduction

Throughout history, human advancement has coincided with the development of increasingly complex tools and materials. Moving from stone tools to metal ones inevitably led to the modification of these metals by changing their composition. Indeed, the first three epochs of human pre-history are famously the Stone Age, the Bronze Age and the Iron Age. Bronze, the defining material of the second of these epochs which is an alloy of copper and tin, shows that even prehistoric man realised the potential for the modification of the physical properties of materials by varying their chemical composition. As humanity has progressed, so too did our command of materials. Eventually this led to the development of perhaps the most famous case of physical property modification by the inclusion of another element in the crystal lattice: steel. Steel is produced from iron by the inclusion of interstitial carbon in the lattice which opposes the movement of crystalline planes and reduces the ductility of the iron. This makes steel much harder and more durable than elemental iron. The earliest recorded evidence of steel production dates from 1800 BC in Turkey (Akanuma, (2005)) and many more examples have been found in ancient China dating from around 403 BC (Wagner, (1993)).

In more recent times, the modification of the physical properties of materials is used to fine tune far more complicated properties than simple hardness. The doping of electron rich or poor elements into semi-conductors allows improvement of the conductivity by either populating the conduction band or by creating holes in the valence band to help electrons flow. This principle is used to make the p-n junctions that drive most electronic devices, forming the root of our current technological prowess by allowing the movement of electrons between a material with an excess of electrons and one with a deficit. This can be accomplished in a large variety of ways including substitution and insertion.

Among the most promising modifications of the chemical composition of a material to improve its properties is the adjustment of the magnetic properties for bespoke applications. Magnetism has long been used in one form or another, however, it is only in the last century or so that we have truly begun to harness some of its true potential. Today, magnets are used in every facet of modern life, from the generation of electricity and the storage of data to sorting magnetic and non-magnetic scrap metals or Maglev (magnetic levitation) trains. Magnets and magnetic materials are likely to form the backbone of future technology with potential uses in transport (such as the aforementioned superconducting Maglev trains in Japan) or the cooling of our homes through the use of the magnetocaloric effect. Research is even underway to develop magnetic nanoparticles for the targeted treatment of cancer. This is why control and understanding of all the factors which can influence the magnetic properties of a material are absolutely key to the continued advancement of humankind. While there is a dearth of understanding of the mechanisms behind magnetism and how it arises in materials, it is often difficult to design new materials completely from scratch. The knowledge that doping a particular element in place of another or that the inclusion of a different element in an interstitial site will produce specific, desired, properties will allow future humans to design and synthesise needed materials in a far more targeted manner. This will allow us to replace what is mostly a “fishing” approach that is often used at the moment where serendipity drives the discovery of many new materials.

This work deals with the modification of the physical properties of intermetallic systems, especially the structural and magnetic properties, through the insertion of light elements into vacant interstitial sites. In the first chapter we will present the crystal structures of the materials that we considered, summarising some of the wealth of different physical properties available in these systems. We will also review the history of the insertion of light elements into intermetallic systems. The second chapter will detail the experimental details of the syntheses and characterisation techniques used during this work. The following chapters will present the experimental work we have performed on the insertion of hydrogen (chapter 3) and carbon (chapter 4) into the pristine intermetallics and the insertion of hydrogen into these new carbide compounds (chapter 5).

Akanuma, H. ((2005)) ‘The Significance of Early Bronze Age Iron Objects from Kaman-Kalehoyuk, Turkey.’, *Anatolian Archaeological Studies: Kaman-Kalehoyuk*, 14, pp. 147–158.

Wagner, D. B. ((1993)) Iron and steel in ancient China. E.J. Brill.

Chapter 1: Introduction and Overview of the Insertion of Light Elements in Intermetallic Systems

The controlled modification of the properties of solid materials is increasingly important in a modern world that is grappling with issues such as climate change, durable design and clean energy generation. For this reason, the targeted and controlled creation of new materials with specific properties, which has always been of great scientific interest, has become a major focus of research. Intermetallic materials containing empty interstitial sites have seen a lot of research interest due to their ability to accept light elements such as carbon and hydrogen into these vacant sites. These materials normally involve an uncomplicated synthesis, possess interesting magnetic and electrical properties, and are often stable in air which makes their characterisation simpler. As the host material generally exists without the interstitial atom they can also be synthesised and studied before the insertion of the light element(s). This allows investigation of the precise effect of the inserted element and the occupied site on the properties modified. The choice of host materials is not random but rather made as a function of the elements to be inserted and the types of sites available. For example, it is well known that hydrogen is capable of occupying a number of different types of interstitial sites such as tetrahedral sites (Chevalier *et al.*, (2010)b; Rodriguez Fernandez *et al.*, (2010)) and octahedral sites (Isnard *et al.*, (1990); Isnard and Pop, (2011)) depending on the size of the site while larger elements such as carbon or nitrogen typically occupy octahedral sites (Coey and Hurley, (1992)). Therefore, compounds possessing these sites are selected for further study using the different insertion techniques available in our laboratory.

The intermetallics crystallising in the CeFeSi (or PbFCl – type) and CeScSi (or ordered La_2Sb-type) structure types are two examples of structures with vacant interstitial sites for the insertion of light elements. Both structures fall into the larger class of RTX intermetallics (*R* = Rare earth element, *T* = transition metal and *X* = a p block element). These two families of materials crystallise for a very wide range of different elements and we shall present here an overview of their structures and properties. In a second section, some of the work that has been carried out to date on the modification of intermetallic compounds through light elements will be discussed. Finally we shall focus on some of the previous insertion work that has been carried out on the CeFeSi and CeScSi-type compounds.

1.1. Crystal structure

1.1.1. CeFeSi-type

The CeFeSi structure was first described in Bodak *et al.* (1970) as a variant of the PbFCl structure. Crystallising in the *P4/nmm* space group, its structure consists of layers of rare earth (*R*), transition metal (*T*), and *p*-block atoms (*X*) stacked along the *c* axis in the order R-X-T_2-X-R with the T_2 plane being twice as densely populated as the others (Figure 1. 1). The unit cell contains 2 formula units (6 atoms) with the Ce and Si atoms occupying the

2*c* Wyckoff site, (¼ ¼ z) where z_{Ce} = 0.672(2) and z_{Si} =0.175(2), while the iron occupies the 2*a* site at (¾ ¼ 0). This forms a network of empty edge-sharing Ce_4 tetrahedra stacked with layers of Fe_4Si_4 where the Fe atoms occupy the tetrahedral sites formed by the Si atoms. The structure that is presented in Bodak *et al.* (1970) is summarised in Table 1. 1.

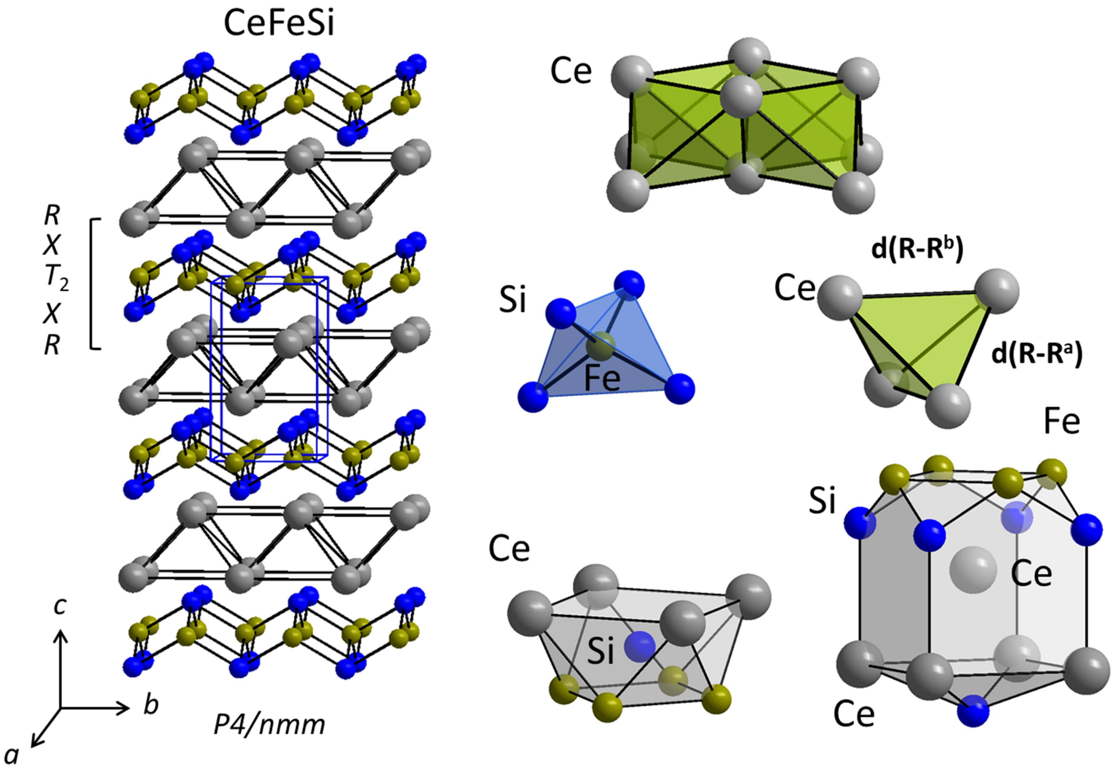

Figure 1. 1. The crystal structure of CeFeSi showing the different layers and coordination polyhedra

Table 1. 1. Crystal structure of CeFeSi as detailed by Bodak *et al.* (1970)

Atom	Wyckoff Site	x	y	z
Ce	2c	¼	¼	0.672(1)
Fe	2a	¾	¼	0
Si	2c	¼	¼	0.175(2)

Thus the structure is defined largely by the two variable coordinates z_{Ce} and z_{Si} which, along with the unit cell parameters, are responsible for the main interatomic distance changes between the various members of this family as *R* and *X* change. There are two inter-rare-earth distances, labelled d$(R\text{-}R)^a$ and d$(R\text{-}R)^b$. The former of these will be used throughout this work to refer to the shortest *R*-*R* distance which is between the rare earth atoms of adjacent planes. The second, $R\text{-}R^b$, corresponds to the longer distance that lies between rare earth atoms within the same plane. This distance is also equal to the unit cell parameter *a*.

The CeFeSi structure type has been documented for a very large range of different compounds. The *RTX* compounds with the CeFeSi structure type have been found in the literature to exist for *R* = Y, La – Ho, and Yb, *T* = Ti, Mn, Fe, Co and Ru, *X* = Si and Ge (Gupta and Suresh (2015), Bodak *et al.* (1970)). While, not every possible combination of the above elements may produce the CeFeSi structure type, Gupta and Suresh (2015) describe 66 different compounds with this structure type (not including substitution work that has been carried out, for example on $Ce_{1-x}La_xTiGe$ by Sereni *et al.*, (2010)).

1.1.2. CeScSi-type

First described by Mokra *et al.* (1979), CeScSi is an ordered variant of the La_2Sb structure crystallising in the *I4/mmm* space group with Sc replacing La on the La2 site. Like the related CeFeSi structure type, this structure consist of a stacking along the *c* axis of alternating square planar layers of *R*, *T* and *X* elements in the order T_2-*X*-*R*-*R*-*X*-T_2-*X*-*R*-*R*-*X*-T_2 with four formula units per unit cell. The CeScSi structure is represented in Figure 1. 2. and the atomic coordinates are presented in Table 1. 2. The major difference between both structures is the mirror plane through the *T* square planes. If we consider a double CeFeSi unit cell along the *c* axis this mirror plane can be created by translating one of the two unit cells by *b*/2. This shift changes the Si_4 tetrahedra willed with Ti atoms into vacant Ce_2Ti_4 octahedra formed from the Ti square planes and the Ce sublattice. The structure contains a number of interstitial sites. For the purposes of the insertion work performed here, two are of particular interest: the R_4 tetrahedra that are also present in the CeFeSi structure type and an R_2T_4 octahedral site. This octahedral site corresponds to the La_6 octahedra in La_2Sb (Wang *et al.*, (1980)).

The CeScSi structure type has been shown to exist for approximately 55 different compositions to date. A thorough examination of the literature reveals *RTX*: *R* = Y, La-Tm, and Lu, *T* = Sc, Ti and Zr, *X* = Si, Ge, Sn and Sb (Gupta and Suresh (2015), Mokra *et al.* (1979), and Morozkin and Sviridov, (2001)). Similarly to the CeFeSi family, not every combination of the above elements forms the CeScSi structure type but the available compounds still represent a large number of different materials with a wide range of properties. It can be pointed out that this family of compounds also exist for magnesium instead of transition metal with the series *R*MgSn and *R*MgPb (Manfrinetti *et al.*, (2009); Provino *et al.*, (2010))

Table 1. 2 The crystal structure of CeScSi described by Mokra *et al.* (1979)

Atom	Wyckoff Site	x	y	z
Ce	4e	0	0	0.326*
Sc	4c	0	½	0
Si	4e	0	0	0.124

* No standard deviations given in Mokra *et al*. (1979)

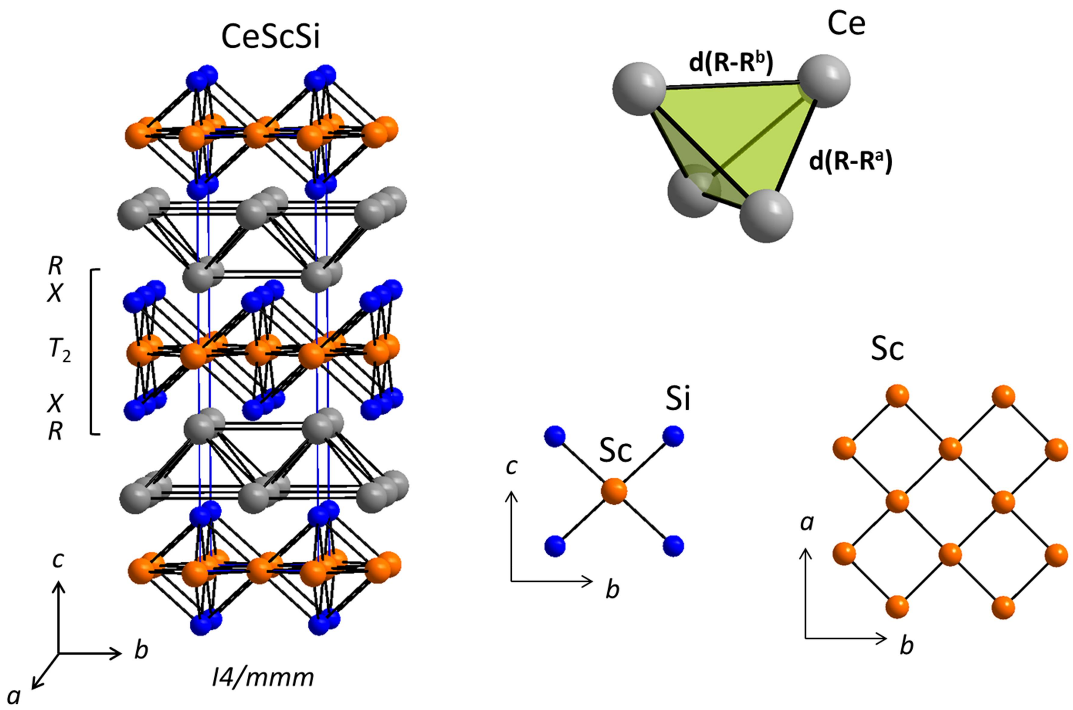

Figure 1. 2. The crystal structure of CeScSi showing the rare earth tetrahedra, square planar coordination of Sc with Si and the Sc square planes

1.1.3. The special case of the *RTiGe* materials

A small subset of the *RTX* materials (*T* = Ti and *X* = Ge) can crystallise in both the CeFeSi and the CeScSi structure type based on annealing temperature and composition. There has been a degree of uncertainty in the literature regarding exactly which forms correspond to the high and low temperature regions and whether non-stoichiometry can play a role in the stabilisation of one form over another.

First described by Morozkin *et al.*, (1998)a for the heavy rare earth elements (Gd-Tm) and Y, The *R*TiGe compounds were found to crystallise in the CeFeSi structure type in the as cast material. This was then expanded to the light rare earth elements (La-Nd, Sm) and Lu by Welter *et al.*, (1999). In the case of the light rare earth elements, annealing for five days at 1273 K was required to produce the main phase with reasonable purity and the CeFeSi structure type was again observed for all the studied materials with the exception of the Gd system. They state that, regardless of the annealing temperatures they attempted (which are not provided in the paper), the CeScSi structure type was always obtained. A more detailed investigation of this system by Morozkin *et al.*, (2000) found that the composition of the material played an essential role in the stabilisation of the CeFeSi or CeScSi structure type. They found that sub-stoichiometric amounts of Ti stabilised the CeScSi form, that the CeFeSi form could be stabilised by sub-stoichiometric amounts of Ge and that a sub-stoichiometric Gd composition stabilised a mixture of the two structure types. Thus it is likely that Welter *et al.*, (1999) studied a GdTiGe compound that was slightly depleted in Ti. Following this, Gaudin *et al.*, (2011) have obtained the CeScSi form of GdTiGe after melting a stoichiometric mixing of the elements without any annealing procedure.

Another conflict in the literature revolves around the CeTiGe compound. Chevalier *et al.*, (2010)b describe a high temperature structural transition from the CeFeSi to CeScSi structure types for this compound by annealing at 1373 K. However, while studying the magnetic properties of this material, Deppe *et al.*, (2012) found that even the samples that were annealed at 1423 K retained the CeFeSi type structure. They posit a similar effect of off stoichiometry to the one seen for GdTiGe as an explanation for this, however, to date no further studies have been carried out on this material to define the exact conditions of the structural transition in CeTiGe. This point has been addressed in the chapter 3 of this work and the effect of annealing (temperature, duration) has been clarified.

1.2. The physical properties of the CeFeSi and CeScSi type materials

Thus the CeFeSi and CeScSi structure types are both layered structures consisting of alternating rare earth, p-block and transition element blocks. These structure types have already been found to exist for a range of compositions with many examples already being known for both. This vastness of composition is mirrored in the extensive range of properties that are exhibited by these materials which often include magnetic transitions at much higher temperatures than expected when the relatively low density of rare earth elements is considered. A summary of some of the many varied properties found in these compounds is presented here to provide an overview. However, due to the sheer number of compounds crystallising in the CeFeSi and CeScSi structure types, a complete summary will quickly become wearisome. For a more exhaustive discussion of the physical properties displayed by these materials readers are referred to the review by Gupta and Suresh, (2015) where over 600 papers on the magnetic properties of *RTX* materials crystallising in a range of structure types including the CeFeSi and CeScSi structures are discussed in detail.

1.2.1. CeFeSi-type

The materials crystallising in the CeFeSi structure type have seen the most research interest out of the two structures discussed here. In the *R*FeSi series of compounds the Fe atom is usually non-magnetic or very weakly magnetic such that it is masked by the more dominant rare earth magnetism which is responsible for the magnetic order in these compounds. This is supported by the fact that LaFeSi is a Pauli paramagnet as found by Welter *et al.*, (1992) during their study of the *R*FeSi family (*R* = La-Sm, Gd-Dy). When *R* is Nd or heavier, the materials are ferromagnetic with T_Cs = 25, 40, 135, 125 and 110 K for Nd, Sm, Gd, Tb and Dy. They could not identify magnetic ordering above 4.2 K for the other compounds in the system. Welter *et al.*, (1992) found CeFeSi to be an intermediate valence Ce compound by comparing the unit cell parameter trends to those seen in similar intermetallics such as $CeFeSi_2$ and $CeFe_2Si_2$.

Another example of the properties available in the compounds with the CeFeSi structure type is the *R*CoSi family (*R* = La-Sm, Gd, Tb). Welter *et al.*, (1994)a showed that, as with LaFeSi, LaCoSi is a Pauli paramagnet which indicates that the transition element carries no magnetic moment for these compounds either. They did not detect any magnetic ordering in the Ce or Pr compounds above 4.2 K but they document that the Nd, Sm, Gd and Tb analogues are all antiferromagnets with T_Ns at 7, 15, 175 and 140 K respectively. It wasn't until the CeCoSi and CeCoGe systems were reinvestigated by, Chevalier and Matar, (2004); Chevalier *et al.*, (2006)a, (2006)b that it was determined that CeCoSi is also an antiferromagnetic system with a T_N of 9 K. Their C_P measurements for CeCoGe show a double peak at 5.5 and 4.8 K which suggests that the antiferromagnetic ordering is potentially complex. This is notably in contrast with the previous measurements on this system by Welter *et al.*, (1994)a.

CeRuSi was described by Rebelsky *et al.*, (1988) as a heavy fermion system with a maximum observed in the C_P/T vs. T plot which is characteristic for these kinds of systems. They did not detect any magnetic order in CeRuSi down to low temperatures which was confirmed down to 1.8 K by Chevalier *et al.*, (2008).

For *R*MnX compounds, a significant antiferromagnetic magnetic contribution of the transition metal is observed because of the increase in the number of d-electrons. Indeed, Welter *et al.*, (1994)b showed that NdMnSi presents two antiferromagnetic transitions at $T_N = 280$ K and 185 K which correspond to the ordering of the Mn and Nd sublattice, respectively.

As has been described, several of the *R*Ti*X* compounds can crystallise in both the CeFeSi and the CeScSi structure type based either on annealing temperature, off-stoichiometry, or both. YTiGe only adopts the CeFeSi structure type and is a Pauli paramagnet (Morozkin *et al.*, (1998)a; Welter *et al.*, (1999); Klosek *et al.*, (2002)). Thus the Ti atoms in these compounds are also non-magnetic. From neutron diffraction studies, the CeFeSi-type *R*TiGe compounds (*R* = Pr, Nd, Tb-Er) are found to be antiferromagnetic below T_N = 62, 128, 312, 185, 124 and 36 K respectively (Vernière *et al.*, (2001)). GdTiGe, stabilised in the CeFeSi-type form after an annealing at 1070 K, was found to order antiferromagnetically below $T_N = 412$ K by Tskhadadze *et al.*, (1999). This is a prime example of an *RTX* compound with an anomalously high transition temperature, exceeding the T_C of Gd metal by almost 100 K despite a lower density of rare earth elements. This is seen to correlate inversely to the number of 3d-electrons of the transition element. Nikitin *et al.*, (1999) show that replacing Mn with Ti in the solid solution $GdMn_{1-x}Ti_xSi$ causes an increase of the T_C from 316 K to 387 K from $x = 0.05 \rightarrow x = 0.3$. CeTiGe, which is also capable of forming both structure types, in its CeFeSi-type form is described by Deppe *et al.*, (2009) as a strongly correlated electronic system and a kondo insulator with $T_K = 55$ K. It undergoes no magnetic order but possess a high field metamagnetic transition ($\mu_0H_c = 13.5$ T Deppe *et al.*, (2010)). Deppe *et al.*, (2010) illustrated that it lies on the non-magnetic side of the quantum critical point where magnetic order is suppressed and Sereni *et al.*, (2010) showed that by replacing some of the Ce atoms by La, the expansion of the unit cell induces a lowering of the Kondo temperature from 55 K to below 4 K.

1.2.2. CeScSi-type

The CeScSi structure type is an ordered variant of the La_2Sb structure (Stassen *et al.*, (1970)), a compound which is quite interesting in its own right as a bulk superconductor with a T_c of 5.3 K (Mizoguchi and Hosono, (2011); Mizoguchi *et al.*, (2012))). These phases are seeing a growing research interest in recent years as they possess many of the characteristics that make the CeFeSi type materials so interesting: quasi-2D structures which can enhance quantum fluctuations (Deppe *et al.*, (2009)), strong coupling between the rare earth atoms that produces anomalously high transition temperatures and a wide range of stable compounds adopting this structure. Like the CeFeSi-type phases, the compounds crystallising in the CeScSi structure type also show a range of different physical properties. Therefore, a brief overview of some of the compounds will be given here rather than an exhaustive encyclopaedia of all the published literature on these compounds.

The high temperature, CeScSi-type, form of CeTiGe was investigated by Chevalier *et al.*, (2010)b. They found that the material does not exhibit any magnetic order above 2 K and that it behaves as a strongly correlated electron system with a large Sommerfeld coefficient, $\gamma = 0.308$ J mol^{-1} K^{-2}. This was comparable to the results for the low temperature form where $\gamma \approx 0.3$ J mol^{-1} K^{-2} (Deppe *et al.*, (2009)).

There was initially a certain ambiguity on the physical properties of CeScSi as it was initially reported by Canfield *et al.*, (1991) to be ferromagnetic and later by Singh *et al.*, (2001) to be antiferromagnetic. However, in their recent publication, Ritter *et al.*, (2016) confirm, by neutron diffraction, the antiferromagnetic (T_N = 26 K) character of CeScSi and show that the magnetic behaviour is more complicated than previously believed from susceptibility measurements alone. They found ferromagnetic double layers of Ce moments, aligned along the *c* axis. These double layers of ferromagnetic Ce atoms are coupled antiferromagnetically along the *c* axis. This then undergoes a spin reorientation to a tilted version of this structure where the angle between the direction of the magnetic moment and the *c* axis changes from 90° to 40° below 22 K. The spin reorientation is coupled with a slight deformation of the unit cell as it changes from the tetragonal CeScSi structure to a triclinic structure.

NdScSi and NdScGe both exhibit ferromagnetic ordering with T_Cs = 171 K and 194 K respectively (Singh *et al.*, (2004)). Cadogan *et al.*, (2005) and later Manfrinetti *et al.*, (2008) describe the magnetic structure of NdScGe, showing that it adopts a collinear ferromagnetic structure below the T_C with all the Nd moments aligned with an angle $\theta = 42(2)$ ° between the direction of the moments and the *c* axis at all examined temperatures. To date the magnetic structure of the NdScSi compound has not been described, however Oleaga *et al.*, (2017) recently investigated the critical behaviour of both compounds to determine the values of the four critical exponents: α, β, γ, and δ which describe the behaviour of different physical quantities near a continuous phase transition. These empirical values are then compared with the predicted values from a mean-field, 3D-Ising, 3D-XY and 3D Heisenberg models. From this they find that NdScSi fits well with a 3D-XY model while NdScGe fits better to a mean-field model. Thus implying that short range interactions in NdScSi are dominant while in NdScGe long-range interactions prevail. This likely arises from the difference in the hybridising of the 3*p* (Si) or 4*p* (Ge) orbitals with the 3*d* orbitals of the Sc atoms to create the conduction band.

The magnetic properties of the series RMgSn and RMgPb where the transition metal is replaced by magnesium were recently studied by Lemoine *et al.*, (2010), (2012)Ritter *et al.*, (2011). Most of these compounds were found to exhibit an overall antiferromagnetic ordering with T_N ranging from 3 to 79 K.

1.3. The insertion of light elements in intermetallic systems

1.3.1. Insertion of light elements

A great deal of research has been carried out on the effects of composition and pressure both in the development of new materials for use in magnetic applications (Skomski *et al.*, (1993)) as well as the development of new superconducting phases (Ren and Zhao, (2009)). For example, once a new superconducting material is identified, often the next step is the study of how pressure affects the superconducting transition temperature (T_c). Generally speaking, pressure augments the transition temperature (Gao *et al.*, (1994)Takahashi *et al.*, (2008)). The application of external pressure is then changed to the application of internal “chemical” pressure by replacing some of the atoms with smaller ones to apply pressure to the crystal from within (Yi *et al.*, (2008). Finally, doping with elements that contain different numbers of electrons (electron or hole doping)((Rotter *et al.*, (2008)) can further increase the T_c by increasing the numbers of charge carriers. A similar logic has been applied to magnetic materials. Through the application of chemical pressure (Chevalier *et al.*, (2008)), doping (Sereni *et al.*, (2010)), and the filling of interstitial sites the magnetic properties can be varied. Furthermore, electronic effects that any guest elements may have when interacting with the magnetic atoms will modify the crystal electric field of the material (Chevalier *et al.*, (2009)). Thus the magnetic properties of a material can be varied in many different ways. To this end, research has been carried out on the filling of vacant interstitial sites with a range of light elements. The lighter elements, due to their small size, show more promise for the formation of insertion compounds as they can better occupy interstitial sites (Coey, (1996)).

Some light elements are unsuitable for insertion into interstitial sites. Elements such as Li and Be are generally considered too large to occupy the vacant sites in rare earth-transition metal intermetallics (Coey, (1996)). On top of this, the use of intermetallic electrodes for Li based electrochemical cells shows that the Li atoms do not undergo insertion reactions with the electrodes but rather combination reactions with the intermetallic species. For example, NiSi alloys undergo reaction with Li to form Li_xSi alloys when used as an anode material for lithium-ion batteries (Wang *et al.*, (2000)) or Co-Sn alloys, which undergo reactions to produce a range of Li-Sn phases (Zhang and Xia, (2006)). A simple consideration of the Pauli electronegativities of the elements will show why oxygen and fluorine are unsuitable for insertion reactions. Due to their high electronegativies, these elements have a tendency to react with the intermetallic compounds rather than to be simply inserted, oxidising them and forming an ionic oxide/fluoride.

We shall now present an overview of the research that has been performed on light element insertion into intermetallic compounds. Initially we shall discuss the work that has been performed on intermetallic compounds from outside the CeFeSi and CeScSi structure types, focusing on hydrogen, carbon, nitrogen and boron. We shall then consider the more focused cases of hydrogen insertion in the CeFeSi and CeScSi type phases and discuss the preliminary work that has been performed on these systems with other light elements.

1.3.1.1. Hydrogen

A significant amount of insertion work has been carried out using hydrogen. The insertion of hydrogen is performed *via* solid-gas reaction under high pressures of hydrogen gas. Coey, (1996) describes the typical diffusion lengths of hydrogen and nitrogen after one hour in solid-gas reactions. At 400°C H typically diffuses 2.1 mm through the sample while N only 1.1 µm. Thus H is roughly 2000 times more mobile than the next lightest gas (with the exception of He which does not undergo an insertion reaction).

With respect to hydrogen insertion the choice of host material is an important factor in determining the viability of a compound. It is well know that, in terms of crystal chemistry, hydrogen has a repulsive interaction with p block atoms. Let us consider the well-studied example of Si and its interaction with hydrogen atoms in a crystal. Here the repulsive interaction causes H to occupy vacant interstitial sites that lead to lower interactions with Si atoms (Yartys *et al.*, (1997)). For example, in $TbNiSiD_{1.78}$ (Brinks *et al.*, (2001)), only the Tb_3Ni sites are occupied while the Tb_3Ni and Tb_3Si tetrahedral sites are both of appropriate size. In contrast, when the hydrogenation of the similar compound $ThNi_2$ is examined (Andresen *et al.*, (1984)) it is seen that hydrogen atoms occupy the Th_3Ni_2 hexahedra (equivalent to the Tb_3NiSi hexahedron formed from adjacent tetrahedral sites in TbNiSi). This suggests that the Tb_3NiSi site is not suitable for H insertion due to the presence of Si atoms. Furthermore, in U_3Si_2, Mašková *et al.*, (2017) postulate that the hydrogen atoms occupy the U_4 tetrahedral sites given that hydrogen occupies sites that minimise its contact with silicon in agreement with the available literature on the topic (Rundqvist *et al.*, (1984)). There are of course examples of Si-H bonding in compounds such as the alkali metal silanide hydrides like $KSiH_3$ (Tang *et al.*, (2016)). However, these contain the complex anion $[SiH_3]^{1-}$ consisting of Si^{4+} and three H^+ ions and so do not offer a good comparison to the interaction of Si and H when both elements may bond to highly electropositive elements, thus both likely carrying at least a partial negative charge.The modification of the magnetic properties of materials with hydrogen insertion has largely remained of purely academic interest due to their relatively low ordering magnetic temperatures. However, there are several clear examples of industrially useful materials that show an improvement in their physical properties at higher temperatures upon hydrogenation. For example the well-known permanent magnets based on $R_2Fe_{14}B$ (Fruchart *et al.*, (1997)) show an increase in their Curie temperature of 150 – 200 K on hydrogenation. This is linked to the negative pressure effect of hydrogenation which improves the Fe-Fe exchange interactions by increasing the short Fe-Fe distances (although an electronic effect from interactions with the H atoms cannot be wholly discounted either). Using the scale for the pressure-T_C relationship put forward by Kamarád *et al.*, (1987), Isnard and Pop, (2011) calculate that each hydrogen atom inserted into $R_2Fe_{14}B$ is roughly equivalent to -7 kbars of pressure. Another example of hydrogen insertion proving interesting for more than simply academic reasons is the promising magnetocaloric material $La(Fe_{1-x}Si_x)_{13}$. Lyubina *et al.*, (2008) demonstrated that hydrogenation of this material drastically improves its desirability as a potential magnetocaloric material by augmenting its T_C and also enlarging the temperature range over which it may operate.

A number of binary intermetallics such as the AB_2 laves phases have seen significant research interest for the insertion of hydrogen. Paul-Boncour and Percheron-Guégan, (1999) describe a detailed investigation of the hydrogenation and deuteration of the YFe_2 system. Deuteration initially increases the Curie temperature of the parent YFe_2 from 560 K to 720 K for $YFe_2D_{1.2}$. Further increasing the deuterium content reduces the T_C to 300 K for the filled deuteride ($YFe_2D_{4.2}$). At the same time, the creation of new Fe-H bonding states causes a progressive filling of the hybridised 4p-3d band of iron. Indeed, the interaction between the localised magnetism of the rare earth element and the more itinerant magnetism of the transition element provide a range of different magnetic properties (Paul-Boncour, (2004)). Coupled with the ability of these compounds to absorb a significant 5 H f.u.$^{-1}$ (Shoemaker and Shoemaker, (1979); Paul-Boncour *et al.*, (2001)) and the sensitivity of the magnetic properties to hydrogen content, they make an interesting class of materials to study for magnetic and electronic structure changes.

Materials with a high ability to absorb hydrogen such as the binary laves phases described above (Paul-Boncour, (2004); Bououdina *et al.*, (2006)) and the well-known $LaNi_5$ (Bououdina *et al.*, (2006)) are of interest as potential hydrogen storage materials. In the continuing search for clean and renewable sources of energy, hydrogen gas receives a lot of attention due to its high energy density and the clean nature of energy produced from H_2 (Sakintuna *et al.*, (2007)). If we put to one side the emissions associated with hydrogen production (the steam reforming of natural gas is the main method for industrially produced hydrogen), hydrogen reaction with oxygen (combustion, fuel cells etc.) simply produces water as a by-product. However, hydrogen gas presents a number of difficulties with regards to its storage. High pressure gas cylinders have an inherent danger and cost associated with them and other forms such as liquid H_2 require very low temperatures which are expensive to produce. Therefore the storage of hydrogen in the form of solid metal hydrides is an attractive option for hydrogen storage providing a safe way to store hydrogen in a solid form. The department of energy of the United States of America predict that, in order to be viable, potential hydrogen storage materials must be able to store 6.5 wt% of hydrogen. On top of this, they will ideally have a low temperature of hydrogen absorption/desorption and good kinetics for these reactions (Sakintuna *et al.*, (2007)), be composed of light, cheap elements with good stability in air (Bououdina *et al.*, (2006)). Much of the research on hydrogen storage materials is based on Mg-rich compounds due to the low weight and high hydrogen storage capacity of Mg metal. Unfortunately, Mg metal possesses reasonably slow hydrogenation kinetics and requires elevated temperatures to undergo hydrogenation. For this reason, the bulk of the work on Mg based hydrogen storage materials focuses either the insertion of hydrogen into Mg alloys or the decomposition of Mg alloys under hydrogen to form binary metal hydrides. This decomposition is interesting as it produces a very fine particle size which accelerates the kinetics of adsorption and desorption (Crivello *et al.*, (2016)). Alternatively, a mixture of Mg alloys can be used in tandem to improve the hydrogenation properties as seen in Løken *et al.*, (2007). Their work details the hydrogenation of an alloy consisting of 72 wt.% Mg, 20 wt.% Ni, and 8 wt.% of a lanthanum Mischmetal alloy. The alloy was crystallised using fast cooling method and subjected to treatment such as high energy ball milling to reduce the crystallite size and refine the microstructure. This has the effect of accelerating the hydrogenation kinetics. The alloy can absorb around 5.5 wt.% of hydrogen in total. The development of hydrogen storage materials often involves techniques such as these to improve the kinetics of hydrogenation and the elements added (such as rare earth metals) are chosen for their ability to catalyse the dissociation of H_2 into H atoms that can diffuse through the material. The materials studied during chapter 3 are not suitable for hydrogen storage applications due to the high molar weight and low amount of hydrogen they can absorb (< 1 wt.%). Instead, they are interesting for the study of their physical properties.

Hydrogenation has been found to produce a particularly unusual and interesting effect by Huiberts *et al.*, (1996). They describe the startling effect of hydrogenation on the optical properties of thin films of trivalent rare earths. When passing from the dihydride to the trihydride (passing from a metallic to a semi-conducting state) it was found that the materials also exhibit a transformation from a shiny to a transparent (in the visible spectrum) state as illustrated in Figure 1. 3. Thus these compounds go from a mirror-like form to optically transparent in what has since been dubbed a “hydrogen switchable mirror”. The name is derived from the reversible nature of this transition which can be controlled by varying the hydrogen pressure around the mirror. Since then a number of intermetallic compounds have also been found to exhibit this effect such as Mg_2Ni (Man and Iannuzzi, (2006)), a range of *R*-Mg alloys (Nagengast *et al.*, (1999); Iannuzzi *et al.*, (2004)) and several Mg-*T* alloys (*T* = Ni, Co, Fe or Mn) (Iannuzzi *et al.*, (2004)).

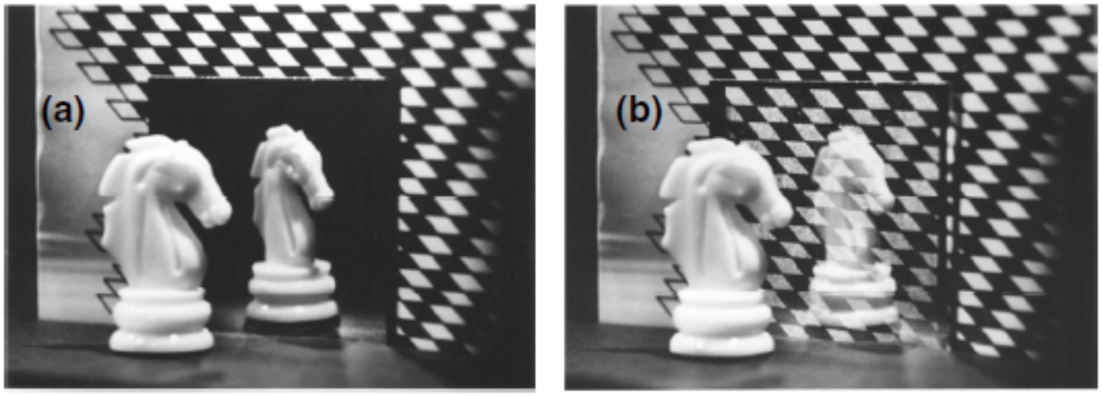

Figure 1. 3. A hydrogen switchable mirror (a) before and (b) after exposure to hydrogen as given in Man and Iannuzzi, (2006)

Hydrogen is thus used in many different fields from the production of magnetocaloric materials (Bez *et al.*, (2013)) and energy storage to more exotic magnetic and physical effects. However, hydrogen insertion also produces a simple physical effect which is quite useful in the working of metallic materials that, due to their hardness, are difficult to machine. Hydrogen insertion causes a significant expansion of the unit cell of most materials. With this comes an inherent fragilisation of the material known as hydrogen decrepitation. Materials that have suffered this effect often exhibit much smaller particle size than before hydrogenation. On top of this, the corresponding hydrides are usually much softer, making mechanical grinding much less time consuming and easier (Senkov and Froes, (1999); Zhao *et al.*, (2010)). An examples of this are used in the production and recycling of Nd-Fe-B permanent magnets (Lixandru *et al.*, (2017) which can reversibly absorb and desorb hydrogen.

1.3.1.2. Boron

Due to the relative lack of boron containing gaseous compounds, boron is normally inserted into intermetallic compounds either through its inclusion in the melt during the initial synthesis, or else through diffusion of solid boron into the parent intermetallic by high temperature treatment. Of all the light elements discussed here, boron insertion is by far the least studied with a fairly limited selection of true insertion compounds available (Roger *et al.*, (2006)). The famous $R_2Fe_{14}B$ compounds likely spring to mind as an example but as they do not exist without the boron atoms they cannot be considered true insertion compounds. One of the truly quintessential compounds for interstitial insertion in intermetallics are the family of R_5Si_3 (R = rare earth) which crystallise in the Mn_5Si_3 structure. The R_5Si_3 structure can be considered to be formed of essentially infinite chains of confacial trigonal anti-prisms (face sharing octahedra) of the R atoms which are then bridged by the Si atoms. Such vacant octahedral sites have been shown to accept a wide range of different interstitial atoms such as B, C and N. For certain compositions, this list of possible guest atoms can contain up to 20 members (Corbett *et al.*, (1998)). Mayer and Felner, (1974) describe, crystallographically, the insertion of boron into these compounds for R = La, Nd, Gd, Tb and Dy by inclusion of boron with the other elements in an arc furnace. The high temperatures achieved by this method allow the boron to melt along with the other elements. Boron is found to occupy the vacant octahedral sites and to cause a slight contraction of the unit cell. Roger *et al.*, (2006) later expanded on this collection and included magnetic characterisation for R = Gd, Dy, Ho, Er, Lu and Y (structure shown in Figure 1. 4.). For these borides they observe a decrease in the Néel temperatures for the antiferromagnetic materials ($R \neq$ Er) while the ferromagnetic $Er_5Si_3B_x$ shows a slight increase in the Curie temperature.

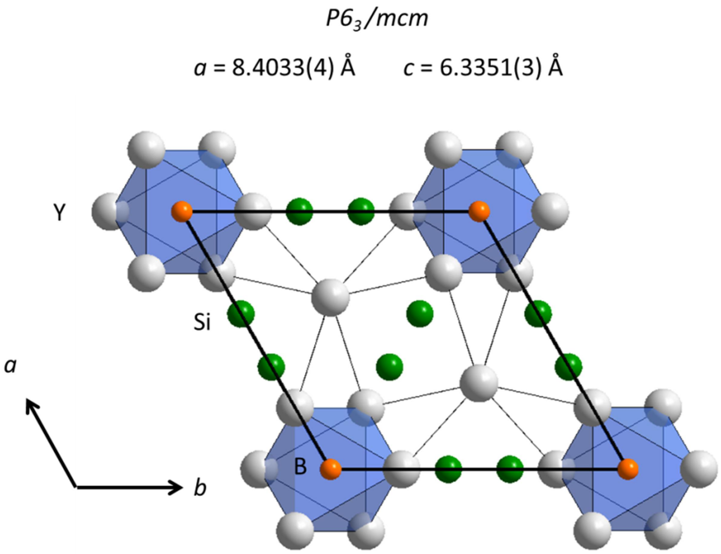

Figure 1. 4. The crystal structure of $Y_5Si_3B_{0.65}$ published in Roger *et al.*, (2006) showing the octahedral sites occupied by the boron atoms

Though it has been studied in less detail than some of the other light element candidates for insertion experiments, boron is an attractive interstitial element for the development of permanent magnets in particular. During this work, attempts were made to insert boron into the vacant interstitial sites, however these attempts were unsuccessful and resulted only in the formation of binary borides such as RB_6, RB_4 and ScB_6 (R = Ce and Nd).

1.3.1.3. Carbon

Historically, the most famous example of light element insertion by far, is steel. The inclusion of C in the interstitial sites of Fe impedes the movement of planes of Fe atoms and greatly increases the strength of the parent Fe. This has been used for thousands of years to produce tools and weapons. Binary metal carbides are prized for their hardness in drilling and similar applications.

In the literature, there are four routes that are used for the insertion of carbon into intermetallic compounds:

i). The inclusion of carbon during the fusion of the initial elements. This is accomplished by adding a source of solid carbon such as graphite or activated charcoal with the starting elements.

ii). The absorption of C by reaction of the parent intermetallic with a carbon containing gas such as methane or butane at high temperature (solid-gas reaction) (Coey *et al.*, (1992)).

iii). Solid-gas reaction using a solid carbon compound (such as anthracene) that decomposes to form a carbon containing gas at high temperature (Fruchart *et al.*, (1994); Khazzan *et al.*, (2010); Phejar *et al.*, (2016)).

iv). The diffusion of solid carbon into the parent intermetallic by high temperature treatment of a mixture of carbon/graphite with the starting intermetallic compound (Ceramic/solid state method) (Skolozdra *et al.*, (1995)

As previously mentioned, high strength permanent magnets such as $R_2Fe_{14}B$ are not, strictly speaking, insertion compounds as the intermetallic cannot be stabilised with the interstitial sites empty. The R_2Fe_{17} type phases are, however, quite capable of forming true insertion compounds such as $Sm_2Fe_{17}C_{3-\delta}$ (Coey and Hurley, (1992)). Fruchart *et al.*, (1994) describe a rigorous investigation of the synthesis of $R_2Fe_{17}C_{x\leq 3}$ (R = Ce, Nd, Sm, Ho, Er, etc.) through solid-gas reaction between the parent R_2Fe_{17} compound and the vapour of a large number of different carbon rich, organic compounds (benzene, toluene, anthracene, etc.). In the temperature range 480 ± 10 °C they obtain a well crystallised, single phase, $R_2Fe_{17}C_x$ using this method. In these compounds carbon is shown to occupy the octahedral [R_2Fe_4] 9*e* position in the unit cell with a significant increase in the T_C (De Mooij *et al.* 1988 and Coey 1991). The occupation of these sites causes an expansion of the lattice and generally conserves the structure of the parent compound as seen in Figure 1. 5. The increase in the T_C stems from an increase in the exchange interactions between the iron atoms by increasing the Fe-Fe distance (as seen in the $R_2Fe_{14}B$ hydrides). It is important in the production of permanent magnets that materials possess high coercivity, T_C and remanent magnetisation. While these carbides show good coercivity and T_C, they do not exhibit a sufficiently large remanence and so in practice they are not used.

The R_2Fe_{17} phases to be used as permanent magnets can be improved by substituting a large, non-magnetic, element onto the Fe sites. Khazzan *et al.*, (2010) describe the magnetic properties of $Sm_2Fe_{17-x}Mo_x$ and the further improvement of this compound through carbon insertion to form $Sm_2Fe_{17-x}Mo_xC_y$. The substitution of the non-magnetic transition element causes a reduction in the planar magnetocrystalline anisotropy from the Fe sublattice and causes the R sublattice to win out, thus producing an axial magnetocrystalline anisotropy for R = Sm. After this, interstitial inclusion of an element such as carbon drastically improved the properties such as the thermal stability and Curie temperature. However, as with the $Sm_2Fe_{17}C_{3-\delta}$ compounds this causes a reduction in their coercive field and remnant magnetism and thus are unattractive in practice.

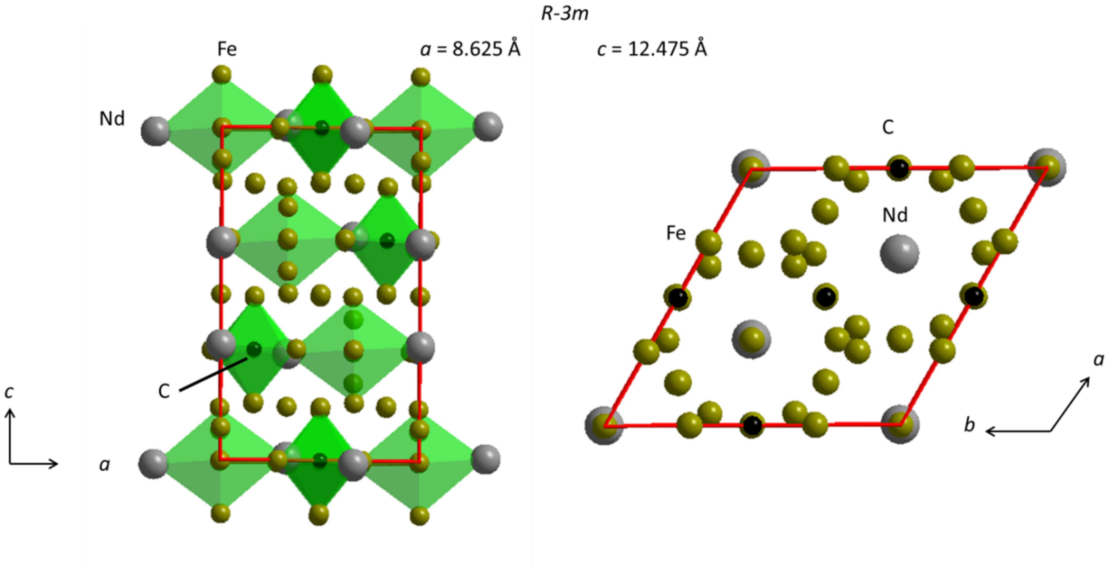

Figure 1. 5. The crystal structure of $Nd_2Fe_{17}C_{0.4}$ from De Mooij and Buschow, (1988) in the *ac* (left) and *ab* (right) planes. The 9*e* octahedral sites occupied by C are also emphasised in the left image.

The accessibility of octahedral crystallographic sites for carbon is seen also in the Mn_5Si_3-type (Mayer and Felner, (1974)), or $La(Fe_{1-x}X_x)_{13}$ compounds (where X = Si, Al or Ga) (Shcherbakova *et al.*, (2003). Indeed, the $La(Fe,Si)_{13}$ compounds and other members of the $NdZn_{13}$ structure type are interesting for magnetocaloric applications due to their large magnetocaloric effect and low cost of materials. However, stabilisation of the phase often requires lengthy annealing times. Zhang *et al.*, (2013) illustrate that, by including small amounts of carbon in the crystal structure of $La(Fe_{1-x}Si_x)_{13}$ during the synthesis, the annealing time can be reduced from 40 to 10 days. This had the added benefit of increasing the T_C from 195 K to 250 K for $LaFe_{11.6}Si_{1.4}C_x$ when x increases from 0 to 0.6. It should be noted that a similar effect was previously observed during insertion of hydrogen (see above).

Skolozdra *et al.*, (1995) describe the insertion of carbon in $RFe_{12-x}Mo_x$ type materials for the case of x = 1.5 using the diffusion of solid state carbon at high temperatures into the intermetallic lattice. This causes a significant expansion of the unit cell and a large increase in the T_C. The Nd, Tb, Dy and Ho compounds all show an increase in the magnetocrystalline anisotropy on carbon insertion while the Y, Gd and Er compounds show a change in the easy axis direction from axial (along the *c* axis) to planar.

Clearly the inclusion of carbon into the crystal structure can produce a wide range of interesting and useful materials with the potential for applications in some areas of materials research. Given the tendency of carbon to occupy octahedral sites in these crystal structures and the presence of the octahedral interstices in the CeScSi structure type, we have successfully attempted to insert carbon into these materials. In chapter 4 the effects of carbon insertion on the crystallographic, magnetic and transport properties of the host *R*Sc*X* (*R* = La, Ce, Nd and Gd, *X* = Si and Ge) are investigated and discussed.

1.3.1.4. Nitrogen

Like carbon, nitrogen is capable of occupying the octahedral interstitial sites of intermetallic systems. From a practical stand point nitrogenation has many attractive features: as an inert, gaseous element in its natural state it is easy to insert via solid-gas reaction routes with less experimental risk than something like hydrogen. The resulting nitrides tend to be reasonably stable (although they do sometimes decompose at high temperatures). The major inconvenience of using nitrogen arises from the N≡N triple bond. In order for nitrogen atoms to diffuse into a material, it is necessary to break this strong triple bond. Such an endeavour, while not impossible, often requires high temperatures or long reaction times. Also the large size of the nitrogen atom when compared to the very small and mobile hydrogen atom makes its diffusion through a solid matrix relatively slow. Coey, (1996) provides the typical diffusion lengths for hydrogen and nitrogen after 1 hour of reaction. This data suggests that, at 400°C, hydrogen diffuses 2000 times faster than nitrogen in the same matrix. Thus nitrogen insertion is best performed on finely ground powder samples or porous materials.

Nitrogenation studies have been extensively carried out on the R_2T_{17} and $R(T_{1-x}T'_x)_{12}$ materials where *R* is a rare earth element and *T* is a transition metal element. Like carbon, nitrogen was found to occupy the 2*b* octahedral sites of these materials, causing an expansion of the unit cell volume (Coey *et al.*, (1992). The resulting nitrides show a general improvement of the magnetic properties with $Sm_2Fe_{17}N_x$ increasing of Curie temperature from 117 K for x = 0 to 473 K for x = 2.94 (Katter *et al.*, (1992). This effect is widely observed in the Fe based permanent magnetic materials that undergo insertion reactions. Interestingly, the opposite effect is observed in $Sm_2Fe_{17}N_x$ where Liu *et al.*, (1993) observe a lowering of the Curie temperature from 1195 K for pristine Sm_2Co_{17} (Buschow, (1977)) to 840 K with a reduction of the rare earth and cobalt moments. The effect of nitrogen must therefore be compared to carbon for these materials as the two elements may both cause an increase in the T_C. It is found, however, that nitrogen causes larger increases in the T_C of the parent materials (Coey and Hurley, (1992)) and so many of these nitrides provide very interesting candidates for permanent magnets produced through light element insertion.

1.3.2. Insertion of light elements in the CeFeSi and CeScSi structure types

We have clearly demonstrated that light element insertion is a valuable and widespread technique in the development of bespoke materials for many applications in the general case of intermetallic systems. Before starting this work it is, of course, necessary to also summarise the work that has been performed on the compounds crystallising in the CeFeSi and CeScSi structure types. Thus far, insertion work on these compounds has been focused on the insertion of hydrogen. Therefore we shall present here a summary of this hydrogenation work along with preliminary work on insertion of carbon and boron. As discussed, the CeFeSi and CeScSi structures both contain vacant tetrahedral sites that provide interesting candidates for the insertion of light elements. A notable difference between the CeScSi and CeFeSi structure types, however, is the presence of vacant octahedral sites in the CeScSi structure. This was first detailed by Wang *et al.*, (1977), (1980) when they found that phases crystallising in the La_2Sb structure could contain interstitial oxygen atoms in the R_6 octahedral sites.

1.3.2.1. CeFeSi

Hydrogen insertion in the CeFeSi materials has been very well studied in the literature. Chevalier *et al.*, (2005) demonstrated that, once hydrogenated, these materials adopt the ZrCuSiAs-type structure. The full occupation of the rare earth tetrahedral sites in these compounds by hydrogen results in the stoichiometric composition $RTXH_{1.0}$. No $RTXH_x$ solution solid solution with $0 < x < 1$ has been reported. This insertion induces an anisotropic expansion of the unit cell with the *a* parameter slightly decreasing and the *c* parameter strongly increasing.

The initial motivation for this hydrogenation work, has been to study the competition between RKKY (Ruderman-Kittel-Kasuya-Yosida) magnetic interactions, Kondo interaction and intermediate valence states in Ce compounds. Therefore Ce systems have a seen a significant research interest over the years.

An example of this is the hydrogenation of CeCoSi described by Chevalier and Matar, (2004); Chevalier *et al.*, (2006)b where the *a* parameter decreases from 4.041(2) Å to 3.955(2) Å (-2.1 %) while the *c* parameter increases from 6.990(2) Å to 7.861 Å (+12.5 %). This produces an overall expansion of the unit cell volume of 7.8 % which equates to a very large negative pressure effect. Hydrogenation of this compound results in the destruction of the antiferromagnetic order of the parent material leading to a spin fluctuation behaviour with T_{sf} = 130 K. The homologous germanide, CeCoGe, exhibits a similar effect with the destruction of the antiferromagnetic order (T_N = 5 K) and the onset of spin fluctuation behaviour below T_{sf} = 15 K (Chevalier *et al.*, (2009)).

While some CeFeSi-type materials show a reduction of the magnetic properties on hydrogenation, this is not always the case. The hydrogenation of non-magnetic materials such as the heavy fermion CeRuSi can be used to induce magnetism in the compound. Chevalier *et al.*, (2008) and Tencé *et al.*, (2008) found that CeRuSiH presents a complex antiferromagnetic order with two Néel temperatures at T_{N1} = 7.5 K and T_{N2} = 3.1 K. Here, the driving effect is the negative pressure of the lattice expansion ((Chevalier *et al.*, (2009)). This is similar to the effect seen in $(Ce_{0.8}La_{0.2})Ru_2Si_2$ (Besnus *et al.*, (1985)) and $CeRu_2(Si_{0.9}Ge_{0.1})$ (Godart *et al.*, (1986)) where magnetism has been induced through the inclusion of larger elements in the lattice. This causes an expansion of the heavy fermion $CeRu_2Si_2$ lattice and induces antiferromagnetic order as in CeRuSi.

Therefore, hydrogenation provides a method of pushing Ce magnetic compounds towards quantum criticality through the suppression of the magnetic order or, inversely, by moving a non-magnetic material towards the magnetic state. This may be accomplished through a mixture of doping/compositional changes, magnetic field or pressure. The interest of a quantum critical point, which occurs at the boundary between a magnetic and a non-magnetic state, is that the thermal fluctuations that generally govern these transitions become null at 0 K. Thus the order parameters are governed entirely by quantum fluctuations within the material and these fluctuations can produce other, interesting effects such as superconductivity and exotic physical properties at finite temperatures above 0 K. Examples of materials that can be driven to a superconducting state in this way include UCoGe (Slooten *et al.*, (2009)), which becomes superconducting around the quantum critical point on the border of the ferromagnetic and non-magnetic state when tuned using pressure. $CeIn_3$ and $CePd_2Si_2$ can both also be tuned to a superconducting state by pushing them to the boundary between magnetic and non-magnetic states using pressure.

Interestingly, the ZrCuSiAs-type adopted by the CeFeSi-type hydrides is the same structure as the iron based superconductors (LaFePO, $CeFeAsF_{1-x}H_x$, $SmFeAsO_{1-x}F_x$, etc (Chen *et al.*, (2008); Zhao *et al.*, (2008); Ren and Zhao, (2009); Ju *et al.*, (2010); Taylor *et al.*, (2013)) with H atoms in the rare earth tetrahedra instead of O or F. The crystal structure of $SmFeAsO_{1-x}F_x$ and some resistivity curves which show the superconducting transition, reproduced from Chen *et al.*, (2008), are shown in Figure 1. 6. Therefore, to a lesser extent this hydrogenation work on CeFeSi type intermetallics is done in the hope of finding new superconducting materials. One recent example described by Tencé *et al.* (un-published work, arXiv:1701.05010) of work on the LaFeSiH hydride system shows the onset of superconductivity below 9 K through hydrogenation. Thus this route does indeed have the potential to produce superconductivity. A particular interest of working with these materials is that, unlike the iron pnictide superconductors, they can be synthesised with empty tetrahedral sites. This allows their properties to be studied and modelled before and after the filling of the tetrahedral sites to better understand the true effect of the inserted element on the physical properties.

Hydrogenation is thus a powerful way to modify the magnetic interactions in CeFeSi-type compounds. While a number of examples have been provided for the Ce*TX* compounds, hydrogen insertion also provides an interesting way to modify the magnetic properties of other *RTX* compounds in this structural family.

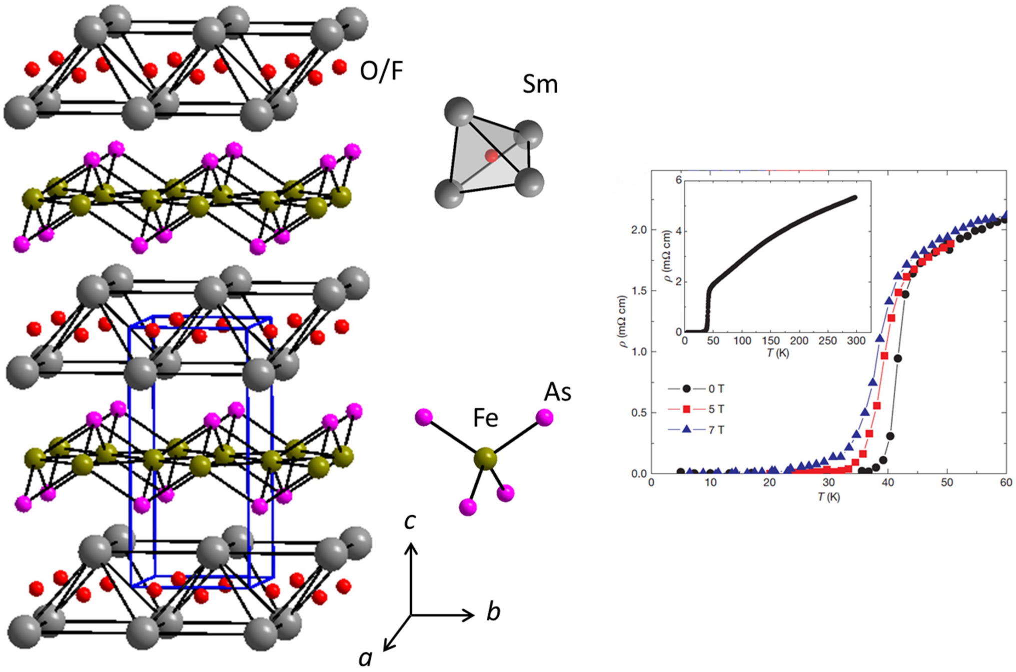

Figure 1. 6. The crystal structure of $LaFeAsO_{1-x}F_x$ and measures of the electrical resistivity in the absence and presence of an external magnetic field from Chen *et al.*, (2008). The inset shows a larger temperature range.

The CeFeSi-type compound NdMnSi is antiferromagnetic showing two magnetic ordering temperatures, T_{N1} = 280 K and T_{N2} = 185 K. These correspond to the magnetic ordering of the Mn and Nd sublattices respectively (Welter *et al.*, (1994)b). A spin reorientation of the Mn lattice is also observed around T_S = 80 K. Tencé *et al.*, (2009) describe the hydrogenation of this compound and find that it causes an opposite effect on the magnetic order of the two sublattices. The T_{N1} of the Mn sublattice increases to 565(5) K while the T_{N2} for the Nd sublattice decreases to 103(4) K. In the hydride, the ordering of the Nd sublattice and the spin reorientation of the Mn sublattice were found to occur simultaneously *via* neutron diffraction. Tencé *et al.*, (2009) link the increase in T_{N1} to a decrease in the intralayer $d_{Mn\text{-}Mn}$ distance from 2.901 Å to 2.847 Å on hydrogenation which in turn increases the exchange interaction between the Mn atoms.

Hydrogenation of NdCoSi and NdCoGe has been shown to have a striking effect on the magnetic properties of these compounds by Tencé *et al.*, (2010). NdCoSi and NdCoGe are antiferromagnetic below T_N = 7.5 K and 8.3 K. They both readily absorb hydrogen, undergoing similar structural changes as the other hydrides in this family. However, hydrogen causes a change in the type of magnetic order from antiferromagnetic to ferromagnetic below 20.5 K and 15.9 K in the silicide and germanide respectively. They established from electronic structure calculations that this arises from a reduction in the number of conduction electrons through the creation of Nd-H bonds.

1.3.2.2. CeScSi

The CeScSi structure is interesting for insertion studies due to its strong structural similarities with the CeFeSi one. To date it has seen far less research than the CeFeSi compounds but that is beginning to change with a number of papers published on the hydrogenation of CeScSi-type compounds. Like the CeFeSi-type materials, the CeScSi structure type contains vacant rare earth tetrahedral sites that are attractive candidates for hydrogen insertion.

The short list of CeScSi-type materials that have been studied for their hydrogenation properties includes the high temperature form of GdTiGe and *R*ScSi and *R*ScGe (*R* = La, Ce). GdTiGe, like the aforementioned CeTiGe, can exist in both the CeFeSi and CeScSi structure types. Tskhadadze *et al.*, (1999) describe the mechanical hydrogenation of this material stating that the CeScSi-form was capable of absorbing 4 atoms of hydrogen per formula unit. This result is surprising given that the CeFeSi-type materials all absorb only one atom of hydrogen per unit cell. A further investigation of this was performed by Gaudin *et al.*, (2011) where they determined that in fact the CeScSi-form of GdTiGe absorbs only one atom of hydrogen per formula unit. The initial aim of their experiment was to determine if the T_C = 376 K of the ferromagnetic CeScSi-type GdTiGe could be tuned by hydrogen content to produce a useful room temperature magnetocaloric effect (MCE). However, no solid solution GdTiGeHx has been observed, and the complete filling of the R_4 tetrahedra (leading too GdTiGeH phase) produced a near total destruction of the magnetism of the parent compound with paramagnetic behaviour above 4 K and a slight negative value of the paramagnetic Curie temperature, θ_P, of -13.5 K which indicates predominant local antiferromagnetic interactions around the Gd atoms.

In their studies of the hydrogenation of, *R*ScSi and *R*ScGe (R = La or Ce) phases Chevalier *et al.*, (2010)c detail that these materials also appear to absorb one atom of hydrogen per formula unit. The Ce compounds also show a destruction of the magnetic order with CeScSi and CeScGe showing a decrease of the T_N from 26 K to 3 K and from 46 K to 3 K respectively upon hydrogenation. The hydrogenation of the materials also causes an onset of Kondo behaviour in both compounds and calculations using the density functional theory (DFT) indicate the presence of strong Ce-H bonding.

As mentioned, some preliminary work has been carried out on the insertion of other light elements into the CeScSi-type materials. In the doctoral thesis of Lemoine, (2011), chap. 4, attempts to insert boron into *R*TiGeB$_x$ (*R* = Gd-Er) are described. This work states the presence of a metastable *R*TiGeB$_x$ phase with the CeScSi structure type that crystallises from the melt and is destroyed on annealing. Single crystal studies could not locate the boron atoms within the crystal structure; however, neutron diffraction measurements indicated that the boron is located in the R_2Ti_4 octahedra with a low occupation. No conclusive changes in the magnetic properties was detected after boron insertion in these compounds and to our knowledge, no further work has been published on this topic to date.

During the doctoral work of (Klosek, (2002)), the insertion of carbon into the *R*TiGe systems (*R* = Y, Gd-Tm) to form *R*TiGeC$_x$ was investigated by diffraction (both X-ray and neutron) and magnetic susceptibility measurements. While these materials can normally crystallise in both the CeFeSi and CeScSi structure types, they describe that a small amount of carbon (x = 0.05) could be inserted in the main phase and stabilised the CeScSi form. By neutron diffraction the carbon was localised to the 2*b* Wyckoff position (0 0 ½). Unfortunately, the magnetic susceptibility could not unambiguously assign a magnetic ordering temperature to this new phase and no further work has been published on the subject.

Thus the insertion of light elements into CeScSi-type materials has thus far not seen the same rigorous research interest as the CeFeSi-type compounds. It is for this reason that this thesis work is focused predominantly on the study of these phases.

1.4. Conclusions and aims

Thus the insertion of light elements has been used for many years as a way of varying the physical properties of intermetallic systems containing empty interstitial sites. It can be used to create interesting effects such as, for example, superconductivity or Kondo-effect, as well as to improve the mechanical or magnetic properties of active magnetic materials like permanent magnets based on the $Nd_2Fe_{14}B$ system and magnetocaloric materials used for magnetic refrigeration like $LaFe_{13-x}Si_x$.

Intermetallic systems possessing vacant interstitial sites are attractive candidates for the study of light element insertion as they are stable with the sites empty. This allows us to analyse the true effect of the light element addition and the influence of the crystallographic site environment. Among such intermetallics, those crystallising in the CeFeSi and CeScSi structure types are particularly interesting. They each possess vacant interstitial sites and exist for a huge range of compositions with an equally vast range of physical properties. The host structure is also conserved through light element insertion. Thus they provide an attractive suite of materials for the study of the impact of light element insertion on the crystal structure and the physical properties. The aim of this thesis work is, therefore, to expand on the existing literature on the hydrogenation of CeFeSi and CeScSi-type compounds as well as to study the insertion of other light elements such as carbon.

Chapter 2 will provide the details of the syntheses and characterisation techniques used for the various compounds studied. In chapter 3 we will elaborate further on some of this hydrogen work, attempting to clear up discrepancies in the literature. In chapter 4 we will demonstrate for the first time unambiguously the possibility of inserting carbon into the CeScSi-type materials, describing the effect of carburation on the crystal structure and physical properties. Finally, Chapter 5 will present the results of hydrogenation performed on the carbide materials described in chapter 4.

1.5. Bibliography

Besnus, M. J., Kappler, J. P., Lehmann, P. and Meyer, A. ((1985)) 'Low temperature heat capacity, magnetization, resistivity of $CeRu_2Si_2$, with Y or La substitution', *Solid State Communications*, 55(9), p. 779–782. doi: 10.1016/0038-1098(85)90796-3.

Bez, H. N., Teixeira, C. S., Eggert, B. G. F., Lozano, J. A., Capovilla, M. S., Barbosa, J. R. and Wendhausen, P. A. P. ((2013)) 'Synthesis of room-temperature magnetic refrigerants based on La-Fe-Si by a novel process', *IEEE Transactions on Magnetics*, 49(8), p. 4626–4629. doi: 10.1109/TMAG.2013.2256111.

Bououdina, M., Grant, D. and Walker, G. S. ((2006)) 'Review on hydrogen absorbing materials - Structure, microstructure, and thermodynamic properties', *International Journal of Hydrogen Energy*, 31(2), p. 177–182. doi: 10.1016/j.ijhydene.2005.04.049.

Buschow, K. H. J. ((1977)) 'Intermetallic compounds of rare-earth and 3d transition metals', *Reports on Progress in Physics*, 40(10), p. 1179–1256. doi: 10.1088/0034-4885/40/10/002.

Cadogan, J. M., Ryan, D. H., Gagnon, R. and Voyer, C. J. ((2005)) 'Magnetic structure of NdScGe', *Journal of Applied Physics*, 97(10), p. 10A916. doi: 10.1063/1.1851884.

Canfield, P. C., Thompson, J. D. and Fisk, Z. ((1991)) 'Novel Ce magnetism in CeDipnictide and Di-Ce pnictide structures', *Journal of Applied Physics*, 70(10), p. 5992–5994. doi: 10.1063/1.350071.

Chen, X. H., Wu, T., Wu, G., Liu, R. H., Chen, H. and Fang, D. F. ((2008)) 'Superconductivity at 43 K in $SmFeAsO_{1-x}F_x$', *Nature*, 453(7196), p. 761–762. doi: 10.1038/Nature07045.

Chevalier, B., Gaudin, E., Tencé, S., Malaman, B., Fernandez, J. R., André, G. and Coqblin, B. ((2008)) 'Hydrogenation inducing antiferromagnetism in the heavy-fermion ternary silicide CeRuSi', *Physical Review B* - Condensed Matter and Materials Physics. American Physical Society (APS), 77(1), p. 1–10. doi: 10.1103/PhysRevB.77.014414.

Chevalier, B., Hermes, W., Gaudin, E. and Pöttgen, R. ((2010)a) 'New high temperature modification of CeTiGe: structural characterization and physical properties', *Journal of Physics: Condensed Matter*. IOP Publishing, 22(14), p. 146003. doi: 10.1088/0953-8984/22/14/146003.

Chevalier, B., Hermes, W., Heying, B., Rodewald, U. C., Hammerschmidt, A., Matar, S. F., Gaudin, E. and Pöttgen, R. ((2010)b) 'New Hydrides REScSiH and REScGeH (RE = La, Ce): Structure, Magnetism, and Chemical Bonding', *Chemistry of Materials*. American Chemical Society (ACS), 22(17), p. 5013–5021. doi: 10.1021/cm101290f.

Chevalier, B. and Matar, S. F. ((2004)) 'Effect of H insertion on the magnetic, electronic, and structural properties of CeCoSi', *Physical Review B*, 70(17), p. 174408. doi: 10.1103/physrevb.70.174408.

Chevalier, B., Matar, S. F., Ménétrier, M., Marcos, J. S., Fernandez, J. R. and Rodriguez Fernandez, J. ((2006)a) 'Influence of Ce-H bonding on the physical properties of the hydrides $CeCoSiH_{(1.0)}$ and $CeCoGeH_{(1.0)}$.', *Journal of physics: Condensed matter*, 18(26), p. 6045–56. doi: 10.1088/0953-8984/18/26/022.

Chevalier, B., Matar, S. F., Sanchez Marcos, J. and Rodriguez Fernandez, J. ((2006)b) 'From antiferromagnetic ordering to spin fluctuation behavior induced by hydrogenation of ternary compounds CeCoSi and CeCoGe', *Physica B: Condensed Matter*, 378–380(SPEC. ISS.), p. 795–796.

doi: 10.1016/j.physb.2006.01.291.

Chevalier, B., Pasturel, M., Bobet, J. L. and Isnard, O. ((2005)) 'Influence of hydrogenation on the structural and magnetic properties of compounds based on cerium and crystallizing in the tetragonal CeFeSi-type structure', *Solid State Communications*, 134(8), p. 529–533. doi: 10.1016/j.ssc.2005.02.040.

Chevalier, B., Tencé, S., Gaudin, E., Matar, S. F. and Bobet, J.-L. L. ((2009)) 'Various magnetic behaviors of the hydrides deriving from the tetragonal CeFeSi-type compounds', *Journal of Alloys and Compounds,* 480(1), p. 43–45. doi: 10.1016/j.jallcom.2008.09.183.

Coey, J. M. D. ((1996)) 'Interstitial intermetallics', *Journal of Magnetism and Magnetic Materials,* 159(1–2), p. 80–89. doi: 10.1016/0304-8853(95)00603-6.

Coey, J. M. D. and Hurley, D. P. F. ((1992)) 'New interstitial rare-earth iron intermetallics produced by gas phase reaction', *Journal of Magnetism and Magnetic Materials*, 104–107(PART 2), p. 1098–1101. doi: 10.1016/0304-8853(92)90506-J.

Coey, J. M. D., Otani, Y., Sun, H. and Hurley, D. P. F. ((1992)) 'Magnetic Properties of Interstitial Compounds $Sm(Fe_{11}Ti)X_{1-\delta}$; (X=N,C)', IEEE Translation Journal on Magnetics in Japan, 7(8), p. 613–617. doi: 10.1109/TJMJ.1992.4565464.

Corbett, J. D., Garcia, E., Guloy, A. M., Hurng, W., Kwon, Y. and Leon-Escamilla, E. A. ((1998)) 'Widespread Interstitial Chemistry of Mn_5Si-Type and Related Phases. Hidden Impurities and Opportunities'*, Chemistry of Materials*, 10(10), p. 2824–2836. doi: 10.1021/cm980223c.

Crivello, J. C., Denys, R. V., Dornheim, M., Felderhoff, M., Grant, D. M., Huot, J., Jensen, T. R., de Jongh, P., Latroche, M., Walker, G. S., Webb, C. J. and Yartys, V. A. ((2016)) 'Mg-based compounds for hydrogen and energy storage', *Applied Physics A: Materials Science and Processing*, 122(2), p. 1–17. doi: 10.1007/s00339-016-9601-1.

Deppe, M., Canales, N. C.-, Sereni, J. G. and Geibel, C. ((2010)) 'Evidence for a metamagnetic transition in the heavy Fermion system CeTiGe', *Journal of Physics: Conference Series*, 200(1), p. 12026. doi: 10.1088/1742-6596/200/1/012026.

Deppe, M., Caroca-Canales, N., Hartmann, S., Oeschler, N. and Geibel, C. ((2009)) 'New non-magnetically ordered heavy-fermion system CeTiGe', *Journal of Physics: Condensed Matter*. IOP Publishing, 21(20), p. 206001. doi: 10.1088/0953-8984/21/20/206001.

Deppe, M., Lausberg, S., Weickert, F., Brando, M., Skourski, Y., Caroca-Canales, N., Geibel, C. and Steglich, F. ((2012)) 'Pronounced first-order metamagnetic transition in the paramagnetic heavy-fermion system CeTiGe', *Physical Review B*, 85(6). doi: 10.1103/physrevB.85.060401.

Fruchart, D., Bacmann, M., de Rango, P., Isnard, O., Liesert, S., Miraglia, S., Obbade, S., Soubeyroux, J.-L., Tomey, E. and Wolfers, P. ((1997)) 'Hydrogen in hard magnetic materials', *Journal of Alloys and Compounds*, 253–254, p. 121–127. doi: 10.1016/S0925-8388(96)03063-0.

Fruchart, D., Isnard, O., Miraglia, S., Pontonnier, L., and Soubeyroux, J. L. ((1994)) 'R_2Fe_{17} and RM_{12} carbide and carbonitride synthesis from heavy hydrocarbon compounds', *Journal of Alloys and Compounds*, 203(C), pp. 157–163. doi: 10.1016/0925-8388(94)90728-5.

Gao, L., Xue, Y. Y., Chen, F., Xiong, Q., Meng, R. L., Ramirez, D., Chu, C. W., Eggert, J. H. and Mao, H. K. ((1994)) 'Superconductivity up to 164 K in $HgBa_2Ca_{m-1}Cu_mO_{2m+2+d}$ (m = 1, 2, and 3) under quasihydrostatic pressures', *Physical Review B*, 50(6), p.4260–4263. doi: 10.1103/PhysRevB.50.4260.

Gaudin, E., Matar, S. F., Pöttgen, R., Eul, M. and Chevalier, B. ((2011)) 'Drastic Change of the Ferromagnetic Properties of the Ternary Germanide GdTiGe through Hydrogen Insertion', *Inorganic Chemistry*. American Chemical Society (ACS), 50(21), p. 11046–11054. doi: 10.1021/ic201579r.

Godart, C., Umarji, A. M., Gupta, L. C. and Vijayaraghaven, R. ((1986)) 'Magnetism and spin fluctuation effects in heavy-fermion $CeRu_2Si_2$ induced by partial substitution of Ru and Si', *Physical Review B*, 34(11), p. 7733–7737. doi: 10.1103/PhysRevB.34.7733.

Gupta, S. and Suresh, K. G. ((2015)) 'Review on magnetic and related properties of RTX compounds', *Journal of Alloys and Compounds*, 618, p. 562–606. doi: 10.1016/j.jallcom.2014.08.079.

Huiberts, J. N., Griessen, R., Rector, J. H., Wijngaarden, R. J., Dekker, J. P., de Groot, D. G. and Koeman, N. J. ((1996)) 'Yttrium and lanthanum hydride films with switchable optical properties', *Nature*, 380(6571), p. 231–234. doi: 10.1038/380231a0.

Iannuzzi, D., Lisanti, M. and Capasso, F. ((2004)) 'Effect of hydrogen-switchable mirrors on the Casimir force.', *Proceedings of the National Academy of Sciences*, 101(12), p. 4019–4023. doi: 10.1073/pnas.0400876101.

Isnard, O., Miraglia, S., soubeyroux, J. L., Fruchart, D. and Stergiou, A. ((1990)) 'Neutron diffraction study of the structural and magnetic properties of the $R_2Fe_{17}H_x(D_x)$ ternary compounds (R Ce, Nd and Ho)', Journal of The Less-Common Metals, 162(2), pp. 273–284. doi: 10.1016/0022-5088(90)90343-I.

Isnard, O. and Pop, V. ((2011)) 'Effect of hydrogen as interstitial element on the magnetic properties of some iron rich intermetallic compounds', *Journal of Alloys and Compounds*. Elsevier B.V., 509(SUPPL. 2), p. S549–S554. doi: 10.1016/j.jallcom.2011.01.011.

Ju, J., Huynh, K., Tang, J., Li, Z., Watahiki, M., Sato, K., Terasaki, H., Ohtani, E., Takizawa, H. and Tanigaki, K. ((2010)) 'Superconducting properties of $SmFeAsO_{1-x}$ prepared under high-pressure condition', *Journal of Physics and Chemistry of Solids,* 71(4), p. 491–494. doi: 10.1016/j.jpcs.2009.12.019.

Kamarád, J., Arnold, Z. and Schneider, J. ((1987)) 'Effect of pressure on the curie and spin reorientation temperatures of polycrystalline $Nd_2Fe_{14}B$ compound', *Journal of Magnetism and Magnetic Materials*, 67(1), p. 29–32. doi: 10.1016/0304-8853(87)90715-3.

Katter, M., Wecker, J., Kuhrt, C., Schultz, L. and Grössinger, R. ((1992)) 'Magnetic properties and thermal stability of $Sm_2Fe_{17}N_x$ with intermediate nitrogen concentrations', *Journal of Magnetism and Magnetic Materials*, 117(3), p. 419–427. doi: 10.1016/0304-8853(92)90099-A.

Khazzan, S., Mliki, N., Bessais, L. and Djéga-Mariadassou, C. ((2010)) 'Rare-earth iron-based intermetallic compounds and their carbides: Structure and magnetic behaviors', *Journal of Magnetism and Magnetic Materials,* 322(2), p. 224–229. doi: 10.1016/j.jmmm.2009.08.047.

Klosek, V. ((2002)) Contribution to the study of the structural and electronic properties of equiatomic RTX (T = Ti, V, Cr, Mn, Fe; X = Si, Ge) and the quaternary $RTiGEC_x$ and RCr_2Si_2C, where R is an alcaline earth, yttrium, lanthanum or a lanthanide. Université Henri Poincaré, Nancy 1, France.

Klosek, V., Vernière, A., Ouladdiaf, B. and Malaman, B. ((2002)) 'Magnetic properties of CeFeSi-type RTiSi compounds (R = Gd-Tm, Lu, Y) from magnetic measurements and neutron diffraction', *Journal of Magnetism and Magnetic Materials,* 246(1–2), p. 233–242. doi: 10.1016/S0304-8853(02)00060-4.

Lemoine, P. ((2011)) Contribution à l ’ étude des propriétés structurales et magnétiques de composés intermétalliques isotypes de CeScSi et Th_6Mn_{23}. Université Henri Poincaré, Nancy, France.

Lemoine, P., Vernière, A., Marêché, J. F. and Malaman, B. ((2010)) ‘Magnetic properties of the ternary RMgSn (R=Pr, Nd, Sm, Gd–Tm): First series of antiferromagnetic CeScSi-type structure compounds’, *Journal of Alloys and Compounds,* 508(1), p. 9–13. doi: 10.1016/j.jallcom.2010.08.020.

Lemoine, P., Vernière, A., Venturini, G., Marêché, J. F., Capelli, S. and Malaman, B. ((2012)) ‘Magnetic properties and magnetic structures of the CeScSi-type RMgPb (R=Ce-Nd, Sm, Gd-Tm) compounds’, *Journal of Magnetism and Magnetic Materials,* 324(19), p. 2937–2952. doi: 10.1016/j.jmmm.2012.03.037.

Liu, J. P., Brabers, J. H. V. J., Winkelman, A. J. M., Menovsky, A. A., de Boer, F. R. and Buschow, K. H. J. ((1993)) ‘Synthesis and magnetic properties of $R_2Co_{17}N_x$ type interstitial compounds’, *Journal of Alloys and Compounds*, 200(1–2), p. L3–L6. doi: 10.1016/0925-8388(93)90461-U.

Lixandru, A., Poenaru, I., Güth, K., Gauß, R. and Gutfleisch, O. ((2017)) ‘A systematic study of HDDR processing conditions for the recycling of end-of-life Nd-Fe-B magnets’, *Journal of Alloys and Compounds*, 724. doi: 10.1016/j.jallcom.2017.06.319.

Løken, S., Solberg, J. K., Maehlen, J. P., Denys, R. V., Lototsky, M. V., Tarasov, B. P. and Yartys, V. A. ((2007)) ‘Nanostructured Mg-Mm-Ni hydrogen storage alloy: Structure-properties relationship’, *Journal of Alloys and Compounds*, 446–447, p. 114–120. doi: 10.1016/j.jallcom.2006.11.200.

Lyubina, J., Nenkov, K., Schultz, L. and Gutfleisch, O. ((2008)) ‘Multiple metamagnetic transitions in the magnetic refrigerant $La(Fe,Si)_{13}H_x$.’, *Physical Review Letters*, 101(17), p. 177203. doi: 10.1103/PhysRevLett.101.177203.

Man, S. de and Iannuzzi, D. ((2006)) ‘On the use of hydrogen switchable mirrors in Casimir force experiments’, New Journal of Physics, 8(10), p. 235–235. doi: 10.1088/1367-2630/8/10/235.

Manfrinetti, P., Morozkin, A. V., Isnard, O., Henry, P. and Palenzona, A. ((2008)) ‘Magnetic structure of the CeScSi-type RScGe compounds (R = Pr, Nd, Tb)’, *Journal of Alloys and Compounds,* 450(1–2), p. 86–91. doi: 10.1016/j.jallcom.2006.11.057.

Manfrinetti, P., Provino, A. and Gschneidner, Jr., K. A. ((2009)) ‘On the RMgSn rare earth compounds’, *Journal of Alloys and Compounds,* 482(1–2), p. 81–85. doi: 10.1016/j.jallcom.2009.03.178.

Mašková, S., Miliyanchuk, K. and Havela, L. ((2017)) ‘Hydrogen absorption in U3Si2 and its impact on electronic properties’, *Journal of Nuclear Materials*, 487, pp. 418–423. doi: 10.1016/j.jnucmat.2017.02.036.

Mayer, I. and Felner, I. ((1974)) ‘Nowotny phases of M_5X_3-type rare-earth silicides and germanides with boron’, *Journal of the Less Common Metals,* 37(1), p. 171–173. doi: 10.1016/0022-5088(74)90021-6.

Mizoguchi, H. and Hosono, H. ((2011)) ‘La_2Sb, a layered superconductor with metal-metal bonds.’, *Chemical communications*, 47(13), p. 3778–80. doi: 10.1039/c0cc05384h.

Mizoguchi, H., Kamiya, T. and Hosono, H. ((2012)) ‘Superconducting compounds with metallic square net’, *Solid State Communications,* 152(8), p. 666–670. doi: 10.1016/j.ssc.2011.12.016.

De Mooij, D. B. and Buschow, K. H. J. ((1988)) 'Formation and magnetic properties of the compounds $R_2Fe_{14}C$', *Journal of the Less Common Metals,* 142, p. 349–357. doi: 10.1016/0022-5088(88)90194-4.

Morozkin, A. V., Seropegin, Y. D. D., Leonov, A. V., Sviridov, I. A., Tskhadadze, I. A. and Nikitin, S. A. ((1998)) 'Crystallographic data of new ternary CeFeSi-type RTiGe (R=Y, Gd-Tm) compounds', *Journal of Alloys and Compounds*, 267(1–2), p. L14–L15. doi: 10.1016/S0925-8388(97)00473-8.

Morozkin, A. V. and Sviridov, I. A. ((2001)) 'New ternary CeScSi-type RZrSb compounds (R = Y, Gd-Tm, Lu)', *Journal of Alloys and Compounds*, 320(1), p. 2–3. doi: 10.1016/S0925-8388(01)00943-4.

Morozkin, A. V., Viting, L. . M., Sviridov, I. . A. and Tskhadadze, I. . A. ((2000)) 'CeScSi- and CeFeSi-type structures in compounds derived from GdTiGe', *Journal of Alloys and Compounds*, 297(1–2), p. 168–175. doi: 10.1016/S0925-8388(99)00583-6.

Nagengast, D. G., van Gogh, A. T. M., Kooij, E. S., Dam, B. and Griessen, R. ((1999)) 'Contrast enhancement of rare-earth switchable mirrors through microscopic shutter effect', *Applied Physics Letters*, 75(14), p. 2050–2052. doi: 10.1063/1.124912.

Nikitin, S. A., Tskhadadze, I. A., Morozkin, A. V. and Seropegin, Y. D. D. ((1999)) 'The influence of Ti on the itinerant magnetism of RTX compounds', *Journal of Magnetism and Magnetic Materials*, 196–197, p. 632–633. doi: 10.1016/S0304-8853(98)00880-4.

Oleaga, A., Liubachko, V., Manfrinetti, P., Provino, A., Vysochanskii, Y. and Salazar, A. ((2017)) 'Critical behavior study of NdScSi, NdScGe intermetallic compounds', *Journal of Alloys and Compounds*. Elsevier B.V, 723, p. 559–566. doi: 10.1016/j.jallcom.2017.06.289.

Paul-Boncour, V. ((2004)) 'Comparison of the influence of hydrogen on the magnetic properties of RMn_2 and RFe_2 Laves phase compounds', *Journal of Alloys and Compounds*, 367(1–2), p. 185–190. doi: 10.1016/j.jallcom.2003.08.035.

Paul-Boncour, V., Filipek, S. M., Percheron-Guégan, A., Marchuk, I. and Pielaszek, J. ((2001)) 'Structural and magnetic properties of (RFe_2H_5) hydrides {(R=Y, Er)}', *Journal of Alloys and Compounds*., 317–318, p. 83–87.

Paul-Boncour, V. and Percheron-Guégan, A. ((1999)) 'The influence of hydrogen on the magnetic properties and electronic structures of intermetallic compounds: YFe_2–D_2 system as an example', *Journal of Alloys and Compounds*, 293–295, p. 237–242. doi: 10.1016/S0925-8388(99)00323-0.

Phejar, M., Paul-Boncour, V. and Bessais, L. ((2016)) 'Investigation on structural and magnetocaloric properties of $LaFe_{13-x}Si_x(H,C)_y$ compounds', *Journal of Solid State Chemistry,* 233, p. 95–102. doi: 10.1016/j.jssc.2015.10.016.

Provino, A., Gschneidner, Jr., K. A. and Manfrinetti, P. ((2010)) 'Structure and thermal stability of the RMgPb rare earth compounds, and the anomalous melting behaviour of SmMgPb', *Journal of Alloys and Compounds*, 497(1–2), p. 131–138. doi: 10.1016/j.jallcom.2010.03.083.

Rebelsky, L., Reilly, K., Horn, S., Borges, H., Thompson, J. D., Willis, J. O., Aikin, R., Caspari, R. and Bredl, C. D. ((1988)) 'Heavy fermion behavior in CePtSi and CeRuSi', *Journal of Applied Physics,* 63(8), p. 3405–3407. doi: 10.1063/1.340775.

Ren, Z.-A. and Zhao, Z.-X. ((2009)) 'Research and prospects of iron-based superconductors', *Advanced Materials*, 21(45), p. 4584–4592. doi: 10.1002/adma.200901049.

Ritter, C., Provino, A., Manfrinetti, P. and Gschneidner, Jr., K. A. ((2011)) 'The magnetic structures of RMgSn compounds (R=Ce, Pr, Nd, Tb)', *Journal of Alloys and Compounds*, 509(41), p. 9724–9732. doi: 10.1016/j.jallcom.2011.07.100.

Ritter, C., Provino, A., Manfrinetti, P. and Pathak, A. K. ((2016)) 'Tetragonal to triclinic structural transition in the prototypical CeScSi induced by a two-step magnetic ordering: a temperature-dependent neutron diffraction study of CeScSi, CeScGe and LaScSi', *Journal of Physics: Condensed Matter*. IOP Publishing, 29(4), p. 45802. doi: 10.1088/1361-648X/29/4/045802.

Rodriguez Fernandez, J., Rojas, D. P., Sal, J. C. G., Tencé, S. and Chevalier, B. ((2010)) 'Pressure effects on the antiferromagnetic order of the hydride CeRuSiH', *Journal of Physics: Conference Series*, 200(1), p. 12167. doi: 10.1088/1742-6596/200/1/012167.

Roger, J., Ben Yahia, M., Babizhetskyy, V., Bauer, J., Cordier, S., Guérin, R., Hiebl, K., Rocquefelte, X., Saillard, J. Y. and Halet, J. F. ((2006)) 'Mn5Si3-type host-interstitial boron rare-earth metal silicide compounds RE_5Si_3: Crystal structures, physical properties and theoretical considerations', *Journal of Solid State Chemistry*, 179(8), p. 2310–2328. doi: 10.1016/j.jssc.2006.04.023.

Rotter, M., Tegel, M. and Johrendt, D. ((2008)) 'Superconductivity at 38 K in the Iron Arsenide $(Ba_{1-x}K_x)Fe_2As_2$', *Physical Review Letters*, 101(10), p. 107006. doi: 10.1103/PhysRevLett.101.107006.

Rundqvist, S., Tellgren, R. and Andersson, Y. ((1984)) 'Hydrogen and Deuterieum in transition metal-p element compounds: crystal chemical aspects of interstitial solubility and hydride phase formation', *Journal of the Less Common Metals*, 101, pp. 145–168. doi: 10.1016/0022-5088(84)90092-4.

Sakintuna, B., Lamaridarkrim, F., Hirscher, M., Lamari-Darkrim, F. and Hirscher, M. ((2007)) 'Metal hydride materials for solid hydrogen storage: A review', *International Journal of Hydrogen Energy*, 32(9), p. 1121–1140. doi: 10.1016/j.ijhydene.2006.11.022.

Senkov, O. N. and Froes, F. H. ((1999)) 'Processing of Titanium Alloys', *International Journal of Hydrogen Energy*, 24, p. 565–576.

Sereni, J. G., Berisso, M. G.-, Canales, N. C.-, Deppe, M. and Geibel, C. ((2010)) 'Tuning ground state degeneracy and quantum criticality in $Ce_{1-x}La_xTiGe$', *Physica Status Solidi (B) Basic Research*, 247(3), p. 707–709. doi: 10.1002/pssb.200983029.

Shcherbakova, Y. V., Ivanova, G. V., Gaviko, V. S. and Gabay, A. M. ((2003)) 'Crystal structure of novel ferromagnetic $LaFe_{13-x}Ga_xC$ compounds', *Journal of Magnetism and Magnetic Materials*, 267, p. 26–34. doi: 10.1016/S0304-8853(03)00300-7.

Shoemaker, D. P. and Shoemaker, C. B. ((1979)) 'Concerning atomic sites and capacities for hydrogen absorption in the AB_2 Friauf-Laves phases', *Journal of the Less Common Metals*, 68(1), p. 43–58. doi: 10.1016/0022-5088(79)90271-6.

Singh, S. K., Dhar, S. K., Manfrinetti, P., Palenzona, A. and Mazzone, D. ((2004)) 'High magnetic transition temperatures in RScT (R = Pr, Nd and Sm; T = Si and Ge) compounds: Multiple spin reorientations in PrScGe', *Journal of Magnetism and Magnetic Materials,* 269(1), p. 113–121. doi: 10.1016/S0304-8853(03)00583-3.

Singh, S. K., Dhar, S. K., Mitra, C., Paulose, P. L., Manfrinetti, P. and Palenzona, A. ((2001)) 'The Nature of magnetism in CeScSi and CeScGe', *Journal of Physics: Condensed Matter*. IOP Publishing, 13(16), p. 3753–3766. doi: 10.1088/0953-8984/13/16/306.

Skolozdra, R. V., Tomey, E., Gignoux, D., Fruchart, D. and Soubeyroux, J. L. ((1995)) 'On the new interstitial $RFe_{10.5}Mo_{1.5}C_x$ series (R=rare earth metal): synthesis and magnetic properties', *Journal of Magnetism and Magnetic Materials*, 139(1–2), p. 65–76. doi: 10.1016/0304-8853(95)90029-2.

Skomski, R., Murray, C., Brennan, S. and Coey, J. M. D. ((1993)) 'Interstitial modification of rare-earth intermetallics', *Journal of Applied Physics*, 73(10), p. 6940–6942. doi: 10.1063/1.352441.

Slooten, E., Naka, T., Gasparini, A., Huang, Y. K. and De Visser, A. ((2009)) 'Enhancement of superconductivity near the ferromagnetic quantum critical point in UCoGe', *Physical Review Letters*, 103(9), p. 6–9. doi: 10.1103/PhysRevLett.103.097003.

Stassen, W. N., Sato, M. and Calvert, L. D. ((1970)) 'The crystal structure of La_2Sb', *Acta Crystallographica Section B Structural Crystallography and Crystal Chemistry*, 26(10), p. 1534–1540. doi: 10.1107/S0567740870004442.

Takahashi, H., Igawa, K., Arii, K., Kamihara, Y., Hirano, M. and Hosono, H. ((2008)) 'Superconductivity at 43 K in an iron-based layered compound $LaO_{1-x}F_xFeAs$', *Nature*, 453(7193), p. 376–378. doi: 10.1038/*Nature*06972.

Taylor, A. E., Ewings, R. A., Perring, T. G., Parker, D. R., Ollivier, J., Clarke, S. J. and Boothroyd, A. T. ((2013)) 'Absence of strong magnetic fluctuations in the iron phosphide superconductors LaFePO and Sr_2ScO_3FeP', *Journal of Physics: Condensed Matter*, 25(42) p.425701. doi: 10.1088/0953-8984/25/42/425701.

Tencé, S., André, G., Gaudin, E., Bonville, P., Al Alam, A. F., Matar, S. F., Hermes, W., Pöttgen, R. and Chevalier, B. ((2009)) 'Huge influence of hydrogenation on the magnetic properties and structures of the ternary silicide NdMnSi', *Journal of Applied Physics*, 106(3), p. 33910. doi: 10.1063/1.3190488.

Tencé, S., André, G., Gaudin, E. and Chevalier, B. ((2008)) 'Modulated magnetic structures of the antiferromagnetic hydride CeRuSiH', *Journal of Physics: Condensed Matter*, 20(25), p. 255239. doi: 10.1088/0953-8984/20/25/255239.

Tencé, S., Matar, S. F., André, G., Gaudin, E. and Chevalier, B. ((2010)) 'Hydrogenation Inducing Ferromagnetism in the Ternary Antiferromagnet NdCoSi', *Inorganic Chemistry*, 49(11), p. 4836–4842. doi: 10.1021/ic902079u.

Tskhadadze, I. A., Chernyshev, V. V., Streletskii, A. N., Portnoy, V. K., Leonov, A. V., Sviridov, I. A., Telegina, I. V., Verbetskii, V. N., Seropegin, Y. D. D. and Morozkin, A. V. ((1999)) 'GdTiGe (CeScSi-TYPE STRUCTURE) AND GdTiGe (CeFeSi-TYPE STRUCTURE) AS THE COHERENT PHASES WITH DIFFERENT MAGNETIC AND HYDROGENIZATION PROPERTIES', *Materials Research Bulletin*, 34(99), p. 1773–1787.

Vernière, A., Klosek, V., Welter, R., Venturini, G., Isnard, O. and Malaman, B. ((2001)) 'Neutron diffraction study of the CeFeSi-type RTiGe compounds (R = Pr, Nd, Tb-Er)', *Journal of Magnetism and Magnetic Materials*, 234(2), p. 261–273. doi: 10.1016/S0304-8853(01)00352-3.

Wang, G. X., Sun, L., Bradhurst, D. H., Zhong, S., Dou, S. X. and Liu, H. K. ((2000)) 'Nanocrystalline NiSi alloy as an anode material for lithium-ion batteries', *Journal of Alloys and Compounds*, 306(1–2), p. 249–252. doi: 10.1016/S0925-8388(00)00775-1.

Wang, Y., Calvert, L. D., Gabe, E. J. and Taylor, J. B. ((1977)) 'Europium arsenic oxide Eu4As2O: a filled La2Sb structure and its relation to the K2NiF4 and GeTeU types', *Acta Crystallographica Section B Structural Crystallography and Crystal Chemistry*, 33(10), p. 3122–3125. doi:

10.1107/S0567740877010383.

Wang, Y., Calvert, L. D. and Taylor, J. B. ((1980)) ‘Is there an oxygen atom in La2Sb?’, *Acta Crystallographica Section B Structural Crystallography and Crystal Chemistry*, 36(1), p. 220–221. doi: 10.1107/S0567740880002944.

Welter, R., Venturini, G. and Malaman, B. ((1992)) ‘Magnetic properties of RFeSi (R = La-Sm, Gd-Dy) from susceptibility measurements and neutron diffraction studies’, *Journal of Alloys and Compounds,* 189(1), p. 49–58. doi: 10.1016/0925-8388(92)90045-B.

Welter, R., Venturini, G. and Malaman, B. ((1994)a) ‘High rare earth sublattice ordering temperatures in RMnSi compounds (R LaSm, Gd) studied by susceptibility measurements and neutron diffraction’, *Journal of Alloys and Compounds*, 206(1), p. 55–71. doi: 10.1016/0925-8388(94)90011-6.

Welter, R., Venturini, G., Ressouche, E. and Malaman, B. ((1994)b) ‘Magnetic properties of RCoSi (R = La-Sm, Gd, Tb) compounds from susceptibility measurements and neutron diffraction studies’, *Journal of Alloys and Compounds*, 210(1–2), p. 279–286. doi: 16/0925-8388(94)90150-3.

Welter, R., Vernière, A., Venturini, G. and Malaman, B. ((1999)) ‘High rare earth sublattice ordering temperatures in new CeFeSi-type RTiGe (R=La–Nd, Sm) compounds’, *Journal of Alloys and Compound*, 283(1–2), p. 54–58. doi: 10.1016/S0925-8388(98)00904-9.

Yartys, V. A., Harris, I. R. and Panasyuk, V. V ((1997)) ‘Novel metal-hydride materials and technologies: Recent advances and further prospects’, *Materials Science*, 33(4), pp. 436–449. doi: 10.1007/BF02537542.

Yi, W., Sun, L., Ren, Z., Lu, W., Dong, X., Zhang, H., Dai, X., Fang, Z., Li, Z., Che, G., Yang, J., Shen, X., Zhou, F. and Zhao, Z. ((2008)) ‘Pressure effect on superconductivity of iron-based arsenic-oxide $ReFeAsO_{0.85}$ (Re=Sm and Nd)’, *EPL (Europhysics Letters)*, 83(5), p. 57002. doi: 10.1209/0295-5075/83/57002.

Zhang, H., Hu, F., Sun, J. and Shen, B. G. ((2013)) ‘Effects of interstitial H and/or C atoms on the magnetic and magnetocaloric properties of $La(Fe,Si)_{13}$-based compounds’, *Science China Physics, Mechanics and Astronomy*, 56(12), p. 2302–2311. doi: 10.1007/s11433-013-5357-1.

Zhang, J. and Xia, Y. ((2006)) ‘Co-Sn Alloys as Negative Electrode Materials for Rechargeable Lithium Batteries’, *Journal of The Electrochemical Society*, 153(8), p. A1466. doi: 10.1149/1.2204871.

Zhao, J., Ding, H., Zhong, Y. and Lee, C. S. ((2010)) ‘Effect of thermo hydrogen treatment on lattice defects and microstructure refinement of Ti6Al4V alloy’, *International Journal of Hydrogen Energy*, 35(12), p. 6448–6454. doi: 10.1016/j.ijhydene.2010.03.109.

Zhao, J., Huang, Q., de la Cruz, C., Li, S., Lynn, J. W., Chen, Y., Green, M. A., Chen, G. F., Li, G., Li, Z., Luo, J. L., Wang, N. L. and Dai, P. ((2008)) ‘Structural and magnetic phase diagram of $CeFeAsO_{1-x}F_x$ and its relation to high-temperature superconductivity’, *Nature Materials*, 7(12), p. 953–959. doi: 10.1038/nmat2315.

Chapter 2: Experimental methods

Over the course of this work a large number of synthetic and analytic techniques were used. Here they are presented along with their operating. Specific details of the individual syntheses are provided in the appropriate chapters where required.

2.1 Synthesis

2.1.1. Arc Melting

Samples were prepared for arc melting by cutting and polishing stoichiometric amounts of the pure elements (Si and rare earth metals, 99.99%, supplied by STREM chemicals and Sc 99.999% metal basis purity supplied by Neyco). The rare earth elements are cleaned by polishing blocks of the pure element, arc melting to remove bulk oxide, and a final polish of the required mass to remove residual surface oxide immediately prior to synthesis. The cleaned elements were placed into one of the crucibles in the water cooled copper hearth of an Edmund Bühler GmbG MAM1 Compact Arc Melter with a 230 V connection (Figure 2. 1 and Figure 2. 2).

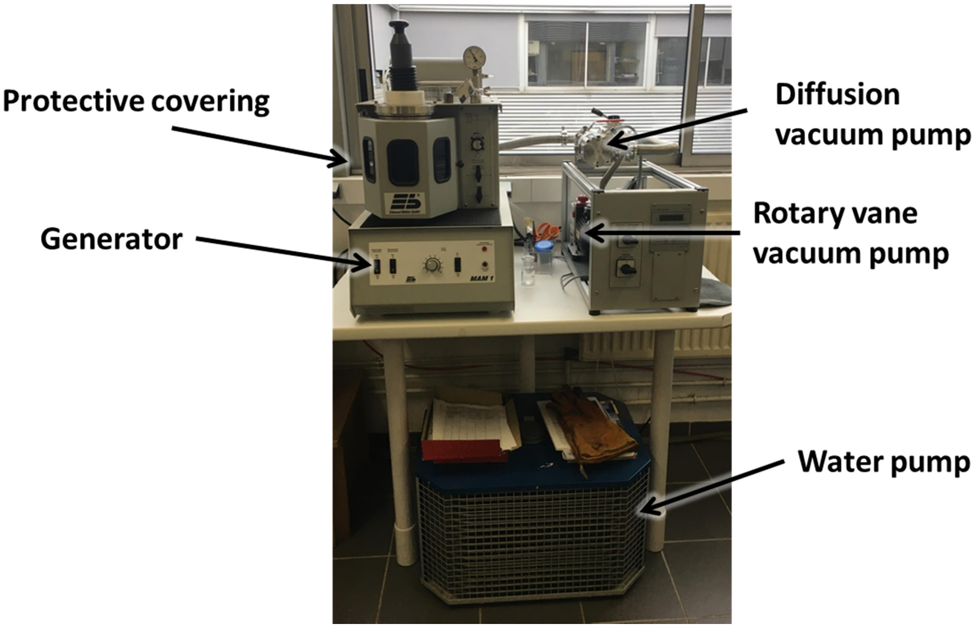

Figure 2. 1. Electric arc furnace with secondary vacuum pump used for primary synthesis of intermetallic ingots

A small bead of titanium "getter" was placed in another crucible to act as a trap for residual oxygen. The furnace was evacuated to a primary vacuum of approximately $4x10^{-2}$ mbar and rinsed with argon three times before activating the secondary diffusion vacuum pump to achieve a vacuum of around $3x10^{-4}$ mbar. The furnace was then filled with argon to 600 mbars. The tungsten electrode creates an electric arc that is capable of melting the metallic elements. Care must be taken to avoid direct contact between the arc and the Si lumps as this can cause them to shatter and expels pieces from the crucible, requiring the synthesis to be restarted. First, the Ti "getter" (shown in Figure 2. 2) was melted to capture any residual oxygen before the metals were melted together using a tungsten electrode. Samples were melted 3-5 times depending on their mass, turning in between each melting to improve homogeneity. Weight losses were generally below 1% by mass.

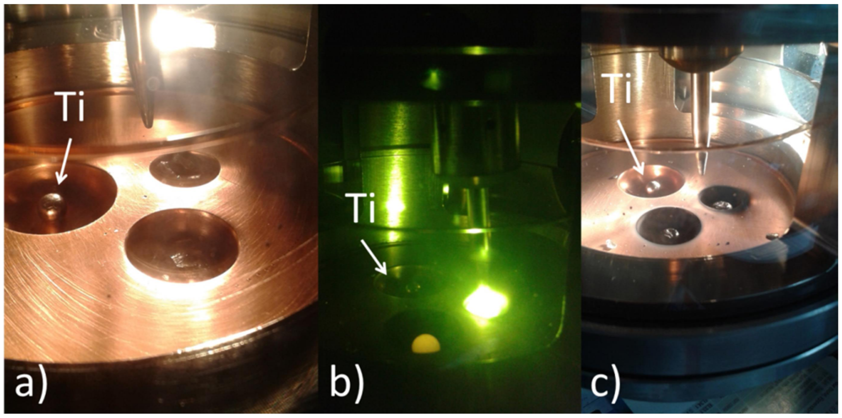

Figure 2. 2.The water cooled copper hearth of the arc furnace containing titanium "getter" and two samples before (a), during (b), and after synthesis (c).

2.1.2. Induction Melting

Insertion of carbon into the pristine intermetallics was performed using an induction furnace (Figure 2. 3.). Induction heating involves the application of a rapidly oscillating magnetic field which in turn creates eddy currents (so-called Foucault currents) of electrons in the metals. These eddy currents produce heating in the material through its own resistance as they move through it. Thus magnetic induction follows Faraday's law (Sommerfeld, (1964), p. 372):

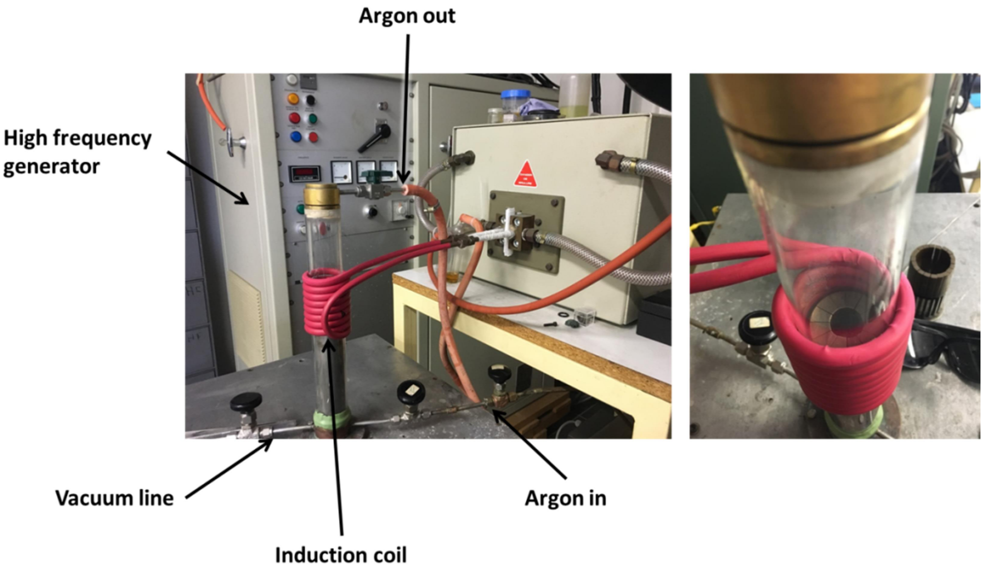

Figure 2. 3. Left) Labelled image of the induction furnace used. Right) zoom of the water cooled copper crucible

$$e = -N_C \frac{d\Phi}{dt}$$

Where the induced electromotive force (e) is equal to the negative of the time rate of change of the magnetic flux (Φ) times the number of turns in the coil that produces the field (N_C). The sample is therefore heated and, eventually, melted through the Joule effect. Once melted, the exciting field can counterbalance the gravitational force and thus the sample levitates. The eddy currents in the liquid metal cause mixing of the sample and help ensure good homogeneity. Because the frequency of the magnetic field oscillations, and therefore the temperature, can be well controlled, this method was used to control the amalgamation of the C into the metal ingots for the carbides. The intermetallic button from the arc furnace was placed in the water cooled crucible of the furnace. A small piece of graphite with the required mass was cut from a cold pressed graphite pellet made from graphite powder supplied by Touzart & Matignon. This was placed on top of the intermetallic button in the crucible. The furnace was evacuated and rinsed with argon gas several times to purify the atmosphere before being left under argon flow for 20 minutes to ensure a clean atmosphere. The argon was purified by passing it through a furnace over magnesium beads at 400 °C. The sample was heated very slowly to just above the melting point. Once the carbon was fully amalgamated the sample was held liquid for 1 minute to ensure good mixing before being slowly cooled.

2.1.3. Thermal Treatment

To improve sample homogeneity and crystallinity, thermal treatment was carried out by sealing the samples inside of evacuated quartz ampoules (Figure 2. 4.). These were then placed in resistance furnaces at a range of temperatures between 973 K and 1373 K to determine the best annealing temperature. Specific annealing temperatures and times for individual samples are provided in the relevant chapters. To prevent reaction with the walls of the quartz tube, samples that were annealed above 900 °C were first wrapped in Ta foil.

Figure 2. 4. Sample sealed in an evacuated quartz ampoule for thermal treatment.

2.1.4. Hydrogenation

Hydrogen absorption was carried out in hermetically sealed stainless steel containers which use either graphite or brass joints respectively. Container choice was made as a function of the temperatures used. For temperatures of up to 350 °C, graphite joints are suitable while temperatures between 350 °C and 450 °C used brass ones. Before hydrogenation the samples are lightly crushed. For hydrogenations performed below 350 °C, the crushed samples were loaded into open quartz tubes where possible to prevent cross-contamination. The quartz tube is then placed inside the bomb before sealing it with the joint. The bomb is then evacuated and purged several times with argon. The sample is heated to the hydrogenation temperature under active vacuum and held at this temperature for 2 hours to activate the surface of the sample. Hydrogenation is performed using hydrogen pressures of between 5 and 40 bars depending on the sample.

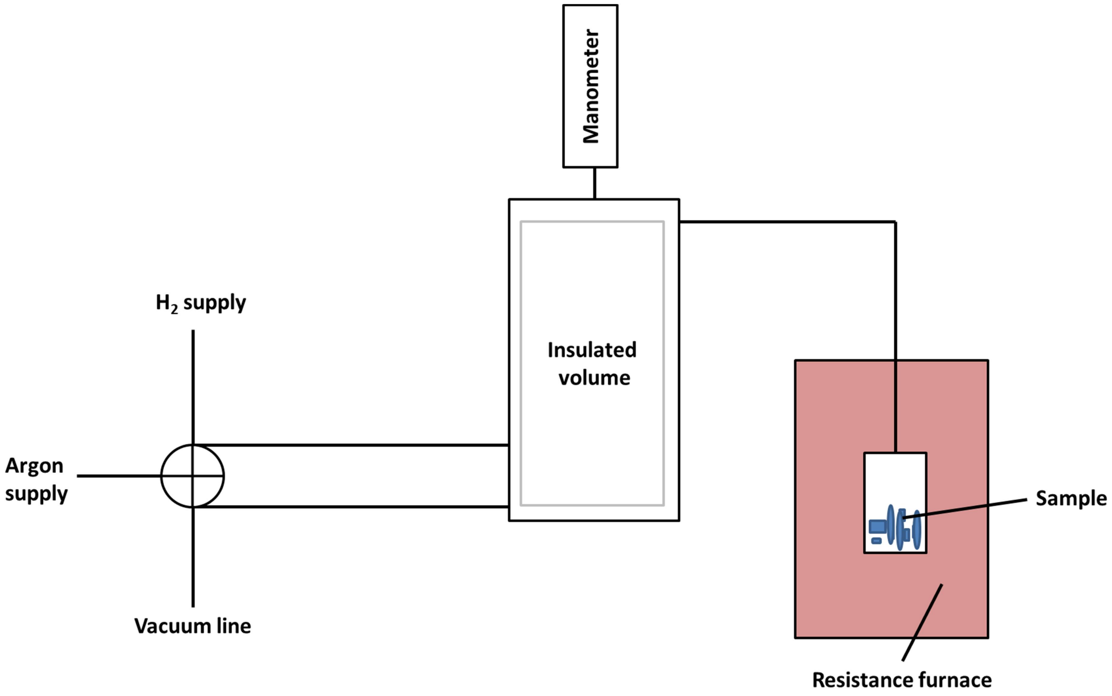

Figure 2. 5. Simplified schematic representation of the apparatus used for the collection of hydrogen absorption curves

For the determination of the total amount of absorbed hydrogen, the above procedure is carried out in a similar apparatus (shown in Figure 2. 5.) with a known volume and equipped with a manometer. By measuring the change in pressure the amount of absorbed hydrogen to be calculated with reasonable accuracy through the use of the ideal gas law:

$$PV=nRT$$

Where P is the pressure, V is the volume, n is the number of moles of H_2 gas, R is the gas constant and T the temperature in Kelvin. While this law is only strictly true for ideal gases, and most gases differ noticeably from ideality, it can provide a reasonable estimate of the amount of absorbed hydrogen. These experiments are performed using stainless steel containers hermetically sealed with brass joints as above. The sample is crushed and placed directly in the container before following the procedure detailed above. After activation, the sample is exposed to H_2 gas and pressure changes inside the apparatus were recorded and used to calculate the amount of hydrogen absorbed.

2.2. Sample Characterisation

2.2.1. X-ray Diffraction

2.2.1.1. Diffraction Theory

X-ray diffraction (XRD) forms the backbone of research in solid state chemistry. The technique relies on the coherent scattering of X-rays by the electron cloud of atoms (Thomson coherent scattering). In a crystalline solid with well-defined long range order, constructive interference between scattered photons produces an ordered pattern of reflections. Diffraction from a three dimensional periodic structure (Bragg diffraction) such as a crystal is governed by Bragg's law. This law was first proposed by William Lawrence Bragg and his father William Henry Bragg in 1913 (Bragg and Bragg, (1913)) for which they won the Nobel prize in physics in 1915 and is expressed mathematically as:

$$n\lambda = 2d_{hkl}\sin\theta$$

Where *n* is a natural number (generally = 1), λ is the wavelength of the incident radiation, *d* is the interplanar spacing between the family of planes given by the miller indices *h, k,* and *l*, and θ is the angle at which the reflection can be seen. The position of the coherent scattering peaks is directly related to the magnitude of *d*, the inter-planar spacing in the crystal lattice. This in turn is directly related to the unit cell parameters. The relationship varies based on the crystal system (cubic, tetragonal etc.) and for a tetragonal lattice (such as the materials studied in this work) it is:

$$\frac{1}{d^2} = \frac{h^2 + k^2}{a^2} + \frac{l^2}{c^2}$$

With *a* and *c* the unit cell parameters. While the positions of the diffraction peaks are determined by the unit cell parameters, their intensities (I_{hkl}) rely on the structure factor, F_{hkl}:

$$I_{hkl} = sJ_{hk}\,L_{hkl}A|F_{hkl}|^2$$

Where s is a scale factor, J_{hkl} is the multiplicity of the atomic sites, L_{hkl} is the Lorentz factor and polarisation and, *A* is the absorption coefficient. The structure factor (F_{hkl}) depends on the location of the individual atoms within the unit cell by the relationship:

$$F_{hkl} = \sum\nolimits_j f_j \exp(2\pi i(hx_j + ky_j + lz_j)\exp\left(-\frac{B_j sin\theta}{\lambda^2}\right)$$

Here f_j is the scattering factor of atom *j* at position (x_j, y_j, z_j) and B is the isotropic atomic displacement parameter. For X-rays, the scattering factor is proportional to the atomic number of the element. Furthermore, crystal size, shape and strain can influence the shape of the peaks in the diffraction pattern. Thus reflections can be used to determine the unit cell parameters of the compound and, if the data are good enough: the atomic positions, strain and crystallite size information, substitution, defects and thermal oscillations of the different atoms (Pecharsky and Zavalij, (2009)).

X-ray diffraction techniques are most powerful when performed on a high quality single crystal. The crystal is suspended in a monochromatic X-ray beam and images are taken of the reflections produced. The crystal is then rotated through different orientations to examine all the crystallographic planes for a full pattern. Single crystal diffraction techniques remain the gold standard for the determination of an unknown structure as they allow for unambiguous determination of the terms above. Using single crystal diffraction methods even very complicated structures can be determined. Unfortunately, it is not always possible to obtain a crystal of sufficient size and/or quality for single crystal experiments. Furthermore, multiphase samples cannot be readily analysed using this technique. Thus powder diffraction experiments are often performed instead. These can be very useful for the identification of phases and the analysis of already known structures. A powder diffraction experiment relies on having many small crystallites with random orientations to provide the complete pattern, rather than rotating the sample in the X-ray beam. Unfortunately, the loss of information from the collapse of 3D space (for a single crystal) to 1D space (for powder studies) causes a loss of some of the information that is available such as accurate intensity data and full extinction conditions for space group determination. For this reason *ab-initio* structure determination is difficult through powder diffraction alone. Also, because X-rays are scattered by the electron cloud, XRD is naturally more sensitive to heavier elements than for lighter ones. Thus when studying a material that contains both heavy and light elements, the diffraction peaks are dominated by the presence of the heavier elements such as, in our case, the rare earth elements. For this reason XRD is often combined with other diffraction techniques such as neutron diffraction (presented in section 2.2.2.) to overcome some of these problems.

2.2.1.2. X-ray Powder Diffraction

Samples for X-ray powder diffraction were first ground in an agate mortar and pestle. A fine layer of powder was then placed on an aluminium sample holder. Routine powder X-ray powder diffraction (PXRD) was performed with the use of a PANalytical X’pert PRO MPD diffractometer in Bragg-Brentano θ-θ geometry, equipped with a secondary graphite monochromator between the sample and the X’Celerator multi-strip detector (Figure 2. 6.a) and b)). Each measurement was made within an angular range of 2θ = 8 - 80 ° with a step size of 0.017 °, lasted for 34 minutes and used Cu-Kα_1 and Kα_2 radiation (λ = 1.5406 Å and 1.5444 Å).

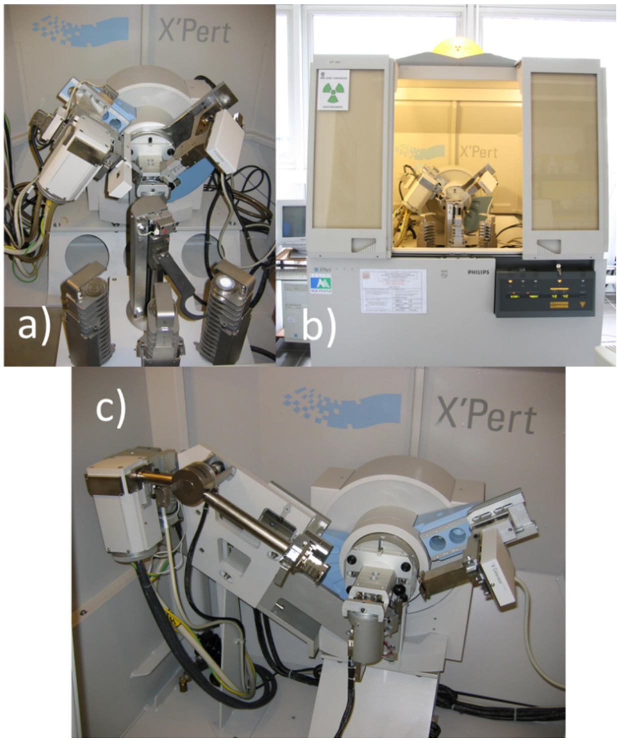

Figure 2. 6. a) and b) show the diffractometer used for routine powder diffraction data in the Bragg-Brentano θ-2θ geometry. c) shows the instrument used for high resolution data collection in the Bragg-Brentano θ-θ geometry.

High resolution X-ray powder data for Rietveld analysis were collected at room temperature using a PANalytical X'pert PRO MPD diffractometer in Bragg-Brentano θ-2θ geometry with a Ge (111) monochromator between the sample and the X-ray source to ensure Cu-Kα_1 radiation (1.5406 Å) (Figure 2. 6.c)). Measurements were performed between 2θ = 5 - 120 ° with a step size of 0.008 °. Each acquisition lasted for between 16 and 48 hours depending on sample quality.

Initial analysis and phase identification was carried out using the DIFFRAC.SUITE EVA software from Bruker. Full pattern matching and Rietveld refinements of the resulting patterns were then carried out using the Fullprof program package (Rodriguez-Carvajal, (1993) using the Thompson-Cox-Hastings pseudo-voigt with axial divergence asymmetry peak profile described in Finger *et al.*, (1994).

2.2.1.3. Single Crystal Diffraction

Single crystal XRD was performed on irregular crystals of NdScSi, NdScGe and $NdScSiC_{0.5}$ isolated from crushed annealed samples and glued to thin quartz or glass fibres. NdScSi and NdScGe crystals were initially examined by Laue photographs on a Buerger camera using white Mo radiation and the Fuji-film image plate technique. This was done to verify the quality of the crystals and the intensity data collection. Further measurements were then collected on NdScSi at ambient temperature using a four-circle diffractometer (CAD4) with Mo-K*α* radiation. A graphite monochromator was used to produce the monochromatic beam and a scintillation counter with pulse height discrimination was also used. After scans were taken in the $\omega/2\theta$ mode, an empirical absorption correction was applied on the basis of the Ψ scan data with spherical absorption corrections. Intensity data of the NdScGe crystal were collected at room temperature by use of a Stoe IPDS-II imaging plate diffractometer in oscillation mode (graphite monochromatised Mo-Kα radiation). A numerical absorption correction was applied to the dataset. All relevant crystallographic data and details of the data collections and evaluations for NdScSi and NdScGe can be found in Tencé *et al.*, (2016). The studies of these crystals were made by our colleagues in Munster University. Single crystals of $NdScSiC_{0.5}$ were measured at ICMCB with a Bruker Kappa Apex II (Mo-radiation) at room temperature. Numerical Absorption Correction (From Face Indices) was used. NdScSi and NdScGe structures were then refined with SHELXL-97 (Tencé *et al.*, (2016)) (full matrix least squares on Fo^2) and $NdScSiC_{0,5}$ structure with Jana2006 software (Petříček *et al.*, (2014)). For the three structural refinements anisotropic displacement parameters for all sites were used. The occupancy parameters have been refined in a separate series of least squares cycles. All sites were fully occupied within two standard deviations. Final difference-Fourier synthesis revealed no significant residual peaks.

2.2.2. Neutron diffraction

Neutron diffraction is a useful technique for structure determination which relies on the diffraction of neutrons by the nuclei of a crystal (rather than the electrons for X-ray diffraction). It offers a number of advantages and disadvantages when compared with X-ray diffraction in relation to structure determination. As neutrons are diffracted by the nucleus rather than the electrons, the mass of an atom has very little effect on an individual element's ability to scatter neutrons. Rather, neutron sensitivity for a particular element varies by isotope of that element with each isotope having its own unique scattering factor, *b* (Table 2. 1.). Because of this, neutron diffraction is often very sensitive to light elements such as hydrogen and carbon even in the presence of much heavier elements that make such elements difficult or impossible to detect using X-rays. Thus, work on light element insertion often includes neutron diffraction for the quantification and/or location of the light elements inside a crystal structure. With the exception of hydrogen and deuterium, all elements used contain their natural isotopic abundances. Therefore the observed scattering factor for these elements is an average of all isotopes, taking into account their relative abundances in nature.

Table 2. 1. The coherent and incoherent neutron scattering factors for the elements used in this work. Specific isotope data is provided for ^{1}H and ^{2}H while the other scattering factors have been normalised based on the relative abundance of their isotopes. Data from Sears, (1992).

Element or isotope	b_{coherent} (fm)	$b_{\text{incoherent}}$ (fm)
^{1}H	-3.7390	25.274
^{2}H	6.671	4.04
C	6.6460	
Si	4.1491	
Sc	12.29	-6.0
Ti	-3.438	
Ge	8.185	
Ce	4.84	
Nd	7.69	

Furthermore, neutrons possess a magnetic moment which can interact with the magnetic moment of unpaired electrons in magnetic atoms. This means that neutrons can be used to determine not only the crystal structure but also the precise magnetic structure. In practice, magnetic structure determination is carried out by first measuring the neutron diffraction pattern in the paramagnetic state. All peaks measured thusly will correspond to the nuclear structure only. Then, the sample is cooled to below the magnetic ordering temperature and further diffraction patterns are collected. The magnetic structure will produce its own set of which may or may not coincide with the peaks for the crystal structure depending on the size of the magnetic unit cell. Thus the magnetic structure can be refined along with the nuclear one, allowing for unambiguous determination of the magnitude and organisation of magnetic moments inside the compound.

Unlike X-rays, neutrons cannot be conveniently produced in large quantities in a standard lab setting. Instead, neutrons for experimental use are produced using specially designed nuclear reactors. These reactors are designed to produce as many neutrons as possible and only a small amount are retained to continue the fission reaction. The rest of the neutrons exit the reactor core where they are used for specialist experiments such as neutron diffraction. Such plants are expensive to build and maintain and so resources for neutron diffraction are much more limited than XRD. Neutron diffraction also requires far larger samples and counting times to produce sufficient intensities for detailed analysis.

Neutron diffraction measurements for the determination of the nuclear and magnetic structures were carried out on the G4.1 (λ = 2.428 Å) (Figure 2. 7), G4.4 (λ = 1.959 Å) and 3T2 (λ = 1.226 Å) beamlines at the Laboratoire Leon Brillouin (LLB), Saclay, France; the D1B (λ = 2.520 Å) (Figure 2. 8.) and D2B (λ = 1.595 Å) beamlines at the Institute Laue-Langevin (ILL), Grenoble France; and the C2 high resolution powder diffractometer at the Canadian institute for neutron scattering, Chalk River, Canada (λ = 1.328 Å). Samples with masses between 3.5 g and 5 g ($0.7 \le V \le 1.0$ cm^3) were ground and passed through a 45 µm sieve. They were then placed inside vanadium sample holders and data was collected at a range of temperatures from ambient temperature down to 1.5 K for magnetic structure investigation. Collected data was treated using the Fullprof program package. (Rodriguez-Carvajal, (1993))

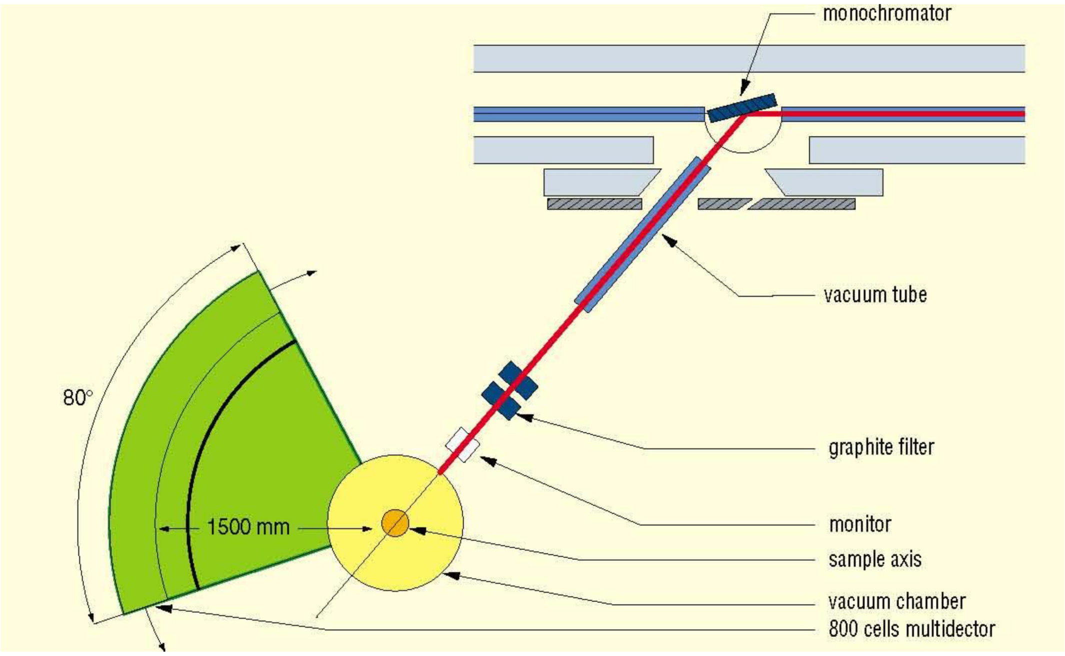

Figure 2. 7. Schematic of the G4.1 diffractrometer at the LLB, Saclay, France. Image from the instrument layout webpage: http://www-llb.cea.fr/spectros/spectro/g4-1.html

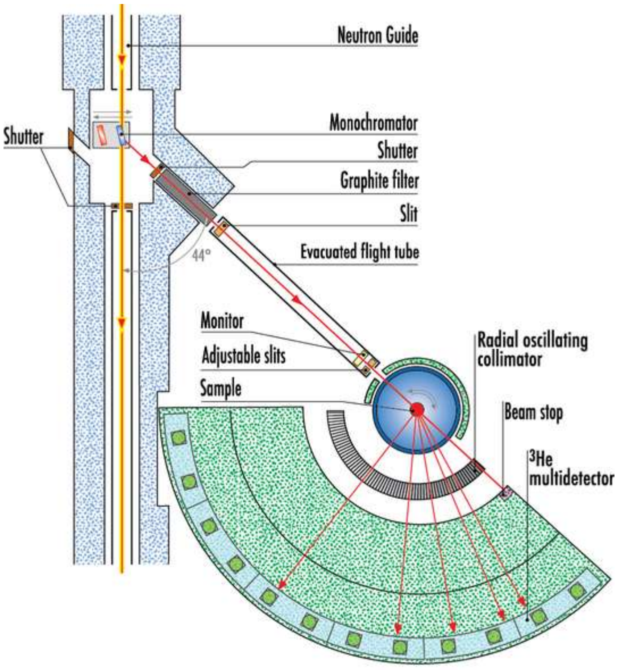

Figure 2. 8. Schematic of the D1B diffractometer at the IIL, Grenoble France. Image from IlL website: https://www.ill.eu/instruments-support/instruments-groups/instruments/d1b/description/instrument-layout/

2.2.3. Magnetisation measurements

Magnetization measurements were performed using a Superconducting QUantum Interference Device (SQUID) magnetometer (Quantum Design MPMS-XL) in the temperature range 1.8 - 300 K and in fields up to 7 T. This instrument is based on the displacement of the sample inside the measurement coils. SQUID magnetometers may function in DC (direct current), AC (alternating current) or RSO (reciprocating sample option) modes. During this work, the DC and sometimes the RSO modes were used. A DC SQUID consists of two Josephson junctions employed in parallel so that the electrons tunnelling through the junctions exhibit quantum interference. This interference is dependent on the magnetic field within the loop and allows for highly sensitive magnetic measurements even in samples with very low magnetic moments.

The DC scan mode involves moving the sample linearly over several centimetres through the detection coils, inducing a SQUID voltage as a function of sample position. The magnetic moment of the sample is derived by fitting the curve of voltage vs. position with a single dipole response function.

The RSO scan mode oscillates the sample around the centre of the coils in a sinusoidal pattern (down, then up, then back to the centre). This scan mode is significantly faster than the DC mode which allows more averaging and better noise rejection. However, it is unsuitable to measuring samples with large magnetic moments and smaller sample masses are used during this scan mode to avoid saturation of the detectors.

Measurements were performed on powders or blocks depending on the sample. Powders were placed in a diamagnetic plastic capsule with some cotton to prevent the sample moving too much while small blocks were wrapped in folded aluminium foil. This was then fixed inside a diamagnetic plastic straw which could be attached to the sample arm of the magnetometer. Sample magnetisation was either measured in a static field with changing temperature (M(T)) or with changing field at a fixed temperature (M(H)).

For the M(T) measurements the sample was first cooled to 1.8 K in the absence of external magnetic field (zero field cooling or ZFC). The target field was applied at 1.8 K and the sample was then heated gradually in constant field to high temperatures (sample dependent but generally around 250 K) before being cooled back to 1.8 K under the external field (Field cooled or FC). Isothermal magnetisation measurements were performed by cooling the sample to the desired temperature in the absence of an external magnetic field. The sample is then held at the target temperature while the field is raised from 0 to 7 T and the response is measured.

2.2.4. Heat capacity and resistivity

Heat capacity and resistance measurements were performed with a standard relaxation method with a Quantum Design PPMS device (Figure 2. 9.). For heat capacity determination, samples of approximately 10 mg were glued to the sample holder using Apiezon N-grease and the heat capacity of the sample holder and grease was measured just before the sample was studied. Measurements were performed using a helium cryostat between 1.8 K and 300 K.

Figure 2. 9. The Quantum Design PPMS device used for heat capactity and resistance measurements.

For resistance and resistivity determination a mixture of small blocks and cold pressed pellets (3 mm diameter) were studied by attaching four wires to the sample using conductive silver paint as shown in Figure 2. 10. An external current (I_{14}) is passed through the sample using the two external wires while the voltage is simultaneously measured between the two middle electrodes (V_{23}). The resistance (R) can thus be calculated using Ohm's law

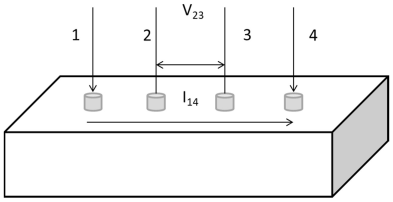

Figure 2. 10. The four point method used for resistivity measurements

$$V = IR$$

When the sample is well compacted with known dimensions (for example a rectangular block as shown in Figure 2. 10.) and the wires are equally spaced, the resistivity (ρ) can also be measured using the relation

$$\rho = \frac{RA}{l}$$

Where R is the electrical resistance of the material, l is the length of sample and A is the cross-sectional area. The measurements were performed in a cryostat allowing measurements between 1.8 K and 400 K. Preliminary measurements were performed on powder samples due to the ease of preparation. The hydride and carbide-hydride samples are too fragile for measurements to be performed on block samples. In the case of the GdScGeH samples, the reduced resistivity, normalised for 290 K (ρ/ρ_{290K}) is used.

2.2.5. Carbon content measurement

Total carbon content determination was carried out by combustion analysis using an Eltra CS800 carbon/sulphur determinator (Figure 2. 11.). The total carbon content is measured using CS-800 infrared cells to detect CO_x species and quantify them with respect to a known standard. The samples are placed in a disposable ceramic crucible and metallic accelerators are added to facilitate complete combustion. For our experiments 700 mg of high purity iron filings and 1.5 g of tungsten (provided by Eltra GmbH) were added as accelerants following the recommendation of the manufacturer. Approximately 50 mg of sample were burned in pure oxygen with the accelerants in a disposable ceramic crucible by heating in a 2.2 kW induction furnace. To remain in the accurate detection zone, the mass of sample used was varied based on nominal carbon mass (lower masses for more carbon rich samples). Pure oxygen allows the consumption of all the carbon present forms CO_x gases which pass through a dust filter to the detectors. To calibrate the instrument, the carbon content of a cast iron standard with known carbon content (3.39(2) ppm C, Eltra GmbH) was measured three times using the same accelerant proportions described above. Approximately 25 mg of the standard was used for each calibration. The accelerants were then measured without the sample or cast iron standard to provide a baseline (again, three times) before the samples were measured.

Figure 2. 11. Eltra CS800 carbon/sulphur determinator used to dose the carbon content.

2.2.6. Electron microprobe analysis

An electron microprobe analyser works on the same principles as a scanning electron microscope (SEM). A beam of electrons is focused on the sample and scanned across the surface using the raster method. An image of the surface can be reconstructed at high resolution by measuring the back scattered electrons (BSE). When used on bulk samples with a flat, polished, surface contrast can be seen between the different phases present due to their different densities. An electron microprobe analyser can quantify the elements present by measuring the X-rays emitted from the atoms in the sample.

When the electron beam interacts with the sample it causes some of the atoms to emit photons in the X-ray part of the spectrum. As each element has a unique electronic configuration the exact pattern of emitted wavelengths is unique to that element. Quantification of the elements present can thus be carried out using either wavelength dispersive X-ray spectroscopy (WDS) or energy dispersive X-ray spectroscopy (EDS). WDS uses Bragg diffraction from crystals to select specific wavelengths for measuring in sealed proportional detectors (by comparison with a standard for that element). EDS measures the entire emitted spectrum of X-rays simultaneously. WDS is more precise than EDS due to better resolution and lower background noise. However, it also requires a longer measurement time.

Both the composition and the homogeneity of the as-cast and annealed samples were checked by microprobe analysis using a Cameca SX-100 instrument. The analysis by EDX (Energy Dispersive X-ray) was performed on the basis of intensity measurements of R-Lα_1 (R = rare earth element), Sc, Co, Ni, Si, and C-Kα_1 X-ray emission lines, which were compared with internal standards of those elements within the instrument. Prior to measurement the samples were first embedded in an electrically conductive phenolic resin and then polished to provide a flat, defect free, surface using a range of SiC sandpaper disks.

2.3. Bibliography

Bragg, W. H. and Bragg, W. L. ((1913)) 'The Reflection of X-rays by Crystals', *Proceedings of the Royal Society A: Mathematical, Physical and Engineering Sciences,* 88(605), p. 428–438. doi: 10.1098/rspa.1913.0040.

Finger, L. W., Cox, D. E. and Jephcoat, A. P. ((1994)) 'A correction for powder diffraction peak asymmetry due to axial divergence', *Journal of Applied Crystallography*, 27(6), p. 892–900. doi: 10.1107/S0021889894004218.

Pecharsky, V. K. and Zavalij, P. Y. ((2009)) "Fundamentals of Powder Diffraction and Structural Characterization of Materials." Boston, MA: Springer US. doi: 10.1007/978-0-387-09579-0.

Petříček, V., Dušek, M. and Palatinus, L. ((2014)) 'Crystallographic Computing System JANA2006: General features', *Zeitschrift für Kristallographie - Crystalline Materials*, 229(5). doi: 10.1515/zkri-2014-1737.

Rodriguez-Carvajal, J. ((1993)) 'Recent Advances in Magnetic Structure Determination by neturon powder diffraction', *Physica B*, 192, p. 55–69.

Sears, V. F. ((1992)) 'Neutron scattering lengths and cross sections', *Neutron News*, 3(3), p. 26–37. doi: 10.1080/10448639208218770.

Sommerfeld, A. ((1964)) Lectures on Theoretical Physics: Electrodynamics. New York: Academic Press.

Tencé, S., Mahon, T., Gaudin, E., Chevalier, B., Bobet, J.-L. J.-L., Flacau, R., Heying, B., Rodewald, U. C. U. C. and Pöttgen, R. ((2016)) 'Hydrogenation studies on NdScSi and NdScGe', *Journal of Solid State Chemistry*, 242, p. 168–174. doi: 10.1016/j.jssc.2016.02.017.

Chapter 3: Hydrogenation of CeScSi-type compounds

The *RTX* (*R* = rare earth, *T* = transition metal and *X* = a *p* block element) phases crystallising in the CeFeSi structure type contain vacant interstitial sites that make them attractive for the study of hydrogen insertion (Chevalier *et al.*, (2009), (2010)a; Tencé *et al.*, (2009)). Hydrogen occupies the vacant rare earth tetrahedral sites of these materials for a filled composition of *RTX*$H_{1.0}$, causing an expansion of the unit cell with *a* decreasing and the *c* parameter strongly increasing (Chevalier *et al.*, (2006)b. In particular, the case of *R* = Ce has seen a lot of research interest since hydrogenation is a powerful tool to play between magnetic ordering, the kondo effect and intermediate valence state. At the same time as the volume increase, the electronic effect of the small, electronegative, hydrogen atoms (through the *R*-H bonds) also greatly influences the magnetic properties of the parent material (Chevalier and Matar, (2004)). The competing effects of hydrogen in a material can be seen by comparing the hydrogenation of CeCoSi and CeRuSi. The lattice expansion can be considered as a negative pressure which drives the change from a non-magnetic heavy fermion system in CeRuSi to an antiferromagnetic order in CeRuSiH (Chevalier *et al.*, (2009)). Meanwhile, the electronic effect of the Ce-H bonding is the predominant factor in the onset of spin fluctuation behaviour in antiferromagnetic CeCoSi with hydrogenation (Chevalier *et al.*, (2009)). For other rare earth elements, hydrogenation of *RTX* systems crystallising in the CeFeSi structure type, has also been shown to produce interesting effects on the physical properties. For example, Welter *et al.*, (1994)b show that NdMnSi is an antiferromagnetic material presenting two different antiferromagnetic orders below T_{N1} = 280 K and T_{N2} = 185 K. These correspond to the magnetic ordering of the Mn and Nd sublattices respectively with a spin reorientation of the Mn sublattice occurring also at T_{N2}. Hydrogenation of this material causes a drastic increase in T_{N1} to 564(5) K while simultaneously decreasing T_{N2} to 103(3) K (Tencé *et al.*, (2009)). There are many more examples of hydrogenation inducing interesting changes in the physical properties of CeFeSi-type *RTX* compounds. For a more detailed list see chapter 1 and the references therein.

Comparatively little research has been performed on the hydrogenation of the *RTX* materials that crystallise in the CeScSi structure type despite the presence of vacant interstitial sites (Mokra and Bodak, (1979)) such as those seen in CeFeSi-type compounds. Hydrogenation of CeScSi itself was studied in Chevalier *et al.*, (2010)c where it was shown that hydrogenation severely reduces the antiferromagnetic order of the pristine compound showing a strong decrease in T_N from 26 K to 3 K. This causes the onset of Kondo-type behaviour in the hydride. A similar destruction of the magnetic properties was observed in the hydrogenation of the high temperature form of GdTiGe by Gaudin *et al.*, (2011). The ferromagnetic transition at 376 K is replaced with paramagnetic behaviour down to 4 K. Thus far, no other work has been performed on the hydrogenation of these compounds in the literature. All current examples of the hydrogenation of CeScSi type intermetallics result in significant reduction of the magnetic ordering temperatures of the rare earth sublattices.

One family of materials that is of particular interest to study is that of the *R*TiGe compounds (*R* = rare earth). These intermetallics have been shown to crystallise in both the CeFeSi and CeScSi structure type (Morozkin *et al.*, (2000)). As described in chapter 1, there remains some uncertainty as to the driving factors behind the formation of the CeFeSi-type or CeScSi-type forms of these phases. The initial part of this work will thus focus on a detailed study of the phase transition between the CeFeSi and CeScSi forms of CeTiGe. We shall then discuss the hydrogenation of these materials and the effect on the physical properties and compare it to the non-magnetic analogue YTiGe and its hydride. The remainder of this chapter will focus on the insertion of hydrogen in the CeScSi-type *R*Sc*X* intermetallics (*R* = Nd, Gd, and *X* = Si, Ge) as they have seen far less research in the literature to date.

3.1. Synthesis

The pristine materials are synthesised by arc melting followed by heat treatment at elevated temperatures in sealed, evacuated, quartz ampoules to avoid contact with air and allow the samples to reach equilibrium composition. A detailed description of the synthesis technique by arc melting can be found in chapter 2. All CeTiGe samples were made using the relative proportions Ce:Ti:Ge of 32.5: 34.5: 33.0 to avoid the formation of the magnetic Ce_5Ge_3 secondary phase. It was also found, by Morozkin *et al.*, (2000), that a slight substoichiometry on the rare earth site can stabilise both forms of *R*TiGe. YTiGe was prepared from a stoichiometric equimolar mix for use as a non-magnetic standard. CeTiGe as cast samples were ground into a powder and cold pressed into 6 mm diameter pellets before being wrapped in tantalum foil and annealed for 2 weeks at 900°C to prepare for further heat treatment or hydrogenation.

The *R*Sc*X* materials were all made using *R*: Sc: *X* ratios of 1.0: 1.05: 1.0 to compensate for the presence of small quantities of scandium oxide that form on the surface of the Sc metal on exposure to air.

3.2. *R*TiGe (*R* = Y and Ce)

3.2.1. Structural transition in CeTiGe

As mentioned in chapter 1 and in the introduction to this chapter, the hydrogenation of CeFeSi and CeScSi type materials produces an expansion of the unit cell volume. Thus the crystal structure can be a useful probe in understanding the effects of hydrogenation on the properties of the material as well as helping to confirm successful hydrogenation. The crystal structures of all the phases presented here have been studied using diffraction techniques and refined using the Rietveld method. This provides information on changes in the unit cell parameters as well as interatomic distances and the bonding. In this chapter, compounds have been studied using both X-ray and neutron diffraction techniques.

CeTiGe can crystallise in both the CeScSi and CeFeSi structure types. However, in the literature there are discrepancies between the exact conditions that are needed to stabilise one form over the other. Chevalier *et al.*, (2010)b describe the CeScSi form as the high temperature one after annealing experiments at 1100°C. However, the same experiment performed by Deppe *et al.*, (2012) did not reproduce these results. Therefore in this section we will reinvestigate the CeTiGe system to determine if the CeScSi structure type truly is the high temperature form or not and attempt to shed light on why the two experiments did not produce the same result.

Figure 3. 1. shows the powder XRD measurements on CeTiGe after the initial heat treatment at 900 °C, of the as cast sample, and two other heat treatments, at 1000 °C and 1100 °C. Both of the higher heat treatments were performed for three days on different pieces of the same sample after treatment at 900 °C. From the diffraction pattern it can be seen that, after the first annealing of a pellet of ground CeTiGe at 900 °C the sample is almost completely single phase CeTiGe in the CeFeSi structure type with only trace amounts of Ti_5Ge_3 and Ce_5Ge_3 as secondary phases. Subsequent annealing of the sample at 1000°C for three days leads to the appearance of a peak at $2\theta = 35.75$ ° (marked with ¤ symbol in Figure 3. 1.). This corresponds to the (105) peak of the CeScSi-type form of CeTiGe as reported by Chevalier *et al.*, (2010)b. This peak is only present in the *I4/mmm* space group of the CeScSi structure and can be used as an indicator of the presence of this structural form. At the same time that this peak appears, the peak at $2\theta = 31.50$ ° (the (102) peak of the CeFeSi-type form, marked with * symbol) decreases significantly in intensity after annealing at 1000 °C for three days. Rietveld analysis of the diffraction pattern shows 73 wt.% of the high temperature form and 17 wt.% of the low temperature form. Moreover, after annealing at 1100°C this (102) peak has completely vanished indicating the disappearance of the CeFeSi-type form. It is clear, therefore, that the CeFeSi form of CeTiGe is the low temperature form (LT) while the CeScSi form is the high temperature (HT) one. This clearly shows that the structural transition begins somewhere between 900 °C and 1000 °C. In order to more accurately place the transition temperature, differential scanning calorimetry (DSC) measurements were performed with a heating rate of 10 °C min^{-1}. Unfortunately, due to the slow kinetics of the structural transition, we were unable to observe it using this method. Thus, a more accurate transition temperature than the temperature range 900 - 1000 °C could not be determined. As mentioned above, annealing the low temperature form of CeTiGe at 1100°C for 3 days completely removes the low temperature form from the initial mixture. This can be attributed to the accelerated kinetics at higher temperature. During these studies of the heat treatment, an investigation was made on the effect of cooling speed by quenching in water and air. It was found that simply removing the samples from the furnace without quenching in water produced very little variation in the final composition when compared with quenching in water. This indicates that the structural transition is very slow, taking place over the course of several days at elevated temperatures. Given that quenching from 1000/1100 °C in water often causes the

quartz tube to crack, exposing the hot sample to water, the samples after this cooling speed study were all simply removed from the furnace and cooled in air.

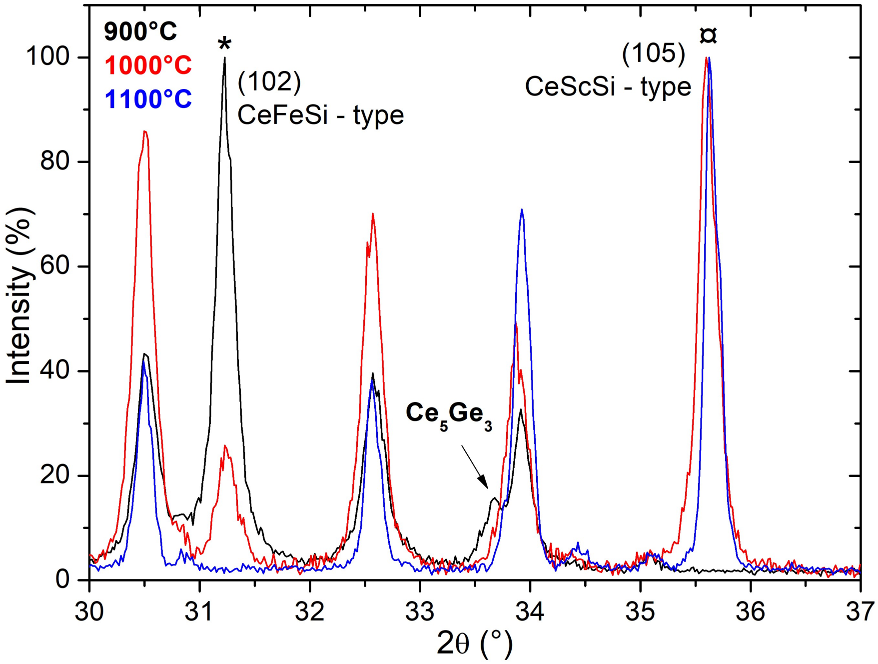

Figure 3. 1. Powder X-ray diffraction patterns of CeTiGe after temperature treatment at 900, 1000 and 1100 °C (pellet of compacted powder).

Finally, the effect of sample morphology on the structural transition was also investigated. Figure 3. 2. shows the XRD patterns of a block and pellet of the same CeTiGe sample after annealing together in the same furnace at 1100°C for 3 days. The labelled peaks in the image are unique to either the HT or LT forms as indicated. It can clearly be seen that the morphology of the sample (block or pellet) has a significant effect on the structural transition. When the sample is annealed in block form, only a small quantity of the HT CeScSi-type CeTiGe is found whereas the same sample, when annealed in identical conditions as a pellet of compacted powder, results in almost total conversion to the high temperature form. This is likely due to strain created during the structural transition which causes a slight expansion of the a parameter (a_{LT} = 4.1443(2) Å while a_{HT} = 4.1543 Å) and the c parameter (c_{LT} = 7.9310(4) Å while $c_{\mathrm{HT}}/2$ = 7.9412(1) Å) with one half of the unit cell shifting by $b/2$ (see chapter 1 section 1.1). The $b/2$ shift is clearly the most important piece of this structural transition and is predominantly responsible for the strain. In the block, the surrounding crystal resists the crystallographic changes associated with the structural transition. However, in the powder form, the smaller crystallites and high porosity allow the structure to change more easily, facilitating the transition. This effect may help to explain the results obtained by Deppe *et al.*, (2012). Neither the exact composition they used for their synthesis nor the form of their samples is provided in the paper but they do state that they introduced substitutions of Zr and Nb for Ti and small amounts of Si on the Ge sites. Morozkin *et al.*, (2000) showed that at least 30 % substitution of Zr or Nb is required on the Ti site to stabilise the CeScSi-form and that low levels of Si substitution on the Ge site (10 %) preserves the coexistence of both forms. Finally, Morozkin *et al.*, (2000) show that, for the GdTiGe case, both structural forms are present in the stoichiometric and when sub-stoichiometry on the rare earth site is introduced. According to the available data on the experiment performed in Deppe *et al.*, (2012) it is conceivable that they should see a coexistence of the two phases. However, if Deppe *et al.*, (2012) performed their annealing on blocks rather than powdered samples, it would explain the lack of any observed high temperature form.

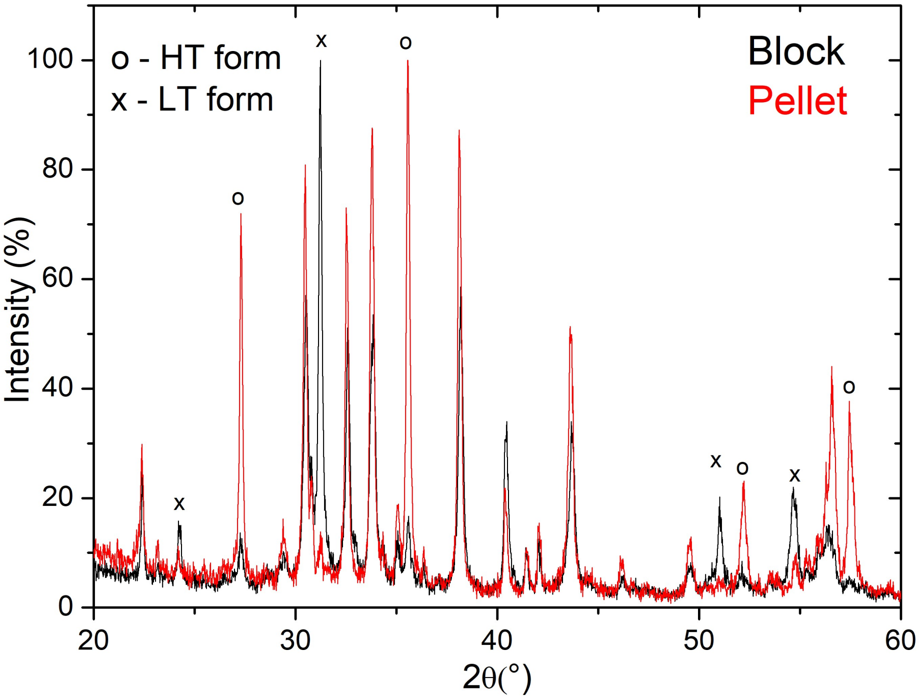

Figure 3. 2. Powder XRD patterns of the same CeTiGe sample after annealing at 1100°C in both pellet and block form.

3.2.2. Hydrogenation of CeTiGe

The hydrogenation of intermetallic materials is performed *via* solid-gas reactions at elevated temperatures and pressures. As hydrogen is a very mobile element within a crystal structure these experiments typically do not require more than a few hours to be performed. Hydrogenation of CeTiGe was performed at 350 °C under 5 bar of H_2 gas after 2 hours of activation under vacuum at this temperature.

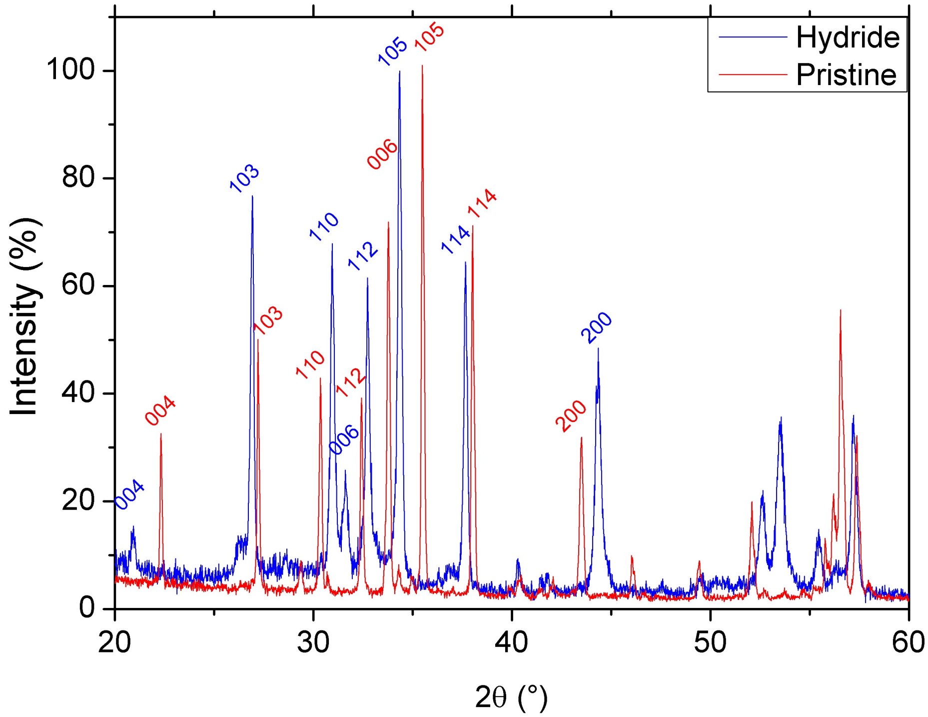

Figure 3. 3. Powder XRD patterns of CeTiGe (HT form) before and after hydrogenation.

CeTiGe is interesting for its structural transition between the CeFeSi and CeScSi structure types but also for its behaviour during hydrogenation. The XRD patterns of the HT-form of CeTiGe and its hydride are shown in figure 3. 3. We observe a decrease in the *a* unit cell parameter from 4.15434(5) Å to 4.0889(2) Å and a large increase in the *c* parameter from 15.8824(2) Å to 16.9917(9) Å. Interestingly, the exact same hydride is obtained whether starting from the HT-form, with the CeScSi structure type, or the low temperature (LT) form with the CeFeSi structure type. That is, the hydride obtained always crystallises in the *I4/mmm* space group of the CeScSi structure type as seen in Figure 3. 4. However, the hydride formed from the low temperature analogue shows much broader XRD peaks than the HT analogue, indicating a larger negative effect on the crystallinity when beginning from the LT form. For example the 006 peak of the hydride is not visible in Figure 3. 4. due to peak broadening which conceals it beneath the larger 110 peak. The structural transition that normally requires extended treatment at very high temperatures can be realised at much lower temperatures and much more quickly during the course of the hydrogenation reaction. This structural change has been seen already by Gaudin *et al.*, (2011) for the hydrogenation of the CeFeSi-form of GdTiGe.

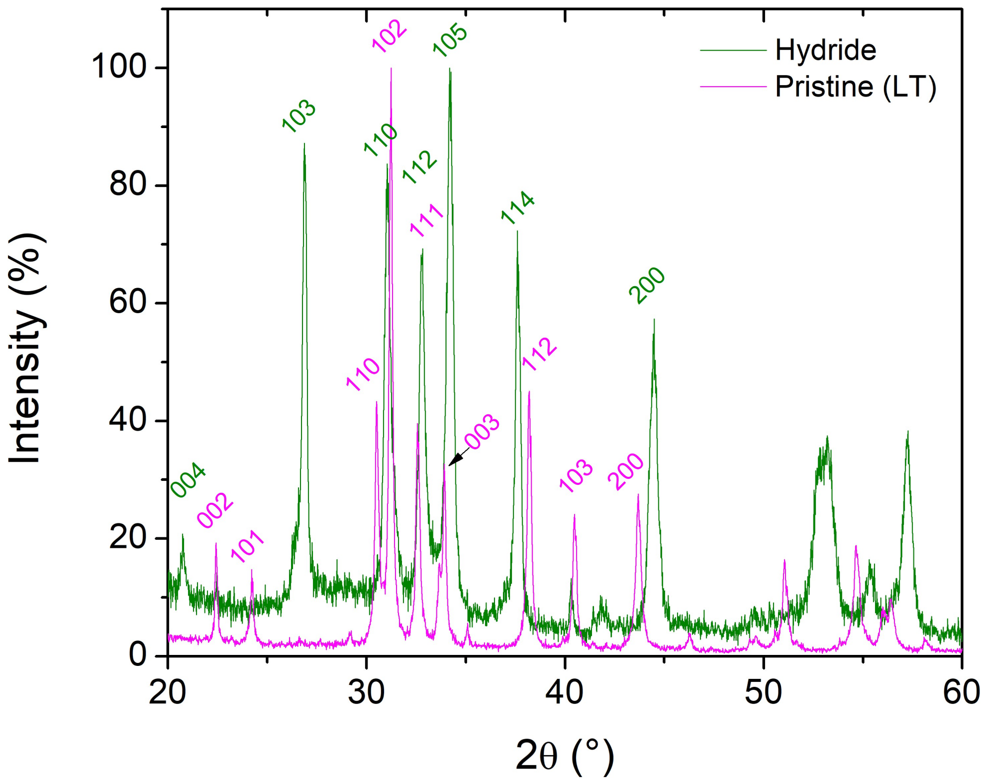

Figure 3. 4. Powder XRD patterns of CeTiGe (LT form) before and after hydrogenation.

3.2.3. Neutron diffraction on CeTiGeH$_x$

Following the realisation that hydrogenation of the CeTiGe materials always produces the hydride form of the CeScSi structure type, we carried out neutron diffraction on CeTiGeH$_x$ to determine the amount of hydrogen inserted as well as its location within the unit cell. This experiment was performed on the 3T2 high resolution diffractometer at the LLB near Saclay, France, using a wavelength of 1.226 Å. The initial refinement was performed based on the known structure of the CeFeSi-type hydrides, with hydrogen in the 4*d* Wyckoff position (0, ½, ¼) inside the rare earth tetrahedral sites. The resulting fit was of poor quality which may indicate another site(s) is occupied by hydrogen atoms. Fortunately there are a number of empirical rules that have been established which can aid us in predicting the location of hydrogen atoms in a crystal structure (Brinks *et al.*, (2001)). In order to accept hydrogen, an interstitial site must have a radius of at least 0.4 Å (Westlake, (1983)a, (1983)b) and not exceeding 0.8 Å (Yartys *et al.*, (1997). By considering the crystal structure of the HT form of CeTiGe from (Chevalier *et al.*, (2010)b) we see that the available sites for hydrogen insertion are the Ce$_4$ tetrahedra (r = 0.50 Å), the Ti$_4$Ge$_2$ octahedra (r = 0.61 Å) and the Ti$_4$Ce$_2$ octahedra (r = 0.61 Å). Another of these rules is that sites containing p block elements are less favourable for H insertion than sites containing elements that form stronger bonds with hydrogen such as the rare earth elements (Yartys *et al.*, (1997). Indeed hydrogen is found to occupy interstitial sites that are most distant from the p block elements (Rundqvist *et al.*, (1984)) as discussed in section 1.3.1.1. Based on these rules we can predict that the Ti_4Ce_2 octahedral sites will be preferentially filled over the Ti_4Ge_2 ones. Occupation of these sites as well would lead to a total of 2 H f.u.$^{-1}$ but high pressure measurements (40 bars) provide no indication that this has occurred.

To investigate this, Fourier difference analysis was carried out on the refinement. This technique can be used to map the nuclear density (or electron density for X-ray diffraction) in the unit cell and in particular to map unassigned nuclear density to find atoms that may not have been included in the refinement. The resulting Fourier difference map is presented in Figure 3. 5.

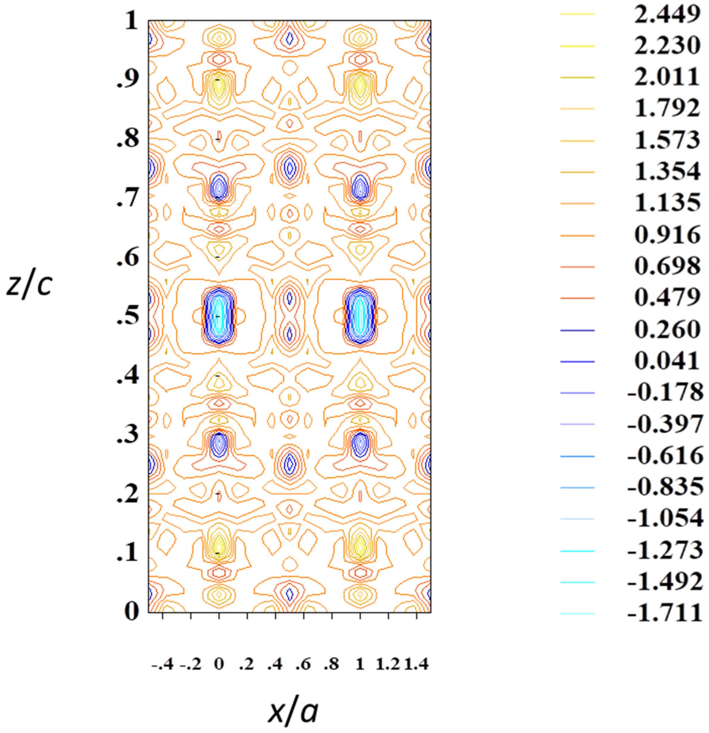

Figure 3. 5. Fourier difference map after the refinement of $CeTiGeH_x$ with the H atom located only in the Ce_4 tetrahedral site. (*y* = 0)

Difference mapping shows clearly a residual, negative, nuclear density around the (0, 0, ½) position inside the Ti_4Ce_2 octahedra, as predicted. This suggests the presence of H atoms which show a negative density due to the negative coherent neutron scattering length of hydrogen (b_C (H) = -3.74 fm) (Sears, (1992)). In light of this, a second hydrogen position was added to the refinement at the (0, 0, ½) position with full occupancy which resulted in a significant improvement of the fit. However, this produced unreasonably large B_{iso} values for the H2 site. For the final refinement, we shifted the hydrogen atoms slightly out of the (0, 0, ½) plane to the 4*e* Wyckoff site (0, 0, 0.521(1)) with occupancy of 0.49(1). This refinement converged with very good agreement with the experimental data and the final refinement is shown in Figure 3. 6. with a summary of the refinement and the refined structure in Table 3. 1. and Table 3. 2.

Thus CeTiGe can absorb 1.5 atoms of hydrogen per unit cell with the hydrogen atoms occupying the vacant rare earth tetrahedral sites as well as the $CeTi_4$ square based pyramidal sites formed from the Ti_4 square plane and one Ce atom. The structural transition from CeFeSi-type to CeScSi-type on hydrogen insertion is believed to be due to an increased stability of the CeScSi-type hydride. This is also observed in the hydrogenation of the GdTiGe system by Gaudin *et al.*, (2011). As GdTiGe was found to only absorb one hydrogen atom per formula unit the structural transition cannot simply be due to the availability of the second site for hydrogen. The crystal structure of $CeTiGeH_{1.5}$ is very similar to that of $NdScSiH_{1.5}$ which is discussed in more detail in section 3.3.3. of this chapter.

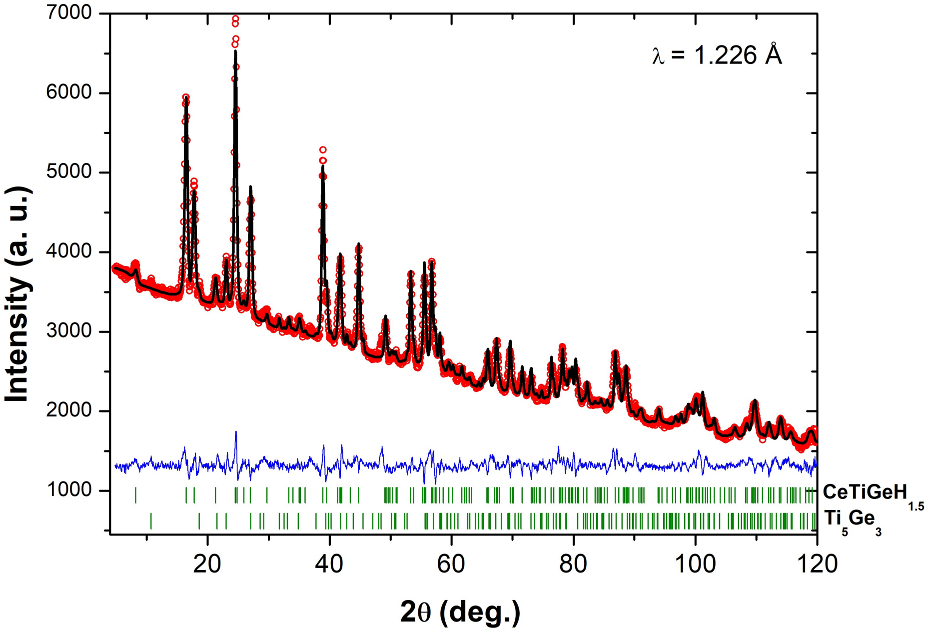

Figure 3. 6. Rietveld refinement of the neutron diffraction pattern of $CeTiGeH_{1.49(1)}$ at room temperature (observed (red circles), calculated (black line), and difference (blue line) profiles).

Table 3. 1. Summary of the nuclear structure refinement parameters of $CeTiGeH_{1.49(1)}$.

a **(Å)**	***c*** **(Å)**	**V ($Å^3$)**	**R-Bragg (%)**	**R_p (%)**	**R_{wp} (%)**
4.0773(1)	17.1047(8)	284.3550	9.0	22.4	18.7

Table 3. 2. The refined nuclear structure parameters of CeTiGeH$_{1.49(1)}$ and those of the published crystal structures of the high and low temperature forms of pristine CeTiGe.

Phase	Atom	Wyckoff	x	y	z	Occ.	U$_{iso}$ (Å^2)
LT-CeTiGe$^{\#}$	Ce	2c	¼	¼	0.652(4)	1.00	-
	Ti	2a	¾	¼	0	1.00	-
	Ge	2c	¼	¼	0.227(6)	1.00	-
HT-CeTiGe*	Ce	4e	0	0	0.3262(2)	1.00	0.0159(14)
	Ti	4c	0	½	0	1.00	0.026(4)
	Ge	4e	0	0	0.1151(5)	1.00	0.019(2)
CeTiGeH$_{1.5}$	Ce	4e	0	0	0.3240(3)	1.00	0.0116(3)
	Ti	4c	0	½	0	1.00	0.021(5)
	Ge	4e	0	0	0.1022(2)	1.00	0.0073(8)
	H1	4d	0	½	¼	1.02(2)	0.022(3)
	H2	4e	0	0	0.521(1)	0.49(1)	0.032(4)

$^{\#}$Morozkin *et al.*, (1999) *Chevalier *et al.*, (2010)b

3.2.4. Magnetic properties of CeTiGe and CeTiGeH$_{1.5}$

As Ce compounds have been shown to exhibit interesting changes in their magnetic properties on hydrogenation (Chevalier *et al.*, (2006)b, (2008)), we have investigated the magnetic properties of the CeTiGeH$_{1.5}$ materials. In order to examine this, the temperature dependence of the susceptibility to an applied magnetic field was measured on both the HT form of CeTiGe and the corresponding filled hydride, CeTiGeH$_{1.5}$ using a S.Q.U.I.D. magnetometer (see chapter 2 for details). The sample was initially cooled in the absence of an external field to 1.8 K before being heated in applied field of 0.05 T (zero field cooled or ZFC curve). The sample's susceptibility is then measured during cooling in the same field from the paramagnetic state (field cooled or FC curve). Figure 3. 7. shows the ZFC-FC curves for both the high temperature form of CeTiGe and its corresponding hydride. The inset shows the reciprocal of the magnetic susceptibility in the paramagnetic state, fitted using the Curie-Weiss law.

The pristine material is known to be a non-magnetic, heavy fermion system (Deppe *et al.*, (2009)) with Curie-Weiss paramagnetic behaviour down to 5 K and an effective magnetic moment consistent with the Ce^{3+} ion (Welter *et al.*, (1999)). This confirms that the Ti is non-magnetic in these systems. The hydride displayed an effective moment of 2.37 μ_B f.u.$^{-1}$ which is close to the value for the free Ce^{3+} ion (2.56 μ_B). From the form of the ZFC-FC curve, it may order magnetically at low temperature (≈ 3 K) but the exact nature of the magnetic order could not be determined. A small amount of the dense Kondo compound Ce$_5$Ge$_3$ was detected in the XRD analysis of this material. This phase shows a spontaneous magnetisation below 6 K (Kurisu *et al.*, (1999)) and may also contribute to the anomalies observed in Figure 3. 7.

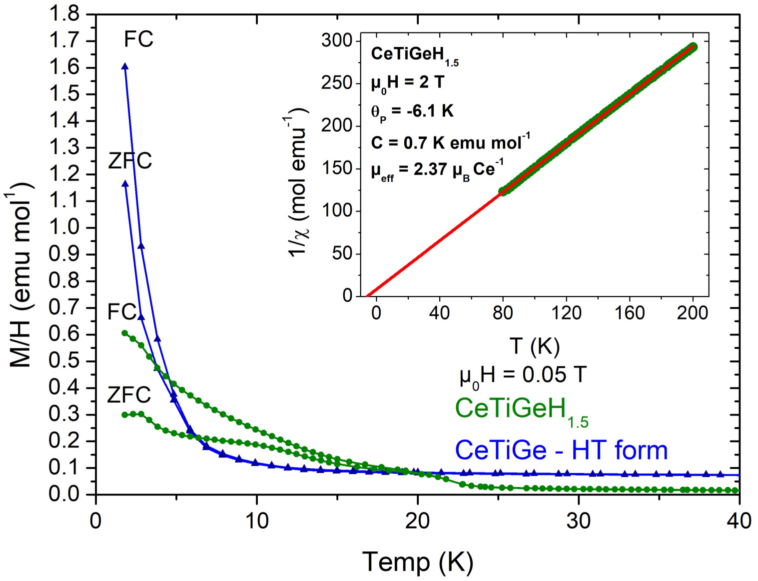

Figure 3. 7. ZFC-FC magnetisation curves of the high temperature form of CeTiGe and its hydride. The inset shows the inverse susceptibility data at high temperature fitted with a Curie-Weiss type law.

3.2.5. Hydrogenation of YTiGe

YTiGe crystallises in the CeFeSi structure type and does not display a structural transition to the CeScSi structure type that other members of the *R*TiGe family do (Nikitin *et al.*, (1998); Morozkin *et al.*, (1999). Morozkin *et al.*, (2000) describe the stabilisation of the CeScSi-type form of YTiGe by substituting Gd on the Y site but this was not studied here. Hydrogenation was performed on this material and an XRD pattern was collected on corresponding hydride. The data was treated by full pattern matching and the fit along with the hydrogen absorption curve is displayed in Figure 3. 8. The unit cell parameters of the YTiGeH phase are given in Table 3. 3. The curve shows unambiguously that YTiGe absorbs one atom of hydrogen per formula unit. Given that YTiGe crystallises in the CeFeSi structure type and does not show evidence of a structural transition, this is the expected result as full occupation of the vacant rare earth tetrahedra should produce YTiGeH$_{1.0}$.

Table 3. 3. Unit cell parameters of YTiGeH and YTiGe

Phase	Space group	*a* (Å)	*c* (Å)	V (Å^3)
YTiGeH	*P4/nmm*	3.9501(3)	8.185(1)	127.71
YTiGe*	*P4/nmm*	4.038(1)	7.619(4)	124.23
*Morozkin *et al.*, (1998)a				

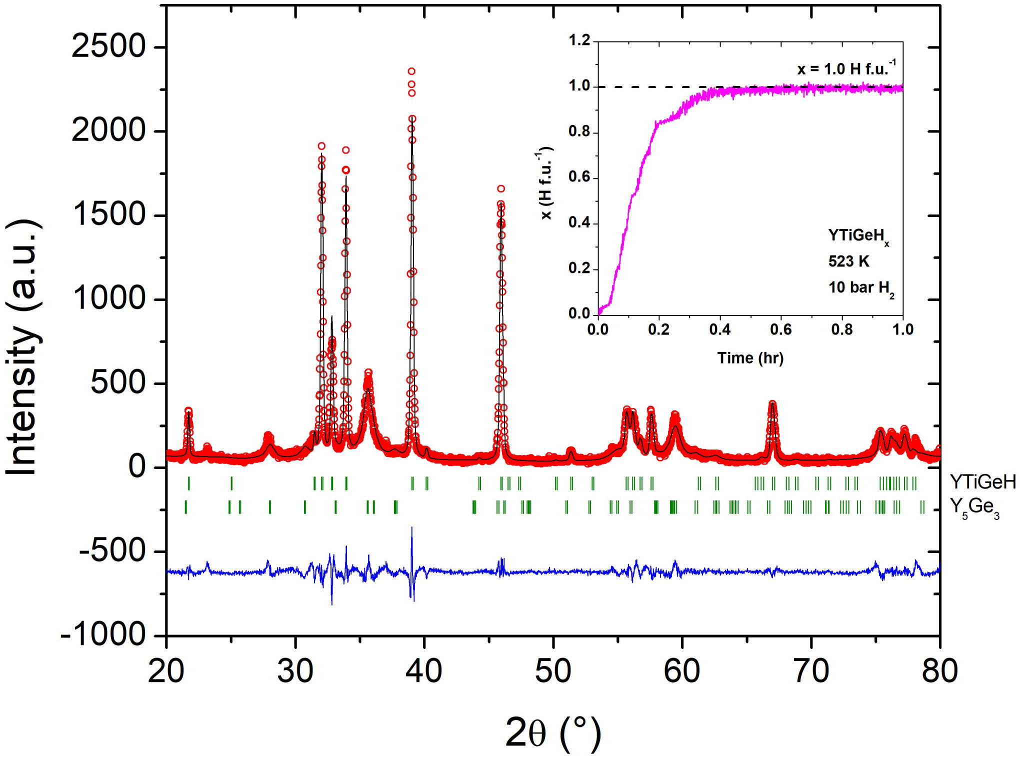

Figure 3. 8. Full pattern matching of the crystal structure of YTiGeH from powder XRD data (λ = 1.5406 Å and 1.5444 Å). Inset shows hydrogen absorption curve of YTiGe under 10 bars H_2 at 523 K.

3.2.6. Magnetic properties of YTiGeH

Non-magnetic rare earth materials, while interesting for comparison with the properties of the magnetic rare earth compounds, are also interesting for superconductivity. For both of these reasons the magnetic properties of YTiGeH were studied. The ZFC magnetisation with respect to temperature for YTiGeH is shown in Figure 3. 9. The pristine compound is a Pauli paramagnet down to at least 5 K (Welter *et al.*, (1999)). Measurements on the hydride yield a small but positive magnetic moment in a field of 0.002 T, suggesting that the hydride material is also a Pauli paramagnet.

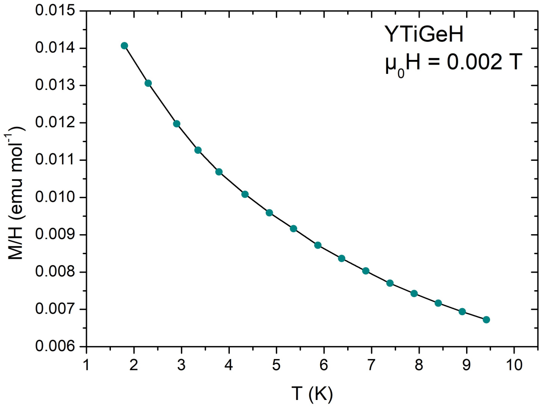

Figure 3. 9. ZFC magnetisation curve of YTiGeH in a field of 0.002 T.

In a superconducting material, low field magnetisation measurements are expected to show evidence of the screening effect through a strong diamagnetic signal in the zero field cooled magnetisation curve. The Meissner effect (also known as the Meissner-Ochsenfeld effect) is the complete expulsion of a magnetic field from a superconductor that occurs during its transition to a superconducting state and would normally be observed in the FC curve when the ZFC curve shows the screening effect. Discovered in 1933 by the titular physicists Walther Meissner and Robert Ochsenfeld it can be considered as a perfect diamagnetic state with susceptibility measurements producing a large diamagnetic signal in response to an applied field (Meissner and Ochsenfeld, (1933)). This effect can be overcome by a large enough magnetic field, hence the use of very low fields to determine its presence. Typically the detection of a superconducting material is performed using both magnetisation and resistivity measurements. However, as we clearly do not see a diamagnetic signal here it is unnecessary to perform resistivity measurements to rule out the presence of superconductivity in YTiGeH above 1.8 K.

3.3. NdScSiH$_{1.5}$

The data in this section corresponds to our recent publication in Tencé *et al.*, (2016).

3.3.1. Hydrogenation of NdScSi

The hydrogen absorption curve for NdScSi is presented in Figure 3. 10. it clearly shows that NdScSi absorbs approximately 1.5 H f.u.$^{-1}$ over the course of several hours at 573 K and 5 bars of H$_2$. This result is surprising when compared with the results typically obtained for other compounds crystallising in the related CeScSi structure type such as GdTiGe which only absorbs one atom of hydrogen per formula unit (Chevalier *et al.*, (2010)c; Gaudin *et al.*, (2011)). However, it is coherent with our results on the CeTiGe system.

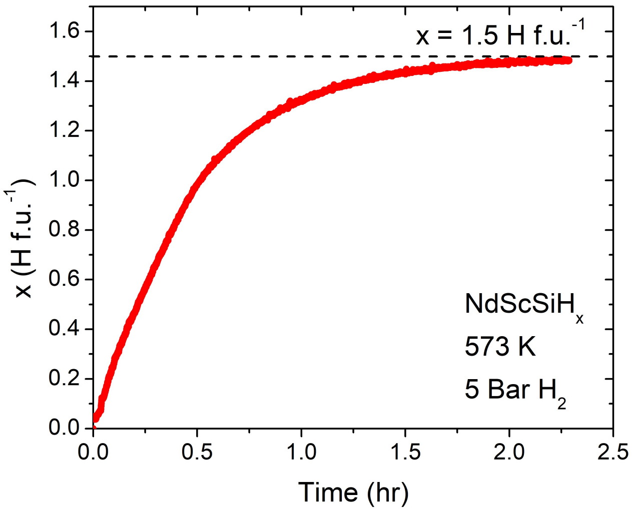

Figure 3. 10. Hydrogen absorption curve of NdScSi at 573 K.

The powder XRD patterns of NdScSi and its hydride are shown in Figure 3. 11. The measurement shows that the hydride retains the *I4/mmm* space group of the parent compound with the same trend in the unit cell parameters that is seen in other similar hydrides. The *a* parameter decreases from 4.2894(6) Å to 4.221(1) Å while the *c* parameter increases from 15.705(3) Å to 16.928(2) Å, representing an increase in the unit cell volume of 4.3%. The *c*/*a* ratio increases from 3.66 to 4.01, showing an elongation of the unit cell.

Complete filling of the empty tetrahedral sites should only produce $NdScSiH_{1.0}$ but the measurements indicate that the real formula is $NdScSiH_{1.5}$. This is in agreement with results of neutron diffraction on $CeTiGeH_{1.5}$. To confirm the hydrogenation measurements and to locate the second hydrogen site neutron diffraction experiments were also carried out on the *in-situ* deuteration of this system.

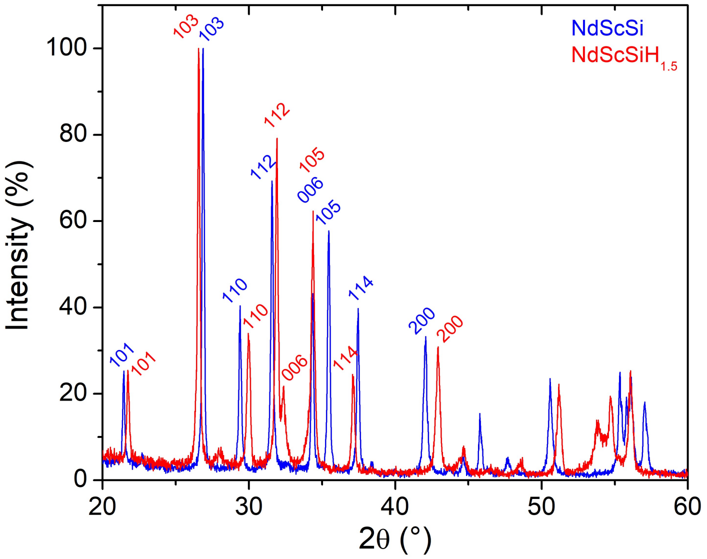

Figure 3. 11. Powder XRD patterns of NdScSi before and after hydrogenation.

3.3.2. *In-situ* neutron diffraction during deuteration of NdScSi

During our investigation of the hydrogenation of NdScSi, *in-situ* neutron diffraction was performed during the deuteration of the compound to determine accurately the crystal structure and examine the way that deuterium insertion occurs (if both sites are filled simultaneously, if intermediate deuterides are present, etc.). The experiment was performed on the C2 diffractometer at the Canadian Neutron Beam Centre using a wavelength of 1.328 Å (Si(531) monochromator). C2 is equipped with a curved 800-wire BF3 position sensitive detector with a wire spacing of 0.1°. The experimental setup is designed so that the sample holder can be filled with hydrogen/deuterium gas up to 40 bar and heated in the 25–400 °C temperature range (Flacau *et al.*, (2012)).

The *in-situ* deuteration was performed under 5 bar of H_2 from room temperature to 400 °C. Above this temperature the vanadium sample holder is no longer tight. Upon heating, additional nuclear peaks appear in Bragg positions slightly shifted from those of NdScSi. This corresponds to the appearance of the deuterated phase which coexists with the parent compound. After 15 h of heating under 5 bar of D2 and up to 350 °C, a small amount of the pristine compound is still present (*ca.* 13 wt%) as visible on the diffractogram of the Figure 3. 12. recorded at room temperature. All extra peaks are indexed with the tetragonal space group I4/mmm suggesting that $NdScSiD_x$ adopts a stuffed CeScSi-type structure upon deuteration. We observe a slight decrease of the *a* parameter from 4.2894(6) Å to 4.1875(6) Å (-2.6%) and a strong increase of the *c* parameter from 15.705(3) Å to 16.631(3) Å (+5.9%). A summary of this refinement can be seen in Table 3. 4. And 3. 4., below.

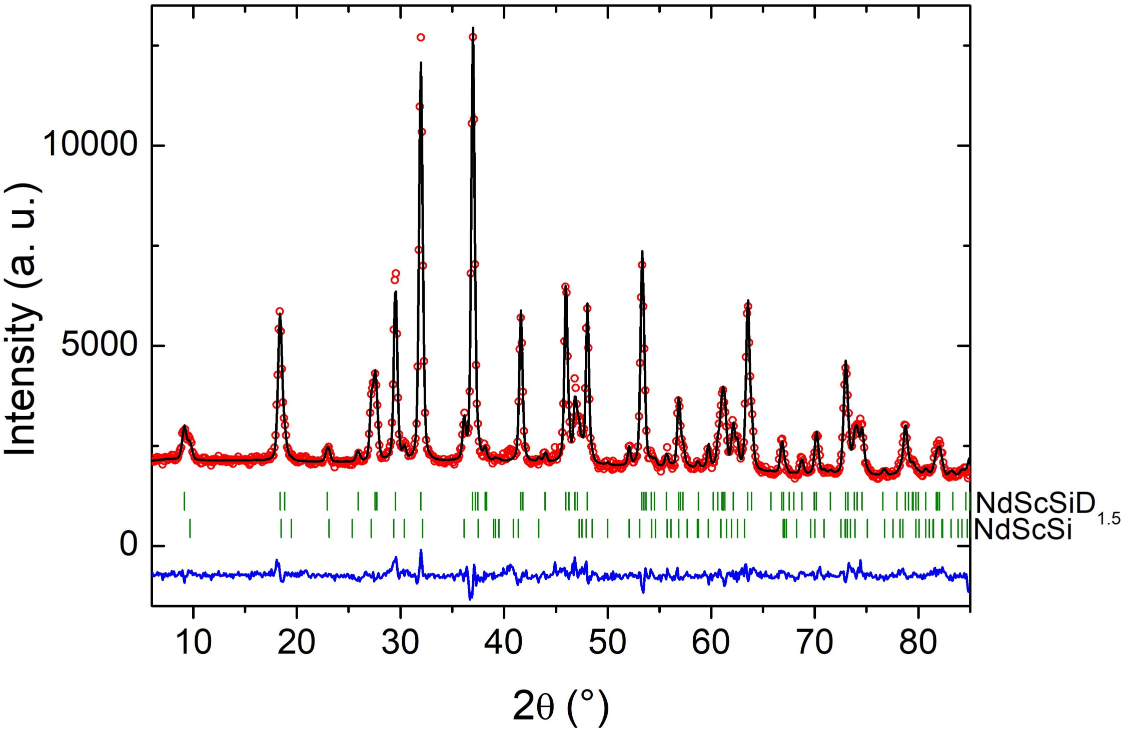

Figure 3. 12. Rietveld refinement of the neutron powder diffraction pattern collected at room temperature after 15 h of deuteration of NdScSi. The upper and lower ticks correspond to the deuteride and NdScSi, respectively.

Table 3. 4. Refined unit cell parameters for the *in-situ* neutron diffraction after *in-situ* deuteration of NdScSi.

Phase	***a* (Å)**	***c* (Å)**	**V ($Å^3$)**	**R-Bragg (%)**	**R_p**	**R_{wp}**
NdScSi	4.2894(6)	15.705(3)	288.956	4.4	13.3	11.7
$NdScSiD_{1.47(3)}$	4.1875(6)	16.631(3)	291.620	9.3		

Table 3. 5. Atomic coordinates and equivalent isotropic displacement parameters (pm^2) of NdScSi and $NdScSiD_{1.47(3)}$. U_{eq} is defined as one third of the trace of the orthogonalised U_{ij} tensor.

Phase	Atom	Wyckoff	x	y	z	U_{eq}/U_{iso}* (pm^2)	Occ.
NdScSi	Nd	*4e*	0	0	0.32347(1)	76(1)	1
	Sc	*4c*	0	½	0	91(1)	1
	Si	*4e*	0	0	0.12285(8)	80(2)	1
$NdScSiD_{1.47(3)}$	Nd	*4e*	0	0	0.316(1)	94(8)*	1
	Sc	*4c*	0	½	0	148(8)*	1
	Si	*4e*	0	0	0.109(1)	86(7)*	1
	D1	*4d*	0	½	¼	195(17)*	1.01(1)
	D2	*4e*	0	0	0.518(1)	234(32)*	0.47(3)

*Marked values correspond to U_{iso} while unmarked are U_{eq}.

Initial refinement was performed using only the D1 positon (the rare earth tetrahedral sites) for the deuterium atoms. However, this produced a poor fit for the data. Considering the hydrogenation measurements on this sample (Figure 3. 10.), it was determined that deuterium must occupy a second site in the structure. To attempt to determine the location of this site (D2), Fourier difference analysis of the refinement was carried out. The results of this map before the inclusion of the D2 atom are shown in Figure 3. 13.

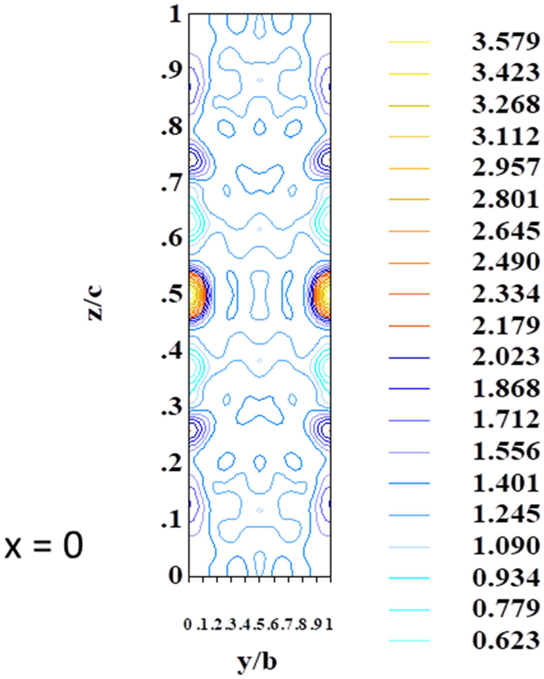

Figure 3. 13. Fourier difference map of $NdScSiD_{1.5}$ without the inclusion of deuterium in the second site (D2).

From Figure 3. 13. it is clear that there is a significant residual nuclear density located around the (0 0 ½) position. The addition of deuterium to this position in the refinement improved the fit significantly. However, the refined U_{iso}(D) was quite large on this site. Such a large thermal displacement parameter can indicate that the atom is not correctly placed in the refinement and so finally the D2 site was moved slightly away from the (0 0 ½) site located in the scandium planes to allow refinement of its position. This produced the (0 0 0.518(1)) position cited in Table 3. 5. with occupancy of one half. The best agreement between the calculated and measured patterns was obtained by using this structural model. The occupancy of one half can be explained by considering the closeness of the two 4*e* D2 sites located on either side of the Sc square plane. The filling of one prevents the filling of the other as it would produce deuterium-deuterium distances that are much too small (on the order of 0.6 Å). Thus $NdScSiD_{1.47(3)}$ adopts the $La_2Fe_2Se_2O_3$-type structure (Mayer *et al.*, (1992)) as presented in Figure 3. 14.

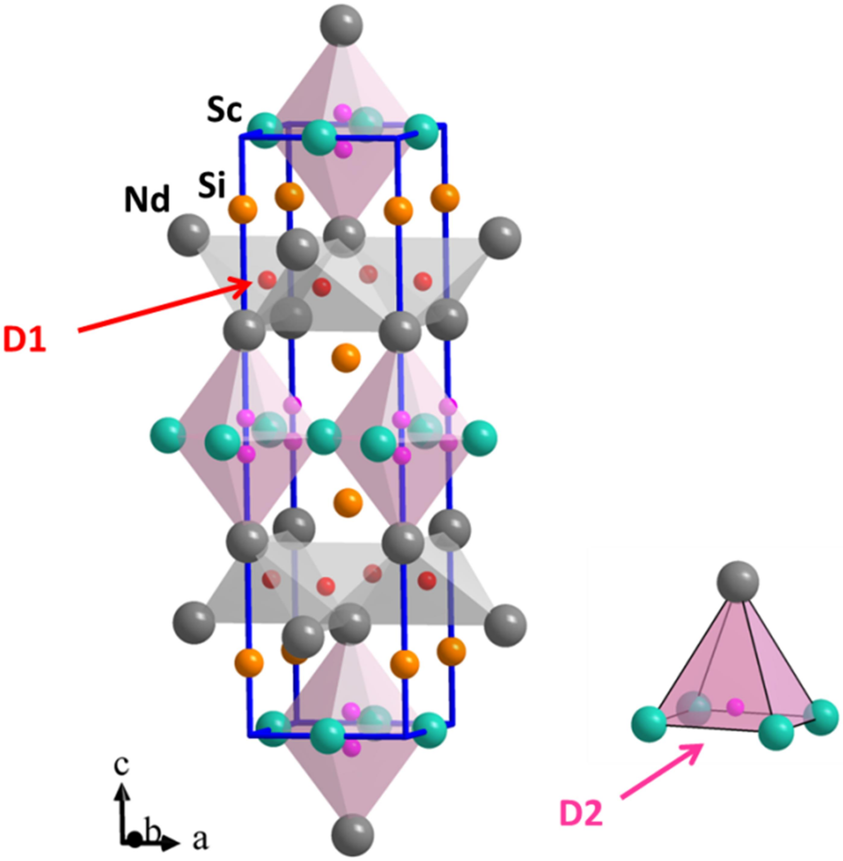

Figure 3. 14. Crystal structure of $NdScSiD_{1.5}$ emphasising the tetrahedral and square based pyramidal sites. The D2 square based pyramidal site is also shown separately.

3.3.3. Discussion of the changes in the interatomic distances

The addition of hydrogen to vacant interstitial sites causes changes in the unit cell parameters and atomic positions. This section will focus on the changes in the interatomic distances of NdScSi on deuteration to $NdScSiD_{1.47(3)}$ as presented in Table 3. 6. For the metallic radii given in this discussion, half the shortest metal-metal distance in the pure metal will be used.

Hydrogenation causes the rare earth double planes to contract as the tetrahedral sites are filled. At the same time, the Sc-Si planes also contract and the *c* axis length increases. As the layers contract and the *c* axis elongates it is clear that the distance between the Nd and Sc-Si planes (equal to *c*/4) also increases, namely from 3.93 Å to 4.16 Å. Thus hydrogenation causes an increase in the 2D character of the substructure of NdScSi.

Table 3. 6. Interatomic distances (Å) in NdScSi calculated with the XRD powder lattice parameters and $NdScSiD_{1.47(3)}$ calculated from the neutron powder diffraction data. Standard deviations are all equal to or less than 0.02 Å. *Td* and *SP* represent the empty tetrahedral# and square based pyramidal° sites respectively.

Atom 1	**Atom 2**	**d (Å)**	
		NdScSi*	**$NdScSiD_{1.47(3)}$**
Nd	**Nd**	3.8112(4)	3.686(14)
	Nd	4.2894(6)	4.1875(6)
	Sc	3.5051(5)	3.71(1)
	Si	3.1480(4)	3.213(9)
	Si	3.1507(14)	3.44(2)
	D1/*Td*	*2.4354(3)*	2.364(8)
	D2/*SP*	*2.49(2)*	2.76(2)
Sc	**Sc**	3.0331(3)	2.9610(3)
	Si	2.8848(9)	2.77(1)
	D2/*SP*	*2.1633(21)*	2.115(2)
Si	**D1/*Td***	*2.9304(9)*	3.14(1)
	D2/*SP*	*3.451(8)*	3.33(1)
D1/*Td*	**D1/*Td***	*4.2894(6)*	2.9610(3)
D2/*SP*	**D2/*SP***	*0.56(2)*	0.60(2)

*Tencé *et al.*, (2016) #Position (0, ½, ¼)
°Position (0, 0, 0.518(1))

In the pristine material, the rare earth tetrahedral sites are not regular, possessing two unequal edge lengths. The ratio of the two sides in NdScSi is 0.89 where, for a perfect tetrahedron, it is expected to be 1.00. The occupation of the rare earth tetrahedra causes them to contract without a noticeable change in the regularity of the site. Indeed, in the deuteride, the side ratio is equal to 0.88, thus the tetrahedra maintain their slightly distorted shape on deuteration. This contraction induces the change in $d_{Nd\text{-}D1/Td}$ during deuteration: in NdScSi $d_{Nd\text{-}Td}$ = 2.435 Å while in the deuteride $d_{Nd\text{-}D1}$ = 2.36 Å (-3.1 %) and the shortest Nd-Nd distance ($d_{Nd\text{-}Nd}$) changes from 3.811 Å to 3.69 Å. Deuteration therefore causes the Nd-Nd distance to move closer to that seen in metallic Nd ($d_{Nd\text{-}Nd}$= 3.658 Å, Spedding *et al.*, (1961)). While this may indicate that the Nd-Nd bonding becomes more metallic, it is much more probable that an electronic interaction with the electronegative deuterium atoms is responsible. $d_{Nd\text{-}D1}$ = 2.36 Å is very close to the Nd-H distance seen in NdH_2 of 2.37 Å (Korst and Warf, (1966)), $d_{Nd\text{-}D2}$ on the other hand is 2.76(2) Å, larger than in the binary hydride. This may indicate that the interaction between the rare earth atoms and the deuterium atoms is larger for the D1 site than the D2. The $d_{Sc\text{-}D2}$ = 2.12 Å lies close to the Sc-H distance of 2.07 Å seen in the binary ScH_2 (Venturini and Morosin, (1977)). The splitting of the D2 position used here is seen also in Sr_4Bi_2O (Wied *et al.*, (2011)) where the oxygen is placed in the same type of split octahedral site, shifted slightly away from the centre of the octahedron into the square based pyramid. In the pristine compound, $d_{Sc\text{-}Sc}$ = 3.033 Å, is smaller than the $d_{Sc\text{-}Sc}$ = 3.25 Å seen in elemental Sc (Kammler *et al.*, (2008)) showing strong Sc-Sc interactions. Deuteration decreases this to 2.961 Å but, as with the Nd atoms, this is more likely due to strong Sc-D interactions pulling the Sc atoms closer together and not a true increase in the strength of the Sc-Sc bonds. The location of D2 slightly out of the Sc square planes is believed to be due to the Nd-D2 interaction. The $d_{Sc\text{-}D2}$ distance does not change significantly if D2 is located in the square plane (d = 2.09 Å) or slightly out of it, as here. However, the $d_{Nd\text{-}D2}$ = 3.060 Å is noticeably reduced to $d_{Nd\text{-}D2}$ = 2.76 Å when D2 is shifted in the $NdSc_4$ square pyramids. Thus by occupying the square based pyramidal site rather than the octahedral site Nd-D2 bonding is facilitated.

While this consideration of the interatomic distances is a useful first step in analysing the bonding in $NdScSiH_{1.5}$, a more rigorous investigation using density functional theory calculations could shed further light on the bonding behaviour and thus complete this section.

3.3.4. Magnetic properties of $NdScSiH_{1.5}$

In order to investigate the effect of hydrogenation on NdScSi, measurements of the magnetisation with respect to temperature were performed in an applied field of 0.05 T. These measurements can be seen in Figure 3. 15. with the inset showing the inverse of the magnetic susceptibility at high field, fitted using the Curie-Weiss law. $NdScSiH_{1.5}$ is a Curie-Weiss paramagnet with a paramagnetic Curie temperature, θ_P, = -16 K, and an effective magnetic moment of 3.71 μ_B Nd^{-1}. This is close to the typical value for a Nd^{3+} magnetic system of 3.62 μ_B Nd^{-1}, confirming that the Nd atoms are the source of the magnetic order in the material. The negative value of θ_P shows the presence of predominantly antiferromagnetic local interactions between spins. Singh *et al.*, (2004) show that NdScSi is a Curie-Weiss paramagnet with an effective magnetic moment of 2.96 μ_B $f.u.^{-1}$ which is significantly below the expected value for a Nd^{3+} magnetic system of 3.62 μ_B $f.u.^{-1}$. Pristine NdScSi orders ferromagnetically below 171 K (Singh *et al.*, (2004)), while the hydride orders magnetically at around 4 K, below which there is a deviation between the ZFC and FC curves. This deviation is a typical feature of the strong magnetocrystalline anisotropy that is often present in rare earth magnetic systems but it may also be due to a spin glass state. Further measurements are required to further investigate if this is the case.

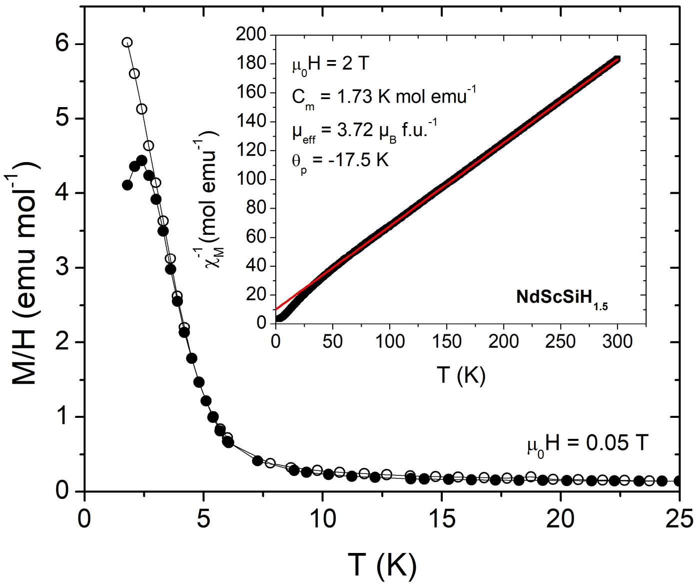

Figure 3. 15. Temperature dependence of the magnetisation for NdScSiH$_{1.5}$ after zero field cooling (filled points) and field cooling (hollow points). The inset shows the inverse of the susceptibility at 2 T with the Curie-Weiss fit in solid line.

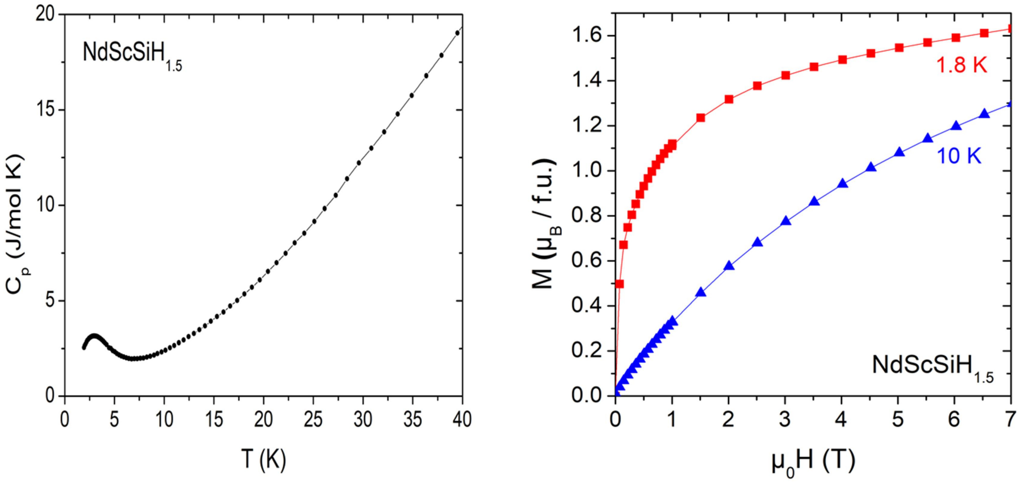

Figure 3. 16. Heat capacity at constant pressure measurement (left) and the isothermal magnetisation measurements at 1.8 K and 10 K for NdScSiH$_{1.5}$ (right).

The magnetic ordering temperature of 4 K is confirmed by specific heat measurements (Figure 3. 16.) which show an anomaly at 4 K. In order to further investigate the magnetic order of NdScSiH$_{1.5}$, high field measurements were performed in the paramagnetic state, as well as isothermal magnetisation measurements at low temperatures. The results of these measurements can be seen in Figure 3. 16. (right). At 1.8 K and 7 T NdScSiH$_{1.5}$ has not reached its saturation magnetisation as evidenced by the lack of a plateau in the M(H) curve. The maximum magnetisation achieved is around 1.6 μ_B f.u.$^{-1}$, close to the value measured for the pristine compound of 2 μ_B Nd^{-1} (Singh *et al.*, (2004)) but lower than the Nd^{3+} free ion value of 3.27 μ_B. The reduction of the moment could be due to the crystal electric field effect which splits the (2*J*+1) fold degenerate level of the free ion but also to the fact that the hydride is not purely ferromagnetic and thus not fully saturated at 7 T.

In an attempt to determine the magnetic structure of $NdScSiH_{1.5}$ we have synthesised another sample of $NdScSiH_{1.5}$ for measurement on the D1B beamline of the ILL, Grenoble, France (λ = 2.52 Å). The neutron diffraction patterns at 20 K and 1.5 K along with the difference curve are plotted in Figure 3. 17. which also shows the ZFC-FC magnetisation curves for this sample. Unfortunately, it is clear from the inset of Figure 3. 17. that the magnetic ordering temperature of this sample is slightly lower than the previous sample. The neutron diffraction patterns show unambiguously that we are unable to observe the magnetic ordering of this sample by neutron diffraction down to 1.5 K.

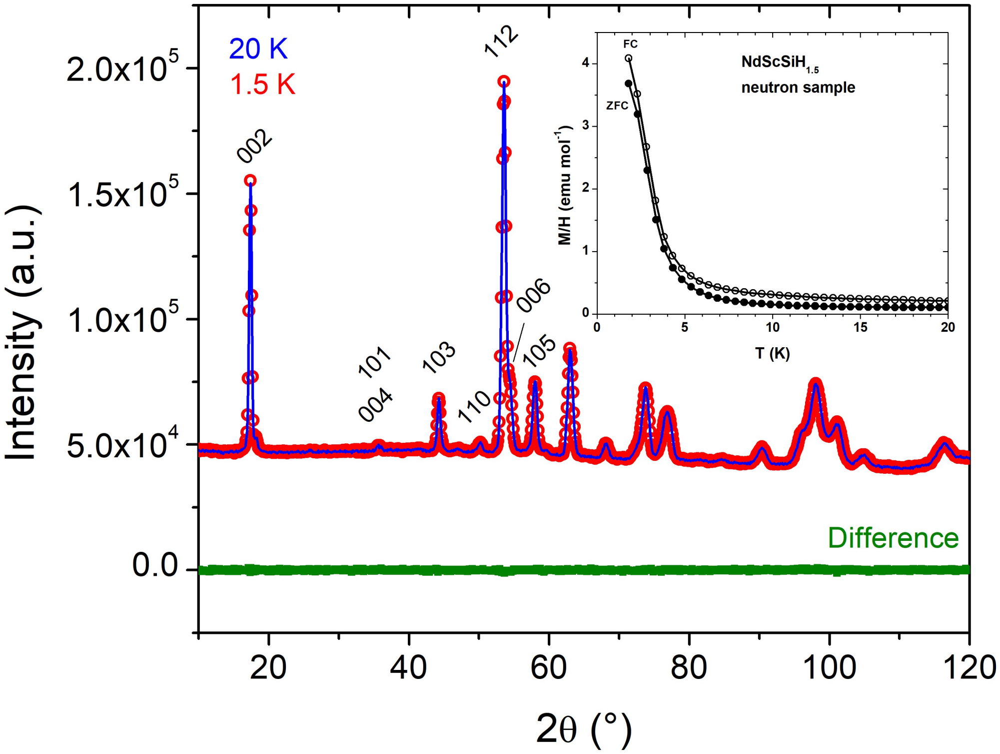

Figure 3. 17. Neutron diffraction patterns of $NdScSiH_{1.5}$ at 20 K (blue line) and 1.5 K (red points) with the difference pattern plotted below. The ZFC-FC magnetisation curve for this sample is shown in the inset. The Miller indices for the low angle peaks are marked

3.4. GdScGeH

GdScGe crystallises in the CeScSi structure type and shows a T_C of 349-350 K (Manfrinetti *et al.*, (2002); Morozkin and Welter, (2002); Couillaud *et al.*, (2011)). We studied the hydrogenation of this material to determine if it absorbs 1.5 atoms of hydrogen per formula unit (as CeTiGe and NdScSi) and if hydrogenation results in destruction of the magnetism (like NdScSi and GdTiGe). Moreover, preliminary investigations (not shown in this manuscript) of the transport properties of the $NdScSiH_{1.5}$ show that hydrogen may have an interesting effect on the electronic transport properties of the parent material. Thus we have also investigated the transport properties of GdScGe and its hydride to examine this further.

3.4.1. Hydrogenation of GdScGe

Hydrogenation was performed on two samples of GdScGe at 523 K under 40 bars (sample 1) and 5 bars (sample 2) respectively. Figure 3. 18. shows the hydrogen absorption curves for GdScGe (sample 2) and GdTiGe (for comparison) at 5 bars of H_2 pressure. The high pressure used for sample 1 caused a small leak in the apparatus and so the curve is not shown here. Both curves saturate at approximately 1 atom of hydrogen per formula unit. This is in contrast to the 1.5 hydrogen atoms per formula unit that we have observed for the filled CeScSi-type hydrides of CeTiGe and NdScSi.

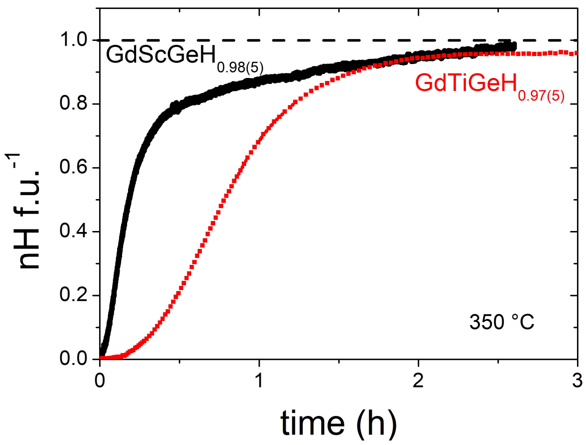

Figure 3. 18. Hydrogen absorption curves for GdScGe (sample 2) and GdTiGe.

3.4.2. Crystal Structure of GdScGeH

PXRD patterns were collected at room temperature for both samples of the GdScGeH. These measurements show that both compounds possess the same unit cell parameters and structure with the sole difference being a significant reduction of the crystallinity of sample 1 as compared to sample 2. This is attributed to the much higher pressure used during its hydrogenation and, as the two samples possess the same unit cell parameters, sample 2 has been used for most of the detailed analysis given its superior crystallinity. The powder pattern for this sample was collected over the course of 3 days using the high resolution apparatus described in chapter 2. A larger than normal background noise is present due to the presence of Gd metal. Investigation of the powder pattern shows the presence of the target GdScGeH as the main phase and $(Gd_{2.42}Sc_{2.58})_5Ge_3$ as a secondary phase which was determined to comprise approximately 4 wt. % of the sample. This is the germanium analogue of $Gd_{5-x}Sc_xSi_3$, described by Morozkin and Welter, (2002) during their study of the Gd-Sc-Si ternary phase diagram. The peak marked with (*) shows the presence of ScO which was also present in the parent compound and the Sc metal used in the synthesis. The presence of this oxide phase appears to have a positive effect on the activation of the sample during hydrogenation that requires further investigation. Analysis of the XRD powder pattern of GdScGeH sample 1 using the Rietveld method and the Jana2006 software package is provided in Figure 3. 19. and the refined positions and U_{iso} values of the metal atoms are given in Table 3. 7. For comparison, the crystal structure of GdScGe is provided in Table 3. 8. The composition given by the hydrogen absorption measurements of $GdScGeH_{1.0}$ implies that hydrogen only occupies the rare earth tetrahedral sites. The refinement provides a good fit of the experimental data with the reliability factors R_p/R_{wp} = 4.13/5.53 % and the Bragg R-factor =8.9 %.

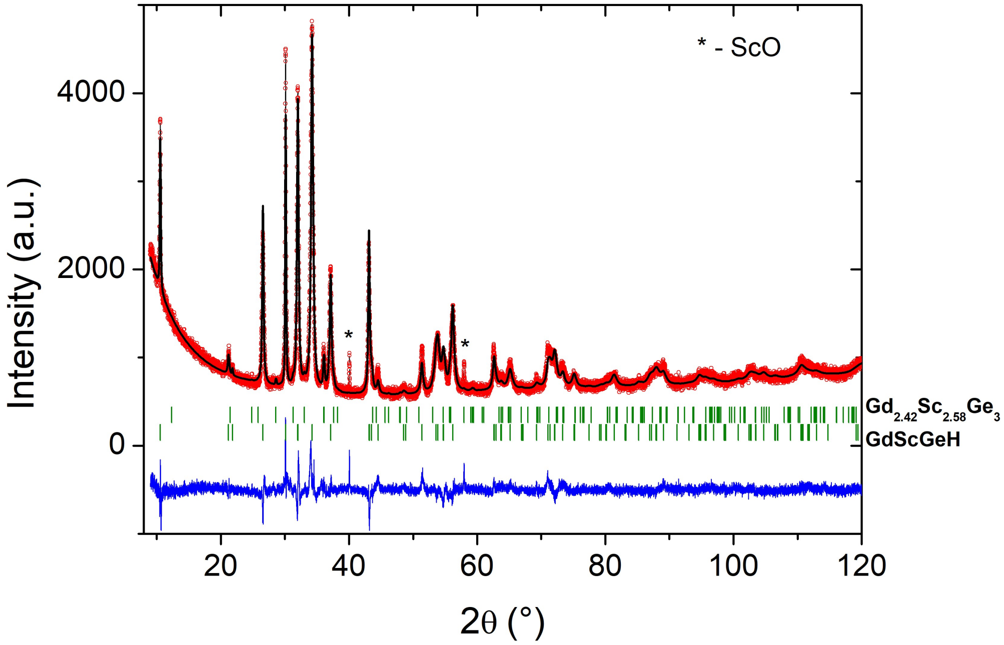

Figure 3. 19. Rietveld refinement of GdScGeH XRD powder pattern. The narrow peak marked by an asterisk corresponds to ScO impurity.

Table 3. 7. Refined atomic coordinates and isotropic atomic displacement parameters (Å^2) for the metal atoms in GdScGeH (space group *I4/mmm*). For comparison, the crystal structure of GdScGe as published by Morozkin *et al.*, (1998)b* is also given.

Phase	Atom	Site	x	y	z	B_{iso} (Å^2)
GdScGe*	Gd	4*e*	0	0	0.322(2)	-
	Sc	4*c*	0	1/2	0	-
	Ge	4*e*	0	0	0.128(2)	-
GdScGeH	Gd	4*e*	0	0	0.3155(5)	0.9(2)
	Sc	4*c*	0	1/2	0	0.9
	Ge	4*e*	0	0	0.1162(7)	0.9

Table 3. 8. The unit cell parameters of GdScGe and GdScGeH.

Phase	*a* (Å)	*c* (Å)	R-Bragg (%)	R_p	R_{wp}
GdScGe$^+$	4.2527(6)	15.563(3)	-	-	-
GdScGeH	4.192(2)	16.740(8)	8.9	4.1	5.5

$^+$Morozkin *et al.*, (1998)b

Hydrogenation causes an anisotropic expansion of the unit cell with the *a* parameter shrinking (from 4.2527(6) Å to 4.192(2) Å) while the *c* parameter strongly increases (from 15.563(3) Å to 16.740(8) Å). We observe an overall expansion of the unit cell volume from 281.5 Å^3 to 294.2 Å^3. The filling of the tetrahedral sites also causes the Gd and Ge atoms to shift along the *c* axis from z_{Ge} =0.1162(7) to 0.128(2) and z_{Gd} to change from 0.322(2) to 0.3155(5). Thus, interatomic distances are significantly modified (given in Table 3. 9.). In particular, the distances within the Gd_4 and Sc_4Ge_4 layers decrease whereas the distances between these layers increase. For example, the distance between Gd atoms located in successive layers of tetrahedra increases significantly from 5.51 Å to 6.18 Å. This suggests that the dimensionality of the crystal structure is reduced by hydrogenation of GdScGe as previously described in the case of NdScSi.

Table 3. 9. Interatomic distances (Å) in the structures of GdScGe and GdScGeH.

Atom1	Atom 2	GdScGe*	GdScGeH
Gd	**Ge**	3.108	3.177(5)
	Ge	3.054	3.336(15)
	Sc	3.480	3.733(7)
	Gd	3.768	3.687(7)
	Gd	4.253	4.192(2)
Sc	**Ge**	2.900	2.860(8)
	Sc	3.007	2.964(1)
Ge	**Sc**	2.900	2.860(8)
	Gd	3.108	3.177(5)
	Gd	3.054	3.336(15)

*Couillaud *et al.*, (2011)

3.4.3. Magnetic properties of GdScGeH

As mentioned, pristine GdScGe is a ferromagnet below T_C = 350 K (Manfrinetti *et al.*, (2002); Morozkin and Welter, (2002); Couillaud *et al.*, (2011)). Like the other compounds studied over the course of our work on the hydrogenation of CeScSi-type materials, hydrogen insertion has a pronounced effect on the magnetic properties of this system.

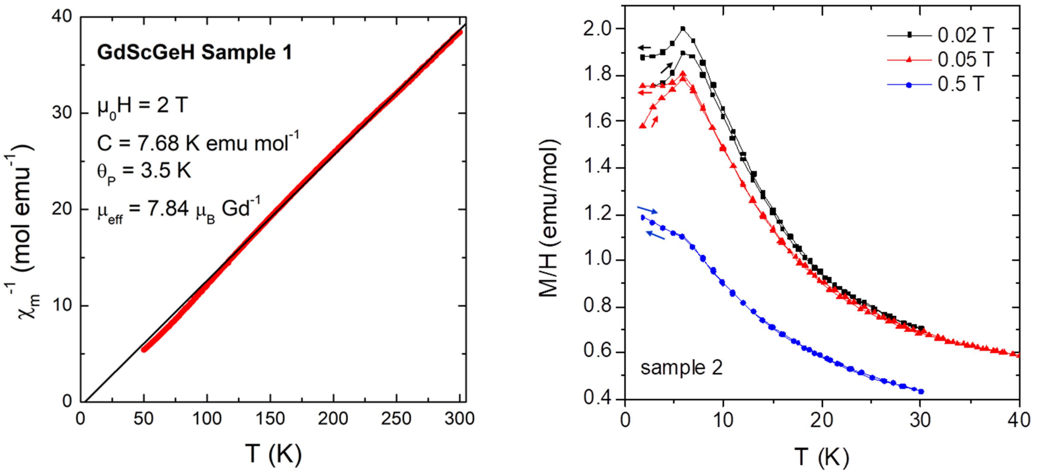

Figure 3. 20. Left) temperature dependence, measured for an applied field of 2 T, of the reciprocal magnetic susceptibility χ_m^{-1} for the GdScGeH hydride. The black line shows the fit with the Curie-Weiss law. Right) temperature dependence of the magnetization, M, of GdScGeH (sample 2) divided by the applied magnetic fields μ_0H. ZFC and FC processes are indicated by arrows towards higher and lower temperatures, respectively

The temperature dependence of the reciprocal magnetic susceptibility, χ_m^{-1}, in a magnetic field of 2 T, fitted using the Curie-Weiss law is plotted in Figure 3. 20. (left). The estimated effective moment, μ_{eff}, is found to be 7.84 μ_B f.u.$^{-1}$. This is slightly smaller than the free-ion moment of the Gd^{3+} ion (7.94 μ_B), showing that only the Gd atoms are magnetic in GdScGeH. The θ_P value of 3.5 K is weakly positive, evidencing mainly ferromagnetic exchange interactions. The temperature dependence of the magnetisation divided by the applied magnetic field is shown in Figure 3. 20. (right). Arrows indicate the zero field cooled and field cooled arms of the curves by pointing to higher and lower temperatures respectively. These magnetic measurements clearly reveal drastic modifications in comparison with the pristine compound. The lowest field measurements show a maximum at 6 K which transforms into a kink in an applied field of 0.5 T. This indicates a magnetic transition at this temperature, below which, there is a slight separation between the ZFC and FC curves. This behaviour may indicate an antiferromagnetic, canted ferromagnetic, or ferrimagnetic ordering. The magnetisation *vs.* field curve (M(H)) at 30 and 1.8 K are shown in Figure 3. 21. A small ferromagnetic signal is still observed in the M(H) curve at 30 K which arises due to a small quantity of residual pristine GdScGe. The non-linear behaviour of M(H) at 1.8 K excludes a simple antiferromagnetic order. The application of increasing field seems to gradually change the initial state into a ferromagnetic one. Furthermore, the magnetisation value at 7 T is close to 7 μ_B f.u.$^{-1}$ evidencing that the material is close to saturation (μ_{Gd3+} = 7.0 μ_B). This behaviour is similar for example to that of Gd_5Si_3 which is believed to be helimagnetic (Ganapathy *et al.*, (1976)). All these measurements suggest that GdScGeH has a complex magnetic behaviour whose exact nature remains unclear so far. Electronic structure calculations using the density functional theory are underway, but at the time of writing these have not been completed. However, preliminary DFT calculations seem to indicate that the strong reduction of the magnetic order does not arise from a volume or a charge transfer effect but from the chemical bonding with hydrogen.

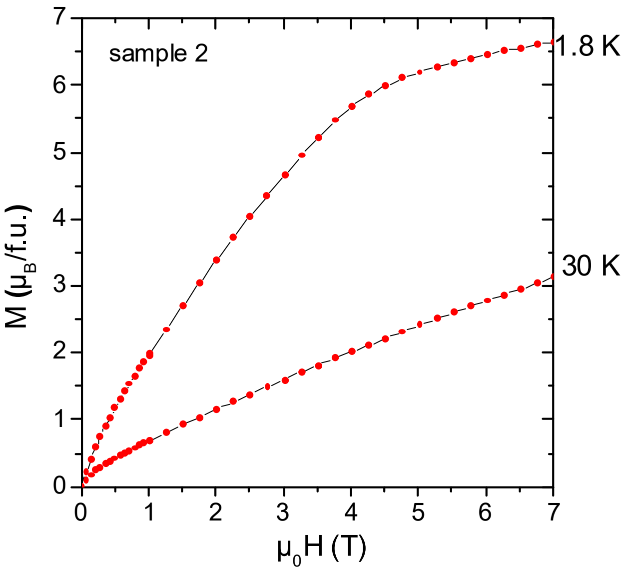

Figure 3. 21. Isothermal magnetisation curves of GdScGeH (sample 2) at 1.8 K and 30 K.

The results of the specific heat, C_P, investigations for GdScGeH (sample 2) are presented in Figure 3. 22. (top). The temperature dependence of this curve in the absence of an applied magnetic field reveals the presence of a sharp λ-peak at 6 K, showing the magnetic transition (see Figure 3. 22. (bottom)). This is consistent with the magnetisation measurements (Figure 3. 20). In order to accurately extract the magnetic contribution ($C_m(T)$) to the total specific heat using the formula $C_p = C_{el} + C_{ph} + C_m$, with C_{el} and C_{ph} the electronic and the phonon contributions, we first evaluated $C_{el}(T)$ and $C_{ph}(T)$. To evaluate these two contributions we measured the specific heat of the nonmagnetic isotype compound LaScGeH, assuming that $C_{el}(T)$ and $C_{ph}(T)$ are very close for both compounds. At low temperature, $C_{el}(T)+ C_{ph}(T) = \gamma T + \beta T^3$ with γ the Sommerfeld coefficient and $\beta=12\pi^4 nR/(5\theta_D^3)$ where n = number of atoms per formula unit, R = gas constant and θ_D the Debye temperature. By plotting Cp/T vs T^2 for LaScGeH (inset of Figure 3. 22. (bottom)), we observe a linear variation of the curve whose fit between T = 2 and 11 K gives γ= 4.9 mJ mol^{-1} K^{-2} and $\beta = 8.010\times10^{-4}$ J mol^{-1} K^{-4}. The β value corresponds to a Debye temperature θ_D of 273 K. We consider a similar electronic coefficient, γ, and Debye temperature for GdScGeH, even if we can expect a slightly smaller θ_D due to small mass difference between both compounds. Note that this correction mass was not performed in this data treatment.

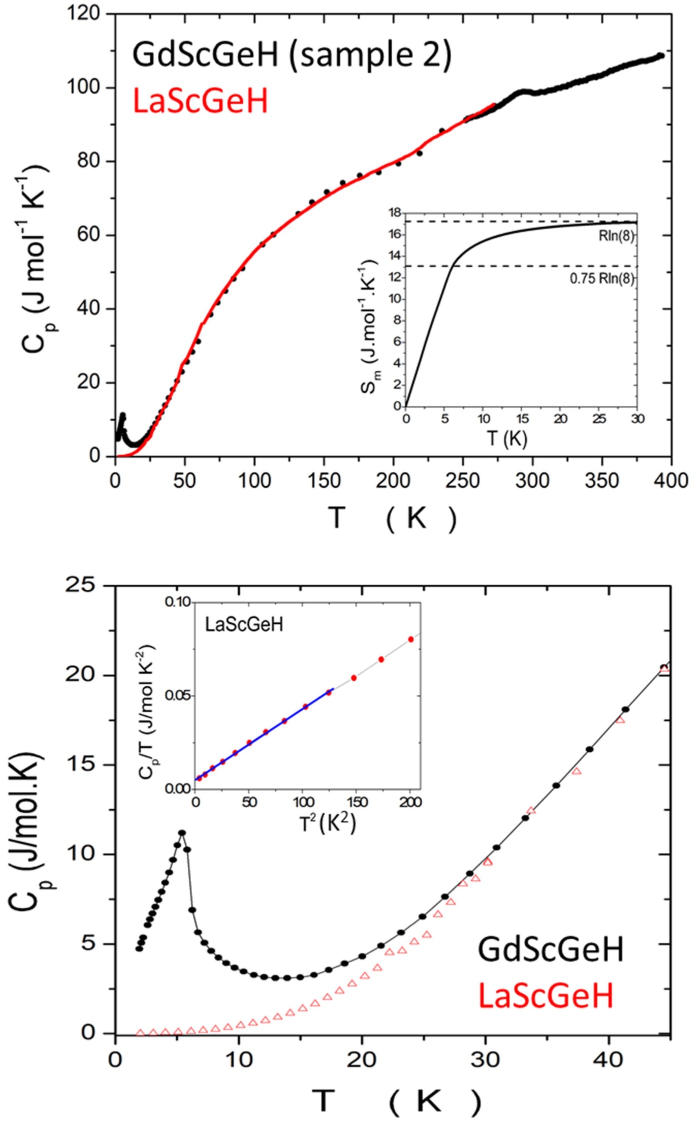

Figure 3. 22. Top) Temperature dependence of the specific heat of GdScGeH (sample 2) and LaScGeH. The insert shows the temperature evolution of the magnetic entropy S_m. Bottom) Zoom of the low temperature region of the specific heat capacity for LaScGeH and GdScGeH. The inset shows the plot of C_P/T vs T^2 for LaScGeH fitted with a linear law.

The magnetic contribution $C_m(T)$ of the Gd hydride was then determined by subtracting the electronic and the lattice contributions to the total specific heat, i.e. by subtracting the C_p curve of LaScGeH to that of GdScGeH. We obtain the magnetic entropy $S_m(T)$ by integrating $C_m(T)/T$ between 0 and T as plotted in insert of Figure 3. 22. (top). It is shown that $S_m(T)$ reaches 12.5 J.mol^{-1}.K^{-1} at the ordering temperature, *i.e.* 72% of the theoretical maximum value, Rln(2J+1) = 17.3 J mol^{-1} K^{-1}, for J = 7/2, value which is almost reached at around 30 K. Thus, this means that the total spin of Gd ion in the ground state of GdScGeH is 7/2.

3.4.4. Transport properties

The temperature dependence of the normalized resistivity ρ/ρ_{290K} of GdScGe as well as sample 1 and sample 2 hydrides are depicted in Figure 3. 23. Due to the low compactness of the pellets, *i.e*. around 75% only, we report the normalized resistivity curves. It is worth noting that the measured resistivity of the pellets is of the order of 10^{-3} Ω.cm for the pristine ($10^{-4}/10^{-5}$ Ω.cm for the bulk GdScGe) and 10^{-2} Ω.cm for the hydride. Thus, the values for the pellets can be considered as an upper limit of the intrinsic resistivity of the compounds. The pristine compound shows a metallic behaviour with $\partial\rho/\partial T > 0$ in the whole temperature range whereas both hydrides exhibit a non-metallic behaviour ($\partial\rho/\partial T < 0$) with an increase of the resistivity at low temperature. This enhancement of the resistivity at low temperature is much stronger for sample 1 than for sample 2. Hydrogenation, therefore, induces a transition from metallic to non-metallic behaviour. Preliminary DFT calculations (not presented in this manuscript) indicate that the density of states (DOS) at the Fermi level, E_F, is strongly modified through hydrogenation. More precisely, while the DOS at E_F of the pristine compound is typically that of a metal system, the DOS is much lower for GdScGeH which looks rather like a semimetal. This would be consistent with the small Sommerfeld coefficient of γ= 4.9 mJ mol^{-1} K^{-2} determined from specific heat measurements. Such modification of the DOS could thus explain the change in the conductivity behaviour of GdScGe through hydrogenation.

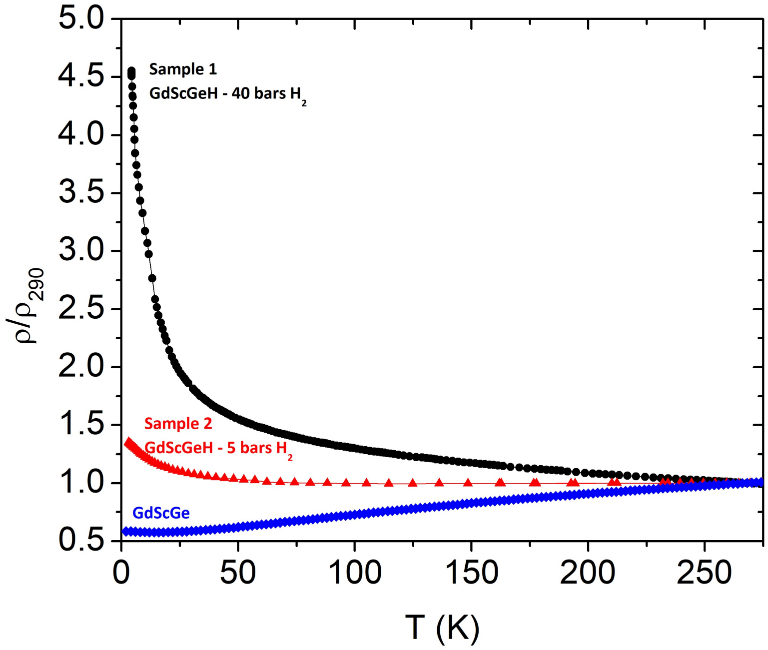

Figure 3. 23. Temperature dependence of the normalized resistivity ρ/ρ_{290K} of the pristine compound GdScGe, sample 1 and sample 2.

3.5. Effect of hydrogen on the structural and magnetic properties of RTX compounds

As we have shown, insertion of hydrogen causes and increase in the *c* parameter and a decrease in the *a* parameter of CeScSi-type materials without inducing a change in the crystal structure. This same trend is seen in the CeFeSi type materials such as those described in chapter 1. Many **c**ompounds with the hexagonal ZrNiAl structure type do not tend to undergo structural transitions either when the volume change is small with compounds with compounds like $GdNiInH_{0.5}$ (André-Filho *et al.*, (2012)), $SmNiAlH_{1.17}$ (He, (2011) and $NdNiInH_{1.7}$ (Bulyk *et al.*, (1999)). However, when the volume change is pronounced enough these materials can undergo a structural transition. An example of this is CeNiAl which transforms from the ZrNiAl type structure to the Fe_2P type structure on the formation of $CeNiAlH_{3.2}$ (Shashikala *et al.*, (2007)) or the AlB_2 type structure for $CeNiAlH_{1.93(5)}$ (Chevalier *et al.*, (2004)). The orthorhombic TiNiSi-type structure represents the most common structure type for intermetallic compounds. Hydrogenation of materials with this structure type has been shown to have a number of possible structural effects. When the amount of absorbed hydrogen is relatively small the hydrides conserve the TiNiSi-type structure for example in CeNiSnD (Yartys *et al.*, (2003)), meanwhile when the amount of absorbed hydrogen is larger it tends to induce a transition to the ZrBeSi structure type, for example: $CeNiGeH_{1.6}$ (Bobet *et al.*, (2006)) or $CeNiSnH_{1.8}$ (Chevalier *et al.*, (2004)).

After examining the effects of hydrogenation on the magnetic properties of three new CeScSi-type materials studied in this manuscript, we can compare these findings with the existing literature on these systems as well as the larger body of work that exists on the hydrogenation of intermetallic materials in general. It has been observed in the existing literature on the hydrogenation of CeScSi (Chevalier *et al.*, (2010)cb) and GdTiGe (Gaudin *et al.*, (2011)), that hydrogenation of magnetic CeScSi-type materials sharply reduces the magnetic ordering temperatures of those compounds. Indeed, the Néel temperature of CeScSi is reduced from 26 K to 3 K while the very high T_C of 376 K in GdTiGe is replaced with paramagnetic behaviour above 4 K. This trend is continued in the hydrogenation of NdScSi (T_C = 171 K (Singh *et al.*, (2004)ref)) and GdScSi (T_C = 350 K (Couillaud *et al.*, (2011)ref)) reducing the magnetic ordering temperatures to 4 K and 6 K respectively.

Generally speaking, with respect to the larger family of *RTX* intermetallics, hydrogenation may have a number of effects depending on the composition and the initial properties of the compound. In the case of magnetic materials where the magnetism derives from RKKY interactions between the rare earth elements, hydrogen insertion may cause a number of different effects based on the structural and electronic changes. Koźlak *et al.*, (2012) describe the deuteration of the LaPtSi-type TbPtIn and ErPtIn enhancing the magnetic ordering temperatures while for TmPtIn it reduces it and Pasturel *et al.*, (2005) report the complete disappearance of magnetic ordering in NdNiSi. Kolomiets *et al.*, (1999) also state that for the *R*NiAl series (*R* = rare earth element) with the ZrNiAl structure type, hydrogenation also induces a reduction of the magnetic ordering temperature. For one final example, hydrogenation of the ZrNiAl-type GdNiIn reduces the T_C of the pristine compound from 85.4(1) K to 53.3(8) K (André-Filho *et al.*, (2012)) and reduces the overall magnetic moment. Indeed this seems to be the predominant effect of hydrogenation throughout the literature with a few exceptions such as those described in chapter 1 for CeFeSi-type compounds.

Cerium is a non-standard rare earth element which can exhibit a range of interesting properties that the other, more standard, rare earth elements do not. Therefore special consideration should be given to the Ce-based materials. The insertion of hydrogen into the heavy fermion CeTiGe appears to induce magnetism in the material although further experiments are needed to determine the exact nature of the induced magnetic order. Similar effects have been seen on the insertion of hydrogen into other heavy fermion systems such as the CeFeSi-type CeRuSi (Chevalier *et al.*, (2008)) or the TiNiSi-type CeNiSn (Yartys *et al.*, (2003)). Hydrogenation of cerium compounds with an intermediate Ce valence, such as the ZrNiAl-type CeRhSn, stabilises the trivalent Ce^{3+} state. CeRhSn absorbs H to produce $CeRhSnH_{0.8}$ with trivalent Ce atoms (Chevalier *et al.*, (2006)c). Similar effects are observed during the hydrogenation of the TiNiSi type system CeNiGe which, along with a structural transition to the ZrBeSi type structure, sees a stabilisation of the trivalent cerium state (Chevalier *et al.*, (2004)). Several other examples of the hydrogenation of other non-magnetic Ce intermetallics have been presented in chapter 1.

3.6. Conclusions

The CeTiGe system can adopt both the CeFeSi and CeScSi structure type. The two different structures can be stabilised by different heat treatment: the CeFeSi structure type is the low temperature form and can be stabilised by annealing at 900 °C or lower while the CeScSi structure type could be stabilised by annealing at 1000 °C or higher. Hydrogenation of CeTiGe always produces the hydride with the high temperature structure regardless of starting state, causing an expansion of the unit cell with *a* decreasing and *c* strongly increasing. Neutron diffraction measurements demonstrate that the filled hydride has the $CeTiGeH_{1.5}$ composition with the hydrogen occupying the rare earth tetrahedral sites and the $CeTi_4$ square based pyramidal sites.

Neutron diffraction shows that $NdScSiH_{1.5}$ has the same structure as $CeTiGeH_{1.5}$. *In-situ* neutron diffraction during deuteration indicates that both sites fill simultaneously with no intermediate hydrides forming. The hydrogenation causes a near total destruction of the magnetism of the parent phase with the onset of magnetic order or a spin glass state below 4 K.

GdScGe absorbs only one atom of hydrogen per formula unit, in contrast to the other investigated compounds in this series. This severely reduces the magnetic order of the parent compound and, interestingly, changes the electrical transport properties from metallic to non-metallic type. In order to adequately explain this electronic structure calculations using the density functional theory are underway, but at the time of writing these have not been completed. Preliminary DFT calculations seem to indicate a strong reduction of the density of states at the Fermi level from that of a metal for GdScGe to that of a semimetal for the hydride. Also, the disappearance of the magnetic order does not arise from a volume or a charge transfer effect but from the chemical bonding with hydrogen.

While hydrogenation clearly has a marked effect on the magnetic properties, from the measurements we present here, we are unable to unambiguously determine the type of magnetic order present in the $CeTiGeH_{1.5}$, $NdScSiH_{1.5}$ and $GdScGeH_{1.0}$ hydrides. Further measurements are required to definitively determine the magnetic ground state of these compounds.

3.6. Bibliography

André-Filho, J., Lapolli, A. L., Coaquira, J. A. H., Mestnik-Filho, J., Carbonari, A. W., ((2012)) 'Structural and magnetic modifications induced by hydrogen atoms occupying interstitial sites in GdNiInH0.5 compound', *Journal of Alloys and Compounds*, 545, pp. 63–66. doi: 10.1016/j.jallcom.2012.08.042.

Bobet, J.-L., Pasturel, M. and Chevalier, B. ((2006)) 'Relationship between structure and sorption kinetic behaviour for ternary CeMX compounds', *Intermetallics*., 14(5), pp. 544–550. doi: 10.1016/j.intermet.2005.09.009.

Brinks, H. W., Yartys, V. A. and Hauback, B. C. ((2001)) 'Crystal structure of TbNiSiD1.78', *Journal of Alloys and Compounds*, 322(1–2), pp. 160–165. doi: 10.1016/S0925-8388(01)01013-1.

Bulyk, I. I., Yartys, V. A., Denys, R. V., Kalychak, Ya. M., Harris, I. R. ((1999)) 'Hydrides of the RNiIn (R=La, Ce, Nd) intermetallic compounds: crystallographic characterisation and thermal stability', *Journal of Alloys and Compounds*, 284(1–2), pp. 256–261. doi: 10.1016/S0925-8388(98)00953-0.

Chevalier, B. Pasturel, M., Bobet, J-L., Decourt, R., Etourneau, J., Isnard, O., Sanchez Marcos, J., Rodriguez Fernandez, J., ((2004)) 'Hydrogenation of the ternary compounds CeNiX (X = Al, Ga, In, Si, Ge and Sn): Influence on the valence state of cerium', *Journal of Alloys and Compounds*, 383(1–2), pp. 4–9. doi: 10.1016/j.jallcom.2004.04.006.

Chevalier, B., Gaudin, E., Tencé, S., Malaman, B., Fernandez, J. R., André, G. and Coqblin, B. ((2008)) 'Hydrogenation inducing antiferromagnetism in the heavy-fermion ternary silicide CeRuSi', *Physical Review B - Condensed Matter and Materials Physics*, 77(1), pp. 1–10. doi: 10.1103/PhysRevB.77.014414.

Chevalier, B., Hermes, W., Gaudin, E. and Pöttgen, R. ((2010)a) 'New high temperature modification of CeTiGe: structural characterization and physical properties', *Journal of Physics: Condensed Matter*, 22(14), p. 146003. doi: 10.1088/0953-8984/22/14/146003.

Chevalier, B., Hermes, W., Heying, B., Rodewald, U. C., Hammerschmidt, A., Matar, S. F., Gaudin, E. and Pöttgen, R. ((2010)b) 'New Hydrides REScSiH and REScGeH (RE = La, Ce): Structure, Magnetism, and Chemical Bonding', *Chemistry of Materials*, 22(17), pp. 5013–5021. doi: 10.1021/cm101290f.

Chevalier, B. and Matar, S. F. ((2004)) 'Effect of H insertion on the magnetic, electronic, and structural properties of CeCoSi', *Physical Review B,* 70(17), p. 174408. doi: 10.1103/physrevb.70.174408.

Chevalier, B., Matar, S. F., Ménétrier, M., Marcos, J. S., Fernandez, J. R. and Rodriguez Fernandez, J. ((2006)) 'Influence of Ce-H bonding on the physical properties of the hydrides $CeCoSiH_{(1.0)}$ and $CeCoGeH_{(1.0)}$.', *Journal of physics. Condensed matter*, 18(26), pp. 6045–56. doi: 10.1088/0953-8984/18/26/022.

Chevalier, B., Tencé, S., André, G., Matar, S. F. and Gaudin, E. ((2010)c) 'From antiferromagnetic to ferromagnetic ordering induced by hydrogenation of the compounds NdCoSi and NdCoGe', *Journal of Physics: Conference Series*, 200(3), p. 32012. doi: 10.1088/1742-6596/200/3/032012.

Chevalier, B., Tencé, S., Gaudin, E., Matar, S. F. and Bobet, J.-L. L. ((2009)) 'Various magnetic behaviors of the hydrides deriving from the tetragonal CeFeSi-type compounds', *Journal of Alloys and Compounds*, 480(1), pp. 43–45. doi: 10.1016/j.jallcom.2008.09.183.

Couillaud, S., Gaudin, E., Franco, V., Conde, A., Pöttgen, R., Heying, B., Rodewald, U. C. U. C. and

Chevalier, B. ((2011)) 'The magnetocaloric properties of GdScSi and GdScGe', *Intermetallics*, 19(10), pp. 1573–1578. doi: 10.1016/j.intermet.2011.06.001.

Deppe, M., Caroca-Canales, N., Hartmann, S., Oeschler, N. and Geibel, C. ((2009)) 'New non-magnetically ordered heavy-fermion system CeTiGe', *Journal of Physics: Condensed Matter*, 21(20), p. 206001. doi: 10.1088/0953-8984/21/20/206001.

Deppe, M., Lausberg, S., Weickert, F., Brando, M., Skourski, Y., Caroca-Canales, N., Geibel, C. and Steglich, F. ((2012)) 'Pronounced first-order metamagnetic transition in the paramagnetic heavy-fermion system CeTiGe', *Physical Review B,* 85(6). doi: 10.1103/physrevB.85.060401.

Flacau, R., Bolduc, J., Bibienne, T., Huot, J. and Fritzsche, H. ((2012)) 'Performance of Cu-coated vanadium cans for in situ neutron powder diffraction experiments on hydrogen storage materials', *Journal of Applied Crystallography*, 45(5), pp. 902–905. doi: 10.1107/S002188981202938X.

Ganapathy, E. V., Kugimiya, K., Steinfink, H. and Tchernev, D. I. ((1976)) 'Magnetic properties of some rare earth silicides: GdSi, Gd_5Si_3, $Dy_{5-x}Nd_xSi_3$', *Journal of The Less-Common Metals*, pp. 245–258. doi: 10.1016/0022-5088(76)90139-9.

Gaudin, E., Matar, S. F., Pöttgen, R., Eul, M. and Chevalier, B. ((2011)) 'Drastic Change of the Ferromagnetic Properties of the Ternary Germanide GdTiGe through Hydrogen Insertion', *Inorganic Chemistry* (ACS), 50(21), pp. 11046–11054. doi: 10.1021/ic201579r.

He, L. ((2011)) 'Zero-magnetization ferromagnet induced by hydrogenation', *Solid State Communications*, 151(14–15), pp. 985–987. doi: 10.1016/j.ssc.2011.05.004.

Kammler, D. R., Rodriguez, M. A., Tissot, R. G., Brown, D. W., Clausen, B. and Sisneros, T. A. ((2008)) 'In-Situ Time-of-Flight Neutron Diffraction Study of High-Temperature Phase Transition in Elemental Scandium', *Metallurgical and Materials Transactions A* 39(12), pp. 2815–2819. doi: 10.1007/s11661-008-9642-y.

Kolomiets, A. V., Havela, L., Sechovsky, V., Andreev, A. V., Yartys, V. A., Harris, I. R., ((1999)) 'Structural and magnetic properties of equiatomic rare-earth ternaries', International Journal of Hydrogen Energy, 24(2), pp. 119–127. doi: 10.1016/S0360-3199(98)00067-6.

Korst, W. L. and Warf, J. C. ((1966)) 'Rare Earth-Hydrogen Systems. I. Structural and Thermodynamic Properties', *Inorganic Chemistry*, 5(10), pp. 1719–1726. doi: 10.1021/ic50044a018.

Koźlak, K., Gondek, L., Przewoznik, J., Szytula, A. ((2012)) 'Structural and magnetic studies on RPtIn deuterides (R=Tb, Er, Tm)', *Solid State Communications,* 152(14), pp. 1234–1236. doi: 10.1016/j.ssc.2012.04.033.

Kurisu, M., Mitsumata, T. and Oguro, I. ((1999)) 'Dense Kondo compound Ce_5Ge_3', *Physica B: Condensed Matter,* 259–261(1), pp. 96–98. doi: 10.1016/S0921-4526(98)01041-2.

Manfrinetti, P., Pani, M., Palenzona, A., Dhar, S. K. and Singh, S. K. ((2002)) 'Single crystal study of the high-Curie-temperature ferromagnet $Gd_{1.02}Sc_{0.98}Ge$ and of $Gd_{2.38}Sc_{2.62}Ge_3$', *Journal of Alloys and Compounds*, 334(1–2), pp. 9–13. doi: 10.1016/S0925-8388(01)01752-2.

Mayer, J. M., Schneemeyer, L. F., Siegrist, T., Waszczak, J. V and Van Dover, B. ((1992)) 'New Layered Iron-Lanthanum-Oxide-Sulfide and -Selenide Phases: $Fe_2La_2O_3E_2$ (E = S, Se)', *Angewandte Chemie International Edition in English*, 31(12), pp. 1645–1647. doi: 10.1002/anie.199216451.

Meissner, W. and Ochsenfeld, R. ((1933)) ‘Ein neuer Effekt bei Eintritt der Supraleitfahigkeit’, *Die Naturwissenschaften,* 21(44), pp. 787–788. doi: 10.1007/BF01504252.

Mokra, I. R. and Bodak, O. I. ((1979)) ‘Crystal structure of the cerium scandium silicide’, *Dopovidi Akademii Nauk Ukrains’koi RSR, Seriya A: Fiziko-Matematichni Ta Tekhnichni Nauki*, 41(3), pp. 312–315.

Morozkin, A. V., Seropegin, Y. D. D., Leonov, A. V., Sviridov, I. A., Tskhadadze, I. A. and Nikitin, S. A. ((1998)a) ‘Crystallographic data of new ternary CeFeSi-type RTiGe (R=Y, Gd-Tm) compounds’, *Journal of Alloys and Compounds*, 267(1–2), pp. L14–L15. doi: 10.1016/S0925-8388(97)00473-8.

Morozkin, A. V., Seropegin, Y. D. D. and Sviridov, I. A. ((1999)) ‘New ternary CeFeSi-type RTiGe (R=La, Ce, Sm) compounds’, *Journal of Alloys and Compounds*, 285(1–2 Complete), pp. 283–285. doi: 10.1016/S0925-8388(98)01046-9.

Morozkin, A. V., Seropegin, Y. D., Portnoy, V. K., Leonov, A. V. and Sviridov, I. A. ((1998)b) ‘Crystallographic data of new ternary La_2Sb-type GdScSi, GdScGe, TbScGe compounds, Ti_5Ga_4-type RScSi (R=Tb-Tm) and RScGe (R=Dy-Tm) compounds’, *Journal of Alloys and Compounds*, 278(1–2), pp. L1–L5. doi: 10.1016/S0925-8388(98)00563-5.

Morozkin, A. V., Viting, L. M., Sviridov, I. A. and Tskhadadze, I. A. ((2000)) ‘CeScSi- and CeFeSi-type structures in compounds derived from GdTiGe’, *Journal of Alloys and Compounds*, 297(1–2), pp. 168–175. doi: 10.1016/S0925-8388(99)00583-6.

Morozkin, A. V. and Welter, R. ((2002)) ‘Phase equilibria in the Gd-Sc-Si and Tb-Sc-Si systems at 1100 K’, *Journal of Alloys and Compounds*, 336(1–2), pp. 202–205. doi: 10.1016/S0925-8388(01)01892-8.

Nikitin, S. A., Tskhadadze, I. A., Telegina, I. V., Morozkin, A. V. and Seropegin, Y. D. D. ((1998)) ‘Magnetic properties of RTiGe compounds’, *Journal of Magnetism and Magnetic Materials*, 182(3), pp. 375–380. doi: 10.1016/S0304-8853(97)01036-6.

Pasturel, M., Weill, F., Vourée, F., Bobet, J-L. and Chevalier, B. ((2005)) ‘Hydrogenation of the ternary silicides RENiSi (RE = Ce, Nd) crystallizing in the tetragonal LaPtSi-type structure’, *Journal of Alloys and Compounds*, 397(1–2), pp. 17–22. doi: 10.1016/j.jallcom.2005.01.015.

Rundqvist, S., Tellgren, R. and Andersson, Y. ((1984)) ‘Hydrogen and Deuterieum in transition metal-p element compounds: crystal chemical aspects of interstitial solubility and hydride phase formation’, *Journal of the Less Common Metals*, 101, pp. 145–168. doi: 10.1016/0022-5088(84)90092-4.

Sears, V. F. ((1992)) ‘Neutron scattering lengths and cross sections’, *Neutron News*, 3(3), pp. 26–37. doi: 10.1080/10448639208218770.

Shashikala, K., Sathya;oorthy, A., Raj. P., Yelon, W. B., Malik, S. K. et al. ((2007)) ‘Hydrogen absorption in CeNiAl: Formation of crystalline and amorphous hydride phases’*, Journal of Alloys and Compounds*. 438(1–2), pp. 84–87. doi: 10.1016/j.jallcom.2006.07.118.

Singh, S. K., Dhar, S. K., Manfrinetti, P., Palenzona, A. and Mazzone, D. ((2004)) ‘High magnetic transition temperatures in RScT (R = Pr, Nd and Sm; T = Si and Ge) compounds: Multiple spin reorientations in PrScGe’, *Journal of Magnetism and Magnetic Materials,* 269(1), pp. 113–121. doi: 10.1016/S0304-8853(03)00583-3.

Spedding, F. H., Hanak, J. J. and Daane, A. H. ((1961)) ‘High temperature allotropy and thermal expansion of the rare-earth metals', *Journal of the Less Common Metals* 3(2), pp. 110–124. doi: 10.1016/0022-5088(61)90003-0.

Tencé, S., André, G., Gaudin, E., Bonville, P., Al Alam, A. F., Matar, S. F., Hermes, W., Pöttgen, R. and Chevalier, B. ((2009)) 'Huge influence of hydrogenation on the magnetic properties and structures of the ternary silicide NdMnSi', *Journal of Applied Physics*, 106(3), p. 33910. doi: 10.1063/1.3190488.

Tencé, S., Mahon, T., Gaudin, E., Chevalier, B., Bobet, J.-L. J.-L., Flacau, R., Heying, B., Rodewald, U. C. U. C. and Pöttgen, R. ((2016)) 'Hydrogenation studies on NdScSi and NdScGe', *Journal of Solid State Chemistry*, 242, pp. 168–174. doi: 10.1016/j.jssc.2016.02.017.

Tokaychuk, Y. O., Filinchuk, Y. E., Sheptyakov, D. V. and Yvon, K. ((2008)) 'Hydrogen Absorption in Transition Metal Silicides: La_3Pd_5Si-Hydrogen System', *Inorganic Chemistry*, 47(14), pp. 6303–6313. doi: 10.1021/ic800382x.

Venturini, E. L. and Morosin, B. ((1977)) 'Low temperature anomaly in $Sc_{0.995}Gd_{0.005}H_{1.9}$', *Physics Letters A*, 61(5), pp. 326–328. doi: 10.1016/0375-9601(77)90630-2.

Welter, R., Venturini, G. and Malaman, B. ((1994)) 'High rare earth sublattice ordering temperatures in RMnSi compounds (R LaSm, Gd) studied by susceptibility measurements and neutron diffraction', *Journal of Alloys and Compounds*, 206(1), pp. 55–71. doi: 10.1016/0925-8388(94)90011-6.

Welter, R., Vernière, A., Venturini, G. and Malaman, B. ((1999)) 'High rare earth sublattice ordering temperatures in new CeFeSi-type RTiGe (R=La–Nd, Sm) compounds', *Journal of Alloys and Compounds*, 283(1–2), pp. 54–58. doi: 10.1016/S0925-8388(98)00904-9.

Westlake, D. G. ((1983)a) 'Site occupancies and stoichiometries in hydrides of intermetallic compounds: Geometric considerations', *Journal of the Less Common Metals*, 90(2), pp. 251–273. doi: 10.1016/0022-5088(83)90075-9.

Westlake, D. G. ((1983)b) 'Hydrides of intermetallic compounds: A review of stabilities, stoichiometries and preferred hydrogen sites', *Journal of the Less Common Metals*, 91(1), pp. 1–20. doi: 10.1016/0022-5088(83)90091-7.

Wied, M., Nuss, J., Hönle, W. and Schnering, H. G. von ((2011)) 'Crystal structures of tetrastrontium dibismuthide oxide, Sr_4Bi_2O, and tetrabarium dibismuthide oxide, Ba_4Bi_2O', *Zeitschrift für Kristallographie - New Crystal Structures*, 226(4), pp. 437–438. doi: 10.1524/ncrs.2011.0195.

Yartys, V. A., Harris, I. R. and Panasyuk, V. V ((1997)) 'Novel metal-hydride materials and technologies: Recent advances and further prospects', *Materials Science*, 33(4), pp. 436–449. doi: 10.1007/BF02537542.

Yartys, V. A. Ouladdiaf, B., Isnard, O., Khyzhun, O.Yu., Buschow, K. H. J. ((2003)) 'Hydrogen induced antiferromagnetism in the Kondo semimetal CeNiSn', *Journal of Alloys and Compounds*, 359(1–2), pp. 62–65. doi: 10.1016/S0925-8388(03)00207-X.

Chapter 4: The *R*Sc*X*C$_x$ carbides (*R* = La, Ce, Nd, Gd, and *X* = Si, Ge)

As seen in the previous chapter, the intermetallics crystallising in the CeFeSi structure type can only accept one atom of hydrogen per formula unit, filling the vacant tetrahedral sites. All attempts to insert carbon into these materials were unsuccessful, since we have seen no indication that carbon had been included in the structure. Indeed, in general carbon simply forms binary carbides when included in the synthesis of CeFeSi type materials such as CeFeSi and the low temperature form of CeTiGe.

The realisation that the closely related CeScSi type compounds contain a second site that is capable of accepting hydrogen atoms was therefore of great interest for our attempts to insert carbon into these kinds of materials. Furthermore, the CeScSi-type compounds, have been studied to a much lesser degree than the CeFeSi type materials. As a variant of the La_2Sb structure which is a superconductor below 5.2 K (Mizoguchi and Hosono, (2011)), the CeScSi-type compounds may also demonstrate novel changes in their physical properties on light element insertion. We thus decided that it would be interesting to attempt to insert a range of other light elements such as carbon or boron into the CeScSi family of materials. Attempts to insert boron were unsuccessful but we managed to insert carbon. In this chapter we present the results of carbon insertion, detailing the presence of a solid solution with carbon, the changes in the crystal structure, and the effect this has on the physical properties of these intermetallics.

4.1. Synthesis

The insertion of carbon into the *R*ScSi systems was attempted using a four step method. For specific details of individual synthesis techniques see chapter 2. The pristine *R*Sc*X* (R = La, Ce, Nd and Gd, X = Si and Ge) were melted together in an arc furnace using the relative molar quantities 1:1.05:1. The excess Sc is to compensate for residual ScO present in the precursor. The resulting buttons were placed in an induction furnace and the required mass of carbon, cut from graphite pellets, was placed on top. The carbon was amalgamated slowly into the intermetallic button by heating slowly and the final liquid product was held liquid for one minute to ensure good mixing. During the amalgamation the formation of binary carbides is seen as the areas around the carbon pellet initially solidify. The slow temperature increase allows the dispersion and re-absorption of these zones. After melting in the induction furnace the sample was weighed before being melted 3-4 more times in the arc furnace to ensure complete melting of the binary carbides that formed during the carbon inclusion. The resulting buttons possess a silvery gray colour with a faceted surface and are stable in air. Heat treatment was carried out in a resistance furnace at 900°C inside evacuated quartz ampoules for 2 weeks. Annealing was also attempted at 800°C and

1000°C, however, the best samples were obtained for annealing at 900°C (*c.f.* Section 2.1.3).

4.2. X-Ray diffraction analysis

A portion of each button was crushed and ground for powder X-ray diffraction (PXRD) before and after annealing. In general annealing produces only a slight improvement in the crystallinity and purity of the Nd samples and a more noticeable improvement of the Ce carbide phases (especially with low carbon content). From these measurements it is seen that annealing below 900°C causes an increase in the concentration of the R_5Si_3 phase and annealing at 1000°C reduces the crystallinity and tends to increase the proportions of secondary phases present. Generally, Sc_2OC (formed from a high temperature reaction between ScO and C) is present in most samples, along with a mixture of binary *RX* compounds such as Sc_5Si_3, R_5Si_3, *R*Si and RSi_{2-x} in low concentrations as secondary phases. During the course of this work it was decided to vary the composition in order to improve the purity of the main phase. This showed that a slight excess of Sc and C could partially compensate for the formation of the parasitic Sc_2OC phase and reduce the concentration of some secondary phases. This chapter discusses samples with the nominal compositions $RScSiC_x$, $RSc_{1.05}SiC_x$, and $RSc_{1.05}XC_{0.55}$.

4.2.1. $CeScSiC_{0.5}$ and $NdScSiC_{0.5}$

The PXRD shows that the major phase in the samples with nominal composition $RSc_{1.05}XC_{0.5}$ (*R* = La, Ce, Nd, Gd, *X* = Si and Ge for *R* = Ce) crystallises in the *I4/mmm* space group. Figure 4. 1. shows a comparison between the PXRD patterns for two carbides (*R* = Ce and Nd) with their pristine compound. The peaks for both the pristine and carbide materials are well defined, indicating that the materials are well crystallised. From this image it is clear that the *hk*0 peaks are shifted to a lower angle, indicating an increase in the *a* parameter, while the 00*l* peaks are shifted to a higher angle, showing a decrease in the *c* parameter. This trend is in sharp contrast to the previously discussed hydrides (*c.f.* chapter 3) where the opposite trend in unit cell parameters (*a* decreasing and *c* increasing) is observed.

From these data it is clear that the inclusion of carbon in the synthesis has an effect on the final structure of the main phase in the samples. This is a promising indication that the carbon has indeed been included in the structure and, to be certain of this, further studies were carried out.

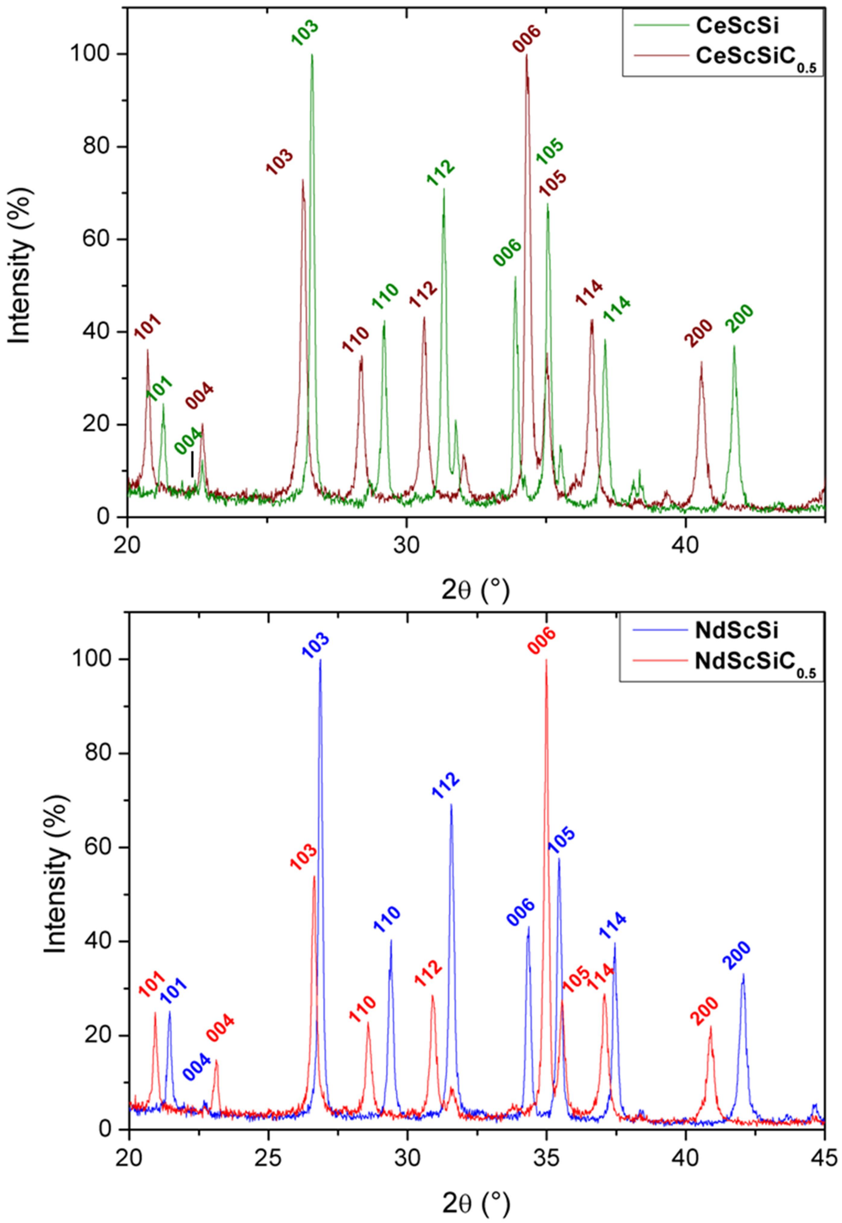

Figure 4. 1. X-ray diffraction patterns of annealed CeScSi with $CeScSiC_{0.5}$ (top) and NdScSi with $NdScSiC_{0.5}$ (bottom)

4.2.2. The existence of a solid solution

During our studies of the hydrogenation of intermetallics, we found that control over the degree of hydrogenation is very difficult. *In-situ* neutron diffraction measurements during the deuteration of NdScSi also show that there is no formation of intermediate deuteride; instead the deuteride phase grows in concentration while the pristine phase is consumed. In order to investigate if it is possible to control the amount of carbon present in the samples, the $NdScSiC_x$ and $CeScSiC_x$ systems were studied in detail. Samples with nominal composition RScSiC$_x$ and RSc$_{1.05}$SiC$_x$ (R = Ce, Nd. $0 \le x \le 1.5$) were synthesised to study how the unit cell parameters vary with changing nominal C content and the change in the unit cell parameters is shown in Figure 4. 2. for $0 \le x \le 1.0$. Trend lines have been added to more clearly show the different regions of the plots. The Nd and Ce systems behave differently as the carbon content is varied.

The Ce samples show linear variation of the unit cell parameters with nominal x until they reach a plateau around x = 0.5. This suggests the existence of a solid solution for 0 ≤ x ≤ 0.5. $CeScSiC_x$ generally needs annealing to achieve maximum concentration and purity of the target phase, especially for low C concentrations. However, the carbide phase could be stabilised for even very low nominal carbon concentrations (x = 0.1) with a corresponding change in the unit cell parameters.

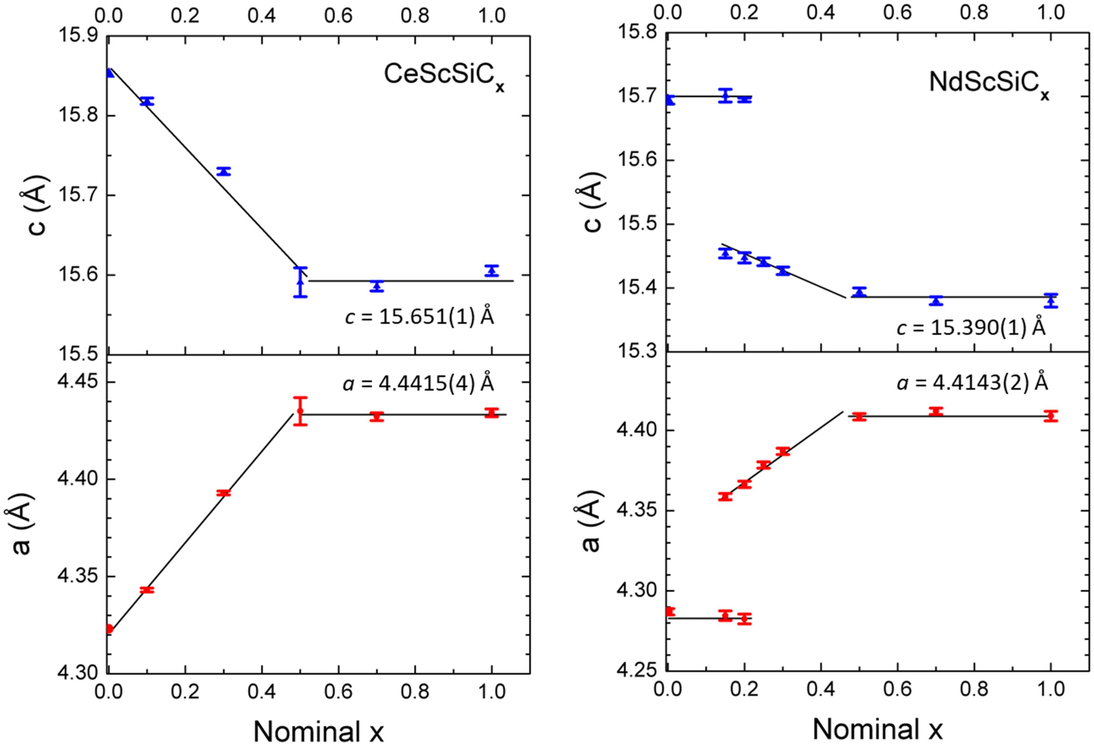

Figure 4. 2. Unit cell parameters vs. nominal carbon content of the $NdScSiC_x$ and $CeScSiC_x$ phases. Error bars show 3 σ. The lines are added as a guide to the eye and do not represent a fit of the data. The unit cell parameters at the plateaus are labelled.

For the $NdScSiC_x$ systems however, as cast samples where x < 0.25 exhibit a biphasic character (Figure 4. 2.) that could not be removed by any investigated annealing. The two phases present both crystallise in the *I4/mmm* space group with one phase having unit cell parameters that correspond to NdScSi and the other showing a decrease in the *c* and increase in the *a* parameters. The biphasic character of the Nd samples is shown by the pairs of points with the same nominal composition. The relative proportion of the pristine phase decreases steadily with increasing x until x ≈ 0.25. Beyond this composition the peaks corresponding to the pristine phase are no longer observed and the unit cell parameters of the carbide phase vary linearly, plateauing around x = 0.5 as in the Ce samples. From this it appears that $NdScSiC_x$ forms a solid solution with solubility limits 0.25 ≲ x ≤ 0.5.

Increasing the carbon content beyond x = 0.5 does not continue to affect the unit cell parameters (Figure 4. 2.) for either the Ce or Nd systems. Instead, the samples begin to show increasing quantities of binary carbides such as Sc_2C_3, ScC and R_2C_3 with reduction in the crystallinity of the RScSiC$_x$ phase. Although samples with x > 1 were synthesised, the samples mostly contain partially amorphous binary carbides and were of such poor quality that no reliable information on the RScSiC$_x$ phases could be extracted from them.

In general, we perform elemental analysis on our samples using electron microprobe analysis with wavelength dispersive spectroscopic (WDS) analysis. Figure 4. 3. shows an example of the back scattered electron (BSE) micrograph of a NdScSiC$_{0.5}$ sample with the measured compositions labelled. The carbon values measured are not physically reasonable as they indicate carbon contents that exceeded the total mass of carbon added by a significant amount. This is most likely due to carbon being very close to the limits of detection for this method, in particular when the matrix contains much heavier elements (to which the technique is more sensitive). The secondary phase seen in Figure 4. 3. is most likely NdSi as this corresponds roughly to the composition if the carbon is disregarded and this phase is observed in the PXRD pattern of this material (Figure 4. 4. c) which is discussed later. To more easily distinguish the two phases present the contrast of the image has been increased. Because of this there appear to be two different grey phases when in fact no difference in composition could be determined between them.

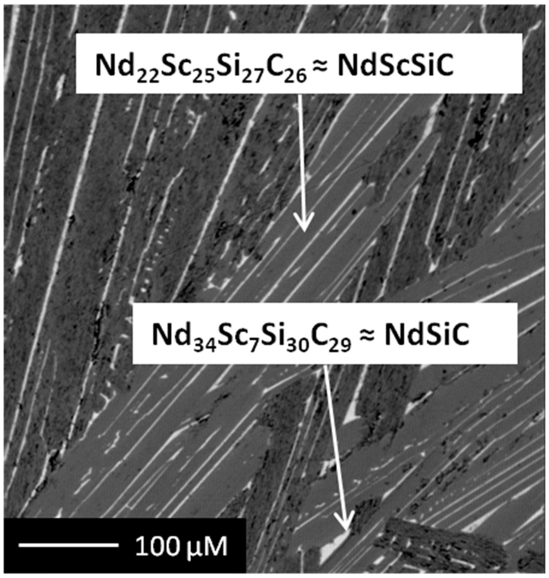

Figure 4. 3. Back scattered electron micrograph of NdScSiC$_{0.5}$ with phase compositions determined by WDS analysis. The image was taken with very high contrast to better show the two phases.

As the usual method for compositional analysis does not provide reliable data for carbon, an alternative method for the determination of the carbon content of the main phase is needed. It was decided to calculate the effective x value by first determining the total carbon content of the entire sample through combustion analysis (Described in section 2.2.5.). This showed that carbon loss during synthesis is typically small. Rietveld refinement of the PXRD patterns was then carried out on the samples to determine the relative proportions of each phase as seen in Figure 4. 4. In order to accurately assign carbon to the main phase this analysis was limited to samples containing only stoichiometric carbides as secondary phases (usually Sc_2OC). Once the relative proportions of each phase had been determined the amount of carbon needed to form the secondary carbide(s) was subtracted from the total value found for that sample. Any remaining carbon is then assumed to be part of the target *R*ScSiC$_x$ phase. The data used for these calculations are shown on the following pages in Table 4. 1. and Figure 4. 4. where the nominal composition, phases present, relative percentages given by the refinements and the respective masses of the individual samples are all summarised. For some of the refinements, due to the high degree of overlap between certain peaks the accurate refinement of each phase proved difficult and so larger error bars are used on effective x to indicate this. This applies particularly to the NdScSiC$_x$ materials with low x content where significant peak overlap makes accurate refinement difficult. Note that the calculation relies on the assumption that all secondary carbide phases are stoichiometric, that the carbon is homogeneously distributed throughout the sample and that no carbon is present in the other secondary phases. As such assumptions may not always hold true this method remains only an approximation.

The refined unit cell parameters are plotted against the calculated effective x values in Figure 4. 5. As expected, the *a* parameter increases with increasing carbon content while the *c* parameter decreases. A strong correlation between the unit cell parameters and effective x is seen. The fit line for the Nd system is extended beyond 0.25 with the dashed line and it can be seen that it intersects the point for the pristine NdScSi. Therefore, this linear relationship between the effective x and the unit cell parameters can be used to determine the carbon content in our samples.

Table 4. 1. Summary of the parameters used to calculate the effective x values plotted in Figure 4. 5. The carbon masses were determined by combustion analysis in O_2 gas.

Nominal Composition	Phases	Wt%	At %	R - Bragg	Sample mass (g)	Total mass of carbon (g)	Total carbon (mol)	Total C in 2° phases (mol)	effective x
$NdScSiC_{0.15}$	$NdScSiC_x$	54.2(3)	57.085	8.58	1.2228(3)	0.0109(5)	$9.1x10^{-4}$	$4.92x10^{-5}$	0.28(3)
	NdScSi	23.9(2)	25.461	8.80					
	Nd_2ScSi_2	20.24(7)	12.050	16.9					
	Sc_2OC	1.70(1)	5.404	7.57					
$NdScSiC_{0.3}$	$NdScSiC_x$	79.25(3)	89.42	10.5	1.0735(3)	0.0189(5)	$1.57x10^{-3}$	$8.75x10^{-4}$	0.40(2)
	NdScSi	4.83(6)	5.53	8.25					
	Nd_2ScSi_2	1.86(7)	1.19	30.3					
	$Sc_{15}C_{19}$	14.1(8)	3.88	25.4					
$NdSciC_{0.5}$	$NdScSiC_x$	94.4(3)	93.95	10.3	1.9213(3)	0.04901(6)	$4.08x10^{-3}$	----	0.50(2)
	NdSi	3.74(1)	4.82	47.6					
	Nd_2O_3	1.86(5)	1.23	35.5					
$CeScSiC_{0.1}$	$CeScSiC_x$	100	100	7.2	1.2781(3)	0.0054(2)	$4.5x10^{-4}$	----	0.08(2)
$CeSc_{1.05}SiC_{0.25}$	$CeScSiC_x$	94.3(3)	95.47	11.6	3.4339(3)	0.0406(4)	$3.4x10^{-4}$	$1.9x10^{-4}$	0.22(2)
	Sc_5Si_3	5.2(1)	3.68	35.5					
	CeC	0.59(3)	0.85	32.5					
$CeSc_{1.05}SiC_{0.5}$	$CeScSiC_x$	90.5(4)	94.83	5.72	1.0100(3)	0.0270(5)	0.017	-----	0.50(2)
	Ce_5Si_3	7.2(8)	2.08	15.3					
	CeSi	2.3(7)	3.10	16.9					

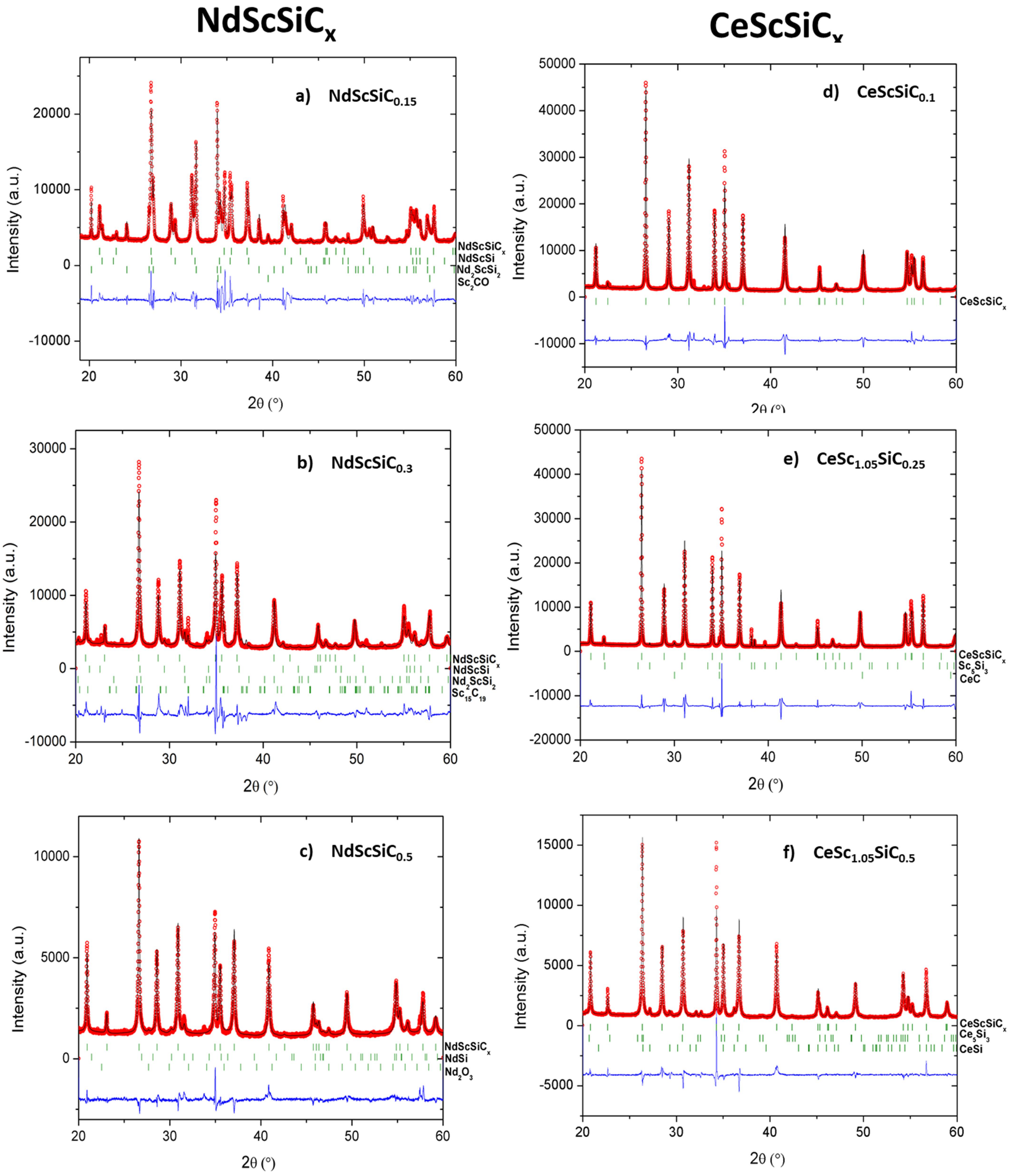

Figure 4. 4. The Rietveld refinements of PXRD data used to plot Figure 4. 5. The compositions shown in the top right of each plot correspond to the nominal compositions used for the synthesis of each sample. Each plot corresponds to one point on the Figure 4. 5. graph.

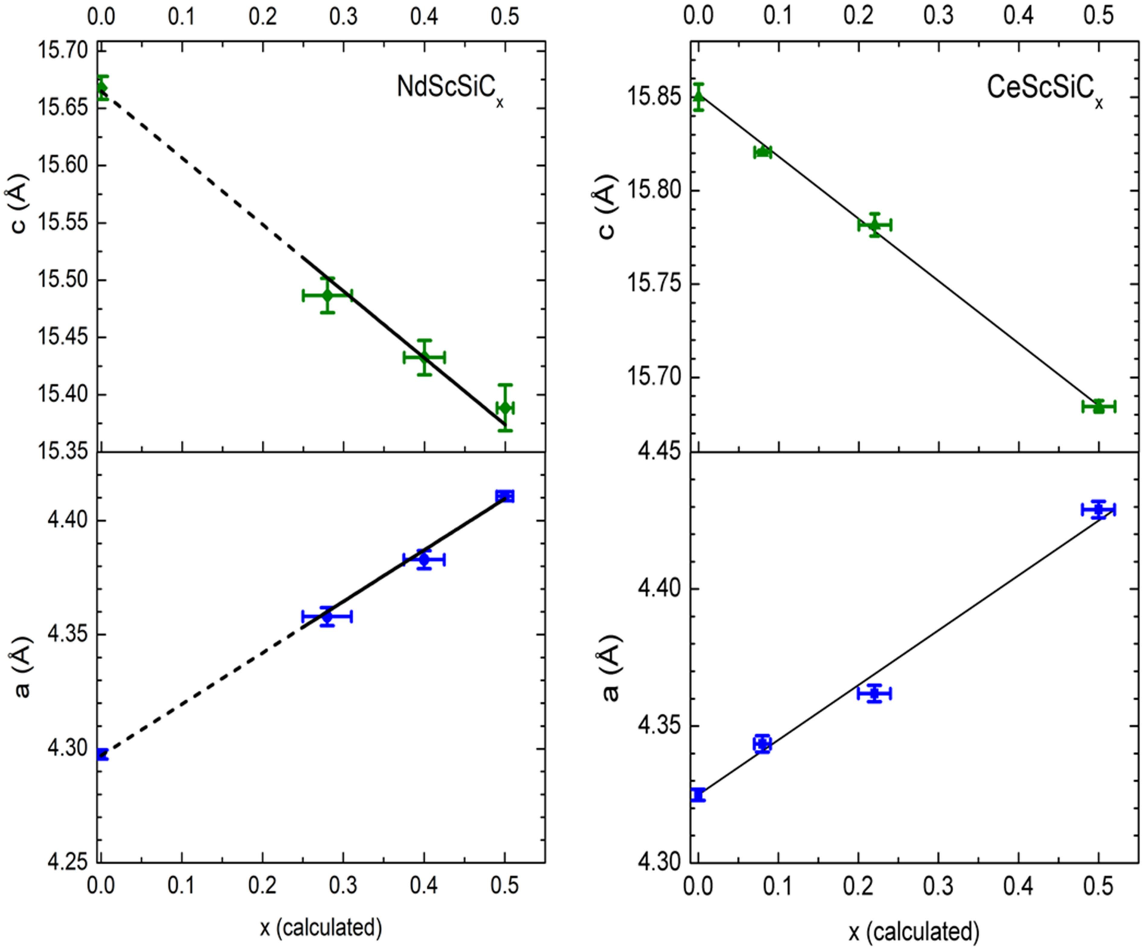

Figure 4. 5. Unit cell parameters against carbon content for the NdScSiC$_x$ (left) and CeScSiC$_x$ (right) systems. Y error bars show 3σ while x error bars show σ. The Full black lines show a linear fit of the data while the dotted black lines shows a linear extrapolation of the fit line.

From these data it can be concluded that, unlike the hydride systems described previously, the insertion of carbon into the CeScSi-type intermetallics produces a solid solution. The NdScSiC$_x$ and CeScSiC$_x$ solid solutions behave very differently in relation to their domains of existence. NdScSiC$_x$ has a composition range of $0.25 \lesssim x \leq 0.5$ while CeScSiC$_x$ exists for the full range $0 \leq x \leq 0.5$. This stoichiometry is lower than that observed for RScSiH$_{1.5}$, showing clearly that not all of the interstitial sites can be occupied by carbon.

4.2.3. Inhomogeneity in the RScSiC$_{0.5}$ system

As described, Rietveld analysis of the high resolution PXRD patterns was carried out on a number of the *R*ScSiC$_{0.5}$ (*R* = Ce and Nd) systems for phase quantification. During the course of this analysis a significant anomaly was detected in the peaks that are highly sensitive to the *c* unit cell parameter such as the (004) and (006) peaks. These peaks clearly consist of the superimposition of more than one peak with slightly different unit cell parameters. To illustrate this, the (006) peaks of three samples are shown in Figure 4. 6. For the samples with masses 1.5 and 3.5 g, the peaks show a strong anisotropic broadening, tapering off towards lower angles. For the larger 5 g sample made for neutron diffraction for the magnetic structure determination (discussed later) there is a very clear shoulder before this tapering effect. In all cases this is believed to correspond to an inhomogeneous distribution of carbon throughout the material, causing a spread of unit cell parameters. This effect is seen only as a slight broadening of the *hk*0 peaks in the diffraction pattern.

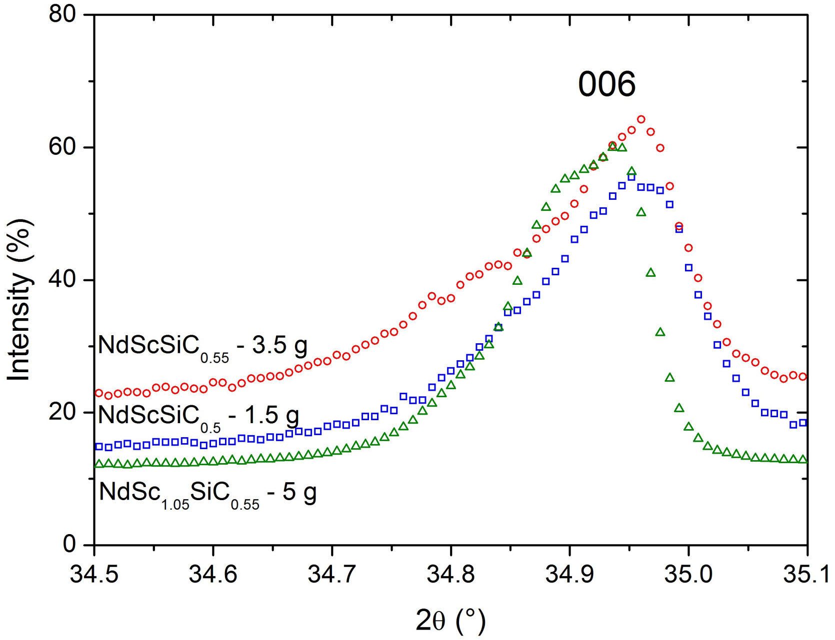

Figure 4. 6. Zoom of (006) peak (measured by XRD) of NdScSiC$_{0.5}$ for samples with marked nominal compositions and masses.

The shoulder present in the 006 peak for the 5 g sample allows a more detailed analysis of this sample as two distinct peaks can be inferred. Figure 4. 7. shows this with the two principle *c* parameters of 15.39 Å and 15.41 Å labelled. Calculation of the effective x using the *a* unit cell parameter as described in Figure 4. 5., yields x = 0.46(2). However, when the two *c* parameters are used to calculate the effective x of the two main NdScSiC$_x$ phases they lead to x = 0.48(2) and 0.44(2) respectively. Thus, the effective x calculated with the *a* parameter is clearly an average value of the different NdScSiC$_x$ phases present and we expect to observe around x = 0.46 by refinement of the neutron diffraction data later.

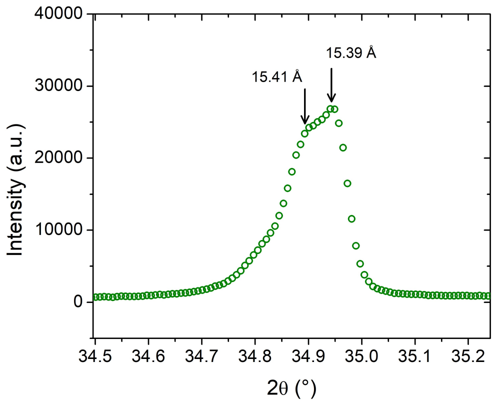

Figure 4. 7. The 006 peak of the 5g NdScSiC$_{0.5}$ (nominal composition) sample made for neutron diffraction with the two *c* parameters used in the fit of this data.

From this we decided that in order to well describe the peaks with a strong *c* component (especially the (00*l*) family of peaks), for some samples it is necessary to include multiple versions of the carbide phase with slightly (manually) varied unit cell parameters. Figure 4. 8. presents the Rietveld refinement of the PXRD pattern collected on the 3.5 g sample whose (006) peak is shown in Figure 4. 6. The two phases: a and a' have *a* parameters 4.40946(6) Å and 4.3867(2) Å and *c* parameters 15.3929 Å and 15.467 Å respectively. Due to the large degree of overlap the unit cell parameters could not be individually refined and were instead determined by manually varying the unit cell parameters to better describe the observed peaks. The details of the refinement of the two variants of the main phase can be seen in Figure 4. 8. The effective x values of each of these two phases were calculated, using the *a* unit cell parameters and Figure 4. 5., as x(a) = 0.50 and x(a') = 0.42.

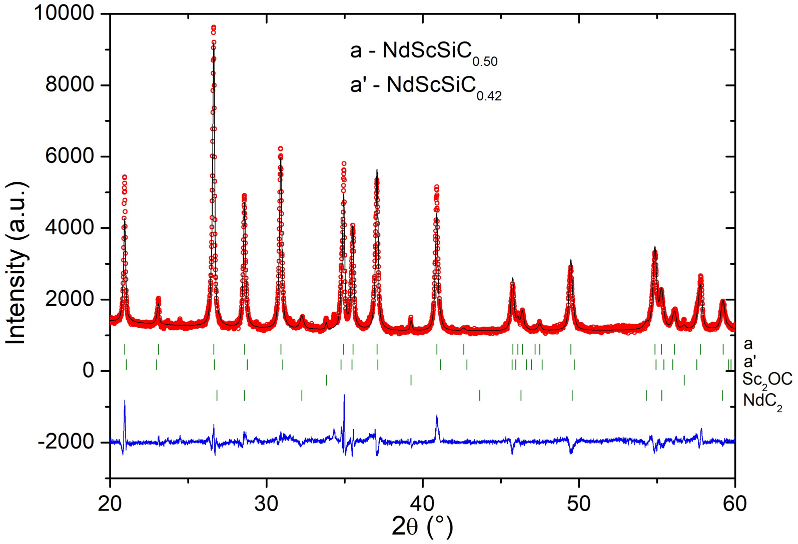

Figure 4. 8. Rietveld refinement of NdScSiC$_{0.5}$ (nominal composition) using Cu-Kα1. R-Bragg (a and a') = 7.0 and 9.7 %. The given carbon content for each phase is the calculated effective x.

Table 4. 2. Summary of the Rietveld refinement of the crystal structure of $NdScSiC_{0.5}$ shown in Figure 4. 8.

	a (Å)	*c* (Å)	V (Å^3)	z_{Nd}	z_{Si}	Occ (C)	effective x (calculated)	R – Bragg (%)	R_P (%)	R_{wp} (%)
a	4.4095	15.3929	299.2893	0.3313(5)	0.132(3)	1.00	0.50(2)	7.0	24.9	19.2
a'	4.3867	15.467	297.6336	0.3361(5)	0.134(3)	0.82	0.42(2)	9.7		

A similar, but much less pronounced, peak shape anomaly is observed in the other studied carbide systems but this will not be discussed in detail here. Figure 4. 9. shows the results of Rietveld refinement on the $CeScSiC_{0.5}$ compound with nominal composition $CeSc_{1.05}SiC_{0.55}$ and a summary can be seen in Table 4. 3. Due to the low quantity and intensity of the secondary phase peaks in the $CeScSiC_{0.5}$ sample, their relative proportions and structural properties could not be adequately refined by the Rietveld method.

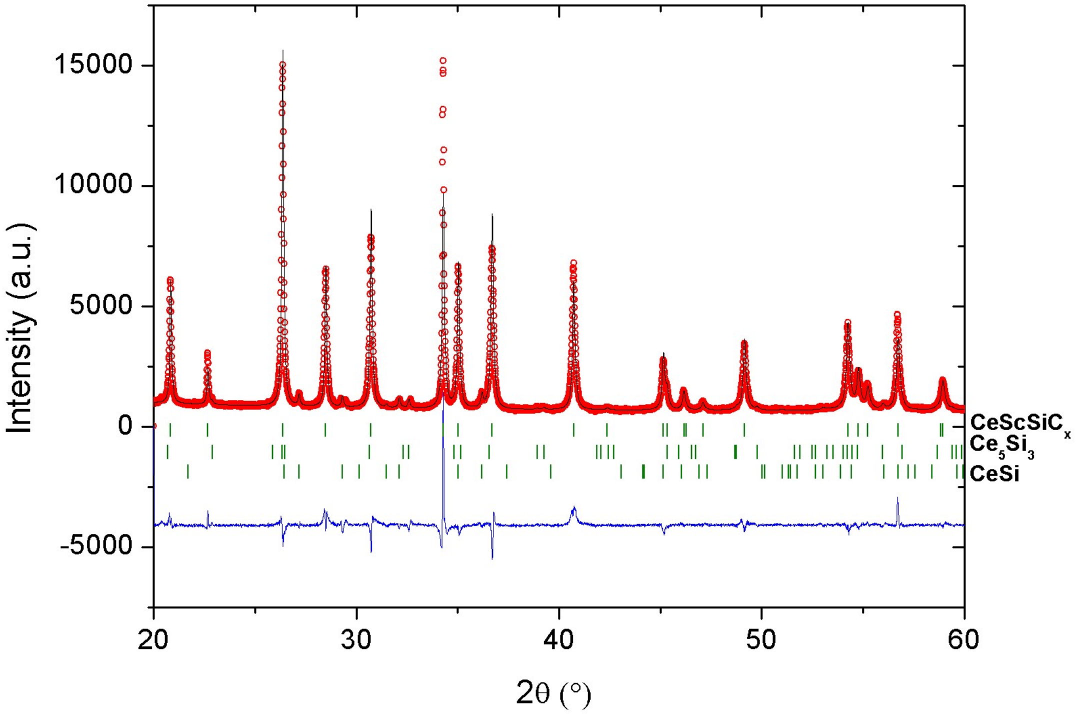

Figure 4. 9. Rietveld refinement of $CeScSiC_{0.5}$ (nominal composition). Due to their low quantities the secondary phases could not be treated by the Rietveld method and were instead fitted using full pattern matching.

Table 4. 3. Summary of the refined parameters of the major phase for the $RScSiC_{0.5}$ (R = La, Ce and Gd) from high resolution XRD data. The R_P and R_w values for the refinements are also shown.

Nominal Comp.	a (Å)	*c* (Å)	V (Å^3)	z_R	z_{Si}	R – Bragg (%)	R_P (%)	R_w (%)	Effective x
$CeScSiC_{0.5}$	4.42878(5)	15.6827(3)	301.654	0.3326(4)	0.1265(2)	5.72	16.7	17.2	0.48
$GdScSiC_{0.5}$	4.3917(1)	15.071(5)	290.675	0.3336(3)	0.1341(2)	8.52	20.8	21.2	
$LaScSiC_{0.5}$	4.45321(5)	15.8335(1)	313.9954	0.3326(1)	0.1326(1)	7.23	13.1	16.3	

A number of other compositions were studied to investigate if the carbides could be stabilised for other rare earth elements, resulting in the successful formation of *R*ScSiC$_{0.5}$ materials for all investigated rare earth elements (*R* = La, Ce, Nd and Gd.). The results of the Rietveld structural refinements for *R* = La and Gd are given in Table 4. 3. A single germanide was also successfully synthesised (CeScGeC$_{0.5}$) to determine if the carbides might also be stable for the non-silicon case. From these samples the unit cell parameters of the LaScSiC$_{0.5}$, CeScSiC$_{0.5}$, CeScGeC$_{0.5}$, NdScSiC$_{0.5}$ and GdScSiC$_{0.5}$ materials were determined and these results are all summarised in Table 4. 4. along with the unit cell parameters of their pristine analogues for comparison. This table shows that carburation always has the same effect on the unit cell parameters: the *a* parameter always increases while the *c* parameter always decreases.

Table 4. 4. Unit cell parameters of *R*Sc*X* and *R*Sc*X*C$_{0.5}$ (nominal compositions) refined from XRD data.

	a **(Å)**	***c*** **(Å)**	**V (Å^3)**	***c/a***	**reference**
LaScSi	4.3492(5)	16.020(3)	303.023	3.6834	Chevalier *et al.*, (2010)c
LaScSiC$_{0.5}$	4.4532(1)	15.834(1)	314.003	3.5556	[a]
Δ (%)	+2.39	-1.16	+3.62	-3.47	
CeScSi	4.3283(5)	15.820(2)	296.261	3.6668	Chevalier *et al.*, (2010)c
CeScSiC$_{0.5}$	4.4288(1)	15.683(1)	307.611	3.5411	[a]
Δ (%)	+2.32	-0.87	+3.83	-3.43	
CeScGe	4.342(1)	15.986(3)	298.475	3.6817	Singh *et al.*, (2001)
CeScGeC$_{0.5}$	4.4437(1)	15.635(1)	308.736	3.5185	[a]
Δ (%)	+2.34	-2.20	+3.43	-4.43	
NdScSi	4.2894(6)	15.705(3)	288.956	3.6614	Tencé *et al.*, (2016)
NdScSiC$_{0.5}$*	4.4107(4)	15.389(1)	299.382	3.4890	[a]
Δ (%)	+2.72	-1.77	+3.60	-4.64	
GdScSi	4.2556(5)	15.542(3)	281.468	3.6521	Couillaud *et al.*, (2011)
GdScSiC$_{0.5}$	4.3917(1)	15.071(5)	290.675	3.4317	[a]
Δ (%)	+3.20	-3.03	+3.27	-4.03	

[a] **This work** * from single crystal measurements

4.3. Structural characterisation

As the carbide solid solutions only exist up to x = 0.5, a more rigorous investigation of the structure is needed to determine what site(s) are occupied by carbon and also their degree of occupation. We investigated this using both single crystal XRD and neutron diffraction. These techniques provide powerful, complementary, routes for the determination of crystal structures that contain light elements.

4.3.1. Single Crystal X-ray diffraction

Single crystal X-ray diffraction remains the gold standard for solid structure determination. This is because a lot of the useful information from a diffraction pattern (such as precise integrated intensities which can provide the structure factor) is lost when moving from the 3D single crystal diffraction to 1D powder diffraction. For this measurement a sample with nominal composition NdScSiC$_{0.5}$ was gently crushed and a useable single crystal was isolated. The single crystal X-ray diffraction measurements were carried out as described in section 2.2.1.3. They show that the material conserves the CeScSi structure type (*I4/mmm*) of the pristine compound. To attempt to locate the carbon atoms, the collected data was refined using the Jana2006 software package with the NdScSi structure (Tencé *et al.*, (2016)) without any carbon included.

Fourier difference analysis of the refinement shows that there is no residual electronic density in the tetrahedral sites but a significant residual density in the [Nd_2Sc_4] octahedral 2*b* site at (0 0 ½) (Figure 4. 10., left). After carbon inclusion in the refinement at this site with full occupancy, the Fourier difference analysis shows no remaining electron density in the octahedral sites (Figure 4. 10., right) or at any other point in the lattice. Thus, it is safe to conclude that C is only located in the [Nd_2Sc_4] octahedral sites.

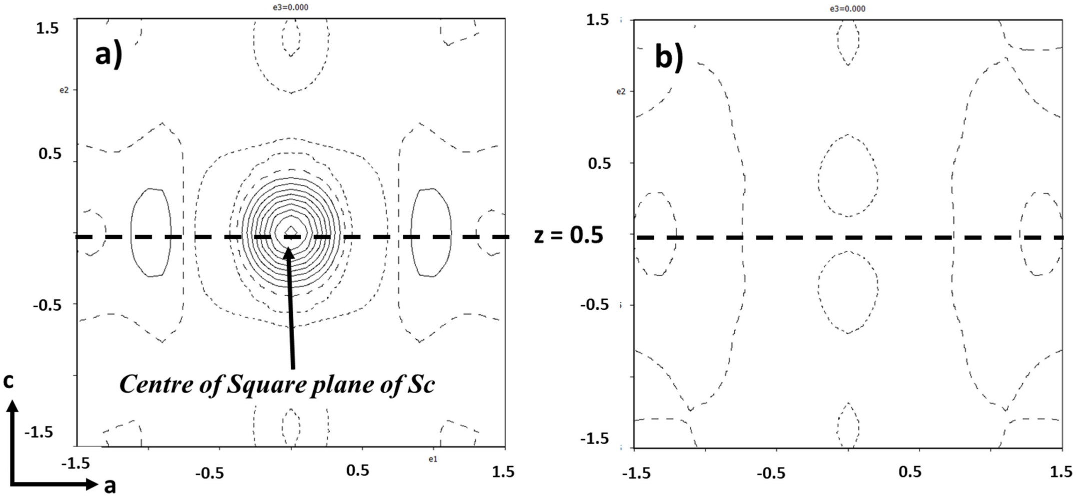

Figure 4. 10. Fourrier difference plot of the single crystal refinement of $NdScSiC_{0.5}$ before (a) and after (b) the inclusion of C in the 2*b* Wycoff site (0 0 ½). The scale is in fractions of the *a* unit cell parameter. Each contour line corresponds to 1 e^- $Å^{-3}$.

Table 4. 5. Atomic parameters refined from the single crystal XRD measurements on $NdScSiC_{0.5}$

$R(F^2)$ / $R_{w(all)}(F^2)$ / S = 2.97% / 5.89% / 1.04 $\Delta\rho_{max}$ and $\Delta\rho_{min}$ (e.$Å^{-3}$) = 0.71 and -2.23

Atom	Wyck.	x	y	z	B_{eq} ($Å^2$)	Occ.
Nd	4*e*	0	0	0.33297(3)	0.564(8)	1
Sc	4*c*	0	½	0	0.36(3)	1
Si	4*e*	0	0	0.12859(1)	0.51(3)	1
C	2*b*	0	0	½	0.44(14)	1

The results of the structural refinement from the single crystal data are summarised in Table 4. 5. All crystallographic sites are fully occupied with no discernible mixing of elements between sites. The *z* coordinates of the Nd and the Si atoms are also slightly displaced in comparison to the NdScSi material and the carbon site is fully occupied. Thermal displacement values for each of the elements are comparable to those seen in the pristine compound. Recall that, for the hydrides, attempts to place the hydrogen atoms directly in the 2*b* site during refinement of the neutron diffraction data result in very large thermal displacement values. This eventually led to the assignation of the half occupied 4*e* site (0 0 0.518(2)) for the hydrogen atoms, placing them in a Sc_4Nd square based pyramids rather than the 2*b* R_2Sc_4 octahedral site. The refinement of single crystal data for the $NdScSiC_{0.5}$ sample does not indicate especially large displacement values for the carbon atom, illustrating that the carbon atoms are well centered in the Sc square planes of the octahedral sites in the lattice. The complete occupation of the 2*b* site corresponds to a final composition of $NdScSiC_{0.5}$ which explains the plateau in the unit cell parameters observed in Figure 4. 2. The crystal structures of NdScSi and $NdScSiC_{0.5}$ are shown in Figure 4. 11., below.

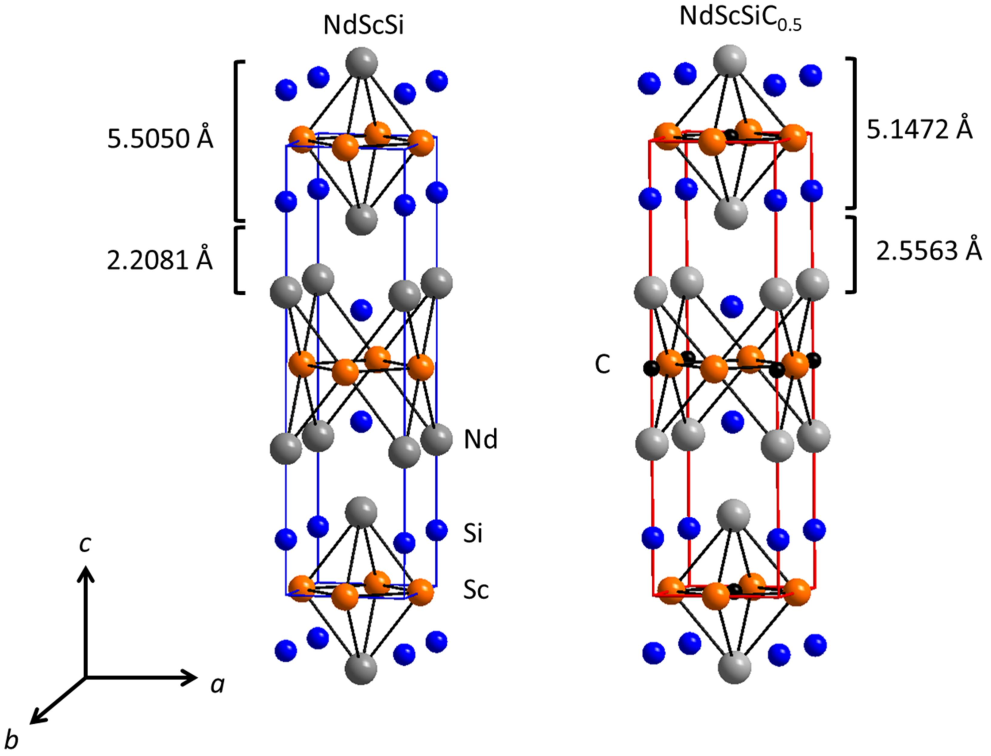

Figure 4. 11. The crystal structures of NdScSi and $NdScSiC_{0.5}$ with the distances between the Nd atoms across the octahedral sites and between adjacent Nd planes.

4.3.2. Neutron diffraction

Due to its sensitivity to light elements, neutron diffraction provides a powerful complement to single crystal XRD for structure determination. In particular it allows a confirmation and accurate dosing of the positions and quantities of light elements present in the structure. We performed neutron diffraction on a sample of $NdScSiC_{0.5}$ to determine the nuclear structure using a wavelength of 2.428(1) Å on the G4.1 beamline at the LLB, France. The crystal structure was refined using the Rietveld method, starting from the atomic positions deduced from the single crystal measurements. This refinement can be seen in Figure 4. 12. and shows a good agreement between the structural model and the observed pattern with Sc_2OC as the main secondary phase observed. Also present are small quantities of Nd_5Si_3 and $NdSi_{1.8}$. The results of this refinement are summarised in Table 4. 6. where an occupancy of 94(2) % was found for the octahedral (2*b*) site occupied by the carbon atoms corresponding to a refined composition of $NdScSiC_{0.47(1)}$. This indicates that the site is almost completely filled with carbon atoms and provides good agreement with all other measurements on the $NdScSiC_{0.5}$ samples. Since the neutron diffraction peaks are broader than those obtained by high resolution X-ray diffraction, the inhomogeneity that was discussed previously is less immediately visible and the refinement was carried out using only a single $NdScSiC_x$ phase.

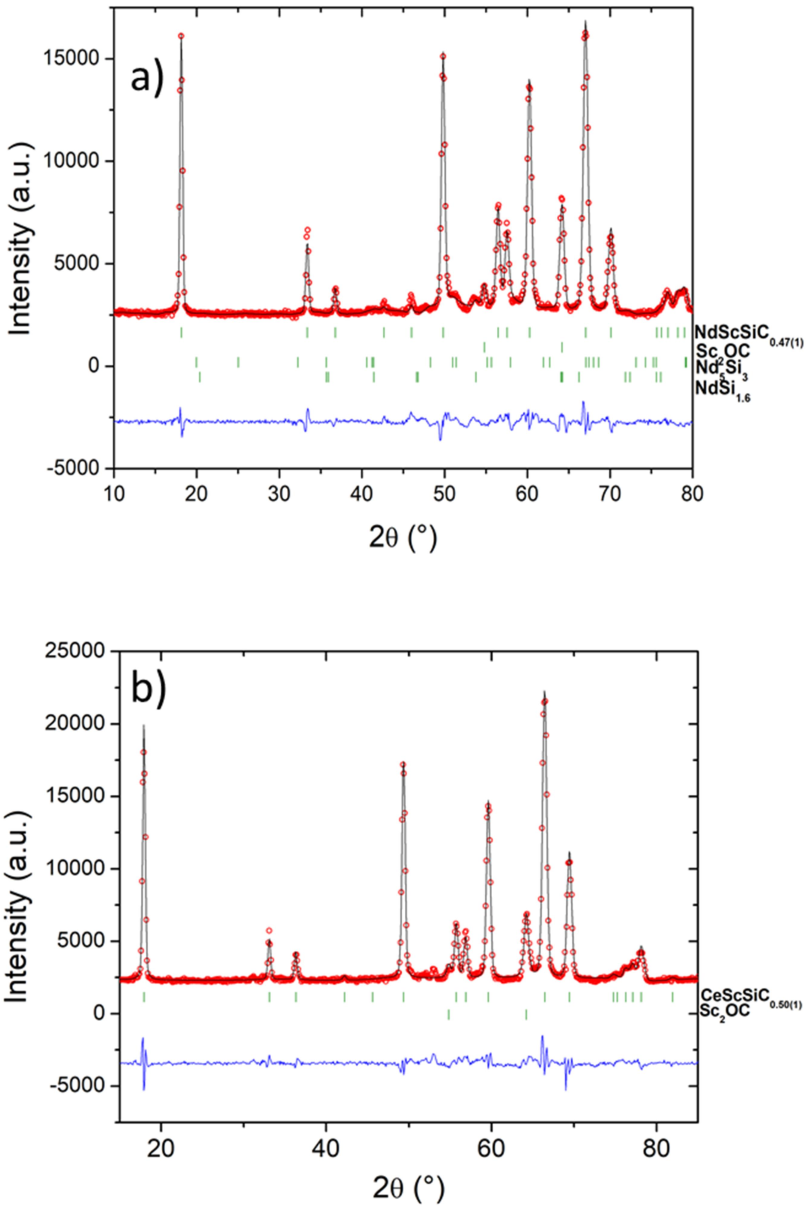

Figure 4. 12. Nuclear structure refinement of a) $NdScSiC_{0.47(1)}$ and b) $CeScSiC_{0.50(1)}$ from neutron diffraction data at 150 K and 30 K respectively. λ = 2.428(1) Å

Table 4. 6. Summary of phase data from neutron diffraction refinement of the $NdScSiC_{0.47(1)}$ and $CeScSiC_{0.50(1)}$ phases at 150 K and 30 K respectively.

Nom. Comp.	a (Å)	*c* (Å)	V (Å^3)	R – Bragg (%)	R_P (%)	R_w (%)
$NdScSiC_{0.5}$	4.39694(7)	15.4011(5)	297.7501	3.07	13.7	11.6
$CeScSiC_{0.5}$	4.4331(1)	15.587(1)	306.322	5.98	17.6	14.4

Table 4. 7. The refined structural data from neutron diffraction measurements, carbon contents, and calculated carbon contents for the samples present in Table 4. 6. above. Effective composition is calculated using the *a* unit cell parameter from Rietveld refinements of PXRD data.

Nom. Comp.	z_R	z_{Si}	Occ (C)	B_{iso} (C) (Å^2)	Refined x	Eff. Comp.
$NdScSiC_{0.5}$	0.335(2)	0.1290(5)	0.94(2)	0.84(2)	0.47(1)	0.46(2)
$CeScSiC_{0.5}$	0.334(6)	0.1295(8)	1.00(2)	1.32(2)	0.50(1)	0.50(2)

Table 4. 7. presents the refined and calculated effective carbon contents of the $NdScSiC_{0.5}$ and $CeScSiC_{0.5}$ (nominal) samples used for neutron diffraction. The refined composition of $NdScSiC_{0.47(1)}$ represents a similar carbon content to the calculated x = 0.46(2) using the *a* unit cell parameter and the method described above. For the $CeScSiC_{0.5}$ sample, the effective (0.50(2)) and refined compositions (0.50(1)) are also in very good agreement. The *a* parameter was chosen to calculate the effective compositions as the *hk*0 peaks are less sensitive to the distribution of C. This means that the *a* parameter is less prone to error in the determination of the unit cell parameter during refinement. However, it also only provides an indication of the average carbon content for the whole sample. The refinement of neutron diffraction data is considered to be more reliable for dosing carbon content than calculation via the calibration curves in Figure 4. 5. used for most samples. So while our method of calculating the effective x of the phase almost agrees exactly with the refined experimental results of neutron diffraction, in the absence of neutron data for all samples it provides a fair approximation. An ideal confirmation of the validity of the calculated effective x would be to investigate the carbon content of one sample using both the combustion analysis method and neutron diffraction. Time constraints and a lack of sufficient powder from the neutron samples prevented this.

4.3.3. Discussion of the changes in Interatomic distances

The interatomic distances for the *R*ScSi and $RScSiC_{0.5}$ systems (*R* = La, Ce, Nd and Gd) from the literature and derived during this work are given in table 4. 8. As the same general trends have been found for all investigated carbides, this section will focus on a detailed discussion of NdScSi and $NdScSiC_{0.5}$ only. The quoted metallic radii are half the shortest metal-metal distances in the pure metals. All quoted covalent radii are from the 91st edition of the handbook of chemistry and physics (Haynes, (2010)) section 9 pages 49 and 50.

Contrary to what was observed after hydrogenation of the pristine NdScSi, insertion of carbon induces a decrease of the distance between Nd and Sc-Si blocks and an increase of interatomic distances inside them. The distance between the two blocks (equal to *c*/4) decreases from 3.926 Å to 3.847 Å for the carbide whereas it increases to 4.158 Å for the hydride, showing clearly that carbon insertion reinforces the 3D character of the pristine compound. Thus the distance between Nd and the Sc or Si atoms decreases on carbon insertion, moving from 3.505 Å to 3.386 Å for Nd-Sc and from 3.148 to 3.145 Å for Nd-Si. In the two block-types all the distances increase slightly (Nd-Nd, Sc-Si, Nd-Nd, see table 4. 8.). For instance, the new $d_{Nd\text{-}Nd}$ = 4.0309(5) Å is larger than that seen in Nd metal and NdScSi, which suggests that the Nd-Nd interactions are reduced in the carbide. This different behaviour compared to the hydride seems to be directly correlated to the Nd-C bonding in the Nd_2Sc_4 octahedral site. In NdScSi the distance between the 2*b* site (occupied by C in the carbide) and the neighboring Nd, equal to 2.77 Å, is reduced to 2.57 Å (= $d_{Nd\text{-}C}$) in the carbide. This is achieved by a decrease of the *c*-parameter (-1.77 %, table 4.4.) and a slight shift of z_{Nd} coordinate. This latter distance is comparable to the values observed for the two binary Nd carbides: NdC_2 (Atoji, (1966)) and Nd_2C_3 (Atoji, (1978)) where $d_{Nd\text{-}C}$ = 2.553 Å and 2.611 Å respectively. Moreover the filling of the Sc square plane by carbon induces an increase of the *a*-parameter to manage more realistic Sc-C distances from 2.145 in the pristine to 2.205 Å in $NdScSiC_{0.5}$. This distance is comparable to the ones observed in ScC (Nowotny and Auer-Welsbach, (1961)), Sc_3C_4 (Pöttgen and Jeitschko, (1991)), Sc_4C_3 (Krikorian *et al.*, (1969)), and $Sc_{15}C_{19}$ (Jedlicka *et al.*, (1971)) for which the Sc-C distances are ranging between 2.25 and 2.35 Å.

Table 4. 8. Table of the interatomic distances at room temperature for *R*ScSi and *R*ScSiC$_{0.5}$ (*R* = La, Ce, Nd and Gd) from the literature and this work. All distances are calculated using the structural parameters from XRD measurements. The NdScSiC$_{0.5}$ distances are calculated from the single crystal data.

Atom	D (Å)							
	LaScSi[a]	LaScSiC$_{0.5}$	CeScSi[b]	CeScSiC$_{0.5}$	NdScSi	NdScSiC$_{0.5}$	GdScSi	GdScSiC$_{0.5}$
R*–*R[c]	3.878	4.0936(14)	3.8498(5)	4.09(9)	3.8112(2)	4.0309(5)	3.766(1)	3.999(4)
R*–*R[d]	4.349	4.4532(1)	4.3283(5)	4.4288(1)	4.2894(4)	4.4107(4)	4.2556(5)	4.3917(1)
***R*–Sc**	3.564	3.4617(12)	3.5288(5)	3.42(7)	3.5051(7)	3.3868(4)	3.4799(10)	3.333(4)
***R*–Si**	3.211	3.166(2)	3.1822(9)	3.18(2)	3.1480(4)	3.1452(5)	3.062(5)	3.007(6)
***R*–Si**	3.284	3.1967(4)	3.207(3)	3.21(9)	3.1507(2)	3.1744(2)	3.1133(13)	3.1433(8)
R*–C/*Oh	*2.824*	2.6505(16)	*2.7873(6)*	2.60(9)	*2.7724(6)*	2.5704(5)	*2.7536(12)*	2.508(5)
Sc–Sc	3.075	3.1489(1)	3.0606(3)	3.1316(1)	3.0331(4)	3.1188(2)	3.0092(3)	3.1054(1)
Sc–Si	2.889	3.0604(11)	2.890(2)	3.005(9)	2.8848(5)	2.9630(2)	2.890(3)	2.984(2)
Sc–C/*Oh*	*2.175(1)*	2.2266(1)	*2.1641(3)*	2.2144(1)	*2.1447(3)*	2.2053(3)	*2.1278(3)*	2.1958(1)
Si–C/*Oh*	*3.616(2)*	3.7846(9)	*3.611(2)*	3.733(7)	*3.5947(7)*	3.6937(2)	*3.589(3)*	3.7051(15)

[a] Chevalier *et al.*, (2010)c
[b] Singh *et al.*, (2001)
[c] distance between adjacent layers
[d] distance within the same layer

4.4. Magnetic properties

For the CeScSi type materials we have already shown in chapter 3 that hydrogenation greatly reduces the magnetism of a compound. In CeScSi, hydrogenation reduces the antiferromagnetic transition from T_N = 27 K to a transition temperature of 3.0 K (Chevalier *et al.*, (2010)c). In NdScSi, hydrogenation was shown to cause magnetic ordering below 4 K in $NdScSiH_{1.5}$ while the pristine compound is ferromagnetic below 171 K Tencé *et* *al.*, (2016). Crystallographically we have shown that the carbide exists for the *R*ScSiC$_x$ (*R* = La, Ce, Nd and Gd) compounds as well as showing that the Ce and Nd systems form solid solutions ($0 < x < 0.5$ for Ce and $0.25 \lesssim x < 0.5$ for Nd). The study of the magnetic properties of these systems is presented here.

4.4.1. Magnetisation and specific heat measurements on NdScSiC$_x$ ($0.25 \lesssim x \leq 0.5$)

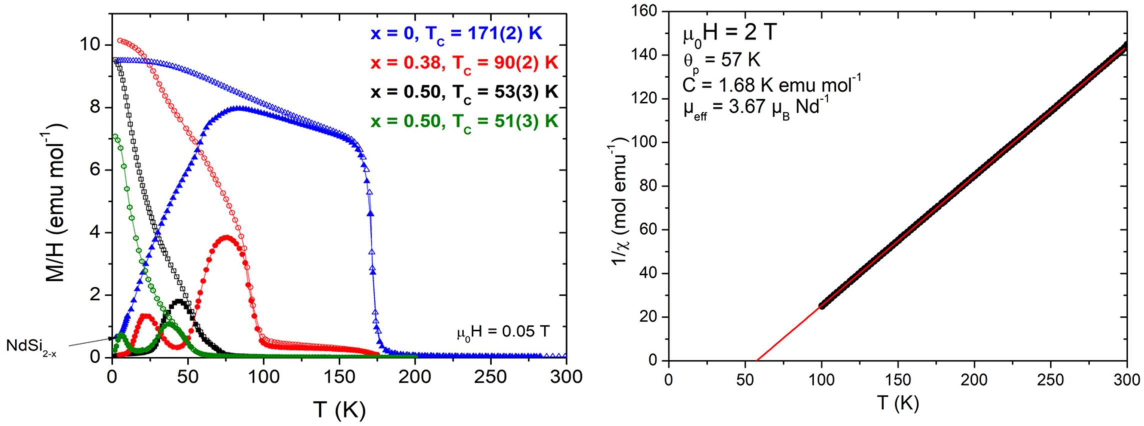

Figure 4. 13. ZFC-FC magnetisation curves for the NdScSiC$_x$ for effective x =0, 0.38, and two samples where effective x = 0.5 at 0.05 T (left). The filled symbols show the zero-field cooled measurement and the hollow ones the field cooled measurement. The image on the right shows temperature dependence of the inverse of the magnetic susceptibility at μ$_0$H = 2 T for effective x = 0.50 fitted using the Curie-Weiss law.

A selection of ZFC-FC magnetisation curves for the NdScSiC$_x$ system with effective x (calculated from the *a* unit cell parameter and Figure 4. 5.) of 0, 0.38 and two samples with effective x = 0.5 are shown in Figure 4. 13. This image also shows (right) the inverse susceptibility at high field (μ$_0$H = 2 T) against temperature fitted using the Curie-Weiss law. These measurements show that the carbides display ferromagnetic order. However, Carbon insertion causes a reduction in the T$_C$ (determined from the point of inflection of the ZFC curves) of the system with increasing carbon content from 171 K for the pristine NdScSi (Manfrinetti *et al.*, (2008) and this work) to approximately 50 K for NdScSiC$_{0.5}$. It should be noted that, while convenient, the point of inflection may underestimate the T$_C$ for the carbon rich samples where significant magnetisation is observed above this point. The most precise method to determine the T$_C$ would be to trace the Arott plots. However, given that a large number of magnetisation isotherms are required for this method and the limited experiment time this was not performed. Also, the difficulties associated with the inhomogeneity of these samples makes it unlikely that this will provide much more accuracy for the value of the T$_C$. From the curves shown in Figure 4. 13. there is a clear divergence between the ZFC and FC parts of the measurement. This is often observed in rare earth based magnetic compounds and stems from their generally large magnetocrystalline anisotropy (Singh *et al.*, (2004)). Several small transitions associated with secondary phases can be observed in the M(T) curves in Figure 4. 13. (left). Two transitions arising from secondary phases are observed at low temperatures in the x = 0.38 and x = 0.50 plots (T$_C$ =

51(3) K) respectively. The transition around 10 K for x = 0.50 is due to the $NdSi_{2-x}$ secondary phase (Boulet *et al.*, (2001)). A very small amount of residual NdScSi is also visible in the x = 0.38 curve that could not be observed from X-ray diffraction alone on this sample. The transition around 25 K for the other x = 0.50 sample could not be identified. As other samples do not show this transition it is not intrinsic to the major phase and thus must belong to a secondary phase, possibly to the $ScNd_2Si_2$ phase observed in the microprobe analysis. As the magnetic properties of this phase have not been previously documented this cannot be confirmed here. Figure 4. 13. (right) shows a plot of the inverse susceptibility against temperature in a high field of 2 T fitted using the Curie-Weiss law. $NdScSiC_{0.5}$ is a Curie-Weiss paramagnet with a paramagnetic Curie temperature (θ_P) of 57 K. The positive value of θ_P indicates predominant ferromagnetic local interactions and the value is close to the measured Curie temperature of around 50 K. The calculated effective moment of 3.67 μ_B Nd^{-1} corresponds very well with the 3.62 μ_B for the free Nd^{3+} ion. From this, it can be concluded that only the rare earth atoms are magnetic in these compounds.

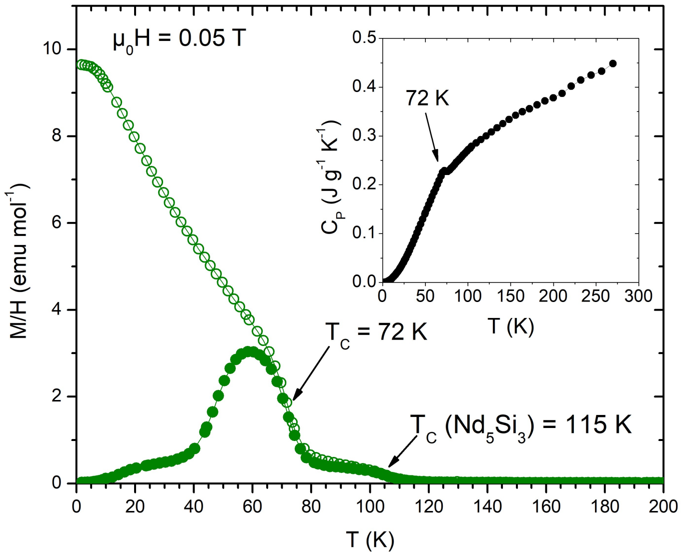

Figure 4. 14. ZFC-FC magnetisation curves and C_P measurements for the $NdScSiC_x$ system with effective x = 0.41. Filled points show the ZFC curve and the hollow ones show the FC curve.

Heat capacity measurements at constant pressure (C_P) provide a useful confirmation for the determination of magnetic transition temperatures as the onset of magnetic order can be observed from these measurements. The size anomalies seen during the onset of magnetic order are related to the proportion of the sample that orders magnetically. Thus C_P measurements are a useful confirmation that a magnetic transition is due to the major phase and not a secondary one. Figure 4. 14. shows the ZFC-FC and C_P curves for a sample with effective composition $NdScSiC_{0.41}$. The C_P measurements confirm the T_C of 72 K is the ordering of the major phase. The sample also contains a small amount of the ferromagnetic secondary phase Nd_5Si_3 ((Boulet *et al.*, (2001)) as seen in the ZFC-FC curves which is not observed in the C_P measurements.

In Figure 4. 15. the Curie Temperatures for a number of the carbide phases are plotted against the sample effective x (calculated from the *a* unit cell parameter using the the calibration curves in Figure 4. 5.). This plot shows that there is a roughly linear dependence of the T_C of the material on the carbon content. It is also clear that the transition becomes less well defined as the carbon content increases. Instead of seeing the sharp transition of a well-defined single phase sample such as the pristine NdScSi, the transition observed here is blurred by the small distribution of carbon content across the sample. The decrease in the T_C of the materials is most likely due to the modification of the RKKY interactions between the rare earth elements. This may be caused by a change in the density of states around the Fermi level by the interaction between the Nd, Sc and C atoms as well as the changes in the distances between the Nd atoms. Density of states calculations are required to investigate this.

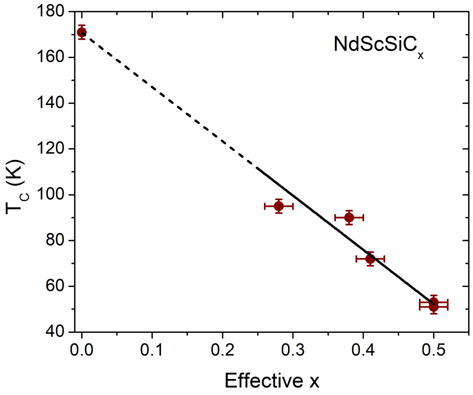

Figure 4. 15. The change in Curie temperature with respect to the calculated effective carbon content of the NdScSiC$_x$ system.

Isothermal magnetisation measurements, M(H), of NdScSiC$_{0.50(2)}$ for several temperatures between 1.8 and 120 K are shown in Figure 4. 16. To reduce the effects of magnetocrystalline anisotropy these measurements were performed on powder samples. The sharp increase in magnetisation with field confirms the ferromagnetic behaviour of the carbide. The curve at 88 K is not completely linear despite being above the T_C, likely due to remaining ferromagnetic correlations above the T_C of 51 K. This is logical as, if we recall the ZFC-FC curves in Figure 4. 13., the sample still shows significant magnetic susceptibility above the cited T_C of 51 K with the magnetisation reaching zero at almost 70 K. At 120 K the linearity of the curve is as expected for a paramagnetic state, thus no residual NdScSi remains in this sample. At 7 T the magnetic moment appears to be almost saturated at 2.67 μ_B f.u.$^{-1}$, significantly below the Nd^{3+} free ion value of 3.28 μ_B f.u.$^{-1}$.

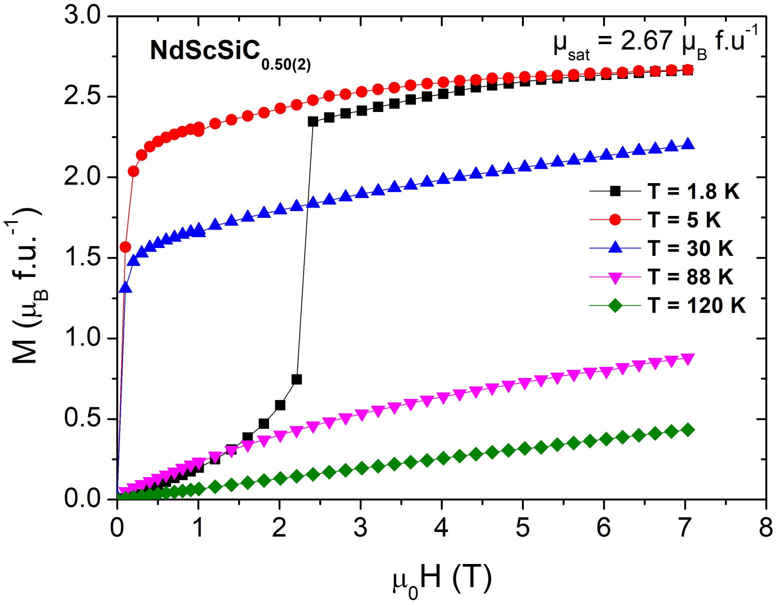

Figure 4. 16. Powder M(H) magnetisation curves for NdScSiC$_{0.50(2)}$ (effective composition) at various temperatures between 1.8 and 120 K in fields of up to 7 T. The curve at 1.8 K represents a virgin magnetisation curve.

Typically for rare earth materials a reduction in magnetic saturation moment can be caused by several things:

- Overall ferrimagnetic order from an antiferromagnetic coupling between sublattices with different moments.
- Magnetocrystalline anisotropy resulting mainly from the crystal electric field (CEF). This will require higher fields to overcome.
- A splitting of the (2J + 1) degenerate ground state into several non-equivalent states by the electric field. This renders some of the higher energy states inaccessible and reduces the magnetic moment.

As there is no indication that any atoms other than Nd are magnetic in this material it is not possible that there is any anti-ferromagnetic coupling between the Nd and Sc. As all Nd sites are equivalent ferrimagnetism is not possible. All magnetic measurements on the carbides were performed on powder samples to reduce the effects of magnetocrystalline anisotropy but this may not be completely overcome. Thus the reduction in the magnetic moment is likely due to a combination of magnetocrystalline anisotropy and splitting of the ground state.

Figure 4. 17. shows the complete cycle of the isothermal magnetisation of a NdScSiC$_{0.50(2)}$ (effective composition) powder sample at 1.8 K in the field range of +7 to -7 T. The virgin magnetisation curve (1.8 K) of the material begins with a gradual increase of the magnetisation with a sudden, sharp jump around 2.3 T, almost reaching the saturation magnetisation. This behaviour suggests a hard magnetic compound with slow movement of

the domain walls. This is often due to the presence of magnetocrystalline anisotropy and defects that pin the domain walls and requires an increase in the field to force their displacement. The presence of large magnetocrystalline anisotropy is in agreement with the separation between the ZFC and FC curves in Figure 4. 13. and Figure 4. 14.

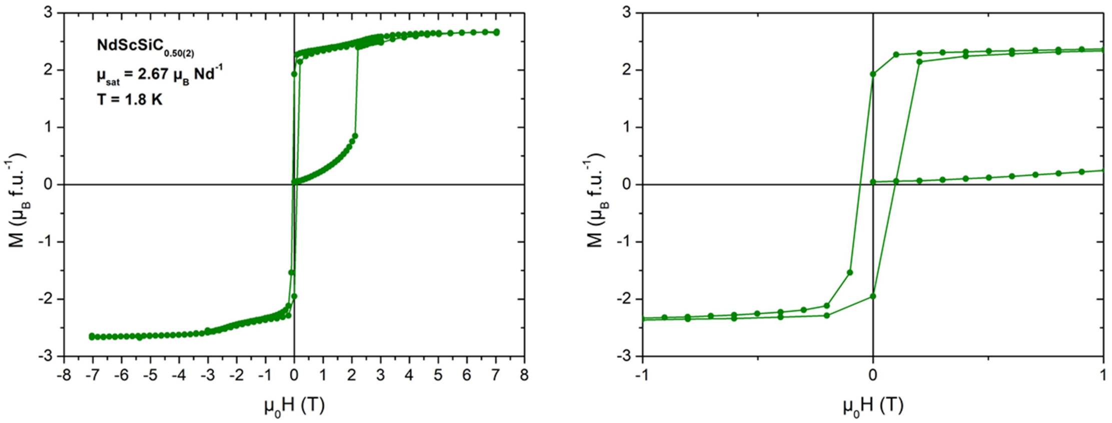

Figure 4. 17. Isothermal hysteresis cycle of a powder sample at 1.8 K between +7 and -7 T for $NdScSiC_{0.50(2)}$ (left) and a zoom on the region 1 to -1 T (right). The measurement was performed on a powder sample.

The hysteresis curve shows that, after initial magnetisation, $NdScSiC_{0.50(2)}$ has a significant remanent magnetisation of 1.93 μ_B Nd^{-1} but a reasonably small coercive field of roughly 0.05 T. It should be noted that, as this measurement was performed on a powder sample it cannot be compared reliably with measurements on block samples of the pristine compound.

4.4.2. The magnetic structure of $NdScSiC_{0.47(1)}$

In order to investigate the magnetic structure of $NdScSiC_{0.47(1)}$, neutron diffraction was performed on the G4.1 beamline at the LLB, France. To solve the magnetic structure, diffraction patterns were collected at a range of temperatures between 1.5 and 150 K. This temperature range was chosen based on the ZFC-FC magnetisation curves shown in Figure 4. 18. (left) which shows two magnetic ordering phenomena. The first, at 115 K is attributed to the secondary phase Nd_5Si_3 (Boulet *et al.*, (2001)), the second transition at 79 K is therefore expected to belong to the magnetic transition of $NdScSiC_{0.47(1)}$. However, by Figure 4. 15., the T_C corresponds to an effective x of approximately 0.40. If we consider the (006) peak of the XRD pattern for this sample (originally given in Figure 4. 7.) more carefully we observe that, as well as the two labelled *c* parameters that yielded effective x values of 0.48(2) and 0.44(2), there is an additional small shoulder at lower angles. Figure 4. 18. (right) illustrates this with the original *c* parameters and an approximate *c* parameter for this shoulder shown. This *c* = 15.4428 Å corresponds to x = 0.39(2) (by Figure 4. 5), in good agreement with the observed T_C.

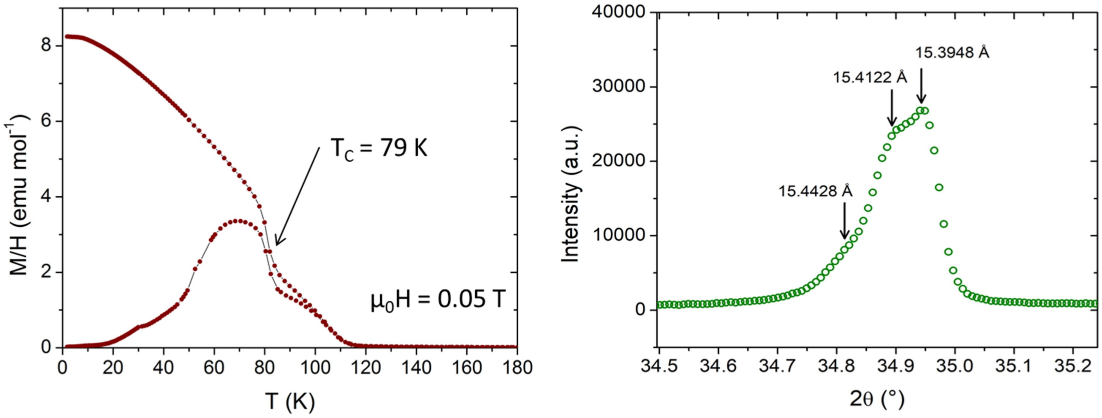

Figure 4. 18. Left) Magnetic susceptibility against temperature for the large (5 g) neutron sample of NdScSiC$_{0.47(1)}$ in a field of 0.05 T. The filled points so the ZFC curve and the hollow points show the FC curve. The transition at 115 K is due to Nd$_5$Si$_3$ secondary phase. Right) The 006 peak from high resolution XRD of this sample with the three *c* parameters labelled.

The neutron diffraction patterns for NdScSiC$_{0.47(1)}$ at 100 K and 1.5 K are plotted together with the difference pattern in Figure 4. 19. The difference pattern emphasises clearly the magnetic peaks. No significant change was observed in the unit cell parameters when moving from the paramagnetic to ferromagnetic state. There is a slight shrinking of the unit cell parameters from *a* = 4.41298(5) Å to 4.39676(7) Å (-0.45 %) and *c* = 15.3825(2) Å to 15.3890(6) Å (-0.15 %), a total change in the unit cell volume of -0.73 %, on cooling of the sample from 100 K to 1.5 K. The magnetic peaks coincide with the nuclear peaks, meaning that they are indexed with the propagation vector **k** = (000). This indicates that the magnetic and crystalline unit cells are the same.

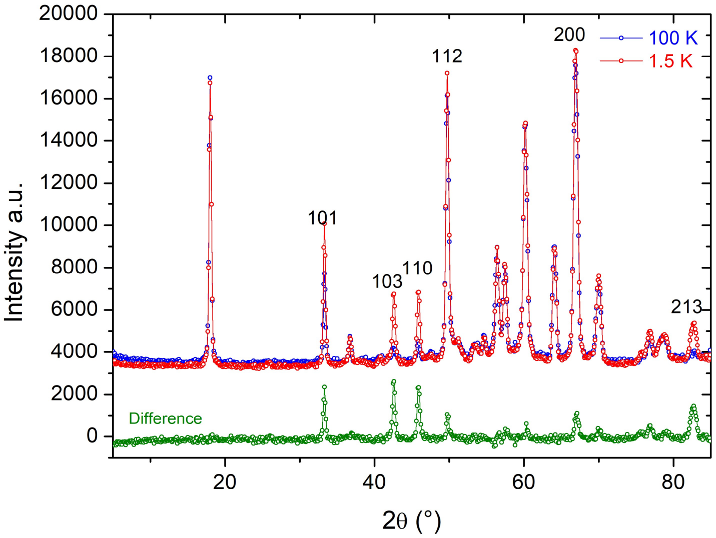

Figure 4. 19. Neutron diffraction patterns for NdScSiC$_{0.5}$ at 1.5 and 100 K with the difference between both patterns shown below. The labels show the main magnetic peaks. λ = 2.428 Å

At 1.5 K, the best fit of the data is obtained with a ferromagnetic structure with the Nd moments parallel to the *c* axis. This was unambiguously determined as there is only one Nd position. The refinement at 1.5 K is shown in Figure 4. 20. with the nuclear and magnetic Bragg R-factors being 5.1 % and 5.7 % respectively. The results of this refinement are summarised in Table 4. 9. and the magnetic structure at 1.5 K is displayed in Figure 4. 21.

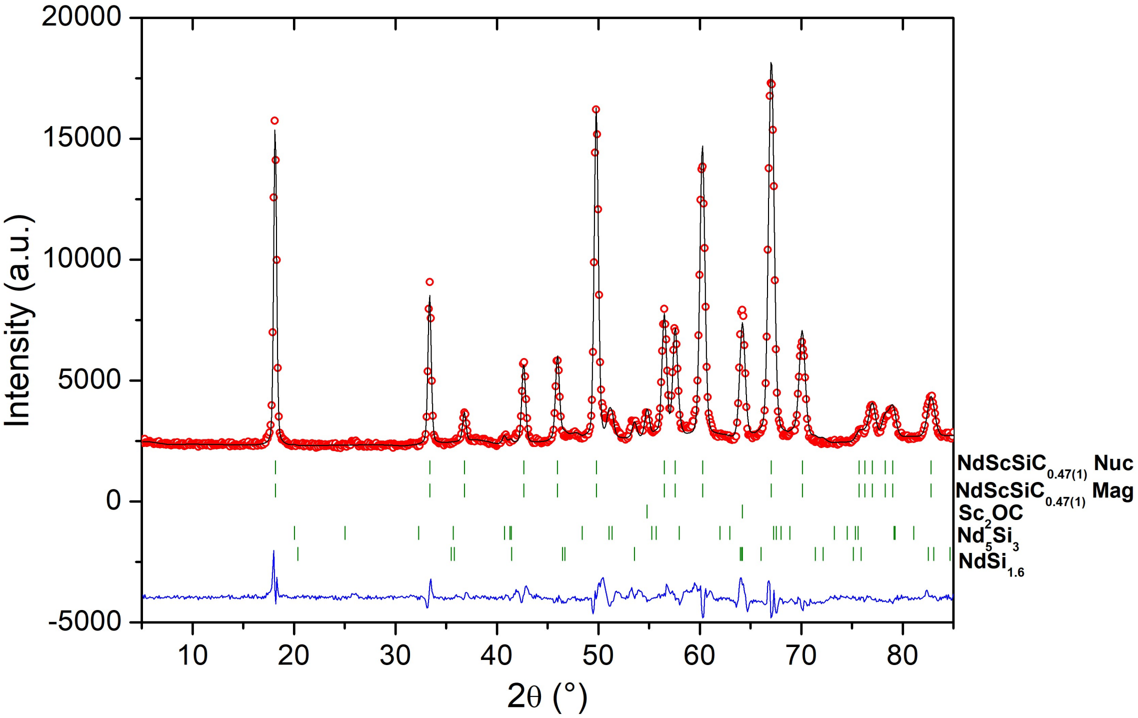

Figure 4. 20. Magnetic structure refinement for $NdScSiC_{0.47(1)}$ at 1.5 K. Bragg R-factors 5.1 % (nuclear) and 5.7 % (magnetic). λ = 2.428 Å

Table 4. 9. Summary of the refined parameters from the nuclear and magnetic structure refinement of $NdScSiC_{0.47(1)}$.

Phase	a (Å)	*c* (Å)	Nd Moment (μ_B)	z_{Nd}	z_{Si}	Occ (C)	R – Bragg (%)	R_P (%)	R_w (%)
$NdScSiC_{0.5}$ Nuclear	4.3967(1)	15.3886(8)	--	3.333(2)	0.1279(8)	0.94(2)	5.1	15.2	13.1
$NdScSiC_{0.5}$ Magnetic	4.3967(1)	15.3886(8)	3.09(4)				5.7		

The magnetic structure of NdScSi has not yet been documented, however, the Ge analogue orders ferromagnetically below 200 K with magnetic moments aligned with an angle of 54(2)° with the *c* axis (Manfrinetti *et al.*, (2008)) (Figure 4. 21.). The magnetic structure of $NdScSiC_{0.47(1)}$ (Figure 4. 21.) differs only slightly from this in that the magnetic moments are aligned along the *c* axis. Attempts to include a moment in the *ab* plane in the refinement either led to very poor fits or to divergence and so they were discarded.

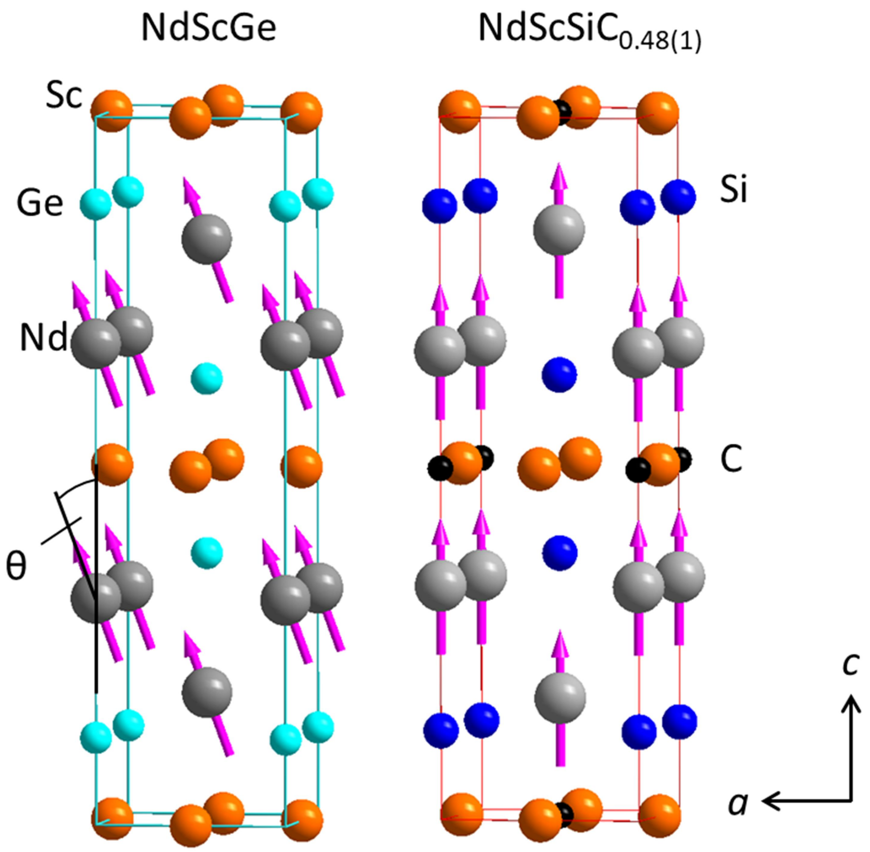

Figure 4. 21. Magnetic structures of NdScGe (Manfrinetti *et al.*, (2008)) and $NdScSiC_{0.47(1)}$ at 1.5 K. θ = 54(2) ° in NdScGe.

The evolution of the refined magnetic moment with temperature was determined using the same ferromagnetic model over the whole temperature range confirming a T_C around 80 K. This is plotted in Figure 4. 22. Above 80 K no change in the intensity of the main phase peaks was observed, confirming our hypothesis that the magnetic transition observed around 105 K is due to the Nd_5Si_3 secondary phase. The refined magnetic moment plateaus around 20 K with only a slight variation observed on further cooling. The refined magnetic moment at 1.5 K is 3.09(4) μ_B Nd^{-1} which is slightly higher than the 2.7 μ_B $f.u.^{-1}$ found at 7 T from the isothermal magnetisation measurements but is close to the magnetisation given by gJ for the Nd^{3+} ion which is 3.27 μ_B. As the sample was not fully magnetised at 7 T (Figure 4. 16.) this result is in reasonably good agreement with the magnetisation measurements. Manfrinetti *et al.*, (2008) document a μ_{Nd} = 3.53(4) μ_B for NdScGe. This is notably higher than that of $NdScSiC_{0.47(1)}$ and indicates a larger splitting of the ground level by the CEF in the carbide than the pristine material.

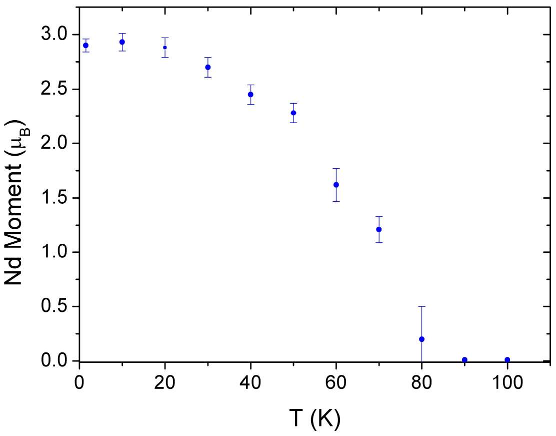

Figure 4. 22. Temperature dependence of the refined Nd moments for $NdScSiC_{0.47(1)}$.

4.4.3. Magnetic properties of $CeScSiC_x$ ($0 \le x \le 0.5$)

While the effect of carbon insertion in the NdScSi system causes a reduction in ordering temperature of the parent compound with a linear dependence on C content, for the $CeScSiC_x$ ($0 \le x \le 0.5$) system the effect is more complex. For this reason we shall consider here the case of $CeScSiC_{0.50(1)}$ and later we shall present the case of $CeScSiC_{0.25}$ to illustrate some of the complexities in this family of materials.

4.4.3.1. Magnetisation and specific heat measurements on $CeScSiC_{0.50(1)}$

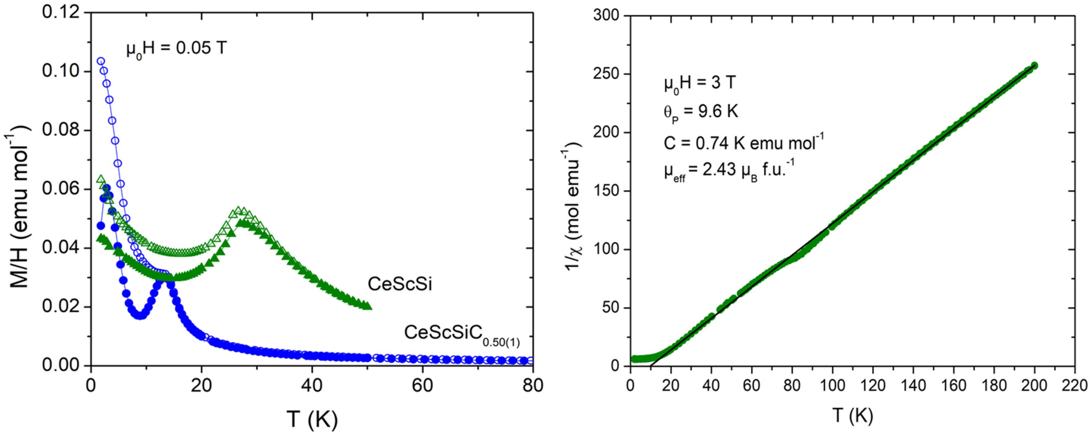

Figure 4. 23. ZFC-FC susceptibility curves for the $CeScSiC_x$ (x = 0 and 0.50(1)) systems at 0.05 T (left) and the plot of the inverse susceptibility vs temperature at 3 T fitted using the Curie-Weiss law for $CeScSiC_{0.50(1)}$ (right).

Figure 4. 23. (left) shows a plot of the temperature dependence of the susceptibility for $CeScSiC_{0.50(1)}$ and pristine CeScSi. Figure 4. 23. (right) shows the inverse susceptibility at 3 T against temperature, fitted with the Curie-Weiss law. $CeScSiC_{0.50(1)}$ is a Curie-Weiss paramagnet with $\theta_P = 9.6$ K and a calculated effective moment of 2.43 μ_B Ce^{-1}. This result corresponds well to the effective moment of the free Ce^{3+} ion of 2.56 μ_B Ce^{-1}, showing that, like with the Nd analogues, only the rare earth atoms are magnetic. The positive value of θ_P indicates mostly ferromagnetic interactions. However, the presence of a prominent

maximum in the M(T) curve suggests that it is antiferromagnetic. The pristine phase has been shown to adopt an antiferromagnetic order below 26 K (Singh *et al.*, (2001); Ritter *et al.*, (2016)), a result which is confirmed here. Ritter *et al.*, (2016) also describes, by neutron diffraction, a spin reorientation in pristine CeScSi. The carbide ordering temperature of 13.5 K (determined by the maximum of the peak in the ZFC curve) is lower than that of the pristine (26 K) and a second transition at 3.3 K is also observed. This second transition may be ascribed to a spin reorientation. The Néel temperature is confirmed by the specific heat measurement with the presence of a peak at 13 K (Figure 4. 24), but no other anomaly is visible around 3.3 K.

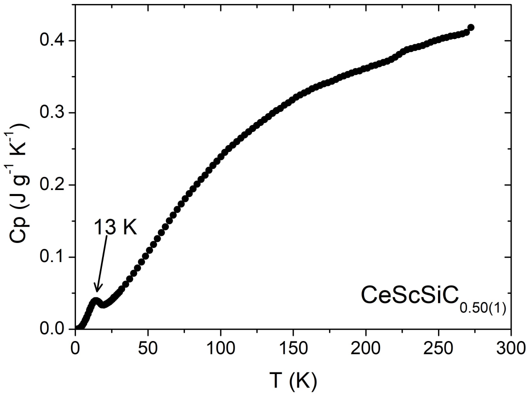

Figure 4. 24. Specific heat capacity curve for CeScSiC$_{0.50(1)}$

To investigate the possible change in magnetic comportment with increasing field that is suggested by the positive paramagnetic Curie temperature in Figure 4. 23, (right), a series of other ZFC-FC curves were measured on the same sample at 1 and 3 T. These curves, displayed in Figure 4. 25., show that increasing the field has a noticeable effect on the magnetic ordering of the material. At 1 T the T_N remains the same but the temperature of the spin reorientation is increased from 3.3 to 6.9 K. Finally, increasing the field to 3 T shows a clear change in magnetic behaviour to ferromagnetic with a T_C of 14 K. This explains the observation of a positive paramagnetic Curie temperature from the fitting of the high field paramagnetic data with a Curie-Weiss law. Thus increasing the field moves the spin reorientation to a higher temperature and eventually pushes the material to a ferromagnetic like behaviour at sufficiently high fields.

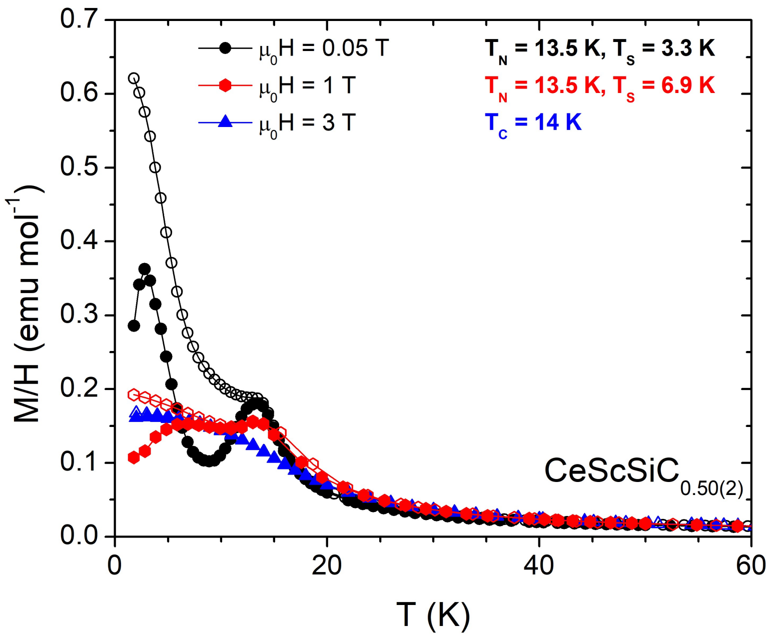

Figure 4. 25. ZFC-FC magnetisation curves for $CeScSiC_{0.50(2)}$ (effective composition) at 0.05, 1 and 3 T. The filled points show the ZFC curves and the hollow ones the FC ones.

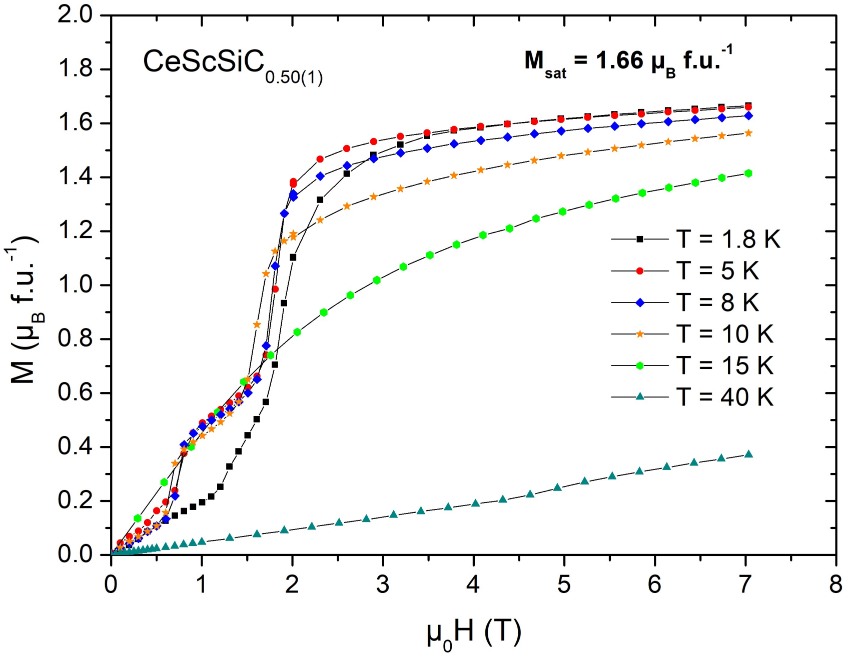

Figure 4. 26. Isothermal magnetisation curves for $CeScSiC_{0.50(1)}$ at a range of temperatures between 1.8 K and 40 K in fields of up to 7 T.

Figure 4. 26. contains the isothermal magnetisation curves for the $CeScSiC_{0.50(1)}$ system. Here it can be seen that the $CeScSiC_{0.50(1)}$ material does not behave like a typical antiferromagnet. Two metamagnetic transitions are observed at all investigated temperatures in the magnetic state except 1.8 K, where only a single metamagnetic

transition is observed. The first metamagnetic transition has a critical field, μ_0H_{C1}, of 0.75 T while the second has a μ_0H_{C2} = 2 T. The linear low temperature parts of the curves correspond well to an anti-ferromagnetic material. The state above the second metamagnetic transition likely corresponds to a ferromagnetic order in agreement with the susceptibility measurement at 3 T (Figure 4. 25.). The magnetisation at 7 T of 1.66 μ_B f.u.$^{-1}$ is lower than the expected value, gJ, of 2.14 μ_B for Ce^{3+} systems. This reduction may be due to a crystal electric field effect.

4.4.3.2. The magnetic structure of CeScSiC$_{0.50(1)}$

The magnetic structure of the CeScSiC$_{0.50(1)}$ material was investigated by neutron diffraction in the temperature range 1.5 – 30 K. Figure 4. 27. shows the diffraction patterns at 30 K and 1.5 K with the difference pattern plotted beneath. An increase in the intensity of several nuclear peaks (labelled) is observed on cooling from 30 K to 1.5 K showing that, like the Nd analogue, the CeScSiC$_{0.50(1)}$ crystalline and magnetic unit cells are the same. Propagation vector determination shows a difference between CeScSiC$_{0.50(1)}$ and the pristine compound. In lieu of the propagation vector **k** = (1 0 0) found in CeScSi (Ritter *et al.*, (2016)), CeScSiC$_{0.50(1)}$ has a propagation vector **k** = (0 0 0).

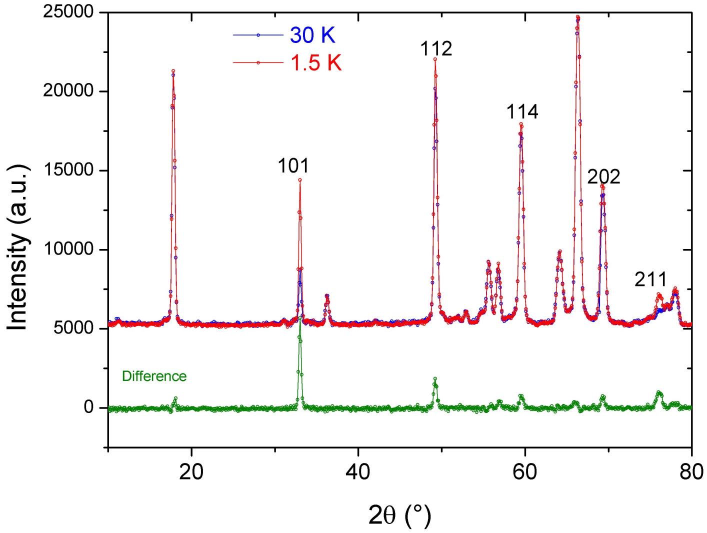

Figure 4. 27. The neutron diffraction patterns of CeScSiC$_{0.50(1)}$ at 30 and 1.5 K with the difference plotted below.

In Figure 4. 28., the refinement of the magnetic and nuclear structures at 1.5 K is shown. The refinement at 1.5 K converges well with the nuclear and magnetic Bragg R-factors being 3.0 % and 4.2 % respectively and an overall R_p of 14.1 % for the whole refinement. The results are summarised in Table 4. 10. The magnetic structure was refined using an antiferromagnetic model consisting of single planes of Ce moments aligned ferromagnetically with an angle of 24.8° to the *c* axis and stacked antiferromagnetically along the *c* axis. This structure is shown in Figure 4. 29(a).

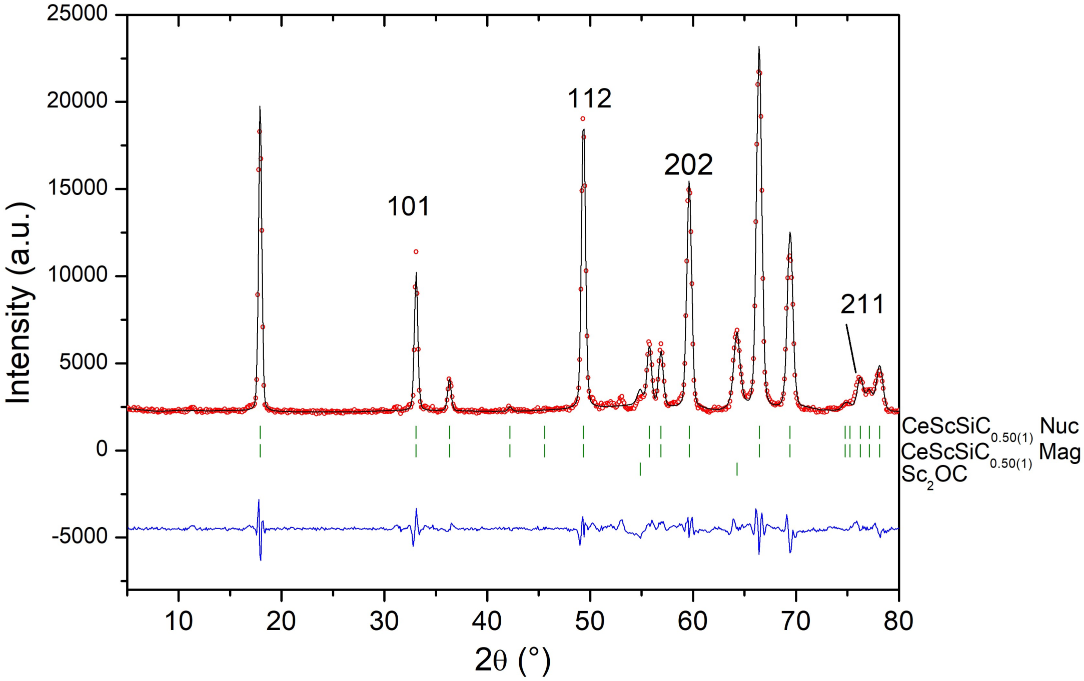

Figure 4. 28. Refinement of the magnetic structure of $CeScSiC_{0.50(1)}$ at 1.5 K.

Table 4. 10. Summary of the refinement at 1.5 K of the magnetic and nuclear structures of $CeScSiC_{0.50(1)}$.

Phase	**a (Å)**	***c* (Å)**	**Total Ce Moment (μ_B)**	**z_{Nd}**	**z_{Si}**	**Occ (C)**	**R – Bragg (%)**	**R_p (%)**	**R_{wp} (%)**
$CeScSiC_{0.50(1)}$ Nuclear	4.4338(1)	15.5817(6)	--	3.336(2)	0.1262(8)	1.00(2)	3.0	14.1	12.2
$CeScSiC_{0.50(1)}$ Magnetic	4.4338(1)	15.5817(6)	1.90(1)	3.336(2)	0.1262(8)	1.00(2)	4.2		

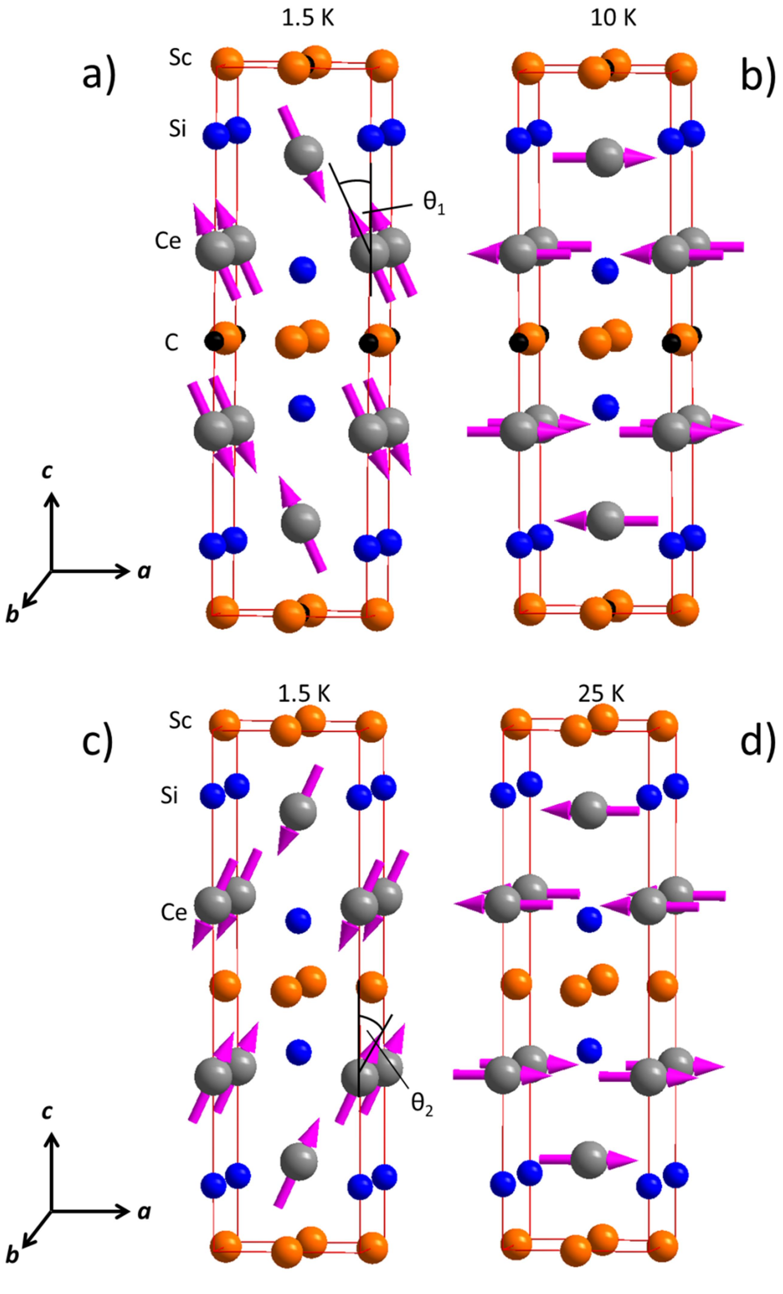

Figure 4. 29. The magnetic structures of $CeScSiC_{0.50(1)}$ at 1.5 K (a) and 10 K (b). (θ_1 = 24.8 °) and the magnetic structure of CeScSi at 1.5 K (c) and 25 K (d) as found by Ritter *et al.*, (2016). (θ_2 = 54 °)

Figure 4. 30. plots the integrated intensities of the 101 and 112 peaks. These two peaks were chosen to represent the relative changes in intensity of the different crystallographic directions and they are both well separated from other peaks, allowing unambiguous determination of their area. The intensity of these peaks starts to increase below 15 K which is close to the T_N of 13.5 K assigned from susceptibility measurements. The integrated intensities of the two reflections do not behave in the same way on cooling. The 101 peak grows very rapidly upon the ordering of the material and reaches a plateau around 8 K while the 112 grows in two steps. It gains a significant amount of intensity

around the Néel temperature, reaching an initial plateau at the same point as the 101. However, upon further cooling of the material the 112 increases once more in intensity below 3.3 K. This may be an indication of a spin a reorientation such as that seen in pristine CeScSi.

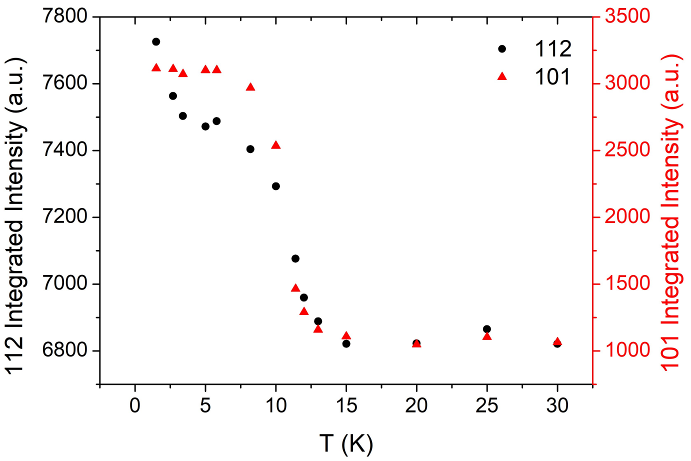

Figure 4. 30. The integrated intensities of the 112 and 101 peaks in the neutron diffraction pattern against temperature for the CeScSiC$_{0.50(1)}$ sample.

Figure 4. 31. shows a plot of the refined total Ce moments, as well as their components in the *ab* plane and along the *c* axis. The initial magnetic moments are in the *ab* plane with a maximum moment of 1.6(3) μ_B Ce^{-1} between 6 and 11 K. For T < 5.5 K the sudden increase in the moment along the *c* axis at the same time as the decrease of the moment in the *ab* plane decreases, confirming the presence of a spin reorientation. This transition takes place between 6 and 3 K, in agreement with T_S = 3.3 K assigned from the maximum in the ZFC arm of the magnetic susceptibility curve. The magnetic structure of CeScSiC$_{0.50(1)}$ above T_S = 3.3 K thus consists of single planes of ferromagnetic Ce with the moments in the *ab* plane (Figure 4. 29 (b)). These single ferromagnetic layers of Ce moments are stacked antiferromagnetically along the *c* axis.

The magnetic structure of the pristine CeScSi has been published recently by Ritter *et al.*, (2016) and is shown in Figure 4. 29 (c and d). It is antiferromagnetic below T_N = 26 K (also shown by Singh *et al.*, (2001)) and they describe the presence of a spin reorientation close to Neel temperature (T_S = 22 K) which was not previously known. Using **k** = (1 0 0), they found that between 26 and 22 K the material is antiferromagnetic, consisting of double planes of collinear Ce atoms ferromagnetically aligned in the *ab* plane and antiferromagnetic coupling across the Sc square planes. Below T_s = 22 K they found that the material undergoes a structural transition from tetragonal to monoclinic with the new structure having unit cell parameters: *a* = 4.3131(4) Å, *b* = 4.3122(4) Å and *c* = 15.8565(3) Å and α = 90.21(1)°, β = 90.20(1)° and γ = 89.954(2)°. The structural transition accompanies the spin reorientation which conserves the local and long range coupling between the Ce moments as they tilt out of the *ab* plane and towards the *c* axis with an angle (θ) of 54° with the *c* axis. The refined moment of approximately 1.42(4) μ_B Ce^{-1} is less than the 2.14 μ_B calculated for Ce^{3+}. Their magnetic structures are presented in Figure 4. 29 (c and d). Therefore, above T_s both structures consist of ferromagnetic planes of Ce with the magnetic moments aligned in the *ab* plane but in the carbide the ferromagnetic coupling between adjacent Ce layers is replaced by antiferromagnetic coupling. Both the carbide and pristine possess a spin reorientation out of the *ab* plane towards the *c* axis with carbon insertion changing the final angle from 54° in CeScSi to 24.8° in CeScSiC$_{0.50(1)}$. Finally the refined moment of 1.90(1) μ_B is larger than the 1.42(4) μ_B Ce^{-1} that Ritter *et al.*, (2016) see for the pristine compound.

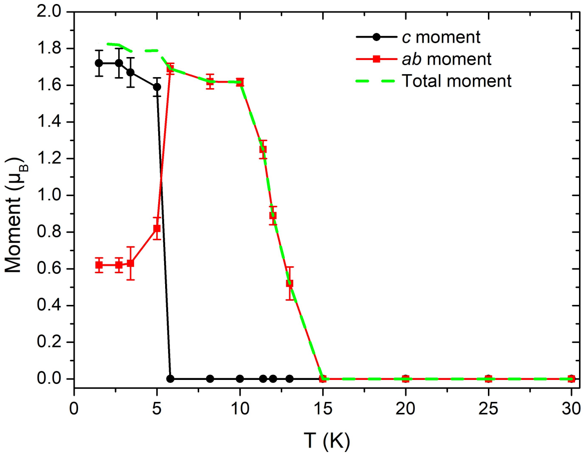

Figure 4. 31. The temperature dependence of the refined Ce moment components in the *ab* and *c* directions as well as the total Ce moment.

No evidence of the structural transition (such as peak broadening or splitting) described by Ritter *et al.*, (2016) was observed from the data on this carbide. However, the structural transition in the pristine compound was determined using high resolution diffraction data and higher Q values than those measured for this magnetic structure determination. As the changes in the structure were very small, the lack of evidence here does not rule out a possible structural transition at low temperatures in CeScSiC$_{0.50(1)}$.

4.4.3.3. The case of CeScSiC$_{0.25}$

The M(T) curve for the samples with effective compositions CeScSiC$_{0.50(1)}$ and CeScSiC$_{0.22(2)}$ are shown in Figure 4. 32. Instead of a sharp peak in the ZFC arm of the curve as seen for CeScSiC$_{0.50(1)}$, a very broad maximum is observed around 33 K suggesting the onset of an antiferromagnetic order. This is very close to the T_N= 27 K of the pristine material (Singh *et al.*, (2001); Ritter *et al.*, (2016)). As we do not observe a continuous decrease of the magnetic ordering temperature with increasing carbon content, it is clear that the effect of carburation on the magnetic properties of the CeScSiC$_x$ system is quite different to that of the Nd analogues. This is likely due to the disordered distribution of C atoms throughout the material. As the occupation of the octahedral site by carbon causes the *R* atoms to move closer to the Sc square planes, disorder in the filling of these sites will lead to a disorder in the Ce-Ce distances throughout the crystal and thus a random exchange RKKY interaction between Ce atoms. It is also possible that this causes the partially filled $CeScSiC_{0.22(2)}$ to adopt a spin glass state with no long range magnetic order. In order to determine if this is the case, magnetisation measurements at different frequencies are required but due to both time and liquid He supply these measurements could not be performed.

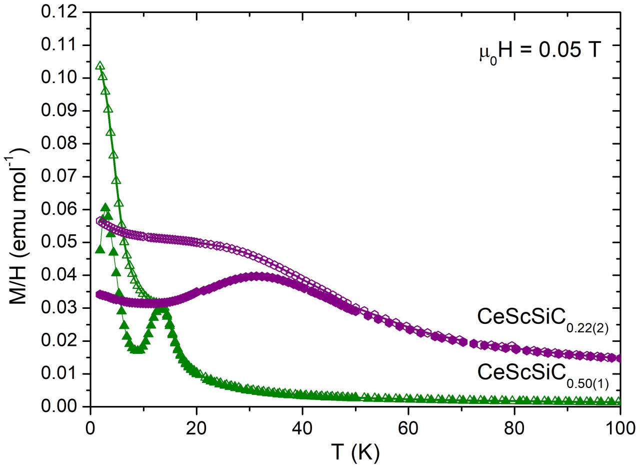

Figure 4. 32. ZFC-FC magnetisation Curves for a sample with effective composition $CeScSiC_{0.22(2)}$ (nominal x = 0.25) with $CeScSiC_{0.50(1)}$. The filled points show the ZFC curve and the hollow ones show the FC.

Figure 4. 33. shows the isothermal M(H) curves for $CeScSiC_{0.22}$. The sample magnetisation shows a linear dependence on field at all temperatures. This is generally consistent with a paramagnetic or antiferromagnetic material but may also occur in a spin glass state. There are no clear indications of the occurrence of a metamagnetic transition but we observe a change in the slope of the M(H) curve above 2 T for T < 30 K. This may be an indication of a non-colinear antiferromagnetic order.

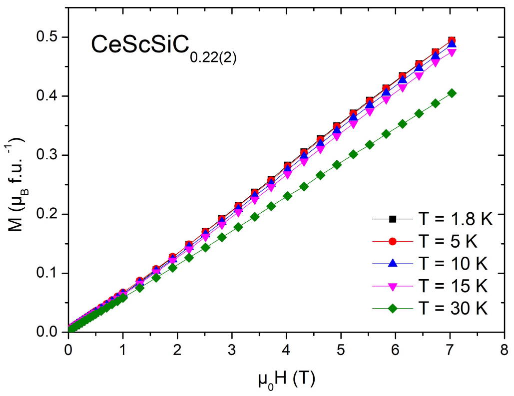

Figure 4. 33. Isothermal magnetisation curves for the sample with effective composition $CeScSiC_{0.22(2)}$.

4.4.4. $CeScGeC_{0.5}$

The M(T) measurements for the Ge analogue $CeScGeC_{0.5}$ show a very similar effect on the magnetic properties of carburation compared to $CeScSiC_{0.50(1)}$. The pristine CeScGe is, like the silicide, antiferromagnetic with a Néel temperature of 36 K (Singh *et al.*, (2001)). The M(T) curves for $CeScGeC_{0.5}$ are shown in Figure 4. 34., they indicate an antiferromagnetic transition at 12 K with a second smaller transition at 3.8 K. The carbide is a Curie-Weiss paramagnet which shows a positive θ_P of 17.5 K which would tend to indicate mainly ferromagnetic interactions. The $\mu_{eff} = 2.58\ \mu_B\ Ce^{-1}$ is consistent with the Ce^{3+} showing that the magnetism arises entirely from the Ce atoms in the material.

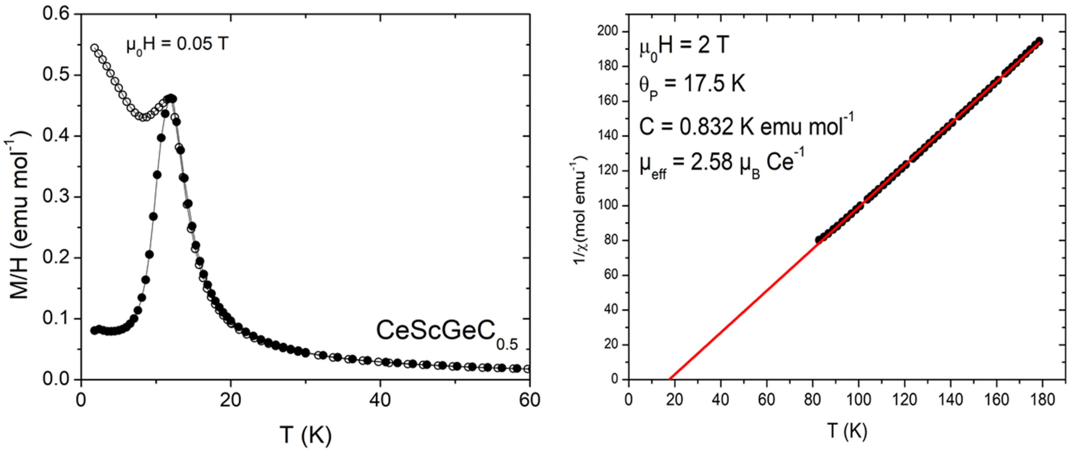

Figure 4. 34. The M(T) curves for $CeScGeC_{0.5}$ in a field of 0.05 T (left) with the inverse susceptibility at high field, fitted using the Curie-Weiss law (right)

4.4.5. $GdScSiC_{0.5}$ and $LaScSiC_{0.5}$

The magnetic properties of the $GdScSiC_{0.5}$ and $LaScSiC_{0.5}$ materials were also investigated. The M(T) curves are shown in Figure 4. 35. with the inset showing a zoom on the M(T) curve for $LaScSiC_{0.5}$. $GdScSiC_{0.5}$ shows the most extreme reduction in the magnetic transition temperature through carbon insertion with its T_C decreasing from 354 K in the pristine GdScSi (Couillaud *et al.*, (2011)) to 113 K in $GdScSiC_{0.5}$ ($\Delta T_C = -241$ K) . The transition is also much broader in the carbide, taking place from 80 - 140 K, likely due to inhomogeneous distribution of carbon throughout the sample.

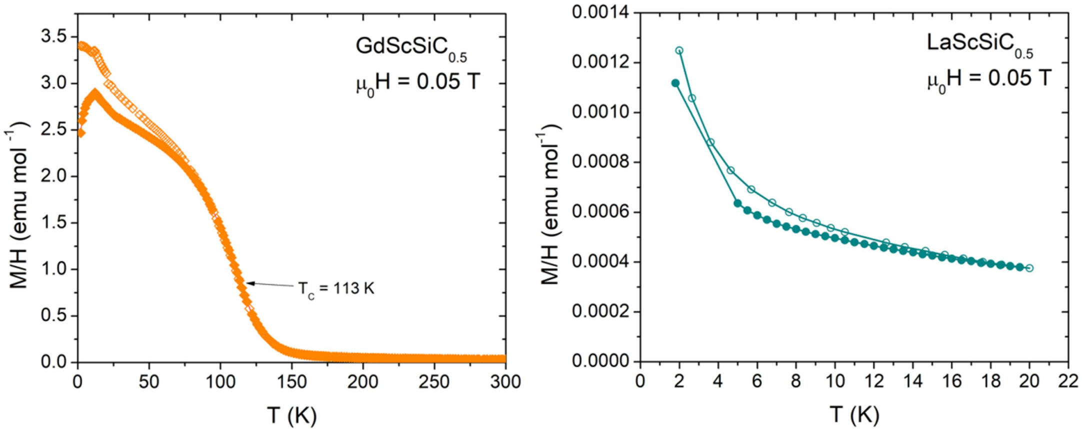

Figure 4. 35. M(T) curves for the *R*ScSiC$_{0.5}$ (*R* = La, Gd) systems for μ_0H = 0.05 T

It is clear that in all of the studied *R*ScSiC$_x$ compounds the magnetism of the rare earth element dominates the magnetic properties of the materials. Therefore it is interesting to examine a compound without this effect. For this purpose we synthesised a sample with the nominal composition LaScSiC$_{0.5}$. A non-magnetic rare earth element such as La is interesting for superconductivity but, also, for comparing with the C$_P$ measurements of the magnetic isotype phase. Such a comparison allows the extraction of the magnetic component of the C$_P$. From the ZFC-FC magnetisation curves for LaScSiC$_{0.5}$ shown in Figure 4. 35. it can be seen that, as expected, LaScSiC$_{0.5}$ is a Pauli paramagnet. There were no indications of superconductivity in the temperature range studied and unfortunately, due to both time constraints and a lack of liquid He, the C$_P$ of LaScSiC$_{0.5}$ could not be measured to provide the non-magnetic reference for these materials. It is, thus, necessary to measure this curve in the future to extract the magnetic portion of the specific heat capacity in a magnetically ordered *R*ScSiC$_{0.5}$ carbide.

4.5. Transport properties

As carbon insertion changes the interatomic distances and the magnetic properties of the parent compound, it was interesting to investigate the electronic transport properties of these compounds. Here we present the preliminary results of this investigation. 3mm pellets of the carbides (*R* = Ce, Nd) and pristine intermetallics were prepared and their resistance measured using the methods and instruments described in section 2.2.4. Due to the fact that the samples were cold pressed pellets rather than blocks or sintered pellets, their density is significantly lower than the theoretical density for the carbides. This means that only the resistance can be measured and not the resistivity which would take into account the size and thickness of the sample but requires a dense material.

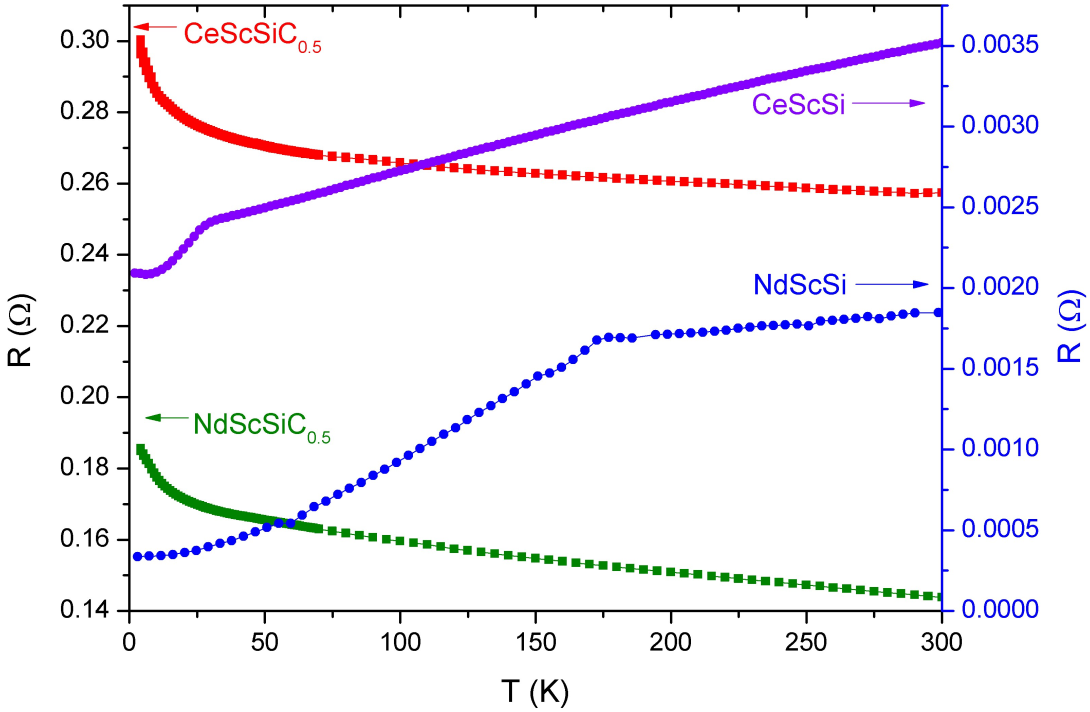

Figure 4. 36. Resistance of NdScSi (right axis), $NdScSiC_{0.41}$ and $CeScSiC_{0.50}$ (left axis)

Figure 4. 36. shows the R(T) measurements for the $NdScSiC_{0.5}$ and $CeScSiC_{0.5}$ samples and the pristine parent compounds. The pristine NdScSi and CeScSi compounds show classic metallic character where the resistance decreases steadily with temperature to a minimum value approaching 0 K. The R(T) curves for NdScSi and CeScSi show a change in the slope at around their Curie/Néel temperatures T_C = 171 K and T_N = 26 K respectively. This stems from the loss of scattering of the conduction electrons caused by the disordered spins in the paramagnetic state. Carburation causes not only a loss of the metallic type conduction of the parent compound but also a significant increase of roughly 100 times in the resistance of the material. The R(T) plots of the carbides show an increase in the resistance at low temperatures which does not correspond with the magnetic ordering temperatures. These preliminary measurements were performed on pellets, a more detailed study of the transport properties is required using blocks that have been well cut from good quality samples to determine the resistivity and also if the differences in magnitude of the resistances seen here are intrinsic to the respective phases or the result of differences between individual pellets. Due to the limited availability of liquid He for low temperature measurements, these experiments have not yet been performed.

4.6. Conclusions

We have developed a method of synthesising $R\mathrm{Sc}X\mathrm{C}_X$ (R = La-Nd, Gd and X = Si and Ge) intermetallic carbides by the inclusion of solid carbon during the synthesis. Carbon occupies the vacant $R_2\mathrm{Sc}_4$ octahedral sites, causing an increase in the *a* parameter and a decrease in the *c* parameter. Carbon content can be varied at the synthesis step resulting in the obtention of $R\mathrm{ScSiC}_X$ solid solutions with $0.0 \leq x \leq 0.5$ for R = Ce and $0.25 \lesssim x \leq 0.5$ for R = Nd. This leads to a reduction of the Curie temperature in the NdScSi system from 171 K for the pristine compound to around 50 K in the filled carbide $\mathrm{NdScSiC}_{0.5}$. Filling of the CeScSi 2*b* octahedral site with carbon causes a decrease in the Néel temperature from 27 K to 13.5 K. The intermediate carbide $\mathrm{CeScSiC}_{0.25}$ shows a more complex effect on the magnetic behaviour however. Neutron diffraction measurements have also been used to determine the magnetic structures of $\mathrm{NdScSic}_{0.5}$ and $\mathrm{CeScSiC}_{0.25}$. $\mathrm{NdScSiC}_{0.5}$ shows ferromagnetic alignment of Nd moments along the *c* axis while $\mathrm{CeScSiC}_{0.5}$ shows single planes of Ce moments coupled ferromagnetically in the *ab* plane and antiferromagnetically along the *c* axis. Above T_s = 3.5 K the magnetic moments are parallel to the *ab* plane. At T_s = 3.5 K $\mathrm{CeScSiC}_{0.5}$ displays a spin reorientation out of the *ab* plane, forming an angle of 65.2 ° with the *c* axis at 1.8 K. Carbon insertion in the CeScSi and NdScSi phases also causes a change in the electronic transport properties. The pristine compounds show resistance that decreases with decreasing temperature as is typical for metallic compounds. On the contrary, the carbides show a marked increase in the resistance with decreasing temperature and an increase in the overall resistance value with respect to that of the pristine compounds. Calculations of the electronic structure are needed in order to adequately explain the modification of magnetic and transport properties of the pristine compounds upon carburation.

4.7. Bibliography

Atoji, M. ((1966)) 'Crystals and magnetic structures of CeC_2, PrC_2 and NdC_2', Physics Letters. Elsevier BV, 22(1), p. 21–22. doi: 10.1016/0031-9163(66)90039-4.

Atoji, M. ((1978)) 'Neutron diffraction studies of Pr_2C_3, Nd_2C_3, and Dy_2C_3 at 300 to 1.6K', Journal of Solid State Chemistry. Elsevier BV, 26(1), p. 51–57. doi: 10.1016/0022-4596(78)90132-9.

Banakh, O. E. and Kotur, B. Y. ((1998)) 'The Sc–Nd–Si ternary system at 870 K', *Journal of Alloys and Compounds,* , 268, p. L3–L5. doi: 10.1016/S0925-8388(97)00593-8.

Boulet, P., Weitzer, F., Hiebl, K. and Noel, H. ((2001)) 'Structural chemistry, magnetism and electrical properties of binary Nd silicides', *Journal of Alloys and Compounds,* 315(1–2), p. 75–81. doi: 10.1016/S0925-8388(00)01304-9.

Chevalier, B., Hermes, W., Heying, B., Rodewald, U. C., Hammerschmidt, A., Matar, S. F., Gaudin, E. and Pöttgen, R. ((2010)) 'New Hydrides REScSiH and REScGeH (RE = La, Ce): Structure, Magnetism, and Chemical Bonding', *Chemistry of Materials*, 22(17), p. 5013–5021. doi: 10.1021/cm101290f.

Couillaud, S., Gaudin, E., Franco, V., Conde, A., Pöttgen, R., Heying, B., Rodewald, U. C. U. C. and Chevalier, B. ((2011)) 'The magnetocaloric properties of GdScSi and GdScGe', *Intermetallics*, 19(10), p. 1573–1578. doi: 10.1016/j.intermet.2011.06.001.

Haynes, W. M. ((2010)) CRC Handbook of Chemistry and Physics, 91st Edition. 91st edn. Edited by W. M. Haynes. Taylor & Francis.

Jedlicka, H., Nowotny, H. and Benesovsky, F. ((1971)) 'Zum System Scandium-Kohlenstoff, 2. Mitt.: Kristallstruktur des C-reichen Carbids', *Monatshefte fur Chemie*, 102(2), p. 389–403. doi: 10.1007/BF00909332.

Kammler, D. R., Rodriguez, M. A., Tissot, R. G., Brown, D. W., Clausen, B. and Sisneros, T. A. ((2008)) 'In-Situ Time-of-Flight Neutron Diffraction Study of High-Temperature Phase Transition in Elemental Scandium', *Metallurgical and Materials Transactions A*, 39(12), p. 2815–2819. doi: 10.1007/s11661-008-9642-y.

Krikorian, N. H., Bowman, A. L., Krupka, M. C. and Arnold, G. P. ((1969)) 'The preparation and crystal structure of Sc_4C_3', *High Temperature Science,* 1, p. 360–366.

Manfrinetti, P., Morozkin, A. V., Isnard, O., Henry, P. and Palenzona, A. ((2008)) 'Magnetic structure of the CeScSi-type RScGe compounds (R = Pr, Nd, Tb)', *Journal of Alloys and Compounds,* 450(1–2), p. 86–91. doi: 10.1016/j.jallcom.2006.11.057.

Mizoguchi, H. and Hosono, H. ((2011)) 'La_2Sb, a layered superconductor with metal-metal bonds.', *Chemical communications*, 47(13), p. 3778–80. doi: 10.1039/c0cc05384h.

Nowotny, H. and Auer-Welsbach, H. ((1961)) 'Uber das Scandiumcarbid', *Monatshefte fur Chemie*, 92(3), p. 789–793. doi: 10.1007/BF00918639.

Obbade, S., Isnard, O., Miraglia, S. and Fruchart, D., ((1991)) 'Hydrogenation, crystal structure and magnetic ordering of R2Fe14C (R ≡ Sm, Er, Tm)', *Journal of the Less Common Metals*, 168(2), pp. 321–328. doi: 10.1016/0022-5088(91)90314-T.

Pöttgen, R. and Jeitschko, W. ((1991)) 'Scandium carbide, Sc_3C_4, a carbide with C_3 units derived from propadiene', *Inorganic Chemistry*, 30(3), p. 427–431. doi: 10.1021/ic00003a013.

Ritter, C., Provino, A., Manfrinetti, P. and Pathak, A. K. ((2016)) 'Tetragonal to triclinic structural transition in the prototypical CeScSi induced by a two-step magnetic ordering: a temperature-dependent neutron diffraction study of CeScSi, CeScGe and LaScSi', *Journal of Physics: Condensed Matter*, 29(4), p. 45802. doi: 10.1088/1361-648X/29/4/045802.

Singh, S. K., Dhar, S. K., Manfrinetti, P., Palenzona, A. and Mazzone, D. ((2004)) 'High magnetic transition temperatures in RScT (R = Pr, Nd and Sm; T = Si and Ge) compounds: Multiple spin reorientations in PrScGe', *Journal of Magnetism and Magnetic Materials*, 269(1), p. 113–121. doi: 10.1016/S0304-8853(03)00583-3.

Singh, S. K., Dhar, S. K., Mitra, C., Paulose, P. L., Manfrinetti, P. and Palenzona, A. ((2001)) 'The nature of magnetism in CeScSi and CeScGe', *Journal of Physics: Condensed Matter,* 13(16), p. 3753–3766. doi: 10.1088/0953-8984/13/16/306.

Spedding, F. H., Hanak, J. J. and Daane, A. H. ((1961)) 'High temperature allotropy and thermal expansion of the rare-earth metals', *Journal of the Less Common Metals*, 3(2), p. 110–124. doi: 10.1016/0022-5088(61)90003-0.

Tencé, S., Mahon, T., Gaudin, E., Chevalier, B., Bobet, J.-L. J.-L., Flacau, R., Heying, B., Rodewald, U. C. U. C. and Pöttgen, R. ((2016)) 'Hydrogenation studies on NdScSi and NdScGe', *Journal of Solid State Chemistry*, 242, p. 168–174. doi: 10.1016/j.jssc.2016.02.017.

Chapter 5: Hydrogenation of the RScSi$C_{0.5}$ carbides (R = Ce and Nd)

In the previous two chapters we have discussed the insertion of hydrogen and carbon separately into CeScSi-type intermetallics. Both elements conserve the *I4/mmm* space group of the pristine compound with a marked change in the unit cell parameters. Carbon insertion causes an increase in the *a* parameter and a decrease in the *c* parameter while hydrogenation has the opposite effect. While hydrogen has been shown to be able to occupy both the R_4 tetrahedral sites and the square based pyramidal RSc_4 sites, carbon can only occupy the R_2Sc_4 octahedra.

As carbon insertion leaves the R_4 tetrahedra empty we attempted to see if hydrogen could be inserted into these empty sites in the carbides. A number of hydride carbide compounds have been described to date in the literature. The preparation of these materials can be carried out using a range of different techniques: Nguyen *et al.*, (2015) describe the electrochemical insertion of hydrogen in sub-stoichiometric TiC_{1-x} materials. $(Ti_{0.8}V_{0.2})C_{0.62}H_x$ materials were prepared using self-propagating high temperature methods by Tashmetov *et al.*, (2005) through reaction of metallic Ti and V powders and carbon. Self-propagating high temperature synthesis relies on a highly exothermic reaction between two or more of the reactants to provide the driving force for the reaction. The most well-known example is undoubtedly the thermite reaction which produces pure iron from Fe_2O_3 and Al metal (Munir and Anselmi-Tamburini, (1989)). It was shown by Lang *et al.*, (2010) that Ca_2LiC_3H, which contains the rare C_3^{4-} ion, could be prepared by the reaction between CaH_2 and carbon in a Ca/Li flux. Our own hydrogenation experiments are carried out by solid gas reaction at high temperature and pressure. This technique has been well documented by, for example, Obbade *et al.*, (1991) who describe the synthesis of $R_2Fe_{14}CH_x$ compounds (R = Sm, Tm and Er), Isnard *et al.*, (1993) where the synthesis of $Th_2Fe_{17}C_xH_{5-x}$ is described and Skripov *et al.*, (2009) who produced a range of $NbC_{1-y}H_x$ compounds which can crystallise in a cubic (*Fm-3m*), orthorhombic (*Pmmm*) and tetragonal (*I4/mmm*) symmetries depending on the hydrogen (deuterium) content with this method. This technique was also used by Zhang *et al.*, (2012) to produce $La(Fe_{1-x}Si_x)_{13}C_{0.2}H_y$ (x = 1.3) in order to study its magnetocaloric effect. In this chapter we will present the results of our attempts to form hydride-carbide phases using the carbides described in chapter 4 as precursors and the effect that hydrogenation has on the structural and magnetic properties of the parent phase.

5.1. Synthesis

The hydride carbide compounds are synthesised by solid-gas reaction between the carbide materials described in chapter 4 and hydrogen gas similarly to the hydride compounds in chapter 3. However, possibly due to the chemical pressure exerted on the tetrahedral site by the filled octahedral sites, the required hydrogenation conditions for the carbides are significantly more extreme than generally needed for the hydrogenation of the pristine intermetallic. In general the pure hydrides could be synthesised by exposing the sample to 5 – 10 bars of H_2 pressure at 250 – 350 °C for several hours. For the hydrogenation of the carbides, these conditions did not provide any evidence that hydrogen had been inserted. We determined that in order to carry out the insertion for the carbides, 450 ^{0}C and 40 bars of H_2 pressure over 24 hours was required. The resulting hydrides are stable in air and show decrepitation as a result of hydrogenation. Their colour had also darkened from silvery to a dark grey colour.

5.2. Crystallographic properties

5.2.1. X-ray diffraction of $R\mathrm{ScSiC}_{0.5}\mathrm{H}_x$ (R = Ce, Nd)

After the hydrogenation was carried out, the samples were crushed and PXRD was performed to determine if any change in the unit cell parameters could be observed. The samples had noticeably decrepitated, being softer and easier to grind than the initial carbide material. Figure 5. 1. shows a comparison of the powder XRD patterns of the samples with nominal compositions $\mathrm{CeSc}_{1.05}\mathrm{SiC}_{0.5}$ and $\mathrm{NdSc}_{1.05}\mathrm{SiC}_{0.5}$ before and after hydrogenation. A small change in the unit cell parameters can be observed by considering, for example, the (00*l*) and (*hk*0) peaks of the $\mathrm{NdSc}_{1.05}\mathrm{SiC}_{0.5}$ sample. The *a* parameter changes from 4.4107(4) Å to 4.3996(4) Å (-0.25%) and the *c* parameter from 15.389(1) Å to 15.4612(3) (+0.47%) Å. This change in the unit cell parameters is consistent with the filling of the tetrahedral sites as seen for the hydrogenation of the GdScGeH and GdTiGeH compounds and provides a promising indication that hydrogen has indeed been inserted into $\mathrm{NdSc}_{1.05}\mathrm{SiC}_{0.5}$. Hydrogenation for longer than 24 hours showed no further change in the unit cell parameters, indicating that no more hydrogen can be inserted under these conditions. The unit cell parameters for all of the compounds in the NdScSi and CeScSi families of insertion compounds (pristine, hydride, carbide and carbide-hydride) are gathered in Table 5. 1. Due to the fragility of these samples, attempts to isolate a useable crystal for single crystal X-ray diffraction were unsuccessful. Structural characterisation was therefore carried out using powder diffraction methods.

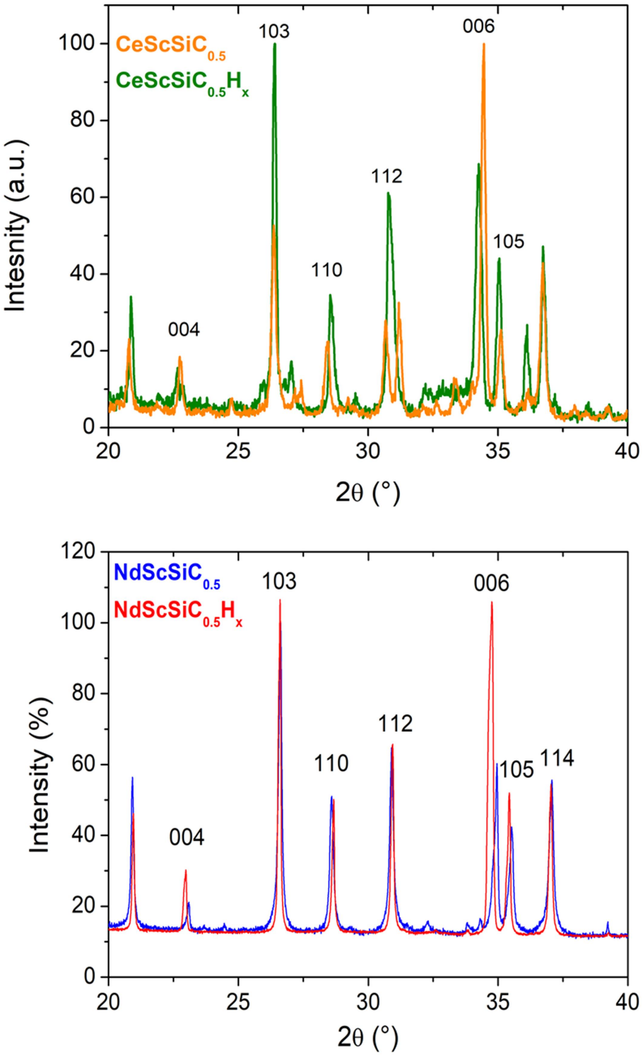

Figure 5. 1. X-ray diffraction patterns for $CeScSiC_{0.5}$ and $CeScSiC_{0.5}H_X$ (top) and $NdScSiC_{0.5}$ and $NdScSiC_{0.5}H_x$ (bottom).

Table 5. 1. Unit cell parameters of *R*ScSi, RScSi$H_{1.5}$, RScSi$C_{0.5}$ and RScSi$H_xC_{0.5}$ phases (*R* = Nd, Ce) from refinement of powder XRD data.

System	*a* (Å)	*c* (Å)	V (Å^3)	*c*/*a*
NdScSi[a]	4.2894(6)	15.705(3)	288.956	3.661
$NdScSiH_{1.5}$[a]	4.221(1)	16.928(2)	301.603	4.010
$NdScSiC_{0.5}$	4.4107(4)	15.389(1)	299.381	3.489
$NdSc_{0.92(1)}Si\ C_{0.5}H_{0.14(1)}$	4.3996(3)	15.4612(3)	299.274	3.514
CeScSi[b]	4.3231(5)	15.852(2)	296.261	3.667
CeScSiH[c]	4.25443(12)	16.751(6)	303.196	3.937
$CeScSiC_{0.5}$	4.4290(4)	15.683(1)	307.638	3.541
$CeSc_{0.90(2)}SiC_{0.49(2)}H_{0.25(4)}$	4.4132(2)	15.6876(1)	305.537	3.555

[a] Tencé *et al.*, (2016)
[b] Singh *et al.*, (2001)
[c] Chevalier *et al.*, (2010)c

5.2.2. High Resolution Neutron Powder diffraction on $NdScSiC_{0.5}H_x$

In order to determine the exact crystallographic location and occupancy of the hydrogen atoms in the new $NdScSiC_{0.5}H_x$ structure, high resolution neutron diffraction data was collected on the D2B diffractometer at the ILL in Grenoble, France. Initial Rietveld refinement of the neutron diffraction data was carried out without including hydrogen in the structural model. Once the refinement had converged, Fourier difference analysis between the observed and calculated data was performed to determine if there was any residual nuclear density. Figure 5. 2.(a) shows the Fourier difference map before the inclusion of hydrogen. The image is the z = ¼ cross-section of the map. It clearly evidences a minimum in the nuclear density in the (0 ½ ¼) position, *i.e.* inside the Nd_4 tetrahedral sites. This suggests the presence of H atoms which have a negative coherent neutron scattering length for neutrons (b_C (H) = -3.74 fm) (Sears, (1992)). The residual nuclear density in the (0 ½ ¼) site is not negative however, which suggests that the site is only partially filled.

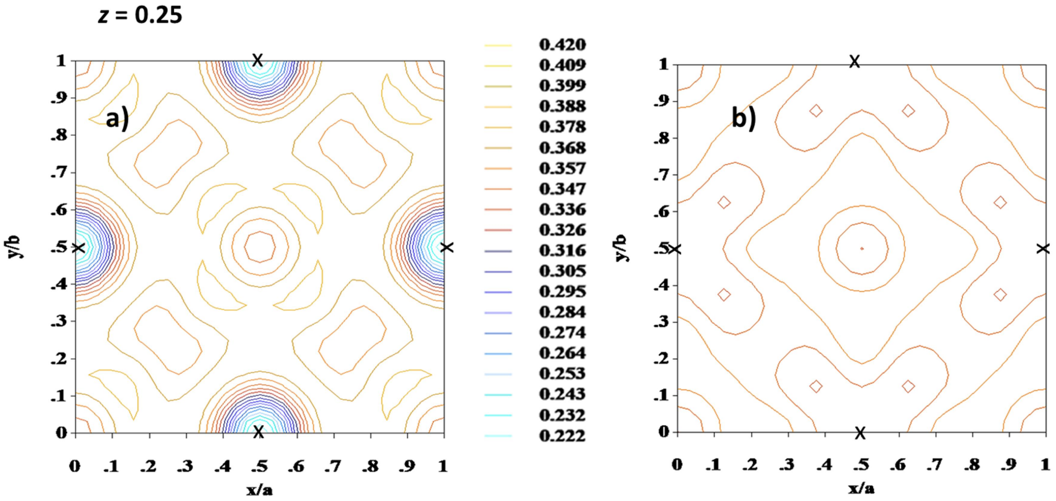

Figure 5. 2. Fourier difference map from the nuclear structure refinement of $NdSc_{0.92(1)}Si\,C_{0.5}H_{0.14(1)}$ before (a) and after (b) the inclusion of H atoms. Images shown are for z = 0.25. The centres of the tetrahedral sites are marked with a cross.

Figure 5. 2. (b) shows the Fourier difference map of the refinement after a hydrogen atom was added to the (0, ½, ¼) site with a refined occupancy of 14 %. It clearly shows that there is no remaining nuclear density on the site. The inclusion of hydrogen has, therefore, accounted for the residue seen in Figure 5. 2. (a). Ritter *et al.*, (2016) describe, in their neutron diffraction experiments on CeScSi, an occupancy of the Sc sites of 0.912(5). The initial Fourier difference analysis of this material was carried out using a filled Sc site. This revealed the presence of too much Sc atoms in our structural model. Subsequent refining of the occupancy of the Sc site gave an improvement of the Bragg-R factor from 5.91 to 5.6 and a final Sc occupancy of 0.92 (1) which is close to the result in Ritter *et al.*, (2016). There is no residual nuclear density in other parts of the structure which confirms that the octahedra are still completely filled by carbon and that hydrogen does not replace the carbon on these sites. Rietveld refinement of the neutron diffraction data over the whole angular range (5 - 150 °) for $NdSc_{0.92(1)}SiC_{0.5}H_{0.14(1)}$ can be seen in Figure 5. 3. The only

detectable secondary phase was Sc_2OC which is present in all of the carbide samples. The parameters of this refinement and the refined crystal structure are shown in Table 5. 2. and Table 5. 3. respectively. The structural model used for the carbides with the addition of hydrogen in the Nd_4 tetrahedra provides a very good fit of the observed data with the hydrogen site only 14(1) % occupied. Such low site occupancy can be explained by considering the antagonistic effect of filling the tetrahedral and octahedral sites by H and C atoms respectively. A representation of the refined nuclear structure is shown in Figure 5. 4.

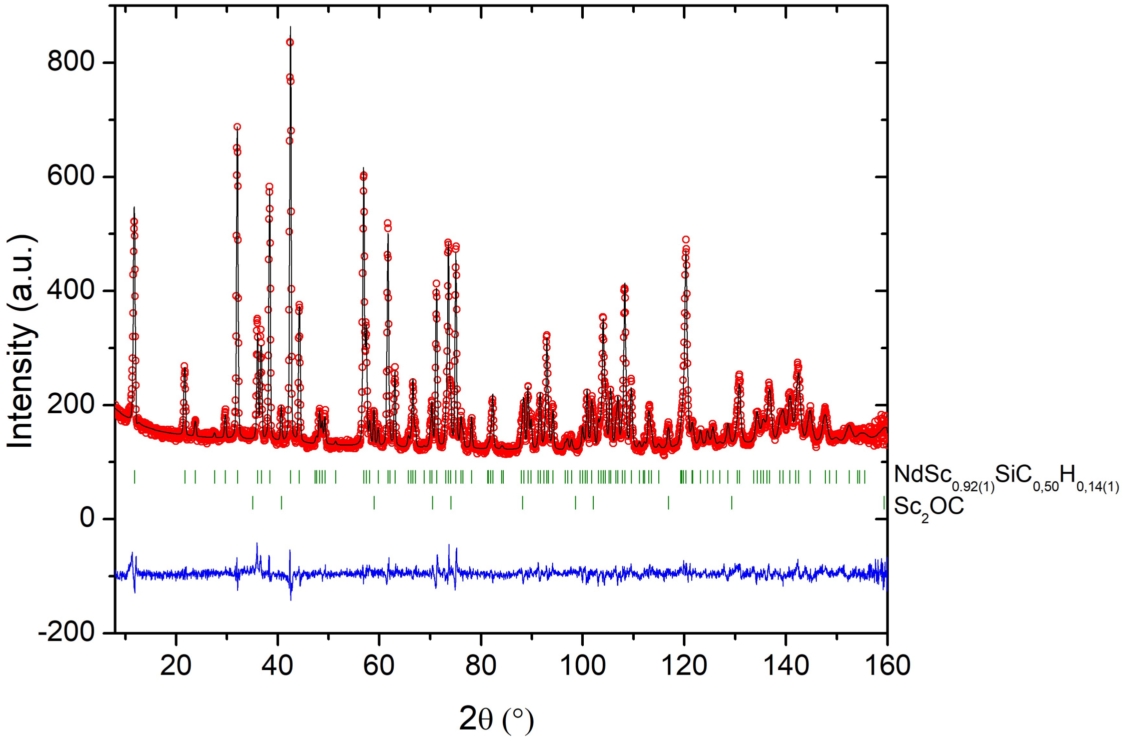

Figure 5. 3. Refinement of the high resolution neutron powder diffraction pattern collected at room temperature with λ = 1.5946 Å.

Table 5. 2. Summary of the phase details for the nuclear structure refinement shown in Figure 5. 3.

Phase	**a (Å)**	***c* (Å)**	**Amount (Wt.%)**	**R-Bragg (%)**	**R_p (%)**	**R_{wp} (%)**
$NdSc_{0.92(1)}SiC_{0.5}H_{0.14(1)}$	4.39986(4)	15.4657(3)	99(1)	5.6	16.6	13.6
Sc_2OC	4.5847(2)	-	1.0(3)	5.2		

Table 5. 3. The refined crystal structure of $NdSc_{0.92(1)}SiC_{0.5}H_{0.14(1)}$.

Atom	x	y	z	B_{iso} (Å^2)	Occ.
Nd	0	0	0.333(1)	0.55(2)	1.00
Sc	0	0.5	0	0.55(2)	0.92(1)
Si	0	0	0.127(2)	0.55(2)	1.00
C	0	0	0.5	0.33(5)	0.50(2)
H1	0	0.5	0.25	1.7(3)	0.14(1)

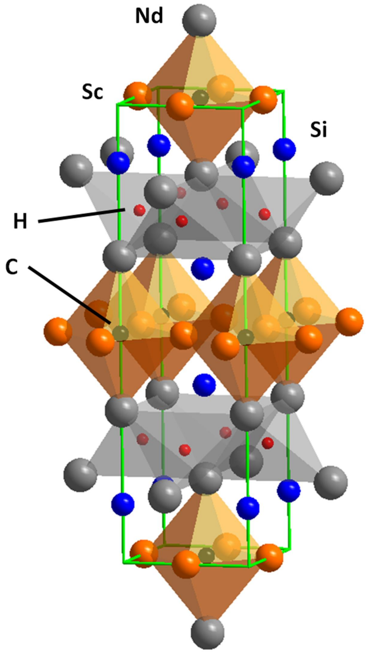

Figure 5. 4. The crystal structure of $NdSc_{0.92(1)}SiC_{0.5}$ $H_{0.14(1)}$ emphasising the octahedral and tetrahedral sites for carbon and hydrogen atoms respectively.

5.2.3. Neutron diffraction of $CeScSiC_{0.5}H_x$

In order to determine the quantity of hydrogen present in $CeScSiC_{0.5}H_x$, neutron diffraction data were collected on the G4.4 beamline at the LLB in Saclay, France using the wavelength λ = 1.9587 Å. The secondary phases were determined to Sc_2OC and $Ce_{15}Si_9C$, in agreement with XRD data on this sample. The latter phase was refined based on the structure for $Ce_{15}Ge_9C$ (filled Ce_5Ge_3 structure) published by Tencé *et al.*, (2014) with modified unit cell parameters. The major $CeScSiC_{0.5}H_x$ phase was refined using the structure of $NdSc_{0.92(1)}SiC_{0.5}H_{0.14(1)}$ as a starting point. This model gives good fit of the experimental data with an occupancy of the hydrogen site of 25(4) % and with a larger B_{iso} value than the other atoms, as seen for the Nd analogue. Also Like the Nd analogue, there is a small substoichiometry on the Sc site. Attempts to include Ce substitution on the Sc site worsened the fit however. The refinement can be seen in Figure 5. 5. while the refinement details are summarised in Table 5. 4. and Table 5. 5.

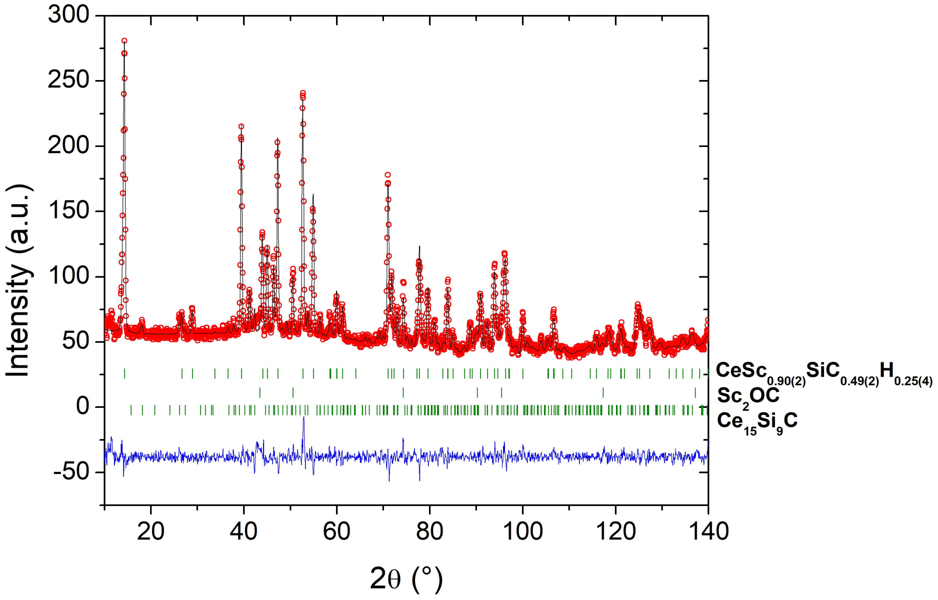

Figure 5. 5. Rietveld refinement of high resolution neutron diffraction data on for CeSc$_{0.90(2)}$SiC$_{0.49(2)}$H$_{0.25(4)}$. Measured on the G4.4 beamline of the LLB, Saclay, France with λ = 1.9587 Å

Table 5. 4. Summary of the phase details for CeSc$_{0.90(2)}$SiC$_{0.49(2)}$H$_{0.25(4)}$ nuclear structure refinement at 100 K shown in Figure 5. 5.

Phase	a (Å)	*c* (Å)	R-Bragg (%)	R$_p$ (%)	R$_{wp}$ (%)
CeSc$_{0.90(2)}$SiC$_{0.49(2)}$H$_{0.25(4)}$	4.4132(2)	15.6876(2)	5.0		
Sc$_2$OC	4.580(1)	-	13.9	20.7	19.1
Ce$_{15}$Si$_9$C	14.355(2)	6.037(3)	6.7		

Table 5. 5. The refined crystal structure CeSc$_{0.90(2)}$SiC$_{0.49(2)}$H$_{0.25(4)}$.

Atom	x	y	z	B$_{iso}$ (Å^2)	Occ.
Ce	0	0	0.332(1)	2.0(4)	1.00
Sc	0	0.5	0	1.2(2)	0.90(2)
Si	0	0	0.125(1)	2.0(4)	1.00
C	0	0	0.5	1.5(4)	0.49(2)
H1	0	0.5	0.25	4.4(8)	0.25(4)

5.2.4. Discussion of the interatomic distances in NdSc$_{0.92(2)}$SiC$_{0.5}$H$_{0.14(1)}$

Within the same family of materials (hydrides, carbides or hydride-carbides) the same general trends in interatomic distances are observed irrespective of rare earth element. Thus a detailed discussion of each compound would quickly become highly repetitive. For this reason the distances of the Nd family of compounds will be discussed here as this compound has received the most rigorous structural investigation of the two studied carbide-hydrides.

The hydrogenation of $NdScSiC_{0.5}$ changes the interatomic distances in the same way that hydrogenation of the pristine NdScSi does. However, the difference in the interatomic distances between the hydride-carbide and the parent carbide are generally quite small. This is unsurprising given the low occupation of the hydrogen site and the relatively small change in the unit cell parameters. All Nd-Nd distances decrease with the insertion of hydrogen, consistent with a very slight contraction of the Nd_4 tetrahedra. The internal tetrahedral angles for the entire $NdScSiC_xH_y$ system (x = 0 and 0.5 y = 0, 0.14(1) and 1.5) are given in table 5. 6. while the interatomic distances for the all studied Ce and Nd systems are summarised in table 5. 7. The distance between the Nd atoms and the tetrahedral centre changes from 2.5483(3) Å to 2.547(8) Å. A similarly small change is observed in the two tetrahedral angles formed by Nd-*Td*-Nd (*Td* = centre of the tetrahedron) contracting from 104.56° to 104.42° and expanding from 119.81° to 120.12 ° respectively (table 5. 6.). In fact carbon insertion into NdScSi causes a regularisation of one of the tetrahedral angles, changing from 102.97° to 104.56, closer to the ideal tetrahedral angle of 109.5°. Meanwhile, the second angle moves further from ideality. Hydrogenation of pristine NdScSi slightly reduces the tetrahedral angle from 102.64° to 102.97° and expands the second angle from 123.44° to 124.21°. Thus the same trend is produced on hydrogenating the carbide and the pristine compound.

Table 5. 6. Evolution of the internal tetrahedral angles of NdScSi during light element insertion .

	Angle (°)			
	NdScSi	**$NdScSiH_{1.5}$**	**$NdScSiC_{0.5}$**	**$NdSc_{0.92(2)}SiC_{0.5}H_{0.14(1)}$**
Nd-*Td*-Nd	102.97	102.64	104.56	104.42
	123.44	124.21	119.81	120.12

There is a slight increase in the Nd-C carbon distances from 2.57 Å to 2.58(2) Å combined with a slight decrease in the Si-C distances from 3.6937(2) Å to 3.679(17) Å. Only a small variation is observed in the other distances. The d_{Nd-H} = 2.547(8) Å in the carbide hydride is significantly larger than d_{Nd-H1} = 2.388(8) Å in the $NdScSiH_{1.5}$ hydride (Tencé *et al.*, (2016)) and binary NdH_2 of 2.368 Å (Korst and Warf, (1966)). Furthermore, it has been documented in the study of other carbide-hydrides such as Y_2CD_x (Maehlen *et al.*, (2003)) that hydrogen and carbon exhibit repulsive interactions in these sorts of systems with this compound undergoing a structural transition during its deuteration to minimise the interaction between carbon and hydrogen atoms. The strong bonding between the carbon and Nd atoms anchors the Nd planes and resists the contraction of the tetrahedral sites. Coupled with a likely repulsive interaction between H and C that prevents the Nd and Sc/Si layers moving closer this inhibits complete filling of the Nd_4 tetrahedra.

The changes in the interatomic distances in the Ce system follow the same trend as the Nd analogue but there is a larger change in the interatomic distances which can be linked to the larger amount of hydrogen inserted.

Table 5. 7. The interatomic distances of the RScSiC$_y$H$_x$ (R = Ce, Nd) x = 0, 0.14(1), y = 0, 0.5) family of intermetallic compounds calculated from refinement of room temperature XRD data. *Oh*, *Td* and *SP* indicate the distances (in *italics*) to the empty octahedral, tetrahedral and square based pyramidal sites respectively.

	d (Å)							
Atom	**NdScSi**	**NdScSiH$_{1.5}$[c]**	**NdScSiC$_{0.5}$**	**NdSc$_{0.92(2)}$SiC$_{0.5}$H$_{0.14(1)}$**	**CeScSi[d]**	**CeScSiH[e]**	**CeScSiC$_{0.5}$**	**CeSc$_{0.90(2)}$SiC$_{0.49(2)}$H$_{0.25(4)}$**
***R*-*R*[a]**	3.8112(4)	3.729(4)	4.0309(5)	4.033(14)	3.8498(5)	3.814(3)	4.09(9)	4.044(14)
***R*-*R*[b]**	4.2894(6)	4.221(1)	4.4107(4)	4.3999(1)	4.3283(5)	4.2544(1)	4.4288(1)	4.4132(2)
***R*-Sc**	3.5051(5)	3.76(1)	3.3868(4)	3.39(1)	3.5288(5)	3.690(27)	3.42(7)	3.437(12)
***R*-Si**	3.1480(4)	3.244(9)	3.1452(5)	3.172(7)	3.1822(9)	3.214(4)	3.18(2)	3.193(5)
***R*-Si’**	3.1507(14)	3.50 (2)	3.1744(2)	3.19(2)	3.207(3)	3.48(1)	3.21(9)	3.25(2)
R*-C/*Oh	*2.7724(6)*	*3.115(17)*	2.5704(5)	2.58(2)	*2.7873(6)*	*3.015(3)*	2.60(9)	2.636(15)
R*-H1/*Td	*2.4354(3)*	2.388(8)	*2.5483(3)*	2.547(8)	*2.4591(3)*	2.4290(16)	*2.5640*	2.554(8)
R*-H2/*SP	*2.49(2)*	2.81(2)*	2.29(2)	*2.30(2)*	*2.502(15)*	2.714(3)*	*2.321(95)*	*2.35(2)*
Sc-Sc	3.0331(3)	2.9847(2)	3.1188(2)	3.1112(1)	3.0331(4)	3.0083(1)	3.1316(1)	3.1206(1)
Sc-Si	2.8848(5)	2.80(1)	2.9630(2)	2.95(2)	2.8848(5)	2.841(7)	3.005(9)	2.95(1)
Sc-C/*Oh*	*2.1147(3)*	*2.1105(5)*	2.2053(2)	2.1999(1)	*2.1447(3)*	*2.1282(1)*	2.2144(1)	2.2066(1)
Sc-H1/*Td*	*3.9262(8)*	4.2320(8)	*3.8472(3)*	3.8664(1)	*3.9550(5)*	4.1879(2)	*3.9207(3)*	3.9219(1)
Sc-H2/*SP*	*2.1633(21)*	2.132(2)	*2.223(2)*	*2.218(2)*	*2.183(2)*	2.1485(1)*	*2.232(2)*	*2.225(2)*
Si-C/*Oh*	*3.5947(3)*	*3.509(9)*	3.6937(2)	3.679(17)	*3.5947(7)*	*2.1272(1)*	3.733(7)	3.686(8)
Si-H1/*Td*	*2.9304(9)*	3.19(1)	*2.8904(2)*	2.908(20)	*3.770(9)*	3.137(7)	*2.911(8)*	2.952(10)
Si-H2/*SP*	*3.451(8)*	3.36(1)	*3.553(7)*	*3.539(17)*	*3.468(8)*	3.399(5)*	*3.5868(98)*	*3.54(1)*

[a] distance between adjacent layers

[b] distance within the same layer

* calculated using z_{H2} = (0, 0, 0.518)

[c] Tencé *et al.*, (2016)

[d] Singh *et al.*, (2001)

[e] Chevalier *et al.*, (2010)c

H1 – R_4 tetrahedra

H2 – RSc$_4$ square based pyramids

5.3. Magnetic properties

5.3.1. Magnetic properties of $NdSc_{0.92(2)}SiC_{0.5}H_{0.14(1)}$

As discussed for the hydrides in chapter 3, hydrogen insertion into the pristine CeScSi-type compound leads generally to reduction or even destruction of the magnetic order. This may be caused by a number of things such as an electronic effect arising from the interaction between the hydrogen and rare earth atoms or the negative pressure effect from the expansion of the unit cell volume.

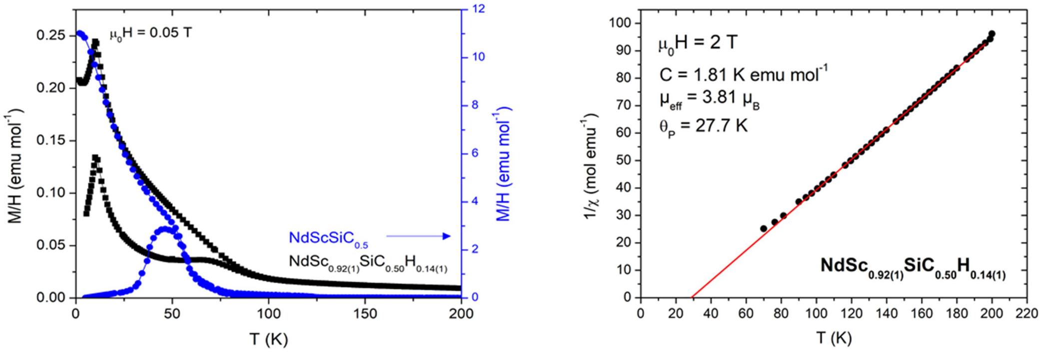

Figure 5. 6. Left) ZFC-FC magnetisation curves for $NdScSiC_{0.5}$ and $NdSc_{0.92(1)}SiC_{0.5}H_{0.14(1)}$ in a field of 0.05 T. Right) inverse magnetic susceptibility fitted using the Curie-Weiss type law.

Figure 5. 6. (left) shows the ZFC-FC magnetisation curves for the $NdSc_{0.92(1)}SiC_{0.5}H_{0.14(1)}$ sample and its parent carbide measured in a field of 0.05 T. It is clear from the ZFC-FC curves in Figure 5. 6. that the insertion of hydrogen induces a change in the type of magnetic order of the material. The jump seen at around T_C = 55 K in the initial ferromagnetic carbide material is replaced by a peak at 10 K, indicating the onset of an antiferromagnetic order. A small shoulder is seen in the ZFC curve of the carbide hydride around 70 K with a corresponding divergence between the ZFC and FC curves. This is linked to the magnetic ordering and anisotropy of a magnetic impurity phase, possibly Nd_5Si_4 or $Nd_{15}Si_9C$ which were observed in X-ray diffraction measurements of earlier samples. The first of these was described by Boulet *et al.*, (2001) as a ferromagnet with a T_C of 67 K and is observed in small amounts in the XRD pattern of the parent carbide. The second phase has not been directly discussed in the literature but Wrubl *et al.*, (2011) and Tencé *et al.*, (2014) describe $Nd_{15}Ge_9C$ as a ferromagnetic material with a T_C of 70 K. No evidence of either phase was observed in the XRD or neutron diffraction patterns of this sample however, so this cannot be confirmed. This change in the type of magnetic order is particularly novel when compared to other previously studied carbide-hydride intermetallics such as $Th_2Fe_{17}C_xH_{5-x}$ (Isnard *et al.*, (1993)) and $R_2Fe_{14}CH_x$ (Obbade *et al.*, (1991)). These compounds are generally studied for possible use as permanent magnetic materials and hydrogen insertion into the carbide has been shown to increase the Curie temperatures of the parent material. However, these systems are rich in iron and it is in fact the Fe-Fe magnetic interactions which drive their magnetic properties and the changes induced by

hydrogenation. As shown in the inverse of the susceptibility versus temperature plot (Figure 5. 6. (Right)) $NdSc_{0.92(1)}SiC_{0.5}H_{0.14(1)}$ is a Curie-Weiss paramagnet like NdScSi and $NdScSiC_{0.5}$. The calculated effective magnetic moment of 3.81 μ_B Nd^{-1} is slightly higher than the value of 3.62 μ_B Nd^{-1} expected from a Nd^{3+} system. Thus the Nd is magnetic in this compound just as in the pristine and carbide materials. The unusually high effective moment may be due to contributions from a magnetic impurity phase. Interestingly, the paramagnetic Curie temperature shows a positive value of 27.7 K suggesting that the predominant local interactions between Nd atoms are ferromagnetic. The θ_P = 27.7 K seen here is rather far from the observed T_N of 10 K. This may be explained either by a shift in the ordering temperature by the field or else by the presence of a magnetic impurity.

The specific heat capacity of $NdSc_{0.92(1)}SiC_{0.5}H_{0.14(1)}$ (Figure 5. 7) displays a lambda peak at 10 K, confirming the Néel temperature assigned from the maximum of the peak in the ZFC-FC magnetisation curve of Figure 5. 6.

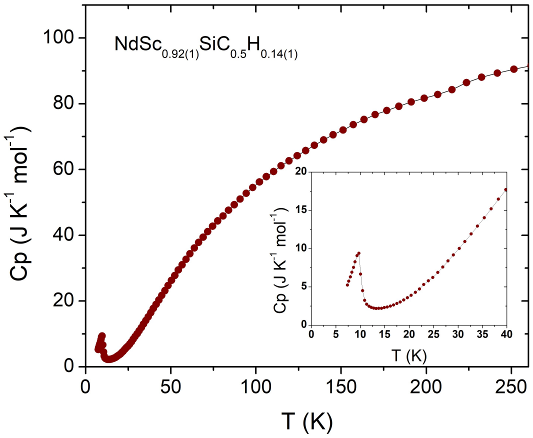

Figure 5. 7. Heat capacity at constant pressure of the $NdSc_{0.92(1)}SiC_{0.5}H_{0.14(1)}$ system down to low temperatures. The inset shows a zoom of the low temperature section.

In Figure 5. 8. the isothermal magnetisation curves for the $NdScSiC_{0.5}H_{0.14(1)}$ sample can be seen for the entire 0 - 7 T range. The curves above the T_N of the material are almost linear, as expected for a paramagnetic state. Below T_N the low field part of the curves is linear, confirming the antiferromagnetic order that was assigned from the ZFC-FC magnetisation measurements. Furthermore, we observe a metamagnetic transition at higher field. For example, the critical field is $\mu_0H_C \approx 2.5$ T at 1.8 K and 1.5 T at 7.5 K. At 7 T the curves show that the material is not fully saturated, but it is likely that the metamagnetic transition changes the antiferromagnetic order to a ferromagnetic one.

To further investigate the metamagnetic transition, ZFC-FC measurements were performed at 4 T (Figure 5. 9.). The form of the 4 T curve suggests ferromagnetic rather than an antiferromagnetic ordering at this field. The Curie temperature, T_C = 7.4 K, was assigned from the inflection point of the ZFC and FC curves. There is small deviation between the ZFC and FC curves below the Curie temperature.

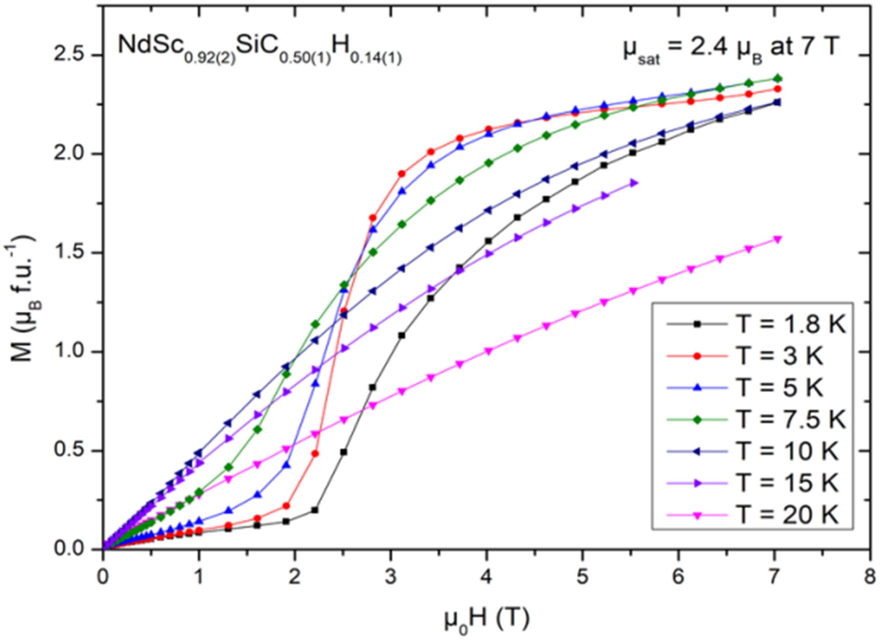

Figure 5. 8. Isothermal magnetisation curves of $NdSc_{0.92(1)}SiC_{0.5}H_{0.14(1)}$. The image on the right shows a zoom on the low field section of the curves on the left.

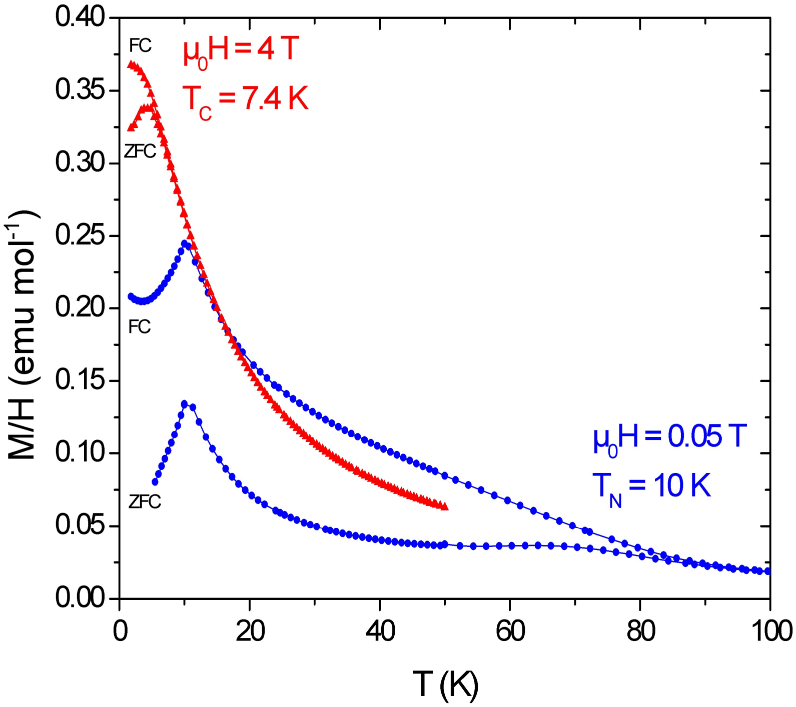

Figure 5. 9. ZFC-FC magnetisation curves for $NdSc_{0.92(1)}SiC_{0.5}H_{0.14(1)}$ at 0.05 T and 4 T.

5.3.2. Magnetic Structure of $NdSc_{0.92(2)}Si\ C_{0.5}H_{0.14(1)}$

The measurements of magnetisation and susceptibility show a change in the type of magnetic order of $NdScSiC_{0.5}$ upon hydrogenation. The effect of this hydrogen insertion on the magnetic structure is therefore of significant interest. In order to further investigate this, neutron diffraction was performed on this sample on the D1B beamline at the ILL in Grenoble, France with λ = 2.52 Å. Diffraction patterns were collected during the cooling of this material from 100 K to 1.5 K. No change in the intensity of the peaks is observed between 100 K and 11 K, magnetic peaks appearing only below 11 K. This is illustrated in Figure 5. 10., showing the patterns collected at 11 K and at 1.5 K with the difference between the two and in Figure 5. 11., plotting the evolution with temperature of the integrated intensities of the 111 and 214 magnetic peaks (as labelled in Figure 5. 10.). This last figure clearly evidences an increase in the intensity of the magnetic peaks below 11 K with a steady increase until 5 K, below which only slight variations in intensity are observed. This is consistent with the ZFC-FC magnetisation and specific heat capacity curves used to assign the T_N = 10 K.

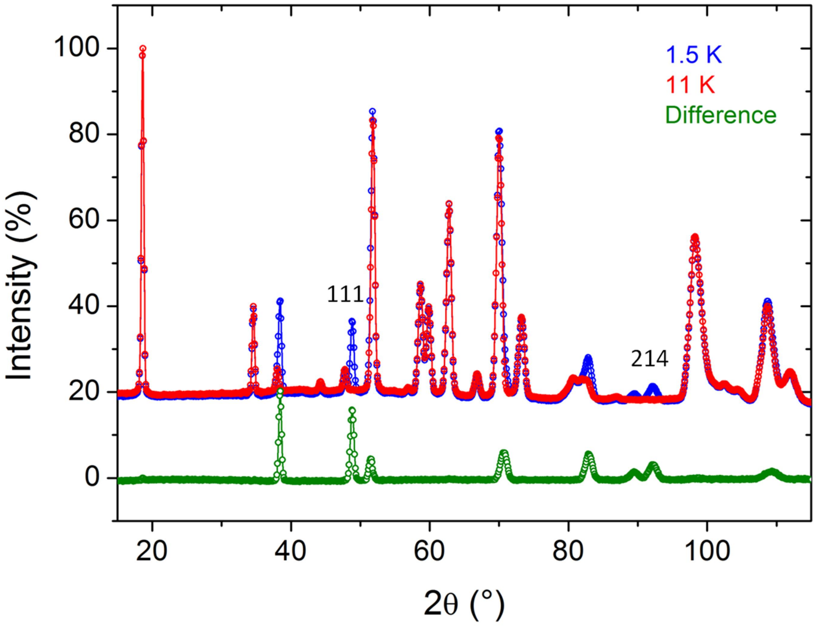

Figure 5. 10. Neutron diffraction pattern of $NdSc_{0.92(2)}SiC_{0.5}H_{0.14(1)}$ at 11 and 1.5 K with the difference pattern plotted below to illustrate the magnetic peaks.

The new magnetic peaks do not correspond with the positions of the nuclear peaks of the main phase but rather with reflections that are forbidden by symmetry in the *I4/mmm* space group of the crystal structure (*h* + *k* + *l* = odd). This indicates that the nuclear and magnetic structures do not share the same symmetry. The difference pattern in Figure 5. 10. was used to index the magnetic peaks and the propagation vector was found to be **k** = (1 0 0). Thus the magnetic and crystal unit cells are the same size but with a loss of the *I* cell centring in the magnetic structure. At 1.5 K, the best model used to refine the neutron diffraction data is an antiferromagnetic structure consisting of Nd moments aligned along the *c* axis in ferromagnetic double layers, stacked antiferromagnetically along the *c* axis as illustrated in Figure 5. 12. with that of the parent carbide for comparison.

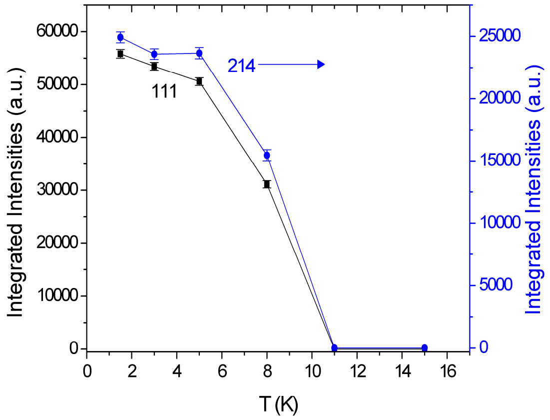

Figure 5. 11. Temperature dependence of the integrated intensities of the 111 and 214 magnetic peaks.

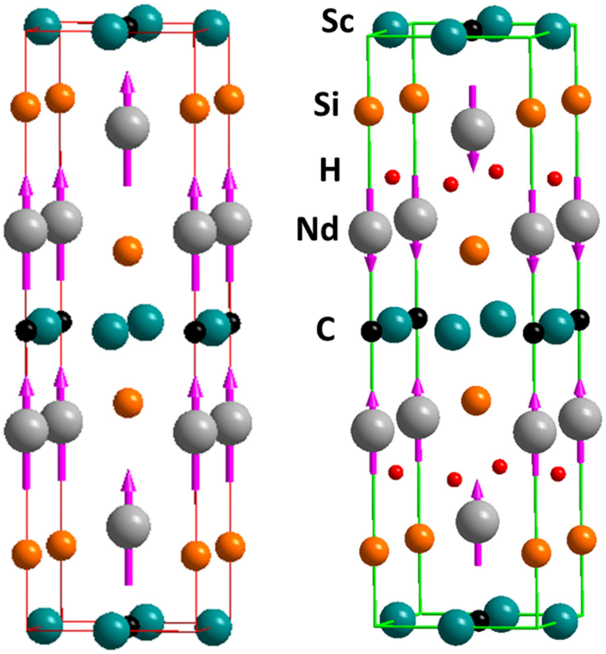

Figure 5. 12. Magnetic structure of $NdScSiC_{0.5}$ (left) and $NdSc_{0.92(2)}Si\ C_{0.5}H_{0.14(1)}$ (right)

The fit of the experimental data using this model is depicted in Figure 5. 13. and a summary of the refined structure parameters is given in Table 5. 8. Therefore it appears that partial hydrogen insertion in $NdScSiC_{0.5}$ modifies the magnetic interactions between the layers of Nd_4 tetrahedra. The refined magnetic moment (which is plotted against temperature in Figure 5. 14.) attains a value of 2.73(2) μ_B at 1.8 K. This is slightly higher than the moment of 2.4 μ_B seen in the M(H) curves at 7 T, as expected since the saturation magnetisation was not completely reached at this field. This confirms that the field induced metamagnetic transition corresponds to a change from an antiferromagnetic to a ferromagnetic state with a spin flip of one out of every two ferromagnetic double layers. The magnetic moment value is significantly below the expected value (gJ) of 3.27 μ_B for a trivalent Nd magnetic system and also smaller than the refined Nd magnetic moment of 3.09(4) μ_B for the parent $NdScSiC_{0.5}$ material. This reduction may stem from the creation of new Nd-H bonding states or, most likely, from a modification of the CEF effect after hydrogenation.

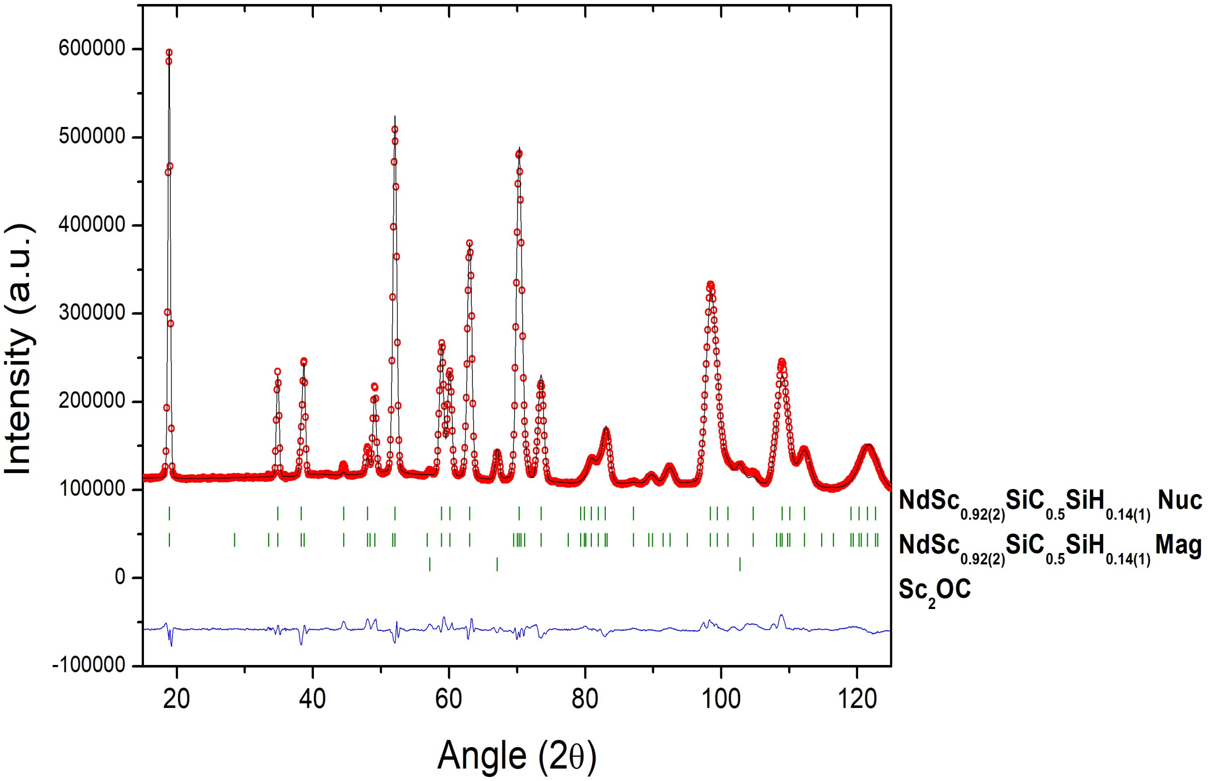

Figure 5. 13. Refinement of the magnetic structure of $NdSc_{0.92(2)}Si\ C_{0.5}H_{0.14(1)}$ at 1.5 K.

Table 5. 8. Summary of refined parameters from the refinement of the magnetic structure of $NdSc_{0.92(2)}Si\ C_{0.5}H_{0.14(1)}$.

T (K)	a (Å)	*c* (Å)	z_{Nd}	z_{Si}	Nd moment (μ_B)	Nuclear R-Bragg (%)	Magnetic R-Bragg (%)	R_P (%)	R_{wp} (%)
1.5	4.37851(6)	15.3765(5)	0.330(2)	0.130(3)	2.74(2)	4.26	7.45	7.64	7.05

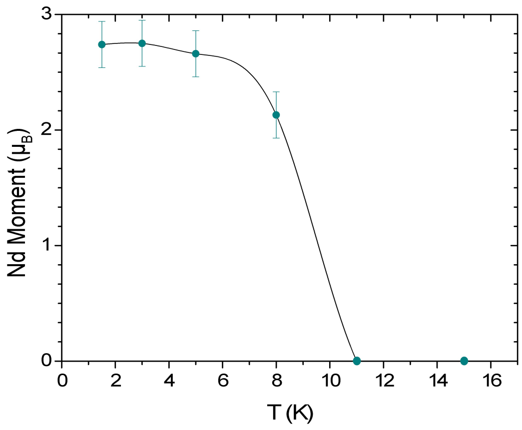

Figure 5. 14 Evolution with temperature of the refined Nd magnetic moment in $NdSc_{0.92(2)}Si\ C_{0.5}H_{0.14(1)}$.

5.3.3. Magnetic Properties of $CeSc_{0.90(2)}SiC_{0.49(2)}H_{0.25(4)}$

Since hydrogenation of the $NdScSiC_{0.5}$ material induces a change in the type of magnetic order, the magnetic properties of the $CeSc_{0.90(2)}SiC_{0.49(2)}H_{0.25(4)}$ material were investigated to determine if a similar effect can be observed for this system through hydrogen insertion. As described in chapter 4 the parent carbide is an antiferromagnet with a Néel temperature of 13 K that undergoes a spin reorientation to a tilted anti-ferromagnetic structure at 3.3 K. The inverse of the magnetic susceptibility, plotted against temperature and fitted with the Curie-Weiss law is shown in Figure 5. 15 (left) as well as the ZFC-FC magnetisation curves at $\mu_0H = 0.05$ T for $CeScSiC_{0.5}$ and $CeSc_{0.90(2)}SiC_{0.49(2)}H_{0.25(4)}$ in Figure 5. 15 (right). $CeSc_{0.90(2)}SiC_{0.49(2)}H_{0.25(4)}$ is a Curie-Weiss paramagnet with $\mu_{eff} = 2.73\ \mu_B\ Ce^{-1}$, which is close to the $\mu_{eff} = 2.56\ \mu_B\ Ce^{-1}$ seen for trivalent Ce systems. The paramagnetic Curie temperature is slightly positive with a value of $\theta_P = 5.4$ K.

The ZFC-FC magnetisation curves of $CeSc_{0.90(2)}SiC_{0.49(2)}H_{0.25(4)}$ show three anomalies: a small jump around 23 K, a broad maximum around 13-14 K and a sharp increase at 3.5 K (assigned from point of inflection of the curve). From this measurement, the ordering temperature of the carbide-hydride as well as the type of order remains unclear. In order to clarify this, we performed specific heat measurements as this characterisation method is usually less hampered by the presence of secondary phases. Figure 5. 16. shows the specific heat capacity measurement for $CeSc_{0.90(2)}SiC_{0.49(2)}H_{0.25(4)}$. The hydride carbide presents a broad peak at 13.5 K as well as a tiny anomaly at lower temperatures, around 3 K. The combination of magnetisation and specific heat measurements suggests that $CeSc_{0.90(2)}SiC_{0.49(2)}H_{0.25(4)}$ orders antiferromagnetically around 13.5 K. Thus the carbide hydride has a Néel temperature close to that of the parent carbide $CeScSiC_{0.5}$. The sharp increase of the magnetisation around 3.5 K could be ascribed either to a spin reorientation of the main phase or to the ferromagnetic ordering of a secondary phase. The small anomaly visible around 23 K on the ZFC-FC curve could also be due to a secondary phase, possibly $Ce_{15}Si_9C$ whose magnetic properties have not yet been reported in the literature.

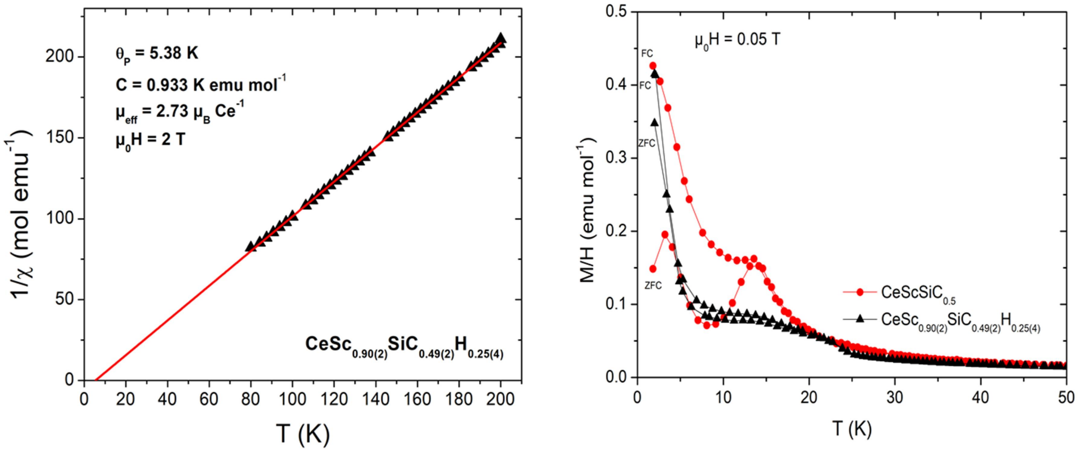

Figure 5. 15. Left) Temperature dependence of the inverse magnetic susceptibility of $CeSc_{0.90(2)}SiC_{0.49(2)}H_{0.25(4)}$ in an applied field of 2 T. Right) ZFC-FC magnetisation curves for $CeScSiC_{0.5}$ and $CeSc_{0.90(2)}SiC_{0.49(2)}H_{0.25(4)}$ at 0.05 T.

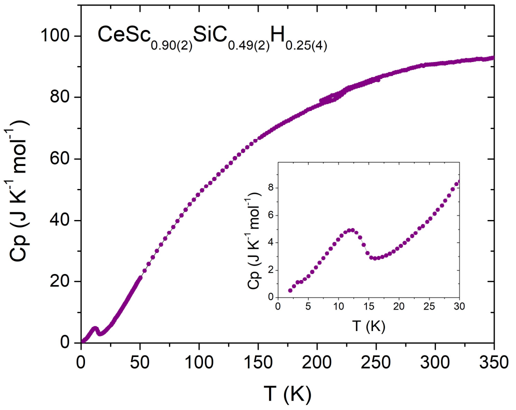

Figure 5. 16. Temperature dependence of the heat capacity, C_P, at low temperature for $CeSc_{0.90(2)}SiC_{0.49(2)}H_{0.25(4)}$. Inset shows a zoom of low temperature region

The isothermal magnetisation M(H) curves in fields of up to 7 T for $CeSc_{0.90(2)}SiC_{0.49(2)}H_{0.25(4)}$ are shown in Figure 5. 17. with the image on the right presenting a zoom on the low field portion of the plot. The M(H) curves exhibit a linear behaviour at low fields followed by a metamagnetic transition at higher fields for the curves below 15 K. For example, the critical field at 1.8 K amounts to μ_0H_C = 3.5 T. This confirms the antiferromagnetic type order in $CeSc_{0.90(2)}SiC_{0.49(2)}H_{0.25(4)}$ below 15 K. At 1.8 K the curvature of the M(H) isotherm at very low field suggests a small additional contribution from a ferromagnetic impurity as theorised previously. The sample is clearly still far from saturation at 7 T with a magnetic moment of 1.5 μ_B f.u.$^{-1}$, but the form of the curves suggests a ferromagnetic or canted ferromagnetic ordering.

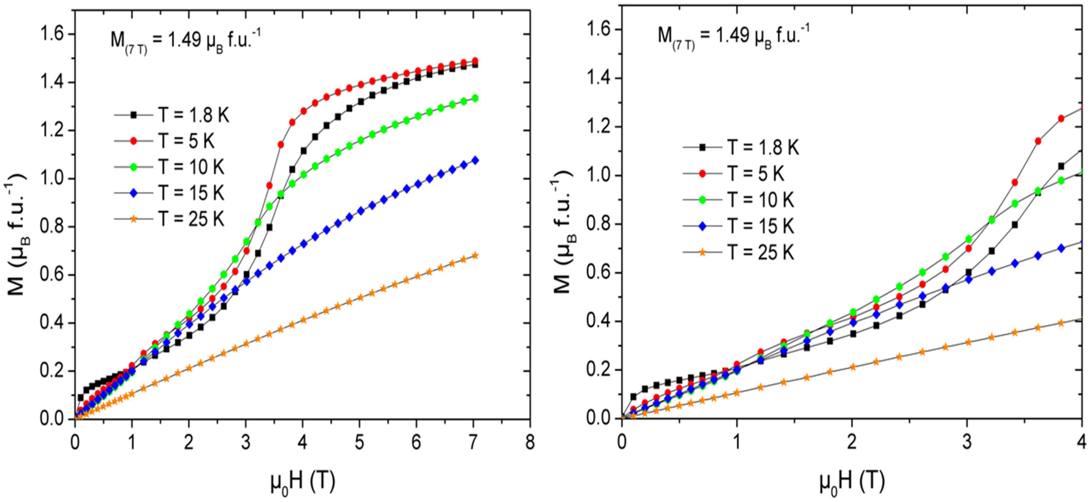

Figure 5. 17. Isothermal magnetisation curves of the $CeSc_{0.90(2)}SiC_{0.49(2)}H_{0.25(4)}$ system. The figure on the right shows the low field portion of the curves.

We have recently received the results of neutron diffraction on $CeSc_{0.90(2)}SiC_{0.49(2)}H_{0.25(4)}$ in order to determine its magnetic structure. At the time of writing we have not yet resolved the magnetic structure. However we observe that, above 15 K, there is no change in the pattern with changing temperature. Below 15 K, we observe the appearance of a number of magnetic peaks coinciding with the nuclear peaks of the major phase. Figure 5. 18. shows a zoom of the principle magnetic peak for $CeSc_{0.90(2)}SiC_{0.49(2)}H_{0.25(4)}$. It shows, unambiguously an increase in intensity below 15 K, providing further confirmation that the major phase orders magnetically between 15 K and 10 K.

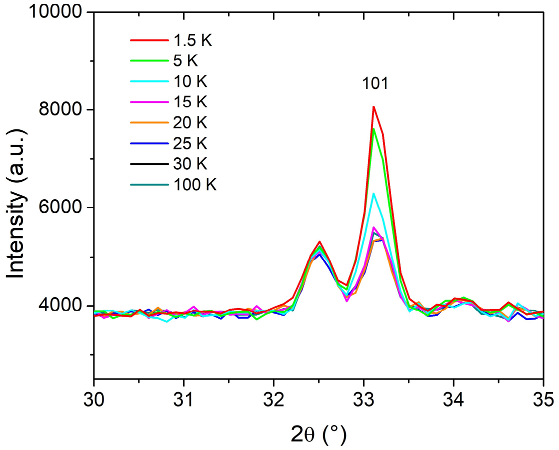

Figure 5. 18. Zoom of the 101 peak in the neutron diffraction patterns of $CeSc_{0.90(2)}SiC_{0.49(2)}H_{0.25(4)}$ collected between 100 K and 1.5 K on the G4.1 beamline at the LLB, France.

5.4 Conclusion

In this chapter we have demonstrated that the empty tetrahedral sites in the RScSiC$_{0.5}$ systems (R = Ce, Nd) can be partially filled with hydrogen by solid gas reaction at 40 bars and 450°C. This causes a slight decrease in the *a* parameter and an increase in the *c* parameter. Due to the chemical pressure applied by the occupied C sites only 14(1) % of the tetrahedral sites can be filled with hydrogen in the Nd system and 25(4) % of the sites in the Ce system. This changes the type of magnetism in NdScSiC$_{0.5}$ from a ferromagnet with T_C = 55 K to an antiferromagnet with T_N = 10 K. The magnetic structure of NdSc$_{0.92(2)}$Si C$_{0.5}$H$_{0.14(1)}$ consists of double layers of ferromagnetic Nd moments aligned along the *c* axis and couple antiferromagnetically between adjacent layers along this axis. Thus hydrogenation of NdScSiC$_{0.5}$ causes a change in the type of magnetic coupling between layers of Nd$_4$ tetrahedra along the *c* axis, along with a slight reduction of the Nd magnetic moment. For the Ce system, preliminary measurements indicate that it remains antiferromagnetic around T_N = 13 K after hydrogenation. Preliminary neutron diffraction data is currently being analysed in order to confirm this assumption.

5.5. Bibliography

Atoji, M. ((1966)) 'Crystals and magnetic structures of CeC$_2$, PrC$_2$ and NdC$_2$', *Physics Letters*, pp. 21–

22. doi: 10.1016/0031-9163(66)90039-4.

Atoji, M. ((1978)) ‘Neutron diffraction studies of Pr_2C_3, Nd_2C_3, and Dy_2C_3 at 300 to 1.6K’, *Journal of Solid State Chemistry* BV, 26(1), pp. 51–57. doi: 10.1016/0022-4596(78)90132-9.

Boulet, P., Weitzer, F., Hiebl, K. and Noel, H. ((2001)) ‘Structural chemistry, magnetism and electrical properties of binary Nd silicides’, *Journal of Alloys and Compounds*, 315(1–2), pp. 75–81. doi: 10.1016/S0925-8388(00)01304-9.

Chevalier, B., Gaudin, E., Tencé, S., Malaman, B., Fernandez, J. R., André, G. and Coqblin, B. ((2008)) ‘Hydrogenation inducing antiferromagnetism in the heavy-fermion ternary silicide CeRuSi’, *Physical Review B - Condensed Matter and Materials Physics*, 77(1), pp. 1–10. doi: 10.1103/PhysRevB.77.014414.

Chevalier, B., Hermes, W., Heying, B., Rodewald, U. C., Hammerschmidt, A., Matar, S. F., Gaudin, E. and Pöttgen, R. ((2010)) ‘New Hydrides REScSiH and REScGeH (RE = La, Ce): Structure, Magnetism, and Chemical Bonding’, *Chemistry of Materials*, 22(17), pp. 5013–5021. doi: 10.1021/cm101290f.

Isnard, O., Miraglia, S., Soubeyroux, J., Fruchart, D., Deportes, J. and Buschow, K. H. J. ((1993)) ‘Structural study and magnetic characterization of $Th_2Fe_{17}D_5$, $Th_2Fe_{17}C_xH_{5-x}$ and $Th_2Fe_{17}N_3$’, *Journal of Physics: Condensed Matter*. 5 (1993) p. 5481-5490. doi: 10.1088/0953-8984/5/31/012

Korst, W. L. and Warf, J. C. ((1966)) ‘Rare Earth-Hydrogen Systems. I. Structural and Thermodynamic Properties’, *Inorganic Chemistry*, 5(10), pp. 1719–1726. doi: 10.1021/ic50044a018.

Lang, D. A., Zaikina, J. V., Lovingood, D. D., Gedris, T. E. and Latturner, S. E. ((2010)) ‘Ca_2LiC_3H: A New Complex Carbide Hydride Phase Grown in Metal Flux’, *Journal of the American Chemical Society*, 132(49), pp. 17523–17530. doi: 10.1021/ja107436n.

Maehlen, J. P., Yartys, V. A. and Hauback, B. C. ((2003)) ‘Structural studies of deuterides of yttrium carbide’, *Journal of Alloys and Compounds*, 351(1–2), pp. 151–157. doi: 10.1016/S0925-8388(02)01028-9.

Munir, Z. A. and Anselmi-Tamburini, U. ((1989)) ‘Self-Propagating Exothermic Reactions: The synthesis of high-temperature materials by combustion’, *Materials Science Reports, 3*, pp. 277–365.

Nguyen, J., Glandut, N., Jaoul, C. and Lefort, P. ((2015)) ‘Hydrogen insertion in substoichiometric titanium carbide’, *International Journal of Hydrogen Energy*, 40(27), pp. 8562–8570. doi: 10.1016/j.ijhydene.2015.05.009.

Obbade, S., Isnard, O., Miraglia, S. and Fruchart, D., ((1991)) ‘Hydrogenation, crystal structure and magnetic ordering of $R_2Fe_{14}C$ (R ≡ Sm, Er, Tm)’, *Journal of the Less Common Metals*, 168(2), pp. 321–328. doi: 10.1016/0022-5088(91)90314-T.

Ritter, C., Provino, A., Manfrinetti, P. and Pathak, A. K. ((2016)) ‘Tetragonal to triclinic structural transition in the prototypical CeScSi induced by a two-step magnetic ordering: a temperature-dependent neutron diffraction study of CeScSi, CeScGe and LaScSi’, *Journal of Physics: Condensed Matter*, 29(4), p. 45802. doi: 10.1088/1361-648X/29/4/045802.

Sears, V. F. ((1992)) ‘Neutron scattering lengths and cross sections’, *Neutron News*, 3(3), pp. 26–37. doi: 10.1080/10448639208218770.

Singh, S. K., Dhar, S. K., Mitra, C., Paulose, P. L., Manfrinetti, P. and Palenzona, A. ((2001)) ‘The nature of magnetism in CeScSi and CeScGe’, *Journal of Physics: Condensed Matter*, 13(16), pp. 3753–3766. doi: 10.1088/0953-8984/13/16/306.

Skripov, A. V., Wu, H., Udovic, T. J., Huang, Q., Hempelmann, R., Soloninin, A. V., Rempel, A. A. and Gusev, A. I. ((2009)) ‘Hydrogen in nonstoichiometric cubic niobium carbides: Neutron vibrational spectroscopy and neutron diffraction studies’, *Journal of Alloys and Compounds*, 478(1–2), pp. 68–74. doi: 10.1016/j.jallcom.2008.12.012.

Tashmetov, M. Y., Em, V. T. T., Lee, C. H. H., Choi, Y. N. N., Lee, J. S. S., Shekhtman, V. S. S. and Dolukhanyan, S. K. K. ((2005)) ‘Neutron diffraction study of $Ti_{0.8}V_{0.2}C_{0.62}$ and $Ti_{0.8}V_{0.2}C_{0.62}H_x$’, *Physica B: Condensed Matter*, 369(1–4), pp. 254–260. doi: 10.1016/j.physb.2005.08.020.

Tencé, S., Isnard, O., Wrubl, F. and Manfrinetti, P. ((2014)) ‘A neutron diffraction study of the $R_{15}Ge_9C$ compounds (R=Ce, Pr, Nd)’, *Journal of Alloys and Compounds*, 594, pp. 148–152. doi: 10.1016/j.jallcom.2014.01.115.

Tencé, S., Mahon, T., Gaudin, E., Chevalier, B., Bobet, J.-L. J.-L., Flacau, R., Heying, B., Rodewald, U. C. U. C. and Pöttgen, R. ((2016)) ‘Hydrogenation studies on NdScSi and NdScGe’, *Journal of Solid State Chemistry*, 242, pp. 168–174. doi: 10.1016/j.jssc.2016.02.017.

Wrubl, F., Shah, K. V., Joshi, D. A., Manfrinetti, P., Pani, M., Ritter, C. and Dhar, S. K. ((2011)) ‘Superstructure and magnetic properties of R15X9C compounds (R=rare earth; X=Si and Ge)’, *Journal of Alloys and Compounds*, 509(23), pp. 6509–6517. doi: 10.1016/j.jallcom.2011.03.092.

Zhang, H., Shen, B. G., Xu, Z. Y., Zheng, X. Q., Shen, J., Hu, F. X., Sun, J. R. and Long, Y. ((2012)) ‘Reduction of hysteresis loss and large magnetocaloric effect in the C- and H-doped La(Fe, Si)13 compounds around room temperature’, *Journal of Applied Physics*, 111(7), pp. 1–4. doi: 10.1063/1.3670608.

Conclusions and Outlook

This thesis is mainly dedicated to studying the influence of light elements insertion on the structural and physical properties of CeScSi-type intermetallics. This work has several principle aims: to resolve some of the uncertainty around the structural transition exhibited by CeTiGe between the CeFeSi and CeScSi structure types, to extend the hydrogenation work that has been performed on the materials crystallising in the CeScSi structure type, and to study the insertion of other light elements such as carbon or boron into the vacant interstitial sites of these compounds.

Through investigations of the thermal treatment of CeTiGe we confirm that the CeScSi structure type corresponds to the high temperature form ($T > 1273$ K), while the CeFeSi structure type belongs to the low temperature form ($T < 1173$ K). We note that the structural transition is significantly faster in powdered samples than block samples. We use the classic technique of solid gas reactions to insert hydrogen into the CeScSi type compounds CeTiGe, NdScSi and GdScGe. This causes an anisotropic expansion of the unit cell with the a parameter decreasing and the c parameter strongly increasing while conserving the *I4/mmm* symmetry of the CeScSi-type parent compound. Interestingly, hydrogenation of both the CeFeSi-type and CeScSi-type CeTiGe always produces the filled CeScSi-type hydride, indicating that this hydride is more stable than the corresponding filled CeFeSi-type hydride. Neutron diffraction and hydrogen absorption measurements evidence that CeTiGe and NdScSi can absorb one and a half atoms of hydrogen per formula unit. The hydrogen in these materials can occupy the vacant R_4 tetrahedral sites (R = rare earth) and the RT_4 square based pyramidal sites (T = Ti or Sc) for filled compositions $CeTiGeH_{1.5}$ and $NdScSiH_{1.5}$. However, hydrogen absorption measurements show that GdScGe absorbs just one atom of hydrogen per formula unit, consistent with the filling of the R_4 tetrahedral sites only.

We also demonstrate that intermetallic carbides can be synthesised by including carbon in the melting step of the synthesis of the RScSi phases (R = La, Ce, Nd and Gd). The $RScSiC_X$ phases crystallise well from the melt and retain the *I4/mmm* space group of the parent compound. Carbon insertion causes an anisotropic expansion of the unit cell with the a parameter increasing and the c parameter decreasing *i.e.* the opposite trend observed during hydrogenation. Single crystal X-ray diffraction and powder neutron diffraction both confirm, unambiguously, that carbon atoms are localised in the R_2Sc_4 octahedral sites, leaving the R_4 tetrahedra empty. Both $CeScSiC_X$ and $NdScSiC_X$ can form solid solutions with $0 \leq x \leq 0.5$ and $0.25 \lesssim x \leq 0.5$, respectively. In our final chapter we show that the empty tetrahedral sites of the $CeScSiC_{0.5}$ and $NdScSiC_{0.5}$ carbides can be partially filled with hydrogen to form $RScSiC_{0.5}H_{\sim 0.2}$. This causes a slight change in the unit cell parameters with a decreasing and c increasing, in agreement with the hydrogenation of pristine CeScSi-type intermetallics. High resolution neutron diffraction measurements confirm that the hydrogen atoms are located in the R_4 tetrahedra. The low occupation of the hydrogen site is attributed to the antagonistic structural effect induced by the filling of the R_2Sc_4 octahedra by carbon atoms.

Thus, in this work we demonstrate clearly that the CeScSi-type intermetallic systems can accept hydrogen and carbon in their crystal structures both separately and simultaneously. Our work represents an important expansion of the existing work on the insertion of light elements into these systems.

Insertion of hydrogen and/or carbon atoms in pristine CeScSi-type intermetallics induces modifications of their physical properties.

Pristine CeTiGe is a non-magnetic strongly correlated electron system. Hydrogenation seems to induce a low temperature magnetic order in this compound; however, we are unable to clearly identify the type of this magnetic order. The pristine NdScSi presents ferromagnetic order below T_C = 171 K which is severely reduced by hydrogen insertion. $NdScSiH_{1.5}$ shows the onset of a magnetic order or a spin glass state below 4 K. Similarly, the ferromagnetic order of GdScGe below T_C = 350 K is almost totally destroyed on hydrogen insertion with the hydride ordering magnetically below 6 K. Thus, it appears that, with the exception of the particular case of *R* = Ce, hydrogenation strongly reduces the magnetic ordering temperature of the pristine compounds. However, the exact nature of the magnetic ground state of the hydrides remains unclear so far due to the low temperature of the transition and/or the lack of neutron diffraction data.

Meanwhile, carbon insertion is found to cause a linear reduction in the Curie temperature of NdScSi with increasing carbon content. This reaches a minimum $T_C \approx 50$ K in $NdScSiC_{0.5}$. The magnetic structure of NdScSi has not yet been determined but $NdScSiC_{0.5}$ shows a ferromagnetic alignment of Nd moments along the *c* axis. Then, when the empty tetrahedra of the $NdScSiC_{0.5}$ carbide are partially filled with hydrogen a truly interesting effect is observed: the ferromagnetic order of the parent carbide changes to an antiferromagnetic order below the Néel temperature of 10 K. Besides, the application of high magnetic fields induces a metamagnetic transition to a ferromagnetic state.

Carbon insertion into CeScSi has a more complex effect on the magnetism. The pristine compound orders antiferromagnetically below 27 K with a spin reorientation occurring around 22 K. Complete filling of the Ce_2Sc_4 sites with carbon causes a reduction of the ordering temperature to T_N = 13.5 K and the spin reorientation to 3.3 K. The carbide shows a similar antiferromagnetic structure to that of the pristine compound but the magnetic coupling between adjacent Ce layers into the Ce_4 tetrahedra blocks changes sign. When the carbon site is only partially filled, as in $CeScSiC_{0.25}$, a more complicated magnetic order is observed. After partial hydrogenation of the carbide $CeScSiC_{0.5}$, the obtained $CeScSiC_{0.5}H_{0.25(4)}$ phase orders antiferromagnetically below around 13.5 K as observed in the pristine carbide. Magnetisation measurements confirm an antiferromagnetic order with the occurrence of a metamagnetic transition to a ferromagnetic state above a critical field of about 3.5 T.

Clearly, the insertion of hydrogen and carbon individually causes a general reduction in the magnetic ordering temperatures of the CeScSi-type intermetallics with the effect of hydrogen being more pronounced than that of carbon. Hydrogenation of the $NdScSiC_{0.5}$ carbide has the especially interesting effect of changing the type of magnetic order from ferromagnetic to antiferromagnetic. Our work therefore illustrates that interesting effects can be induced in the CeScSi-type intermetallics through light element insertion.

The electrical transport properties of a number of our insertion compounds have also been investigated. In GdScGe we note that hydrogenation changes the metallic conduction of the pristine parent compound to a non-classical metallic type. Preliminary measurements on the $CeScSiC_{0.5}$ and $NdScSiC_{0.5}$ phases indicate that carbon insertion has a similar effect. Thus, insertion of light element such as hydrogen or carbon seems to be a powerful way to strongly modify the transport properties of these CeScSi-type materials.

In order to complete the work a number of experiments are still required. In particular, calculations using the density functional theory are required to understand the exact effects of hydrogen and carbon on the magnetic and electronic transport properties. These calculations can also help to confirm our hypotheses that the CeScSi-type $CeTiGeH_{1.5}$ is the most stable of the two possible hydrides in this system and that the position of H and C in the octahedral site R_2Sc_4 is slightly different for chemical bonding reasons, as suggested by the structural changes.

As the most interesting effect of the insertion of these light elements is a drastic modification of the electronic transport properties, further investigations are highly warranted.